Bond of Corroded Reinforcement in Partial Depth Repairs in Reinforced Concrete Elements

by

Hisham Alabduljabbar

A thesis

presented to the University of Waterloo

in fulfillment of the

thesis requirement for the degree of

Doctor of Philosophy

in

Civil Engineering

Waterloo, Ontario, Canada, 2017

Examining Committee Membership

The following served on the Examining Committee for this thesis. The decision of the Examining Committee is by majority vote.

External Examiner	NAME: Michael Bartlett Title: Professor and Associate Dean (Undergraduate Studies)
Supervisor(s)	NAME: Jeffrey West Title: Department Chair, P.Eng., FACI,
Professor	
	NAME: Khaled Soudki Title: Professor, PhD, PEng, FACI 1965 – 2013
Internal Member	NAME: Tim Topper Title: P. Eng., Dist. Professor Emeritus
	NAME: Adil Al-Mayah Title: P. Eng., Assistant Professor
Internal-external Member	NAME: Hamid Jahed Title: Professor, Assoc Chair Grad Studies

AUTHOR'S DECLARATION

I hereby declare that I am the sole author of this thesis. This is a true copy of the thesis, including any required final revisions, as accepted by my examiners.

I understand that my thesis may be made electronically available to the public.

Abstract

The bond in a reinforcement concrete (RC) structure is represented by the force transfer between the reinforcing bar and the surrounding concrete. All the RC structures are designed to have a perfect bond between the reinforcing bar and the surrounding concrete. However, corrosion of the reinforcing bar in the RC members is one of the main reasons that affect the bond efficiency in RC member. The deterioration of bond in RC element leads to decrease the service life of the RC structure and may result in sudden failure. Most of the previous research focuses on repairing the corroded RC member with FRP wrapping without cleaning the corroded reinforcing bar.

The present research investigated the bond behaviour of cleaned corroded reinforcing bar repaired with partial depth repair concrete, transverse reinforcement or fiber reinforced polymer (FRP) sheets. Thirty-six beam-end specimens and twenty-four lap splice beams were cast and tested under static loading. The beam-end dimensions were 600 mm in length, 500 mm in height and 250 mm in width and reinforced with 20M bar. The test variables considered for the beam-end specimens were: four corrosion levels (5%, 7.5%, 10% and 15% mass loss level) and compared with non-corroded bar. Also, four bonded lengths were studied (200 mm, 250 mm, 300 mm, and 350 mm). Moreover, four partial depth repair concrete were used (commercial prepackaged self-consolidating concrete (SCC1), another different commercial prepackaged self-consolidating concrete (SCC2), self-consolidating concrete that was mixed in place and had similar proportions to the monolithic mixes (SCC3) and normal concrete (NC) mix design was also cast in place and had exactly the same proportions as the monolithic mixes but was used as a partial depth repair). All of the partial depth repair concretes were compared with monolithic beam-end specimen.

The lap splice beams dimensions were 2200 mm in length, 350 mm in height and 250 mm in width and reinforced with two 20M lap spliced bars in the tension zone of the constant moment region with 300 mm splice length. Also, the lap splice beams were reinforced with two 10M continuous bars in the compression zone. The test variables considered for the lap splice beams were: commercial prepackaged self-consolidating concrete extended with 50% of 13 mm coarse aggregate (SCC50) was used as the main partial depth repair. It should be mentioned that

SCC50 was the same partial depth repair concrete (SCC2) used for the beam-end specimens. Also, Three lap splice beams repaired with commercial prepackaged self-consolidating concrete without coarse aggregate (SCC0) were also included to study the effect of coarse aggregate on bond behavior. The lap splice beams repaired with partial depth repair concrete were compared with monolithic lap splice beam. Moreover, two types of confinements were considered in the lap splice beams: transverse reinforcement and carbon fiber reinforced polymer (CFRP) sheets. Six lap spliced beams were confined with transverse reinforcement and six were wrapped with CFRP sheets.

This research found that the average bond strength increased as the bar mass loss increased for all bonded lengths. As the bonded length increased, the average bond strength decreased and the corresponding bar slip increased. In the beam-end specimens, the average bond strength of monolithic beam-end specimens was higher than the average bond strength of all types of the partial depth repair regardless the compressive strength of concrete. That was mainly because of internal shear cracks at the interface between the partial depth repair and the substrate concrete. However, since there was not shear at the constant moment region in the lap splice beams, the lap splice beams repaired with partial depth repair concrete with similar properties of monolithic concrete and had higher concrete strength showed higher average bond strength than the monolithic lap splice beams. Although the partial depth repair concrete SCC0 had higher compressive strength than SCC50 and the monolithic concrete; it had the lowest average bond strength. That because the absence of the coarse aggregate in SCC0 led to a decreased splitting strength and reduced fracture energy; and so the average bond strength was decreased. All self-consolidating concrete (SCC) partial depth repairs showed better bonding than the normal concrete (NC) partial depth repair. The bond strength of beams repaired with FRP sheets was higher than that of the beams confined with transverse reinforcement. The transverse reinforcement increased the average bond strength and the corresponding slip by (15% - 29%) and (32% - 62%) compared to the unwrapped beams, respectively. However, the beams confined with FRP sheets showed an increase in the bond strength and the corresponding slip by (34 - 49%) and (56 - 260%) compared to the unconfined beams, respectively.

A multiple linear regression analysis was conducted to predict the effect of mass loss level, bonded length and presence repair concrete on the average bond strength of beam-end specimens. Also, a model was calibrated to predict the average bond strength with increasing the mass loss level of the reinforcing bar of lap splice beams. Moreover, another model was used to allow the design engineers to estimate the bond stress distribution along the spliced reinforcing bars as the splitting crack propagated.

Acknowledgements

First and foremost, I would like to thank and praise Allah for helping and guiding me through this work and giving me the patience and health necessary to complete my PhD degree. I will always be grateful to have had the opportunity of working with my previous supervisor Professor Khaled Soudki, may his soul rest in peace. He supported me and provided help and guidance in planning my research project.

I would like to express my sincere gratitude and appreciation to my Supervisor Prof. Jeffrey West for his patient help, guidance, and encouragement. I would also like to thank my committee members, Professor(s) Michael Bartlett, Hamid Jahed, Tim Topper and Adil Al-Mayah for reviewing my thesis, evaluating my research, and for their insightful feedback. Special thanks to prof. Topper who was helped me patiently and gave me much of his time to help me to understand the fundamental mechanics of my research.

The help of Douglas Hirst, Richard Morrison and Rob Sluban from Civil Engineering in the lab work is appreciated and acknowledged.

I am also grateful to Prince Sattam bin Abdul-Aziz University in Al-Kharj, Saudi Arabia for fully sponsoring my scholarship and also for the continued support from Saudi Arabian Cultural Bureau in Canada throughout my study.

I also would also like to thank my friends and my colleagues who assisted me throughout various stages of this study: Rayed Alyousef, Abdulaziz Alaskar, Ayman Shihata, Omar Alromyah, Talal Alharbi, Omar Alghamdi, Mohammed Aldaej, Salman AL Mushari.

Finally, a heartfelt gratitude to my great mother Shikhah and father Abdulaziz, my wife Rana, my brothers Mohammed, Turki, Fahad and Khaled, and best friend Rayed for their true endless love and honest support that inspired me to work hard and achieve the PhD degree.

Table of Contents

List of Figures

List of Tables

Chapter 1: Introduction

1.1 Background

The design and analysis theories for reinforcement concrete (RC) members are based on the assumption that the strain in the concrete at the reinforcement level is equal to the strain of the reinforcement. This is achieved through the bond between concrete and the reinforcement. The bond between concrete and the reinforcing bar is provided by three mechanisms, which are friction, adhesion and mechanical interaction between the bar ribs and concrete (ACI 408, 2003). According to Valcuende and Parra (2009), the bond between concrete and the reinforcing bar depends on the concrete strength and the bar geometry.

Corrosion of the reinforcement in a reinforced concrete structure is one of the durability issues that may affect the structure capacity. The corrosion causes a reduction in the cross-sectional area of the steel reinforcement which leads to a decrease in the load carrying capacity. In addition, the rust products produced from the corrosion process are larger in volume than the steel itself. This increase in volume leads to tensile stresses within the concrete causing it to crack at the level of the steel reinforcement, thus reducing the bond between the concrete and the reinforcing bar (ACI 222, 2001).

As the severity of the corrosion increases, the number and the width of cracks will increase and the area of the steel reinforcement is decreased. This may lead to an increase in the bar slip and deflection of the concrete member which affect the serviceability of RC member (SLS). Also, severe corrosion may decrease the load carrying capacity of the RC member, which could cause a sudden failure (ultimate limit state) (fib, 2000).

A partial depth repair concrete is a common approach to repair a corroded RC member. The partial depth repair includes removing the concrete damaged from corrosion, cleaning the corroded reinforcing bar from the corrosion products, roughening the surface of the substrate concrete followed by application of the repair concrete. It is important to provide a repair system with good bond between the substrate concrete and the partial depth repair concrete.

Confining the RC member with transverse reinforcement increases the bond ductility and prevents the sudden drop in load after the occurrence of a bond failure due to cracking (Zuo and Darwin, 2000). The transverse reinforcement confinement has more effect on bond strength than increasing the concrete cover (Guizani & Chaallal, 2011). Giuriani et al. (1991) concluded that the transverse reinforcement confinement is the most important factor that enhances the bond strength. The amount of transverse reinforcement strongly affected splitting failure and inhibited the propagation of the cracks; however it does not prevent splitting failure (Tepfers, 1973; Tocci, 1981).

Fiber reinforced concrete polymers (FRP) have been widely used as a rehabilitation material for existing deteriorated reinforced concrete structures. FRPs are advanced composite materials that are available in sheets or plates for repair applications and in bars for new design requirements. FRPs are advantageous due to the fact that they do not corrode, they have a high strength to weight ratio, and are easy to install.

Malumbela et al. (2011) concluded that strengthening of corroded reinforced concrete members with FRP should be considered when performing partial depth repairs in the corroded areas. The reason for this is to enhance the serviceability state of the RC member in terms of crack width due to corrosion. It has been shown that the partial depth repair can improve the load carrying capacity of corroded beams to be similar or slightly lower than the beam without corrosion (Rio et al., 2005).

1.2 Research Motivation

1.2.1 Research Needs

It is known that the bond between concrete and the reinforcing bar is essential to the strength of reinforced concrete members. There is a gap in the literature regarding the behaviour of bond of cleaned corroded reinforced concrete members repaired with partial depth repair concrete and/or transverse reinforcement or FRP sheets under static load. There is a huge number of reinforced concrete structures that are subjected to severe corrosion (e.g, structures subjected to marine environment or to de-icing salts). Most of the studies conducted corroded reinforced concrete members concentrated on affecting of corrosion on flexural strength.

1.2.2 Research Objectives

This research aims to study the bond behaviour of reinforcement concrete members that are subjected to corrosion and rehabilitated by partial depth repair concrete with or without confinement (transverse reinforcement or FRP sheets) under static load. The specific objectives of this research are:

- Investigate the bond behaviour of corroded RC member repaired with four different types of concrete (three self-consolidating concretes and one normal concrete) to study the effect of flowability, coarse aggregate content on bond strength.

- Assess the effect of corrosion level (up to 15% mass loss) on bond behaviour. The mass loss level was chosen up to 15% to exceed the mass loss level that was covered in the literature which was suggested that additional reinforcement may be required if the mass loss level was higher than 10% (ACI 364.10T-14). The cross sectional area of the rebar decreases with increasing corrosion level. Also, the surface roughness of the rebar increasing with increasing corrosion level. These factors may affect the bond strength in a partial depth repair.

- Examine the effect of the bonded length of corroded rebar on bond behavior (changing the bonded length includes changing in bonded area between the partial depth repair and the substrate concrete).
- Examine the effect of partial depth repair concrete properties (particularly coarse aggregate size and content) on bond behavior.
- Investigate the effect of internal transverse reinforcement and external FRP sheets as confinement on the bond behaviour of corroded RC members. This investigation will include a comparison between using confinement with monolithic specimens and specimens repaired with partial depth repair concrete.
- Revise an existing analytical model (ACI 408-03) that predicts the average bond strength of RC member to include the effect of mass loss level.
- Develop an analytical model, which will predict the local bond stress distribution as the splitting crack propagated.

1.3 Research Scope

The proposed research study focuses on assessing the bond strength of a corroded reinforced concrete member that has been repaired with a partial depth repair. The rebar were cleaned and the corroded length of the RC member was repaired with repair concrete. Thirty-six beam-end specimens were tested statically to study the effect of various parameters on bond strength of cleaned corroded rebar. These parameters included mass loss level (control, 5%, 7.5%, 10% and 15%), bonded length (200 mm, 250 mm, 300 mm and 350 mm) and the type and properties of the partial depth repair concrete (normal concrete NC and self-consolidating concrete SCC). The variables considered for the partial depth repair concretes included the coarse aggregate size and content, the bonding agent, silica fume and the water-to-cement ratio. Also, twenty-four lap splice beams were tested statically to study the effect of confinement (transverse reinforcement and FRP sheets) on the bond behavior of cleaned corroded bars. The mass loss level in this phase included (control, 7.5% and 15%) and the splice length was fixed as 300 mm. The best solution of the four partial depth repairs concrete that used for beam-end specimens was used to repair the lap splice beams.

The overview of thesis research plan is divided into three phases as follow:

- Twelve beam-end specimens (Phase 1)
- Twenty-four beam-end specimens (Phase 2)
- Twenty-four lap splice beams

The beam-end specimens were used at the beginning because they were easy to fabricate and simple to test, which provided the opportunity to cast and test four different types of the partial depth repair concretes. The most efficient partial depth repair concrete was used for the lap splice beams. The lap splice beams were used to provide results that could be compared with previous research on bond and repairing corroded lap splice beams to enhance the bond strength. The previous research shows a good correlation with published equations on bond strength.

1.4 Thesis Organization

A general background and literature review is summarized in Chapter 2, with experimental program of beam-end specimens given in Chapter 3. The experimental results and analysis of the beam-end specimens are provided in Chapter 4. Chapter 5 and Chapter 6 discuss the experimental program for the lap splice beams and the experimental results and analysis of the lap splice beams, respectively. Modeling of the experimental results of beam-end specimens and modeling of lap splice beams results is presented in Chapter 7 and Chapter 8, respectively. The conclusions, the recommendations for future work and research contributions are described in Chapter 9.

Chapter 2: Literature Review

2.1 Introduction

The background about the mechanism of the bond in reinforcement concrete member and the factors that affect the bond behaviour will be discussed in this chapter. Also, the bond failure modes and the effect of corrosion on deterioration of the bond between the reinforcing bar and the surrounding concrete will be presented. Moreover, this chapter discusses different methods of rehabilitating or and strengthening the bond such as partial depth repair, internal transverse reinforcement confinement (stirrups) and fiber reinforced polymer (FRP) sheets.

2.2 Bond in Reinforcement Concrete

The bond between the bar and the concrete in a reinforced concrete member is essential when considering the required development length. In a reinforced concrete member, the loads are applied directly to the concrete and are transferred from the concrete to the steel. At cracked concrete section, the tensile forces are resisted by the steel reinforcement because of weakness of concrete in tension. This transfer of the forces between steel ribs and the surrounding concrete is described as bond stresses. The bond at the interface between the steel reinforcement and the concrete consists of three components: chemical adhesion between concrete and steel (V_a), mechanical anchorage between steel ribs and surrounding concrete (V_b) and friction resistance between bar surface and concrete (V_f). Figure 2.1 illustrates the behaviour of each component (ACI 408, 2012). The chemical adhesion resists the bar slippage at the early stage of loading. As the load increases, the reinforcing bar tends to move leading to break the chemical adhesion and activate the friction and the bearing forces through the mechanical anchorage between the bar ribs and the surrounding concrete. The friction force resistance is parallel at the bar surface. The bearing of the steel ribs against the concrete accounts for the majority of the bond between the steel and the concrete compared to the chemical adhesion and friction. Thus, the mechanism of bond resistance relies mainly on the bearing of the bar ribs against the concrete to prevent the relative slip.

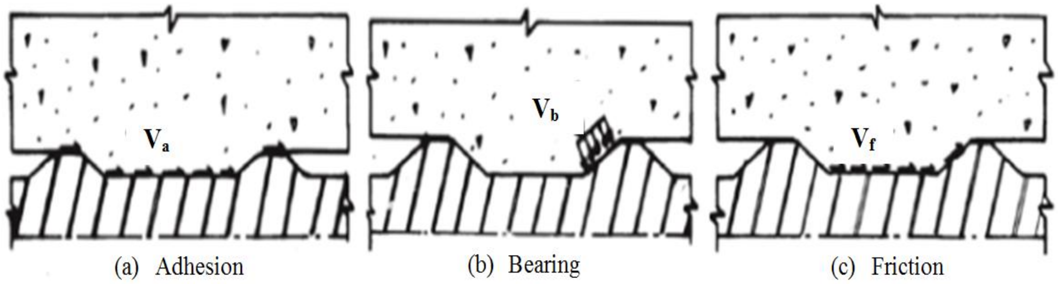

Figure 2.1 Idealized bond mechanisms of deform rebar of reinforcement concrete member (a) Adhesion (b) Bearing bond (c) Friction bond (ACI 408, 2012)

The bond efficiency is expressed as the relationship between bond stress versus bar slippage, which characterizes the variation of the local bond stress on the bar versus the total bar movement through the concrete surrounding that bar (ACI 408, 2012). From this relationship, the maximum bond capacity and the corresponding bar slip could be found. Also, this relationship could give an indication about the failure mode, which could be bond failure, or the bar could yield before the bond failure. The design equations that are proposed in codes are developed to have adequate bond strength of a reinforced concrete member. That means the bond strength will be satisfied to transfer forces from concrete to steel up to yielding of the steel without the occurrence of a bond failure, then by improving the ductility of the reinforcement concrete member (fib, 2000). The action of the bar ribs or compressed concrete wedges bearing against the concrete surrounding the reinforcing bar results in the development of circumferential tensile hoop stresses around the bar (Figure 2.2).

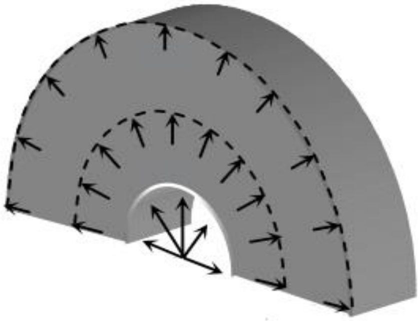

Figure 2.2 Hoop tensile stresses on the concrete surrounding the reinforcing bar (concrete (Tastani and Pantazopoulou 2012)

2.2.1 Bond Stress Development

Bond stress is primarily the result stresses transfer between the reinforcing bar and the surrounding concrete caused by the various factors previously enumerated. It can be described as a local shearing stress per unit area of the bar surface. Figure 2.3 shows the equilibrium condition of the forces where the bond forces are required for equilibrium of the internal forces.

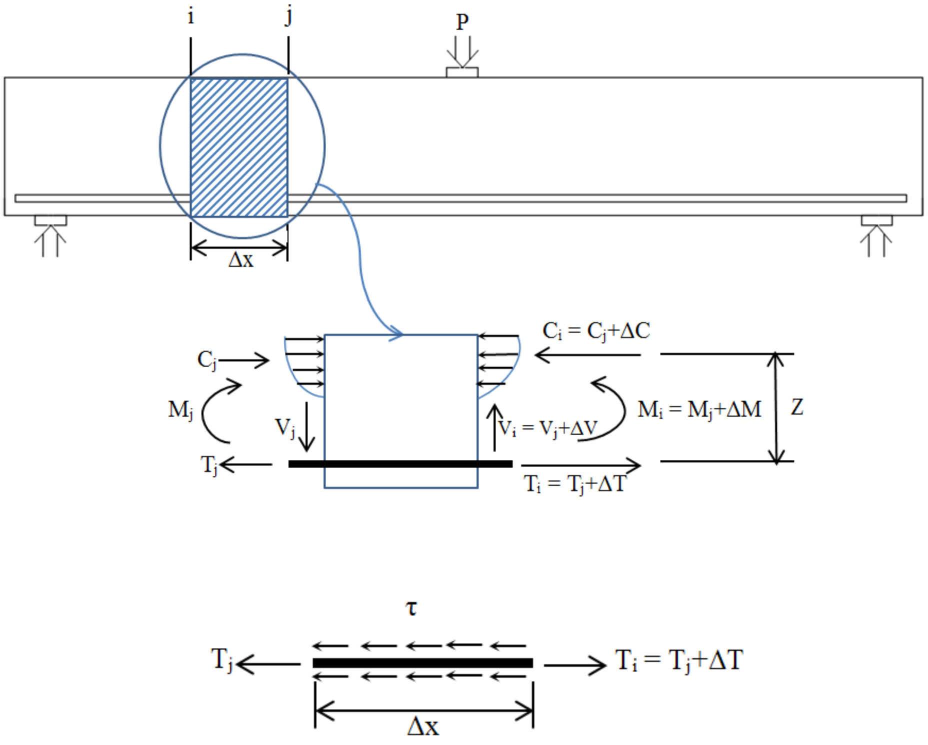

Figure 2.3 Equilibrium condition of forces

Using moment equilibrium of segments

$$M = TZ \rightarrow T = \frac{M}{Z} \rightarrow T + \Delta T = \frac{\mathrm{M}+\Delta M}{Z} \rightarrow \Delta T = \frac{\Delta M}{Z} \qquad \text{Equation (2.1)}$$

For equilibrium of the bar over Δx

$$\sum F_x = 0$$

$$T + \pi d_b \tau_{avg} \Delta x = T + \Delta T \rightarrow \pi d_b \tau_{avg} \Delta x = \Delta T$$

$$\pi d_b \tau_{avg} = \frac{\Delta T}{\Delta x} = \frac{\Delta M}{Z\Delta x}$$ Equation (2.2)

Then, the average bond strength can be written as

$$\tau_{avg} = \frac{\Delta T}{\pi d_b \Delta x} = \frac{\Delta M}{\pi d_b Z \Delta x}$$ (Equation 2.3)

From the free-body diagram

$$\frac{\Delta M}{\Delta x} = V \ \rightarrow \tau_{avg} = \frac{V}{\pi d_b Z}$$ (Equation 2.4)

Where

M: Moment (kN.m)

T: Tensile force (kN)

Z: Arm (mm)

d_b: Bar diameter (mm)

τ_{avg}: Average bond strength (MPa)

Δx: Particular distance (mm)

The bond stresses occurs at the bar surface when the normal stresses on the bar (fs) changes at a given length to maintain the equilibrium. The average bond strength was found based on the summation of forces parallel to the bar as:

$$(f_{s2} - f_{s1}) \frac{\pi d_b^2}{4} = \tau_{avg} (\pi_{db}) l, \text{ thus}$$

$$\tau_{avg} = \frac{(f_{s2} - f_{s1}) d_b}{4l}$$ Equation (2.5)

Where

f_{s1} and f_{s2}: Change in stresses at length (l) (MPa)

l: Bonded length

2.2.2 Bond Test Specimens

There are four common test methods that are used to evaluate the bond strength between steel and concrete. These methods are pullout specimen, beam-end specimen, beam anchorage specimen and beam splice specimen (Figure 2.4).

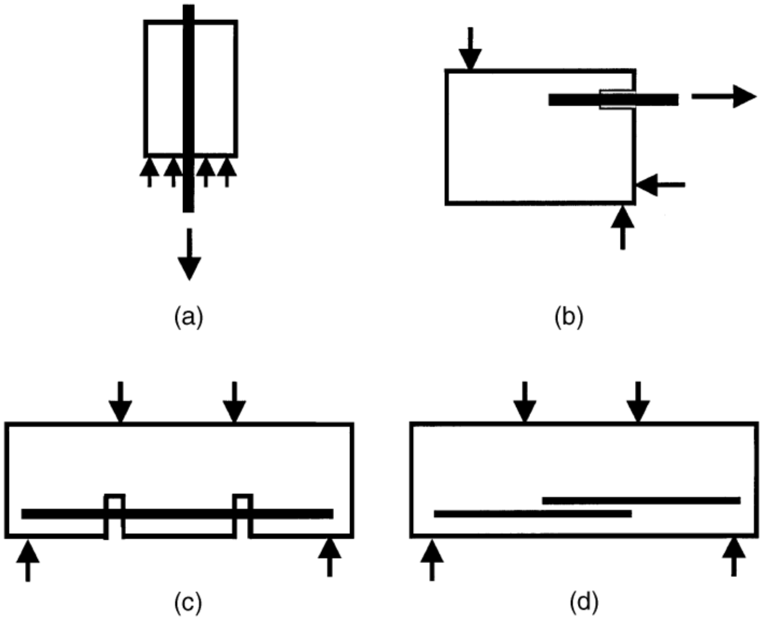

Figure 2.4 Schematic of (a) pullout specimen; (b) beam-end specimen; (c) beam anchorage specimen; and (d) splice specimen (ACI 408, 2003)

The most widely used specimen in the past was the pull-out specimen because it is the easiest test method and very simple to assemble. However, the pull-out test is the least realistic one because during this test, the bar will be subjected to a tensile force and the concrete will be subjected to a compression force near the loaded end of the bar. At the support face, both concrete and the bar surface are placed in compression which may delay bond splitting cracking (Figure 2.5). Also, the bearing stresses of the concrete against that plate cause a frictional component that resists the transverse expansion of the concrete that would result from Poisson’s ratio (MacGregor and Bartlett, 2000). This situation is different from the actual conditions for most structural members where the concrete surrounding the bar is in tension. Thus, rather in the pull out test, during movement of the rebar through the surrounding concrete, the bearing surface of the rebar ribs are subjected to compression.

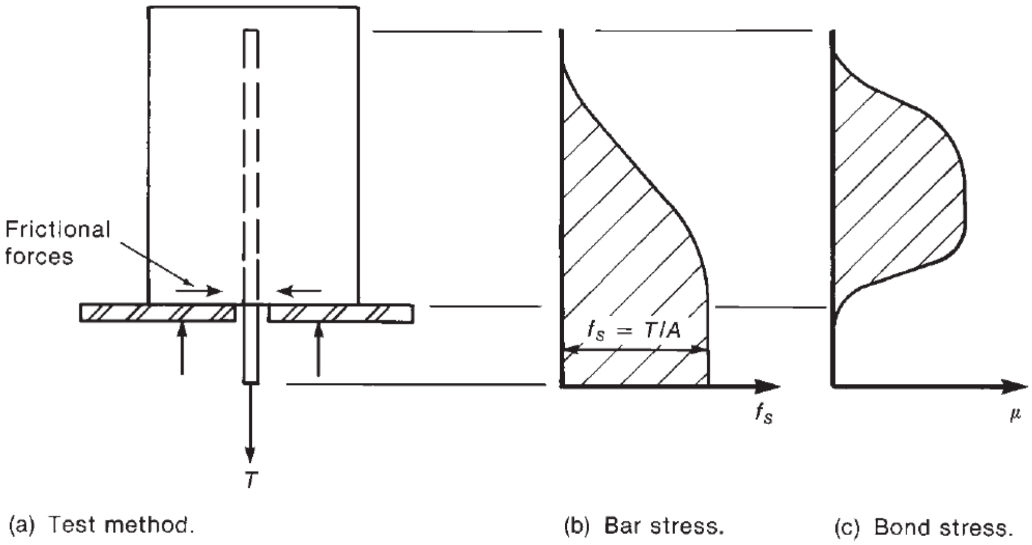

(a) Test method. (b) Bar stress. (c) Bond stress.

Figure 2.5 Pull-out test specimen (MacGregor and Bartlett, 2000)

Splice beam specimens and beam anchorage specimen (or bond beam) are used as full size members to measure splice and development strengths directly (ACI 408, 2003). The most realistic methods to measure the bond strength are the beam-end specimen and splice specimen. The beam anchorage specimen is designed to displace the reactions through pockets to avoid increasing normal stresses at the bar that caused by reactions. However, these pockets cause stress raiser at the location close to concrete face. The beam-end specimen is relatively simple test. In order to gain the required stress state, a compressive force should be located at distance from the bar equal to the bar bonded length. This causes both the bar and the concrete to be subjected to tension. The adjustment of the spacing between the bar and the compressive force of beam-end specimen is identified in ASTM A 944. This ensures that the failure will occur in the bond between the bar and surrounding concrete instead of flexural failure or shear failure. The bond strengths obtained by testing beam-end specimen and by full-scale splice specimens are almost equivalent (ACI 408, 2003).

The beam-end specimen represents the behaviour of the end region of a simply supported beam under four point loading (Figure 2.6). The applied load and the reaction are equal by symmetry. These loads result in a tension force, which resisted by the steel and compression force resisted by the concrete. A diagonal compression strut is created as a result of the compression and tension forces. This diagonal connects the compression load point with the support reaction, which causes the middle section of the specimen to be subjected to compression.

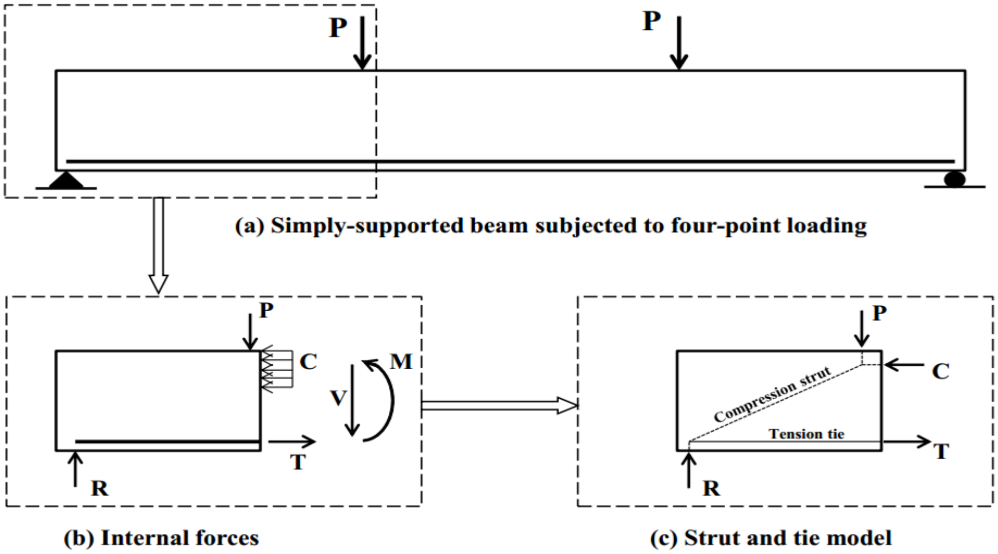

(a) Simply-supported beam subjected to four-point loading

(b) Internal forces

(c) Strut and tie model

Figure 2.6 Beam-end structural idealization (Butler 2012)

2.2.4 Bond Failure Mode

If the reinforcement bar is anchored adequately into the concrete, the bond stress would be distributed over the anchorage length. If the anchorage length is long enough, the tensile stress will be distributed along the length bar reducing the maximum tensile stress in the concrete. Due to this reason, the bar will tend to yield due to high transfer capacity causing the beam to fail by flexure or shear rather than bond. On the other hand, if the bonded length is short (the ratio of development length to bar diameter is less than 15) such that the bar will not reach yielding, the failure can either be because of concrete splitting due to bond stresses or due to bar pullout (Figure 2.7).

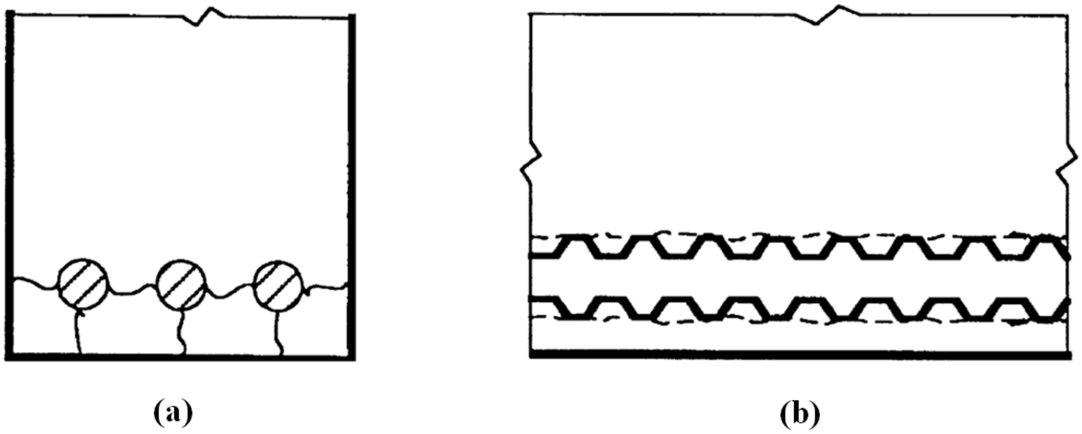

Figure 2.7 Cracking and damage mechanisms in bond: (a) end view of a member showing splitting cracks between bars and through the concrete cover; and (b) side view of member showing shear crack and/or local concrete crushing due to bar pullout (ACI 408, 2003)

The shrinkage of concrete, which occurs during the hydration process, causes tiny cracks in the concrete at the surface of the steel reinforcement that are restrained by the reinforcement. As the concrete shrinks (strains), the shrinkage is restrained by the reinforcing bar creating tensile stresses in the concrete so there will be a compressive stresses in the steel and tensile stresses in the concrete. If the tensile stresses in the concrete are high enough, splitting cracks in the concrete surrounding the reinforcing bar will be initiated. Moving away from the reinforcing bar, the stresses in the concrete due to shrinkage are reduced as the restraint effect diminishes. These cracks due to concrete shrinkage cause stress raisers. Confinement of flexural reinforcement could be by steel stirrups or concrete cover or both. In the case when the confinement is not available in sufficient amount, the cracks start through the hoop tensile stresses and propagate to reach to the surface of the concrete causing splitting of the concrete parallel to the reinforcement bar. The confinement reduces the chances of concrete splitting and increases the shear stresses at the concrete-steel reinforcement interface leading to slip of the bar from the concrete after crushing the concrete keys (pullout failure).

Bond failures are generally brittle in nature. There are three components of bar slip; elastic deformation, inelastic deformation and rigid body motion relative to the concrete. From an experimental point of view, it is quite difficult to separate the three components. Slipping of the bar could be measured from the end of the bar and near the load application. In most of the situations in the field, bond failures are most likely due to splitting rather than pull-out (ACI 408, 2003).

2.2.5 Slip Behaviour of Reinforcing Bar Embedded in Concrete

As the slip of a reinforcing bar increases, the bond between the reinforcing bar and the surrounding concrete is deteriorated (fib, 2000). Figure 2.8 shows the bond stress-slip behavior of bond failure under static load, which was proposed by Harajli et al. (2004). It was explained that the bond stress-slip behavior of the beam could have four stages. The first stage showed that the stiffness of the bond stress-slip curve was similar to that of a pullout bond failure where the bond resistance was gained by the chemical adhesion and the friction between the reinforcing bar and the surrounding concrete until a tensile crack occurred in the concrete. Once a splitting crack developed, the second stage started and continued until the maximum bond stress was reached. This stage was characterized by a lower bond stress-slip curve than a pullout bond failure. After failure defined as the maximum load terminated the second stage, the third stage started with a sudden drop in the bond stress. In the last stage, the bond stress decreased gradually accompanied by increasing bar slip and a widening of the splitting crack.

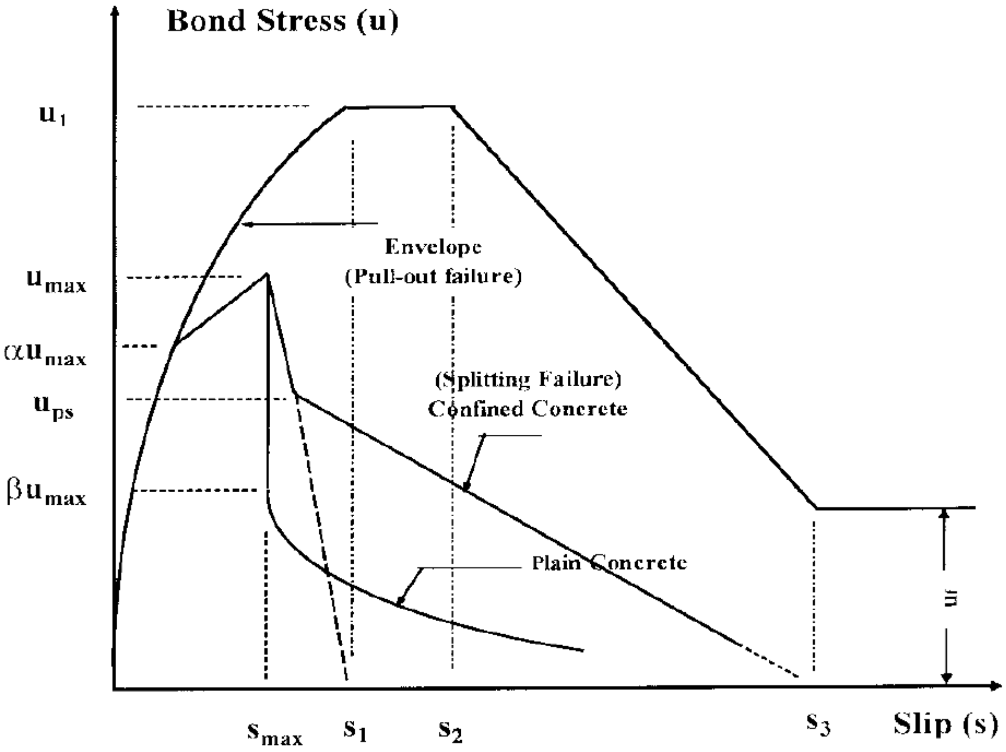

Figure 2.8 Bond stress-slip behavior under static load (Harajli et al. 2004)

The slip measurement could be either the bar elongation or the bar movement. The bar elongation can be calculated as follows:

Measured elongation of the rebar $\delta = s_l - s_f \rightarrow \delta = \Delta L$ Equation (2.6)

$\mathcal{E} = \frac{\Delta L}{L} = \frac{\delta}{L} = \frac{\sigma}{E}$ Equation (2.7)

$\sigma = \frac{P}{A} \rightarrow \varepsilon = \frac{P}{EA}$ Equation (2.8)

$\frac{P}{EA} = \frac{\delta}{L} \rightarrow \delta = \frac{PL}{EA}$ Equation (2.9)

Equation 2.9 above is valid when P, E and A are constant within the length L. For the beam-end specimens, the force in the bar varies. Thus, the calculated elongation of the rebar within bonded length is given by

$(\delta) = \int_0^{L_b} \frac{P(x)}{A_s E}\, dx$ Equation (2.10)

Where

S_l: Measured slip at loaded end (mm)

S_f: Measured slip at free end (mm)

P(x): Force on the bar at location, x, at failure (N)

A_s: Area of the rebar (mm^2)

E: Modulus of elasticity = 200,000 MPa

Equation 2.10 is valid for linear elastic behaviour. If yielding occurs (i.e, P(x) exceeds P_y within a portion of L_b), Equation 2.10 will under predict the actual elongation. Thus, if:

$\delta = S_l - S_f$ → The rebar did not yield

$\delta < S_l - S_f$ → The rebar yielded

2.2.6 General Observation of Bar Slip and Failure Mode

The bond stress-slip relationship behaviour of the beam-end specimens with bonded length of 250 mm and 350 mm was clearly different. Yamao et al. (1986), Hong and Park (2012) found that there is a significant change in the relationship of bond stress-slip in long embedment length and short embedment length (Figure 2.9). The effect of the bar diameter is considered by using a non-dimensional slip (S/d_s).

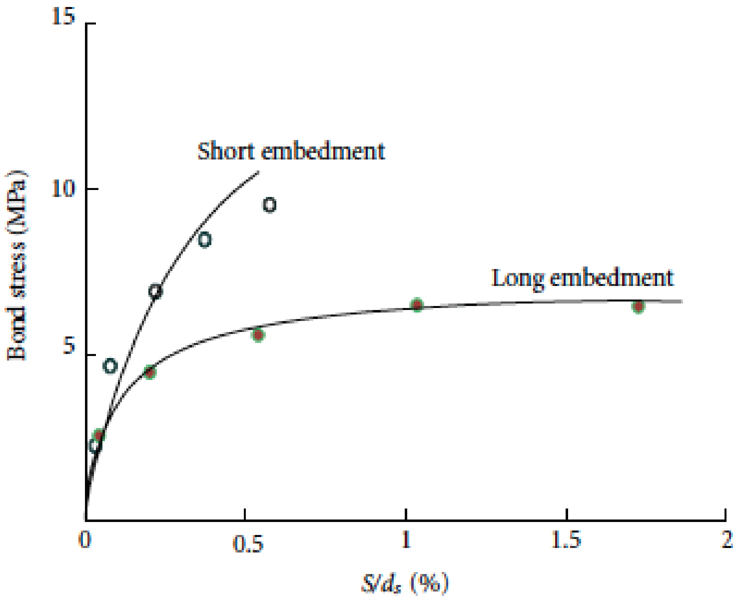

Figure 2.9 Bond stress-slip relationship of short embedment and long embedment (Hong and Park, 2012)

In the current study, the beam-end specimens with 250 mm bonded length were considered as short embedment length and followed load slip behaviour similar to that illustrated in Figure 2.10. They had a clear peak bond stress value followed by sudden drop of bond resistance. The critical slip of these specimens was taken as the slip corresponding to this peak value. However, the specimens with 350 mm bonded length reflected the long embedment length and followed the behaviour similar to that shown in Figure 2.11. In this case, the bond stress increases until almost reaching the bond capacity, and then the bar continued to slip while the bond between concrete and reinforcing bar resisted the splitting of concrete until the failure occurred. The post-failure behaviour depends on the variety of parameters including compressive strength of concrete, bar size, the confinement by concrete, bar surface roughness (residual friction).

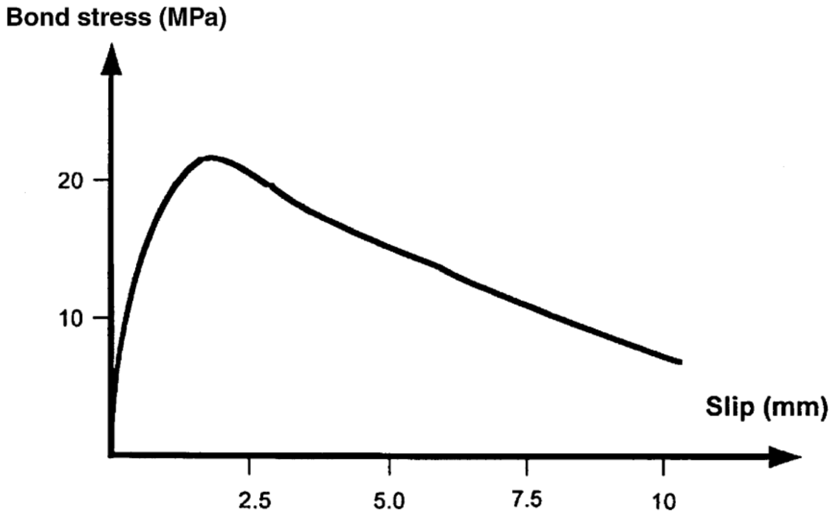

Figure 2.10 Typical bond stress-slip curve for short embedment length (ACI 408, 2003)

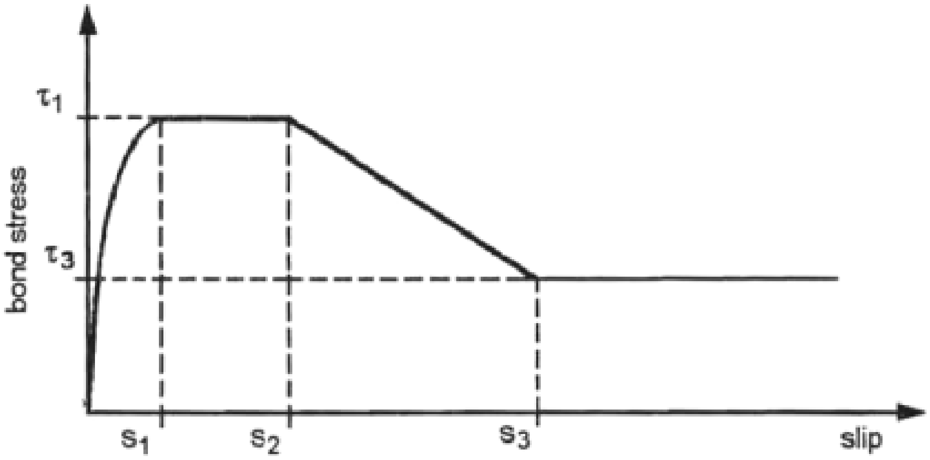

Figure 2. 11 Idealized bond stress – slip relationship for long embedment length (fib, 1990)

2.2.7 Factors Affecting Bond

2.2.7.1 Concrete Compressive Strength

Bond failure can occur as splitting cracks that propagate along the concrete-steel interface or when the concrete keys between the bar ribs shear off. Both of these mechanisms are related to the concrete tensile strength. Usually, the concrete strength is described by its compressive strength. However, the tensile strength is nearly proportional to the square root of the compressive strength (Carino and Lew, 1982). Consequently, the compressive strength is an important factor that affects the bond strength whereas increasing the compressive strength leads to an increase in the bond strength (Alavi-Fard and Marzouk, 2002). Moreover, fracture energy, a tensile property of concrete, expresses the ability to dissipate energy by the concrete once the crack starts. The bond strength of a reinforcement concrete member increases with an increase in the fracture energy (ACI 408, 2003).

2.2.7.2 Concrete Cover and Bar Spacing

There is a positive correlation between bond strength and concrete cover and bar spacing. The bond strength increases as the concrete cover and the spacing between bars increase. The bar spacing and the concrete cover can affect the type of bond failure (Darwin et al. 1996a). Increasing the bar spacing and concrete cover could change the failure mode from splitting to pullout failure which typically leads to an increase in the bond strength. The smaller the bar spacing and the concrete cover, the more likely the beam will fail due to splitting. Figure 2.12 illustrates the pattern of splitting failure for both situations: (a) small cover (C_b) and (b) small bar spacing (C_{si}). In the case of small concrete cover and large bar spacing, the splitting cracks will propagate through the cover under the reinforcement bar. If the bar spacing is small and the cover is large, the splitting cracks will occur either at the side cover or between the reinforcement bars (ACI 408, 2003).

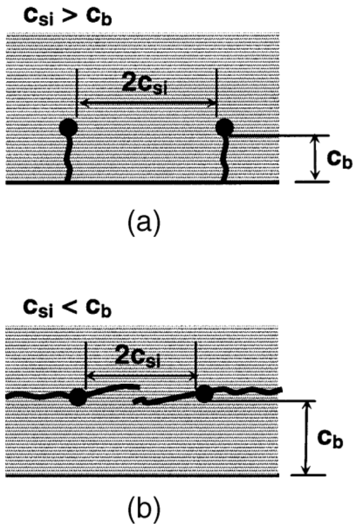

Figure 2.12 Bond cracks: (a) $C_{si} > C_b$; (b) $C_{si} < C_b$ (ACI 408, 2003)

2.2.7.3 Bar Size

Small bars have a higher ratio of the surface area that is in shear to the cross sectional area that carries the axial force. Thus they will have a lower shear stress for a given change in axial bar stress than large bars. Using many small bars size instead of a few large bars improves bond performance as long as the minimum clear distance between the bars required for independent action is maintained (ACI 408, 2003).

2.2.7.4 Bonded Length

The bond capacity (bond resistance) is higher for the larger bonded length. This relationship is non- linear because the distribution of the bond stresses is not constant along the bonded length. When applying a load, the loaded end of the bonded length will carry most of the stresses. Once splitting bond cracks occur, the forces transfer away from the loaded end towards the free end of the bonded length (ACI 408, 2003). Figure 2.13 shows an example of bond stress distribution of a beam-end specimen.

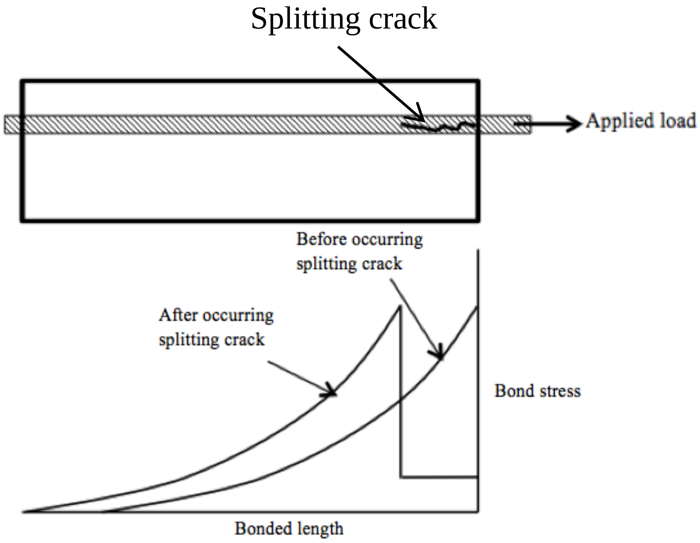

Figure 2. 13 Bond stress distribution along the bonded length

2.2.7.5 Amount and Distribution of Transverse Steel

Transverse reinforcement improves the bond capacity by confining the concrete and delaying the splitting crack width from propagating at different concrete covers (ACI 408, 2012; Garcia et al., 2013). Once spalling of the concrete cover occurs, confinement from transverse reinforcement (stirrups) becomes a major aspect in enhancing the bond capacity (Bamonte and Gambarova, 2007). Transverse reinforcement improves the bond ductility whereas the rate of load drop is reduced after reaching the peak bond strength of the RC member (Zuo and Darwin, 2000). The effect of stirrup confinement on bond strength is more significant than the effect of concrete cover and bar spacing (Sparling and Rezansoff, 1986; Tepfers, 1988). Transverse reinforcement confinement becomes more critical for bar diameters greater than 14 mm (Giuriani et al., 1991). The beams confined with transverse reinforcement have higher maximum load and deflection compared to unconfined beams. In lap splice beams, confining the splice bars with transverse reinforcement delayed or prevents spalling of concrete cover (Seliem et al., 2009; Fagundo et al., 1979). In case of bond failure, the size and the amount of the transverse reinforcement in the bonded region might change the mode of failure from splitting bond failure to pullout bond failure (Sakurada et al., 1993; Orangun et al., 1977; Lukose et al., 1982; Pacholka et al., 1999)

2.2.7.6 Effect of Coarse Aggregate Size and Content on Fracture Energy of Concrete and Bond Strength of Concrete

Fracture energy of concrete (or the crack energy) can be defined as the energy required to open a unit area of crack surface. It is also known as the capacity of the concrete to dissipate energy as a crack opens. The coarse aggregate size and content are main parameters that affect the fracture energy of the concrete. Beygi et al. (2014) studied the effect of three different coarse aggregate sizes (9.5 mm, 12.7 mm and 19 mm) with two different water-to-cement ratios (0.38 and 0.53) and it was concluded that the fracture energy increased significantly with increasing coarse aggregate size. The fracture energy of the self-consolidating concrete increased remarkably when the volume of the coarse aggregate fraction increased from 30% to 60%. Also, an increase of coarse aggregate proportion in the concrete mix led to an increase in the ductility of the concrete. Increasing the coarse aggregate volume and size increased the fracture energy of the concrete more than the other mechanical properties (Nikbin et al., 2014). The compressive strength of the concrete showed a small dependence on the coarse aggregate size; however the flexural strength was not affected by changing the coarse aggregate size (Kozul and Darwin, 1997). El-Hacha et al. (2006) studied the bond characteristics of beam-end specimens and lap-splice beams and found out that the bond strength increased with an increase in the volume of the coarse aggregate.

2.2.7.7 Effect of Self-Compacting Concrete (SCC) on Bond Strength

Zhu et al. (2004) studied the bond strength of self-compacting concrete (SCC) and normal concrete with two different rebar sizes (12mm and 20mm). They found that SCC provided 10-40% higher bond strength than normal concrete. This is due to the uniformity of interfacial transition zone (ITZ) of SCC mixes around the reinforcing bar (Boel, 2006). This uniformity is attributed to the finer microstructure of the SCC, which gives superior ITZ (Khayat and Feys, 2010). It has been found that concrete at the bottom of the horizontal reinforcement bar has lower micro strength and elastic modulus than the upper face. This study supports the theory that the ITZ becomes weaker in the bottom of the reinforcement bar because of internal bleeding. This phenomenon is more pronounced in normal concrete than in SCC (Zhu et al., 2004). It was found that SCC showed an excellent bond with substrate concrete compared with normal concrete. The high flowability of SCC gave it superior role to enhance the bond at the interface with substrate concrete through the ability to fill the cavities in the substrate concrete (Bissonnette et al., 2012).

2.2.7.8 Effect of Corrosion on Bond of Reinforcement Concrete

Several researchers investigated the effect of corrosion on the flexural strength of reinforcement concrete members. Corrosion decreases the yield force and ultimate capacity of reinforced concrete members and increases the deflection at midspan (Masoud et al., 2005). However, if both flexural and anchorage regions are corroded, the beam may fail due to bond splitting failure instead of due to flexure (Uomoto et al., 1984). There are three main causes for decreasing the bond strength between the bar and concrete. First, erosion of the bar ribs which results in a reduction in the interlock area between these ribs and the concrete. Second, the formation of corrosion products generates splitting stress on the concrete around the bar and may lead to formation of longitudinal splitting cracks and spalling of the concrete cover from the reinforced bar. Finally, the friction between the rebar and concrete is reduced because of the presence of corrosion products (rust). The volume of the rust is more than the volume of the respective lost steel, which produces tension forces on the concrete surrounding the reinforcing bar thus leading to concrete cracking. Also, this layer of the rust leads to lubricant surface between the rebar and the concrete (fib, 2000).

Loss of bond decreases the capacity of the reinforced concrete member and increases its deflection as well as the slip of the reinforcement bar (ACI 408, 2003). At the initial stages of corrosion and before cracking starts, the bond strength increases slightly (5%). This increase is due to the formation of the rust layer around the bar that fills the voids and increases the friction force at the interface. After reaching the peak value, the bond strength decreases as the corrosion level increases (Figure 2.14). The bond stress-slip curve stiffness of corroded reinforced concrete members before cracking starts is greater than the equivalent uncorroded member. However, after the corrosion crack is initiated, the stiffness of the corroded members tends to be less than the stiffness of the un-corroded members (fib, 2000).

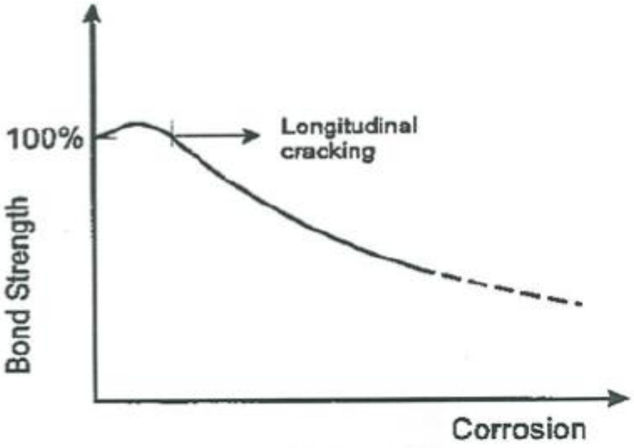

Figure 2. 14 Variation of bond strength with corrosion (fib, 2000)

2.3 Partial Depth Repair

Once the corrosion starts to take place in a reinforcement concrete structure, the repair operation becomes crucial in order to extend the lifetime of the structure. The partial depth repair is one of the common methods used for rehabilitation purposes in corroded RC member. After removing the damaged concrete, there are some steps that should be performed before placing the new concrete. These steps include removing the rust, cleaning the reinforcing bar (by sandblasting or water pressure) and preparing the surface of the substrate concrete (Emberson and Mays, 1996). Figure 2.15 illustrates the steps to prepare the surface of the substrate concrete before casting the partial depth repair concrete.

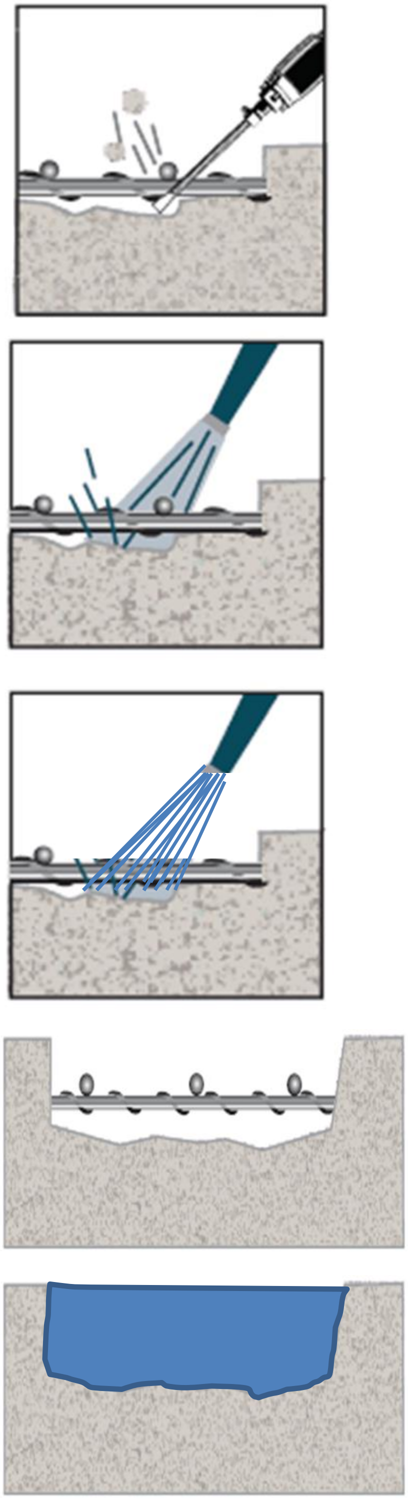

Step 1:

Removing the damaged concrete of the substrate concrete using a hammer and chisel or concrete chippers. Concrete is removed a minimum of 19 mm under the corroded bar.

Step 2:

Cleaning the exposed surface of the substrate concrete and the corroded reinforcing bar from the rust. The cleaning could be by sandblasting or high pressure water.

Step 3:

Roughening the surface of the substrate concrete to enhance the bond between the substrate concrete and the partial depth repair concrete. The surface roughening can be done any acceptable methods such as needle peener

Step 4:

After roughening process, the area to be repaired must be cleaned from the dust by high air pressure to enhance the efficiency of the bond between the substrate concrete and the partial depth repair concrete.

Step 5:

Install the partial depth repair concrete, then curing.

Figure 2.15 General procedures for partial depth repair (Adapted from Precast.org 2008)

Rio et al. (2005) studied the effect of the partial depth repair concrete on the flexural strength of a group of beams and reported that there is an improvement in the load-carrying capacity of the beams that were repaired by partial depth repair compared to the corroded unrepaired beams. However, the strength of the repaired beams was still lower than uncorroded beams, which reflects the reduction in cross-sectional area of the bar. Where possible, it is better to repair a corroded reinforcement concrete member at the early age of corrosion appearance to prevent further cross sectional area loss of the steel. The properties of the concrete used for the partial depth repair and the substrate concrete should be similar to guarantee a good bond between them. Sharif et al. (2006) concluded that the partial depth repair will be more efficient if the loads are partially or totally released from the reinforcement concrete member before the repair application.

The main requirements to have good partial depth repair performance are a high dimensional stability (lower expansion and shrinkage) and high early bond strength of the partial depth repair concrete to the substrate concrete (Keer et al., 1990). Also, the partial depth repair concrete should have specific properties for an optimal long-term structural behaviour including an increase in the coarse aggregate volume and the addition of supplementary cementations materials such as silica fume. Partial depth repair concrete that contained a large amount of coarse aggregate increased the ductility of the concrete repair material. Mangat and Elgarf (1999) Suggested that for a RC structure having a high chance of having a corrosion attack, using a relatively ductile partial depth repair concrete (able to achieve significant deformation) to dissipate the corrosion products impedes the concentrated disruption of bonding at the interface between the reinforcing bar and concrete. Silica fume, which has particles finer than those of cement, can be used as a replacement of some amount of the cement. Replacement the portland cement with silica fume in the partial depth repair concrete reduces the porosity and increases the strength, durability and workability of the concrete (Detwiler et al., 1994). Adding silica fume to the portland cement concrete improved the compressive strength, bond strength and abrasion resistance of the concrete (Shin and Wan, 2011). Momayez et al. (2005) studied the bond between a concrete partial depth repair and the substrate concrete and concluded that adding silica fume of up to 7% increased the bond strength by 25% compared to mixes without silica fume. Applying an epoxy adhesive as a bonding agent between the repair substrate concrete enhances the bond between the partial depth repair and the substrate concrete. Research was done by Yamashita et al. (2012) on flexural bond strength and fracture energy tests of the joint between the partial depth repair concrete and the substrate concrete and they concluded that the epoxy adhesive enhanced both the flexural bond strength and the fracture energy of the interface joint of the two layers of concrete.

While different aspects of partial depth repairs have been studied, there is no published research on the bond of reinforcement in partial depth repairs.

2.4 Corrosion Mechanism in Concrete

Concrete with its high pH value creates a passive protective layer around the steel reinforcement. This passive layer deteriorates by chemical attack from the surrounding atmosphere thus initiating corrosion. The most common chemicals that cause corrosion of steel reinforcing bars are carbon dioxide and chloride ions (Broomfield, 1997). Carbonation reaction is caused by migrating carbon dioxide into the concrete that results in decreasing the pH level leading to a loss of the passive layer. Chloride ions, which may represent in deicing chemicals or sea water ingress through the pores of the concrete and attack the passive layer (ACI 222, 2001).

Corrosion in a reinforced concrete member is an electrochemical process (ACI 222, 2001). Two main reactions are involved during the electrochemical process, which are anodic reaction (releases electrons) and cathodic reactions (consumes electrons). Figure 2.16 shows this process in a reinforced concrete member.

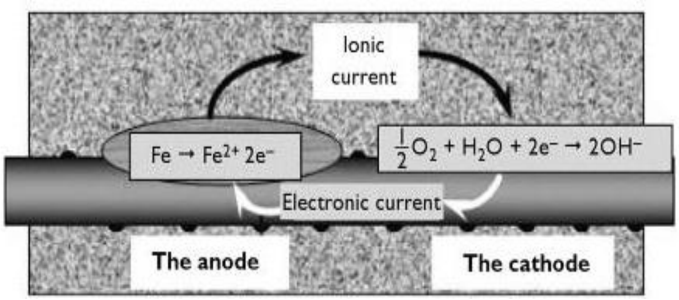

Figure 2.16 Corrosion cell in reinforcement concrete (Broomfield, 2006)

The oxidation of the Iron starts at the anode location that releases electrons that are then absorbed the cathodic location where oxygen and moisture are present resulting in the production of hydroxyl ions. The electrochemical reaction is completed as hydroxyl ions move through the concrete from the cathode to the anode. The electrons continue movement from anode to cathode through the concrete by diffusion. Figure 2.17 illustrates the damage mechanisms for corrosion of reinforced concrete structures (West et al. 1999).

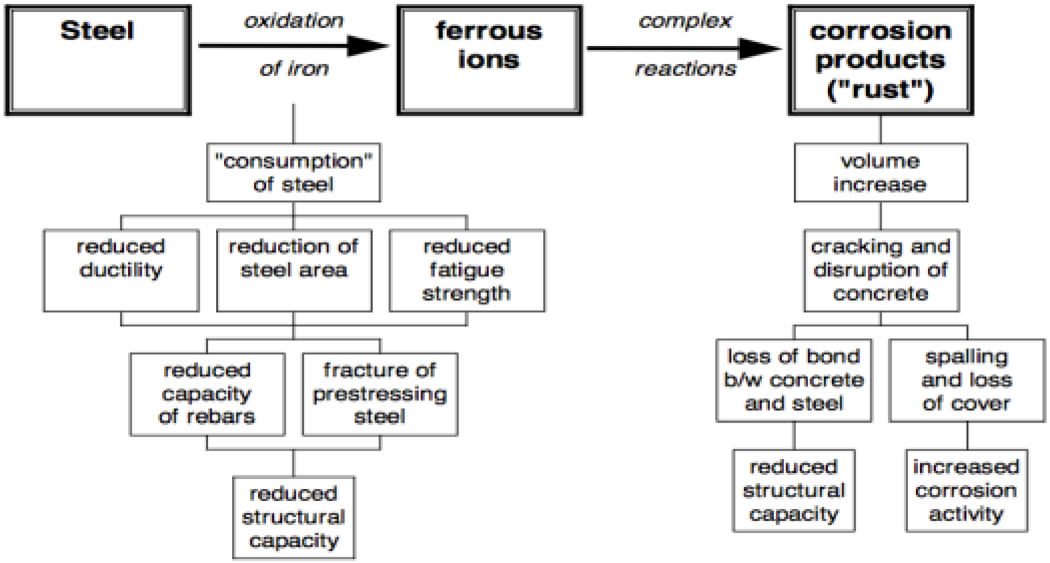

Figure 2.17 Deterioration mechanisms for corrosion of steel in concrete (West et al. 1999)

2.5 Fiber Reinforced Polymers (FRP)

Figurer 2.18 clarifies the components of fiber reinforced polymers (FRP) (also known as fiber reinforced plastics), which are composite materials that consist of fibers and a matrix (Gibson, 1994).

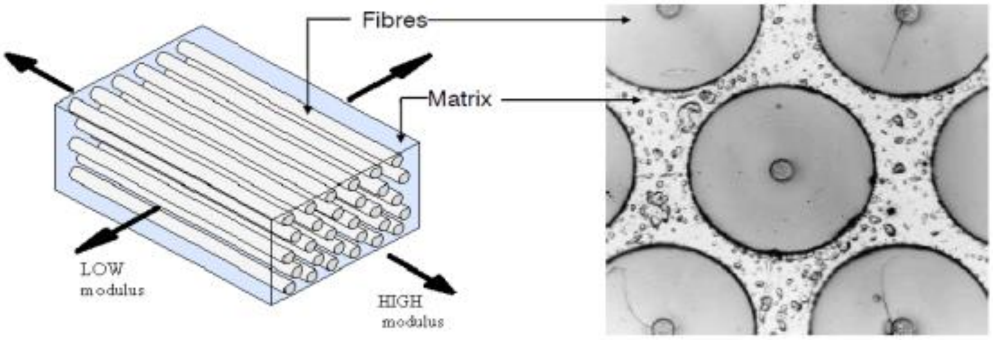

Figure 2.18 Components of FRP (Badawi, 2007)

There are four common fiber materials: Carbon Fiber Reinforced Polymers (CFRP), Glass Fiber Reinforced Polymers (GFRP), Aramid Fiber Reinforced Polymers (AFRP) and Basalt Fiber Reinforced Polymers (BFRP) (ISIS, 2001; Richard, 2012). The CFRP has the highest strength of the FRP materials and GFRP the lowest. The strength of each type of FRP depends on their fiber strength and volume fraction. Generally, all types of FRP have higher strength than the conventional reinforcing steel (Figure 2.19). Also, unlike reinforcing steel, they exhibit linear stress-strain behavior (elastic) until a sudden failure occurs without yielding.

The purpose of the matrix is to bind the fibers together, transfer the stress from the concrete to the fibers, and protect the fibers against mechanical damage and environmental attack (Jones, 1999). The matrix must have a higher failure strain than the fibers so that it does not crack before the fibers reach their maximum capacity (Figure 2.20). There are three common types of polymer matrix: epoxy, polyester and vinyl ester. The suitable choice of the polymer is based on its compatibility with the fibers, simplicity of application and the efficiency of binding the FRP with substrate concrete (ACI 440, 1996).

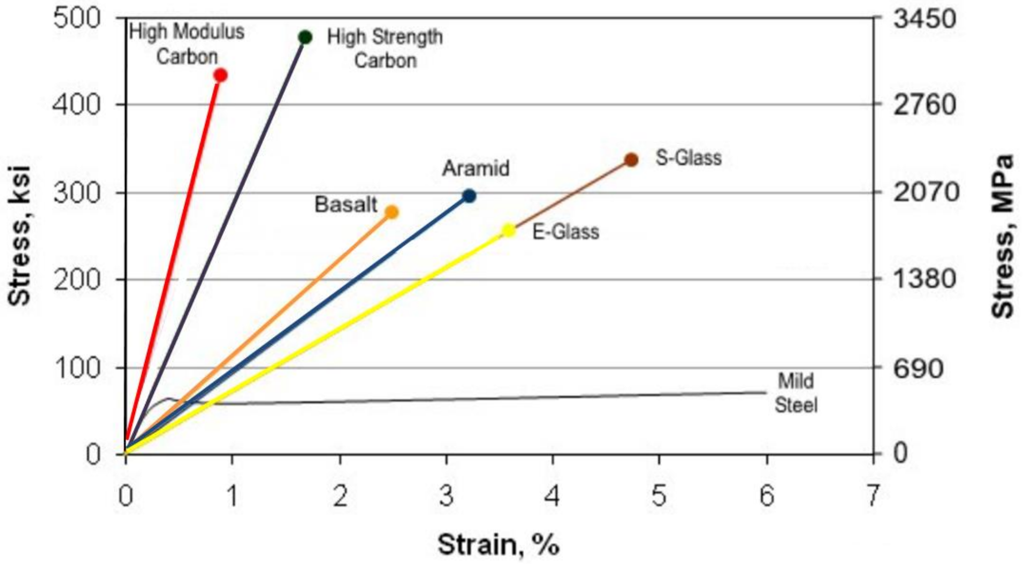

Figure 2.19 Stress-strain behaviour of different types of FRP materials and conventional reinforcing steel (Richard, 2012)

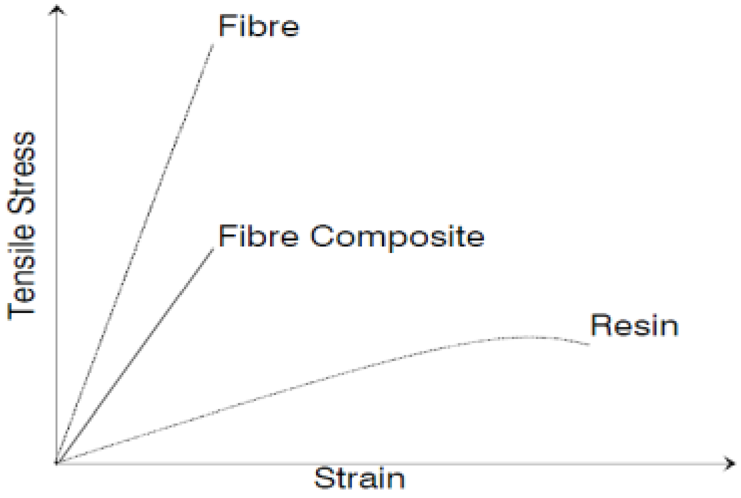

Figure 2.20 Tensile stress versus strain of the components of FRP (ACI 440R, 1996)

2.5.1 Effect of FRP Confinement on Bond Strength of Reinforced Concrete

There are many situations in which existing RC members are repaired or strengthened with FRP sheets (Figure 2.21). In the case of poor design or mistakes during construction FRP sheets may be used to strengthen a RC member instead of replacing it. Also, a reduction in strength of a RC member due to an impact load or corrosion may be resolved by its repair with

FRP sheets to restore its capacity. Moreover, FRP sheets repair may be necessary for a RC member that is subjected to a change in use or an increase in demand on its capacity.

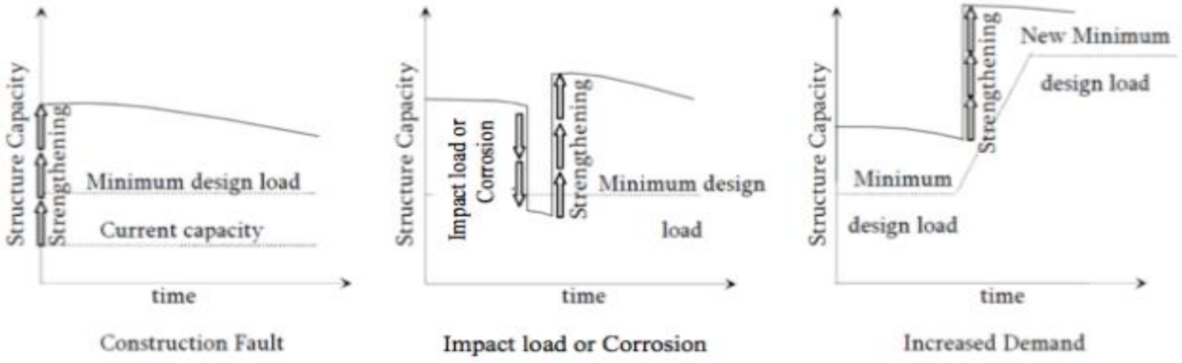

Figure 2.21 Situations of importance to strengthening or repairing a RC member (Badawi, 2007)

FRP is one of the most popular materials used for rehabilitation of reinforced concrete structures. Their advantages include: high strength to weight ratio, ease of installation and the fact that they do not corrode. FRP has linear elastic stress strain behaviour until failure. They do not have the yielding properties of steel, thus no indications before failure (ACI 440, 2007).

FRP sheets are used in the tension area of the beam to support the flexural strength or as U wraps in the shear zone to support the shear and the bond strength of the beam. Also, corroded columns can be repaired by wrapping them with FRP sheets to improve their ductility and strength (ACI 440, 1996). Wrapping reinforced concrete members using FRP sheets help to prevent external expansion caused by corrosion thus improving the bond strength by resisting splitting cracks (Soudki and Sherwood, 2000).

If FRP sheets are applied to the beam before failure occurs, the ductility of the beam will improve compared to the beam without FRP confinement, whereas the FRP sheets reduce the drop of the load rate of post-failure. This is due to fact that external confinement with FRP gave better results than stirrups in preventing the spread of splitting cracks in concrete (Harajli et al., 2004). Externally applied FRP sheets decreased the permeability to hinder oxygen and water to ingress into concrete, thus decreasing the corrosion rate of the repaired member (Khoe et al., 2012). Repairing with FRP sheets can double the bond strength of a reinforced concrete member subjected to a 10% rebar mass loss. Craig and Soudki (2005) conducted tests on pullout specimens and bond anchorage specimens and found that CFRP sheets changed the failure mode of the corroded specimens from splitting failure to a pullout failure (pullout specimen) or flexure failure (bond anchorage specimen).

Bousias et al. (2007) studied the effect of one layer and two layers of FRP wrapping and concluded that bond strength was not proportional to the number of layers. Increasing the thickness of GFRP sheet resulted in an increase the bond strength and the deflection of a beam (Hamad et al., 2004). A study was done on the effect of wrapping with FRP sheets on the behavior of lap spliced beams and it was found that the FRP wrapping enhanced the bond strength of the lap splice by up to 34% compared to the unconfined beams. Also, wrapping lap spliced beams with FRP sheet delayed the initiation and propagation of a splitting crack (Rteil, 2002; Bournas and Triantafillou, 2011). Garcia et al. (2013) found that the splitting crack width of beams confined with FRP was less than that of unconfined beams. Also, the beams confined with FRP exhibited an increased bond strength and bar slip at failure compared to unconfined beams. Reinforced concrete members that were wrapped with CFRP sheets required a higher force to start slip of the reinforcing bar than unwrapped beams.

The FRP sheets resist the expansion of the concrete due to splitting stresses associated with the bond stresses induced by loads on the beam. An increase in the stiffness of the sheet (for example by an increased elastic modulus) will increase this constraint. If the stiffness of the FRP sheet is sufficient, splitting cracks will be prevented from reaching the surface to cause a splitting failure and the failure mode might change to pull-out. The confinement provided by the FRP sheet increases as the thickness of the concrete cover is reduced since the strain in the concrete will be reduced.

Chapter 3: Beam-End Specimen Experimental Program

3.1 General

The beam-end specimen experimental program consisted of testing 36 beam-end specimens with dimensions of 250 x 500 x 600 mm based on guidelines provided in ASTM A944-05. The main purpose of this study is to determine the bond strength of cleaned corroded reinforcing bar at different mass loss level (up to 15%) embedded in beam-end RC member and repaired with different partial depth repair materials. The specimens were designed to fail by bond (splitting or pullout). The slip of the reinforcing bar was measured using linear variable differential transformers (LVDTs). The partial depth repair materials were self-consolidating concrete (SCC) and Normal concrete (NC). The bond strength and failure mode of the beam-end specimens with partial depth repair was compared to the control case of monolithic beam-end specimen.

3.2 Test Program

Thirty-six beam-end specimens were cast focusing on using partial depth repair as a repair method for reinforcement concrete (RC) elements with corroded rebar. The experimental program of the beam-end specimens was divided into two phases: Phase 1, which consisted of 12 beam-end specimens and Phase 2 that consisted of 24 beam-end specimens. The variables in Phase 1 included: two corrosion levels (5% and 10% mass loss) and two anchorage lengths (250 mm and 350 mm). One partial depth repair material was investigated (commercial prepackaged Self-consolidating concrete (SCC1) with about 9% of 8 mm coarse aggregate and was compared with a monolithic beam-end specimen (M1). Two control specimens with no corrosion were cast for both M1 and SCC1. The variables included in Phase 2 were: two corrosion levels (7.5% and 15% mass loss) and two anchorage lengths (200 mm and 300 mm). Three partial depth repair concretes were used: a second commercial prepackaged self-consolidating concrete (SCC2) with 13 mm aggregate size, Self-consolidating concrete that mixed and cast in place with 19 mm aggregate size (SCC3), and normal concrete (NC) that was mixed and cast in place and had the same mix design as the monolithic concrete (M2). Four control specimens with no corrosion were cast (one control for each concrete type including the monolithic beam-end specimen). The specimens were tested to determine the bond strength between the rebar and concrete and the load-slip response under static load. Figure 3.1 shows the test matrix for all of beam-end specimens variables for the two phases.

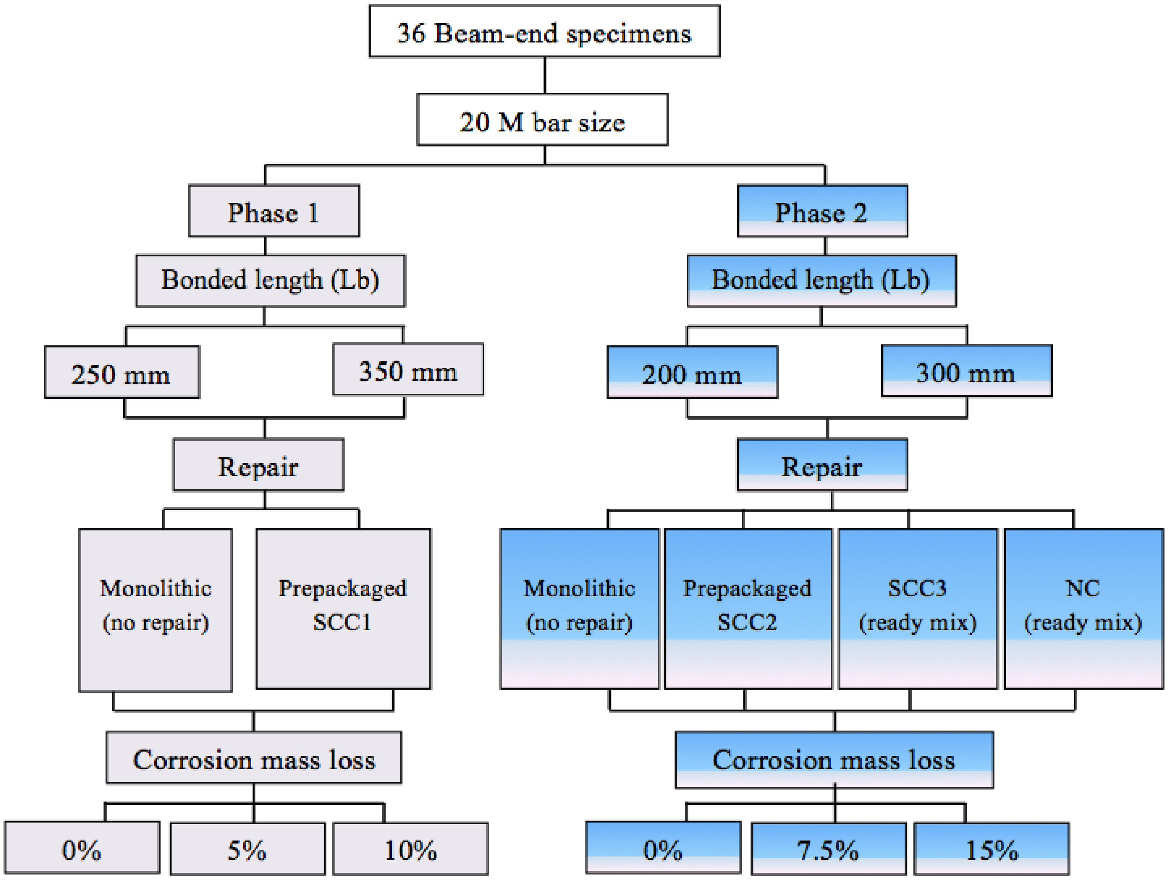

Figure 3.1 Test matrix of beam-end specimens

Given the broad scope of experimental parameters and the size of the test specimens, it was not practical to include replicate specimens. This is not uncommon in large scale structural experimental programs. Since the replicates were not used, care was taken to examine trends in the experimental data to identify any possible inconsistent results. In the rare event that inconsistent data were observed, individual data points were removed from further analysis, but only if a clear reason leading to the outlier result could be determined (e.g, obvious experimental error, non-typical experimental condition)

The bonded lengths were chosen to be shorter than the development length that was estimated using CSA A23.3-04 Clause 12.2.2 to ensure occurrence of a splitting failure. The bonded lengths were varied to assess its effect, and because of the non-uniformity of the corrosion along the bar surface. Thus, with increasing the bonded length, the friction surface will increase and the chance of existing more pits will increase. The concrete cover was chosen to be 25 mm, which is the minimum allowable cover by standards for RC beams. Corrosion mass loss levels up to 15% were considered as a practical upper bound (beyond which the corroded bar would be replaced). Different partial depth repair materials were considered to study the effect of different variable on the bond strength such as coarse aggregate size and content, bonding agent, silica fume. Also, SCC and NC concrete were tested to study the effect of fresh properties of the mix concrete on the bond strength.

3.3 Test Specimen

Beam-end specimens show good agreement with full-scale beam specimens to assess the mechanism of bond strength (ACI 408, 2003), and are easier to construct and simpler to test. As well, beam-end specimens are designed specifically to study the splitting mode of bond failure (fib, 2000), which is the primary mode of interest for bond failure. The details of the beam-end specimens used in this study follow the ASTM A944-05 standard as shown in Figure 3.2.

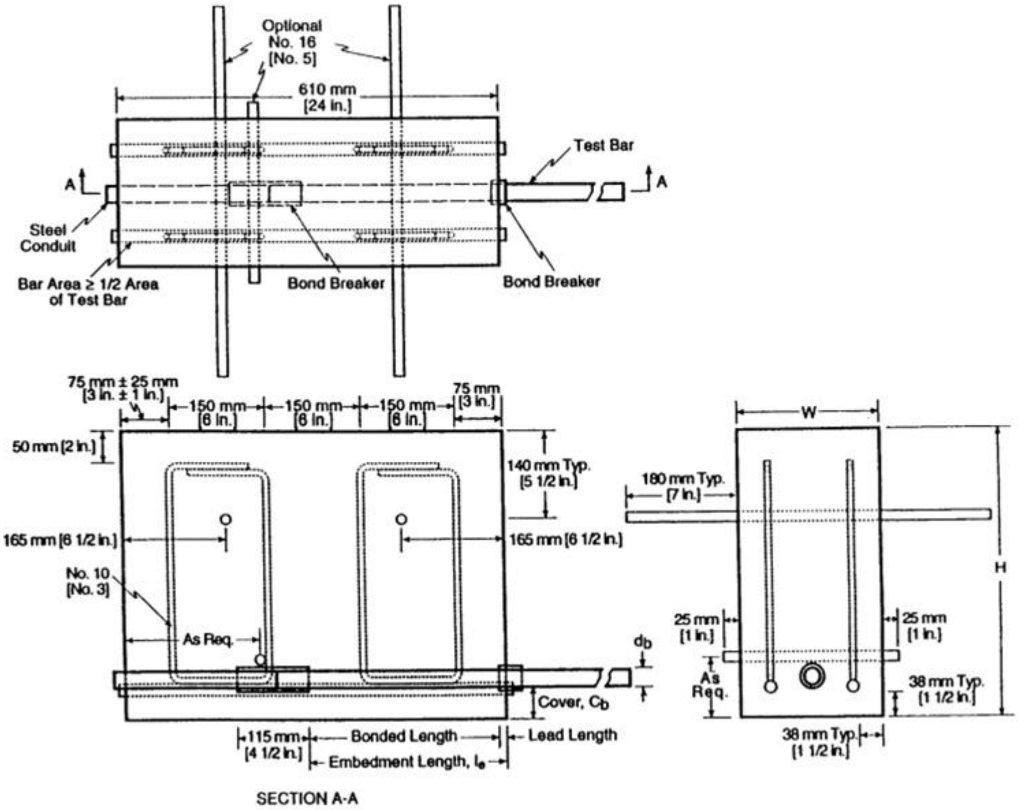

Figure 3.2 Beam-end test specimen (ASTM A944-05)

The specimen is reinforced with four stirrups placed parallel to the main reinforcement bar to limit their effect on splitting failure. These stirrups are used to enhance the shear capacity and make sure that bond failure occurs. Two smaller size bars are placed on both sides of the main rebar to represent additional flexural reinforcement. The sizes of the two bars should be such that their total area is more than or equal to the area of the main bar. Figure 3.3 shows the dimensions and the appearance of the test specimen used in this research. The pocket representing the repair area had a depth of 70 mm and width of 250 mm. The cover of the rebar was 25 mm and there was 25 mm clearance underneath the rebar, meeting the minimum clearance reinforcement of 19 mm or 6 mm larger than the largest aggregate in the repair material (ACI 364, 2014). The length of the pocket was varied based on the desired bonded length (200 mm, 250 mm 300 mm or 350 mm). A 50 mm unbonded region (lead) was provided at the loaded end of the bar to avoid or limit forming a cone failure.

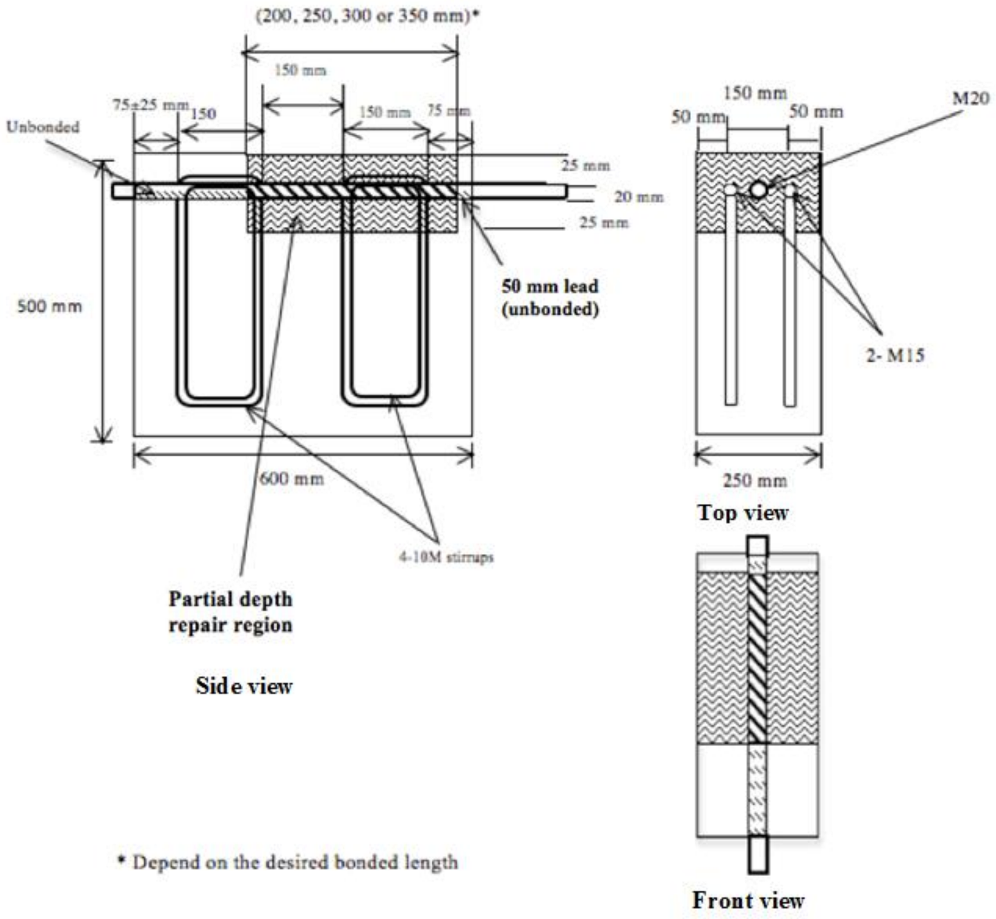

Figure 3.3 The dimensions and the appearance of the beam-end test specimen

3.4 Test Procedure

The test apparatus for the beam-end specimen is shown in Figure 3.4. This apparatus, designed by Butler (2012), was installed in 500 kN servo-hydraulic test frame. The test frame is oriented vertically so that the tensile force is applied to the reinforcing bar by the hydraulic actuator in the test frame. The frame was designed to be able to accommodate a variety of sizes beam-end specimen. To simulate the behaviour of a full-scale beam, the frame was designed with three support reactions. The applied load and the support reactions were represented by the top left and the bottom right horizontal reactions on the specimen, respectively. Once the load was applied to the bar, the top vertical reaction represented the internal compression force whereas the tension force applied by the actuator acted as internal tension force. The actuator was set to be able to apply tensile force on the reinforcing bar up to 500 kN which was the maximum capacity of the frame. The test was performed under displacement control at rate 0.3mm/min to ensure that the test last more than three minutes before occurring failure as it is recommended by ASTM A944-05. Figure 3.5 shows beam-end specimen installed on the frame. The beam-end specimen was instrumented with four LVDTs to measure the loaded end and free end slip of the rebar, and the movement of the partial depth repair concrete relative to the beam-end specimen.

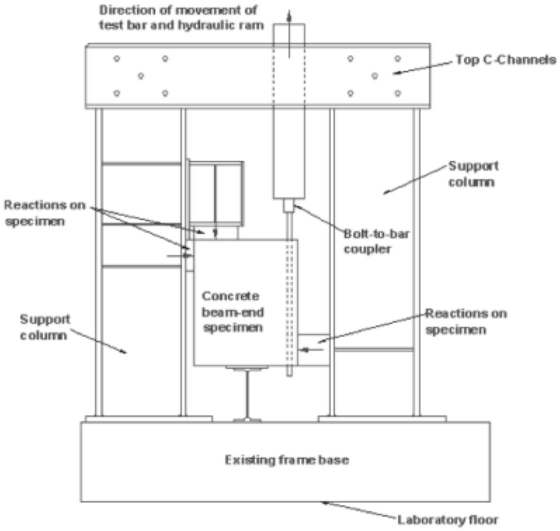

Figure 3.4 Beam-end specimens test frame apparatus (Butler 2012)

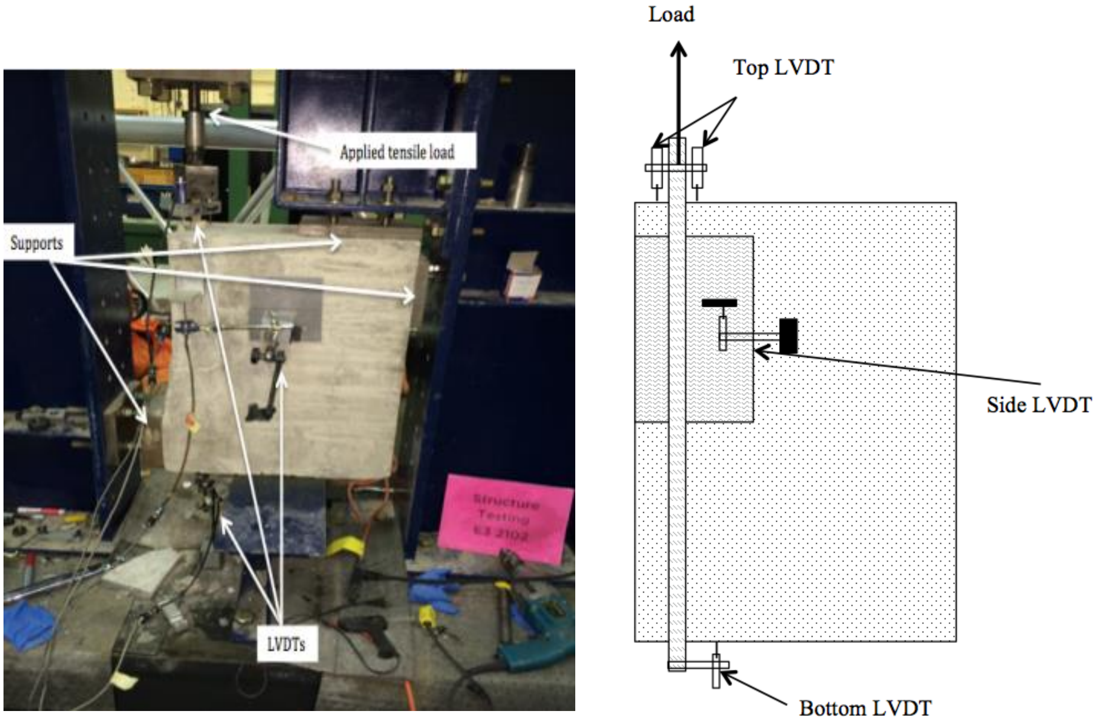

Figure 3.5 The beam-end specimen installed in the frame

3.5 Specimen Fabrication

The beam-end specimens were fabricated in several steps. First, the main reinforcing bar was corroded in a concrete prism to achieve the desired degree of corrosion damage. Next, the beam-end specimens were fabricated. For the monolithic beam-end specimens, the main bar (pre-corroded and cleaned) and other reinforcement were placed in the formwork and the entire beam-end specimen was cast monolithically. For the partial depth repaired specimens, all reinforcement except the main bar was placed in the formwork and the area representing the repair was blocked out using high-density foam, followed by casting of the specimen. After curing, the foam was taken off, the main bar was placed and the partial depth repair concrete was installed. Each step is described in more detail below.

The main tension bars were cast into small concrete prisms (100 X 100 X 400 mm) to be pre-corroded. The concrete mix contained salt at 3.8% of the cement mass, which is equivalent to 2.3% of chloride to initiate and accelerate corrosion. The prisms were placed in a moist environment (100% humidity) to facilitate corrosion. Corrosion was accelerated through an impressed current using power supplies as described in Section 3.6. The duration of accelerated corrosion necessary to reach the desired corrosion mass loss (5%, 7.5%, 10% or 15%) was estimated using Faraday's law as described in Section 3.6. Once the required level of corrosion was achieved, the bars were removed from the prisms and cleaned by sandblasting; thereafter the bars were weighed and the mass loss of each bar was then evaluated through the mass loss equation (see Section 3.6). Figure 3.6 shows corrosion induced cracking and staining of the prism.

Figure 3.6 Corrosion pattern of the rebar in a concrete prism

The bars were threaded at one end to attach it to a coupler through which tensile load was applied. For the specimens that needed to be repaired with partial depth repair concrete, high-density foam was used to isolate the patch region during the main cast (Figure 3.7). Four different development lengths were considered (200 mm, 250 mm, 300 mm and 350 mm). Polyvinyl chloride pipes (PVC) were used to achieve the desired bonded length (Figure 3.8). To prevent a conical failure surface from forming, a lead of 50 mm length of bar was unbonded at the loaded end of the bar (ASTM A944-05). The shear reinforcement was placed in the specimen parallel to the main bar so that the stirrups would not intercept longitudinal splitting cracks that occur at bond failure. Figure 3.9 shows the beam-end specimens in the forms prior to concrete placement. The specimens were cast using ready-mixed concrete with specified compressive strength of 35 MPa. The specimens were removed from the forms after two to three weeks of curing. After 28 days of curing, the high-density foam used to form the repair pockets was removed and the concrete surface in the repair area was roughened using needle peener in preparation for the partial depth repair (Figure 3.10). The surface of the substrate concrete was flushed with water to remove all dust after roughening. Before applying the partial depth repair concrete, the surface of substrate concrete was in a saturated surface-dry condition to prevent rapid drying and weakening of the repair concrete and its bond to the surface. After applying the repair concrete, the repair concrete was cured 28 days before testing. The curing process for both monolithic concrete and repair concrete was the same where the first 7 days were moist curing and the remaining 21 days were air curing. This method of curing was used to simulate typical construction site curing practices.

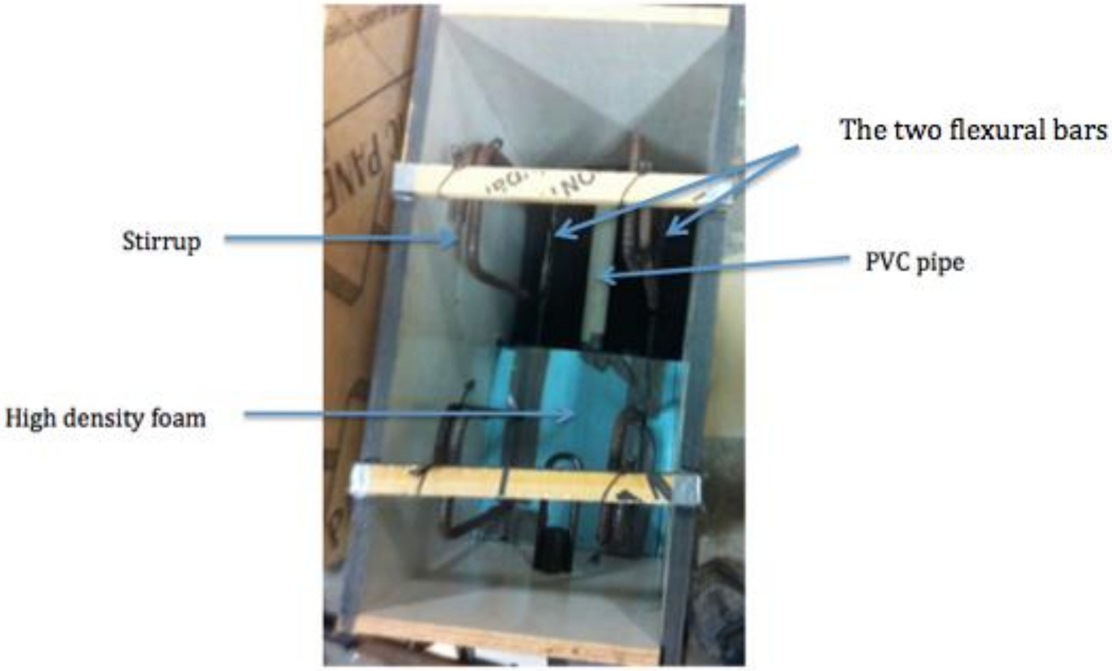

Figure 3.7 Beam-end specimen formwork and reinforcement

Figure 3.8 PVC pipes and foam installation in formwork

Figure 3.9 Finishing stage

Figure 3.10 Surface roughening of region to be repaired

Figure 3.11 Completed specimen after applying partial depth repair concrete

3.6 Corrosion Acceleration Technique and Mass Loss Measurement

An accelerated corrosion technique was used to reach the desired corrosion levels in a shorter period of time. This technique involved using power supplies to impress a constant current in the concrete prisms described in the previous section to produce a steel mass loss according to Faraday's Law (ACI 222, 2001):

$$m_l = \frac{MIT}{zF} \qquad \text{Equation (3.1)}$$

Where:

m_l: Mass loss (g)
M: The atomic weight of the metal = 56g for Fe
I: Corrosion current (A) = i x s_a
i: Corrosion current density (μA/cm^2)
s_a: The surface area of the corroded steel (cm^2)
T: Time (s)
z: The valence of the corroding metal (2 for iron)
F: Faraday's constant = 96,500 A.s

Using Faraday's Law, the time to achieve the desired mass loss of 5%, 7.5%, 10% or 15% was estimated to be 50 days, 75 days, 100 days and 150 days, respectively. The specimens were placed in a special chamber subjected to continuous 100% humidity. The specimens that were to be corroded to the same level were connected in series to ensure that they had a constant current. Every prism had one steel reinforcement bar which works as an anode and one stainless steel bar acting as a cathode (Figure 3.12). The length of all prisms to corrode the bars was limited at 400 mm. In the literature, different current densities were used ranging from 10400 $\mu A/cm^2$ to 45 $\mu A/cm^2$. In order to accelerate the corrosion in the lab, the current density should be less than 200 $\mu A/cm^2$ as recommended by El Maaddawy and Soudki (2003). The direct impressed current through the reinforcing bar in the current study was 150 $\mu A/cm^2$ as a constant current density. This value was used based on El Maaddawy and Soudki (2003) recommendation to produce corrosion similar to those found in the field.

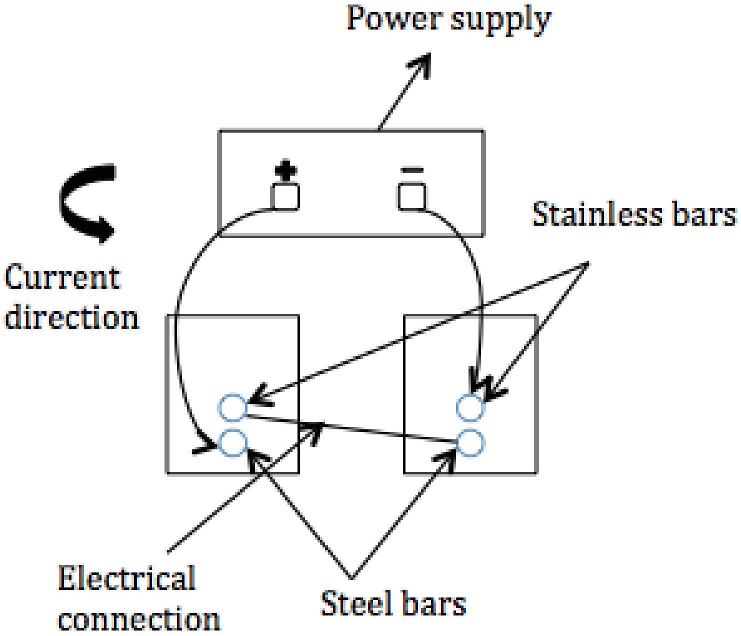

Figure 3.12 Electrical connections for the accelerated corrosion setup

Once the desired level of corrosion was achieved, the bars were removed from the concrete prisms and cleaned by sand blasting to remove all corrosion products, followed by weighing. Prior to corrosion process, each bar was numbered weighed to determine its original mass. The actual mass loss due to corrosion was then calculated as follows:

$$m\% = \frac{mass\ of\ original\ steel - mass\ of\ corroded\ steel}{mass\ of\ original\ steel}$$ Equation (3.2)

Figure 3.13 shows the typical reinforcement surface conditions at different corrosion levels. The bars with 5% corrosion were observed to have uniform corrosion along the bar surface. The bars with 7.5% corrosion were observed to have almost uniform corrosion along the bar surface with very small pits. As the corrosion level increased to 10%, more deep pits were observed. At 15% corrosion level, two different pattern of corrosion distribution were observed. The first one, which was more common, showed a more uniform distribution of corrosion along the rebar (Figure 3.13 (d)). The second pattern showed concentrated corrosion that tended to remove the rebar ribs (Figure 3.13 (e)).

(a) 5% corrosion level

(b) 7.5% corrosion level

(c) 10% corrosion level

(e) 15% corrosion level
with uniform corrosion

(d) 15% corrosion level with localized
corrosion and loss of bar ribs

Figure 3.13 Typical reinforcement surface conditions after corrosion

3.7 Splitting Strength Test

The splitting tensile strength of concrete is typically 8% to 15% of the compressive strength of concrete. This ratio is affected by the coarse aggregate properties (type and size) and by the type of used test to determine the tensile strength of concrete (Sagoe-Crenstil et al. (2001); MacGregor and Bartlett, 2000, Neville, 1997). Also, as compressive strength increases, the tensile strength increases at a decreasing rate. The splitting tensile test, direct tension test and flexural tensile test are common methods to measure the tensile strength of concrete. The splitting tensile strength gives most representative of the behavior of this study because it generates splitting failure from compression stress applied along the length of the concrete cylinder, which is similar to the splitting bond failure in RC member where the splitting crack in concrete is generated generates from radial compression stresses generated by mechanical bond of the reinforcing bar ribs bearing on the concrete. In the current study, the tensile strength of concrete was measured through the splitting tensile test using cylindrical concrete specimens with dimensions of 200 mm in length and 100 mm in diameter. Figure 4.3 shows a schematic of the splitting tensile test. The diameter and the length were measured before testing each specimen. For alignment, bearing strips were placed on the bottom and the top of concrete cylinder to ensure of centering the specimen. The process of measuring the splitting tensile strength followed CSA A23.2-13C and the strength was calculated using Equation 4.1.

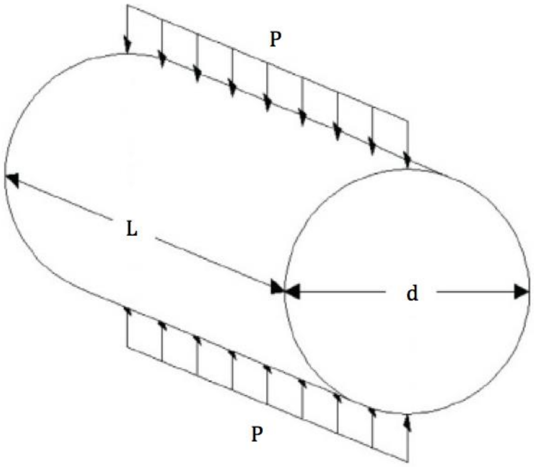

Figure 3. 14 Splitting tensile test of concrete cylinder

$$f_t = \frac{2P}{\pi d l}$$ Equation (3.1)

Where

f_t: Splitting tensile strength (MPa)

P: Maximum applied load (N)

l: Length of concrete cylinder (mm)

d: Diameter of concrete cylinder (mm)

3.8 Fracture Energy of Concrete

The fracture energy of concrete can be evaluated through the area under the stress versus crack opening curve, which represent the energy absorbed in the damage zone (Hillerborg, 1986). There is no standard test method and test sample (specimen dimension and notch dimension) to measure fracture energy of concrete. Butler (2012) adapted the procedures and the fracture energy specimen configurations from three different previous studies including (Martin et al., 2007, Darwin et al., 2001, and RILEM, 1985). The current study followed the procedure that was developed by Butler (2012). Table 3.1 illustrates a summary of the differences between previous studies on the fracture energy test.

Table 3. 1 Summary of the differences between previous studies on the fracture energy test

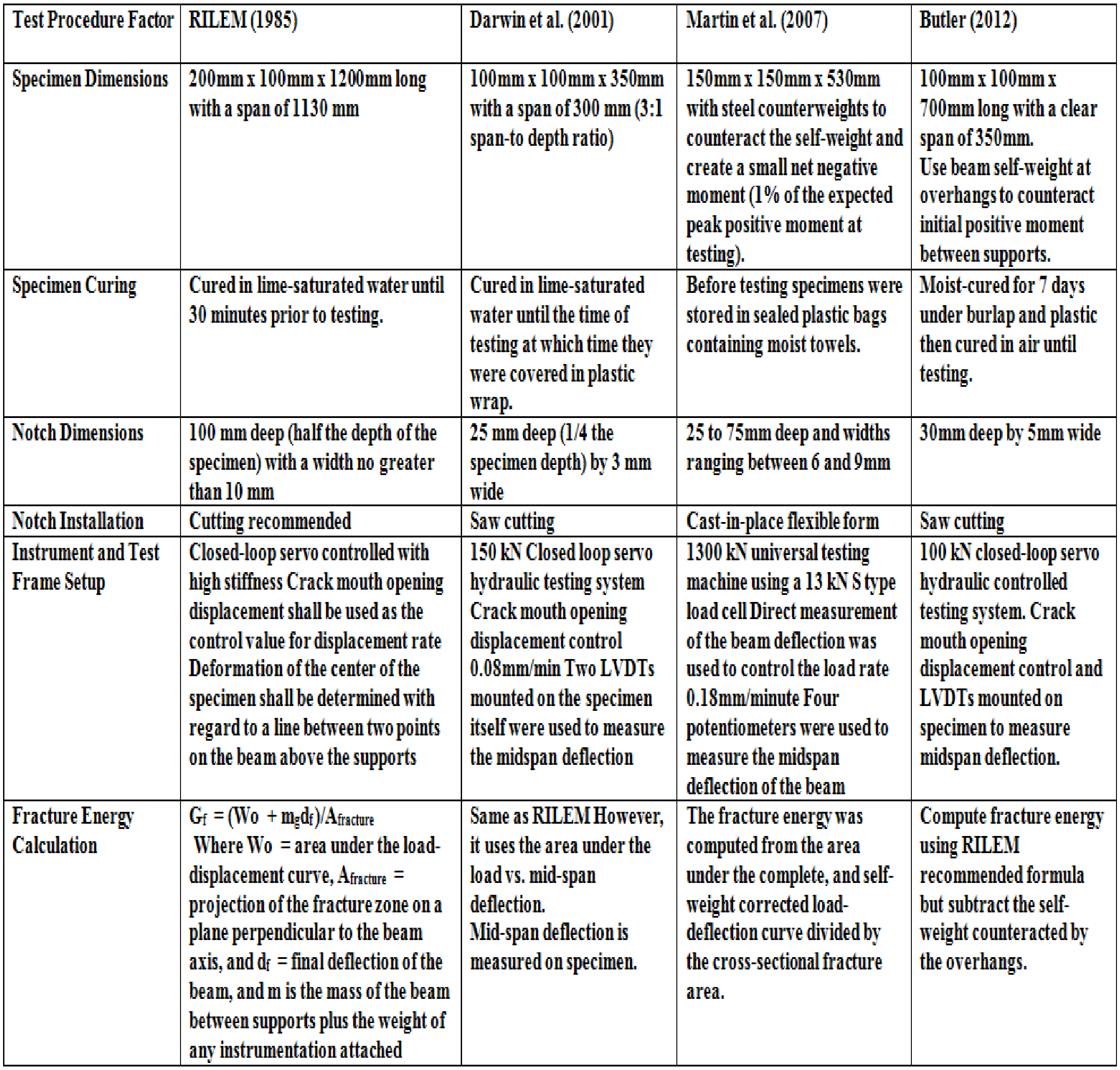

Test Procedure Factor	RILEM (1985)	Darwin et al. (2001)	Martin et al. (2007)	Butler (2012)
Specimen Dimensions	200mm x 100mm x 1200mm long with a span of 1130 mm	100mm x 100mm x 350mm with a span of 300 mm (3:1 span-to depth ratio)	150mm x 150mm x 530mm with steel counterweights to counteract the self-weight and create a small net negative moment (1% of the expected peak positive moment at testing).	100mm x 100mm x 700mm long with a clear span of 350mm. Use beam self-weight at overhangs to counteract initial positive moment between supports.
Specimen Curing	Cured in lime-saturated water until 30 minutes prior to testing.	Cured in lime-saturated water until the time of testing at which time they were covered in plastic wrap.	Before testing specimens were stored in sealed plastic bags containing moist towels.	Moist-cured for 7 days under burlap and plastic then cured in air until testing.
Notch Dimensions	100 mm deep (half the depth of the specimen) with a width no greater than 10 mm	25 mm deep (1/4 the specimen depth) by 3 mm wide	25 to 75mm deep and widths ranging between 6 and 9mm	30mm deep by 5mm wide
Notch Installation	Cutting recommended	Saw cutting	Cast-in-place flexible form	Saw cutting
Instrument and Test Frame Setup	Closed-loop servo controlled with high stiffness Crack mouth opening displacement shall be used as the control value for displacement rate Deformation of the center of the specimen shall be determined with regard to a line between two points on the beam above the supports	150 kN Closed loop servo hydraulic testing system Crack mouth opening displacement control 0.08mm/min Two LVDTs mounted on the specimen itself were used to measure the midspan deflection	1300 kN universal testing machine using a 13 kN S type load cell Direct measurement of the beam deflection was used to control the load rate 0.18mm/minute Four potentiometers were used to measure the midspan deflection of the beam	100 kN closed-loop servo hydraulic controlled testing system. Crack mouth opening displacement control and LVDTs mounted on specimen to measure midspan deflection.
Fracture Energy Calculation	$G_f = (W_o + m_g d_f)/A_{fracture}$ Where W_o = area under the load-displacement curve, $A_{fracture}$ = projection of the fracture zone on a plane perpendicular to the beam axis, and d_f = final deflection of the beam, and m is the mass of the beam between supports plus the weight of any instrumentation attached	Same as RILEM However, it uses the area under the load vs. mid-span deflection. Mid-span deflection is measured on specimen.	The fracture energy was computed from the area under the complete, and self-weight corrected load-deflection curve divided by the cross-sectional fracture area.	Compute fracture energy using RILEM recommended formula but subtract the self-weight counteracted by the overhangs.

Butler (2012) developed fracture energy specimen with dimensions of 700 mm in length, 100 mm and 100 mm in height and with notch dimensions of 30 mm in depth and 5 mm in width (Figure 4.4).

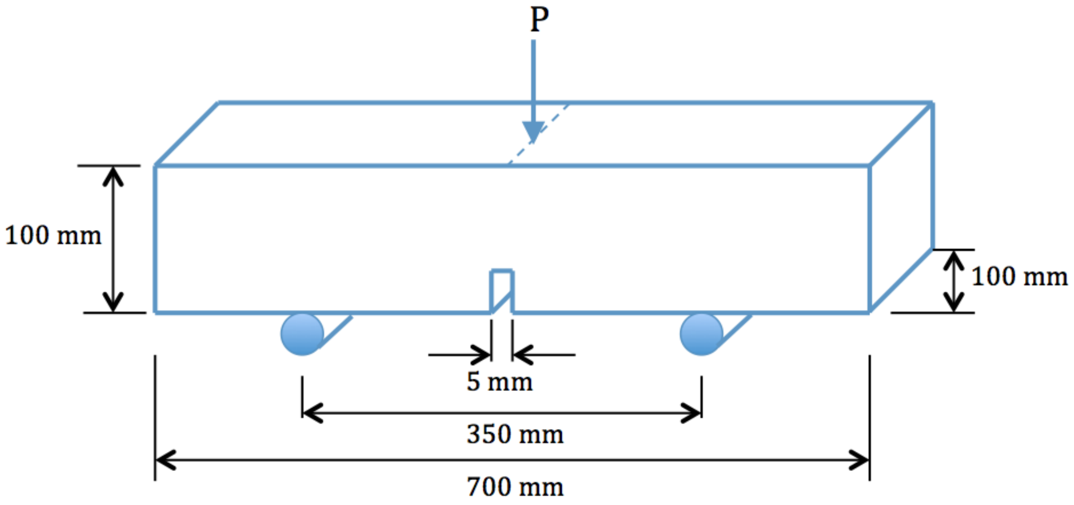

Figure 3. 15 Dimensions of fracture energy specimen

The fracture energy specimen was tested under three point loading with a 350 mm clear span. A cantilever with 175 mm length was provided on each end of the specimen to counteract the mass of the specimen within the clear span. A closed-loop servo-hydraulic testing system with a 100 kN capacity was used for the fracture energy test using the crack mouth opening displacement (CMOD), measured by a clip gauge, to control the load rate. The clip gauge was mounted on two knife-edge strips metal that were glued underneath the specimen (Figure 4.5). Two LVDTs were used to measure the midspan displacement. The test was run in CMOD control at rate of 0.075 mm/min to ensure reaching the maximum load within 30 to 60 seconds as recommended by Butler (2012). After reaching the peak load, the test was continued until the specimen was separated into two parts. The displacement corresponding to the peak load was called crack tip opening displacement ($CTOD_{peak}$) (Figure 4.6). For each type of concrete, three specimens were tested and the average fracture energy was calculated.

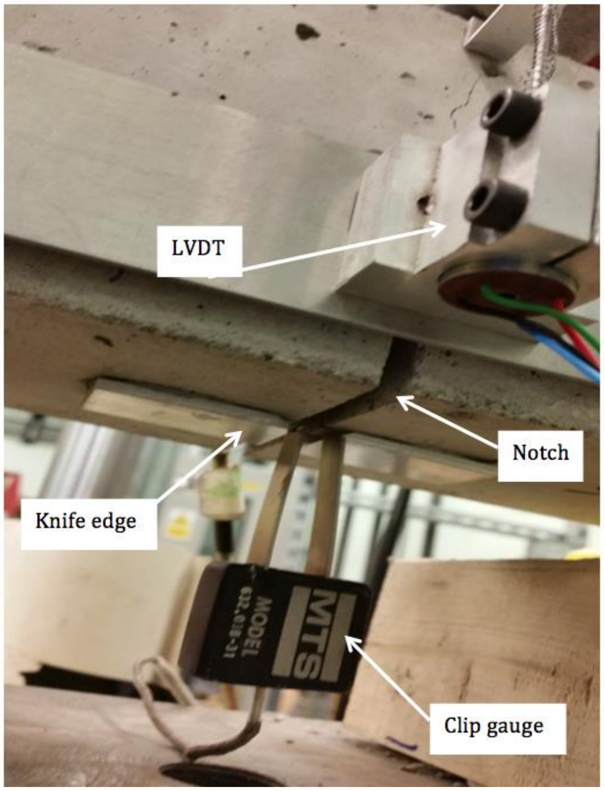

Figure 3. 16 Bottom face of the fracture energy specimen

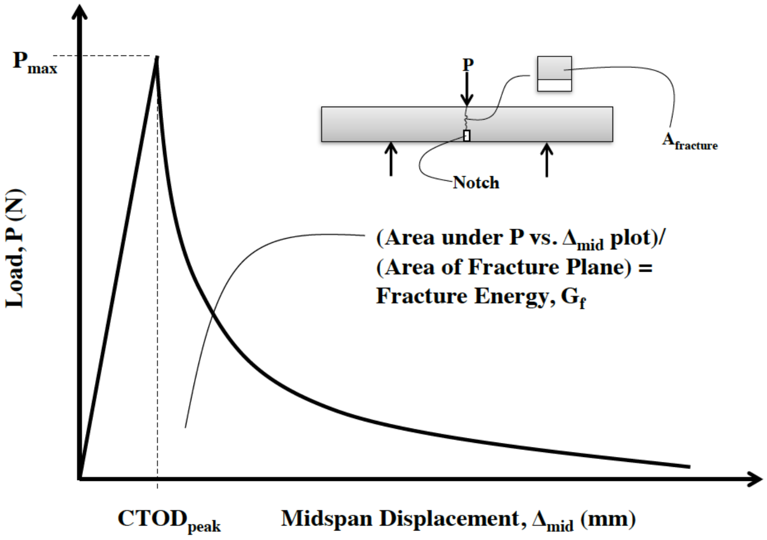

Figure 3. 17 Load versus displacement curve of fracture energy test (Butler 2012)

The fracture energy of concrete was then calculated as follows:

$$G_f = \frac{W_0}{A_{fracture}} \qquad \text{Equation (3.2)}$$

Where

G_f: Fracture energy of concrete (N/mm)

W_0: Area under the load-displacement curve (N-mm)

$A_{fracture}$: Cross sectional area of the beam above the notch (mm^2)

3.9 Material Properties

The prepackaged partial depth repair concretes used in this research were supplied by two companies, and will be referred to herein as SCC1 and SCC2. These partial depth repair concretes are highly flowable and can be used for concrete patch thicknesses of 25 to 450 mm. Both have high bond strength and provide increased resistance to de-icing salts. Table 3.2 illustrates the mechanical properties of prepackaged repair concretes SCC1 and SCC2.

Table 3. 2 Specified mechanical properties of SCC1 and SCC2

SCC1	
Property	**Magnitude**
Slump flow	600 – 700 mm
Set time	25-30 min
Specified compressive strength (28 days)	45 MPa
Specified bond strength (7 days)	2.5 MPa
Specified slant shear	14 MPa
Tested compressive strength (28 days)	65 MPa
SCC2	
Slump flow	500 – 750 mm
Set time	10-15 min
Specified compressive strength	34 MPa
Specified bond strength	N/A
Specified slant shear	20.7 MPa
Tested compressive strength (28 days)	48 MPa

The partial depth repair SCC1 has less than 10% (by weight) of 8 mm coarse aggregate in one bag. The partial depth repair concrete SCC2 has no coarse aggregate as supplied; however unlike SCC1, each bag of concrete SCC2 can be extended by up to 60% of 13 mm coarse aggregate, by weight (as allowed by the suppler data sheet). In the current study, each bag was extended by 50% of 13 mm coarse aggregate to simulate the proportion of the coarse aggregate used in the ready-mixed concrete for the monolithic specimens. The mix design of the ready mixed concrete and SCC3 will be presented in Chapter 4.

The material properties for the 20M test-reinforcing bar provided as mill certificates from the reinforcing steel supplier are presented in Table 3.3.

Table 3. 3 Material properties for 20M reinforcing steel test bar (Mill certificate)

Material Property	Value
Yield Strength	479 (MPa)
Tensile Strength (Ultimate)	609 (MPa)
Elongation	17.5 (%)

3.10 Properties of the Monolithic Concrete and the Partial Depth Repair Concrete (Phase 1)

The partial depth repair concrete that used in Phase 1 was commercial prepackaged self-consolidating concrete (SCC1) with 8 mm maximum aggregate size. Table 3.4 shows the mix design of the monolithic concrete (M1); however the mix design of SCC1 was unknown (proprietary product).

Table 3. 4 Mix design of M1

Concrete type	CA* (kg/m^3)	FA* (kg/m^3)	Cement (kg/m^3)	WR* (%C)	W* (kg/m^3)	W/C	CA%
M1	1110	865	280	0.29	155	0.55	46

*CA: coarse aggregate (19mm), FA: fine aggregate, WR: Water reducer, W: water

The partial depth repair concrete contained 10% of 8 mm maximum size of aggregate (by weight). It was also contained unknown quantity of silica fume, superplasticizer and bonding agent. Table 3.5 shows the hardened properties (Compressive strength and splitting strength) of M1 and SCC1.

Table 3. 5 Hardened properties of M1 and SCC1

Concrete Mechanical properties	M1	SCC1
Compressive strength, f'_c (MPa)	56.4	65.2
Splitting strength, f_t (MPa)	4.8	3.5

3.11 Properties of the Monolithic Concrete and the Partial Depth Repairs Concrete (Phase 2)

The three types of partial depth repair concretes investigated utilized different parameters in order to determine the most efficient repair material to enhance the bond strength compared to the monolithic specimen labeled as (M2). The first type was commercial prepackaged repair concrete, labeled as (SCC2). It had 13 mm coarse aggregate instead of 19 mm that was used in the M1 and M2 concrete. Also, the prepackaged concrete included silica fume, superplasticizer and bonding agent of unknown quantities. The second type was self-consolidating concrete (SCC3), which had the same size of coarse aggregate size (19 mm) to M2 concrete. The mix design of SCC3 was taken from previous research completed at the laboratory by Safiuddin et al., 2010. The last type of partial depth repair was normal concrete (NC), which had the same mix design as that of the M1 and M2 concrete. Table 3.6 shows the mixture properties for the

M2 concrete and the SCC3 concrete; however, the mix design for SCC2 from the producer is unknown. The partial depth repair concrete SCC2 was extended with 13 mm coarse aggregate as permitted by the product data sheet. The proportion of the extension using coarse aggregate was 50% of the concrete mix, having similar aggregate proportions to the other mixes.

Table 3. 6 Mixture proportions for the M2 (NC) concrete and the SCC3 concrete

Concrete type	**CA* (kg/m^3)**	**FA* (kg/m^3)**	**Cement (kg/m^3)**	**WR* (%C)**	**AEA* (%C)**	**W* (kg/m^3)**	**W/C**	**CA%**
M2 (NC)	1110	865	280	0.29	0.003	155	0.55	46
SCC3	928	923	296	0.50	0.006	148.4	0.50	40

CA: coarse aggregate (19 mm), FA: fine aggregate, WR: water reducer, AEA: air entrained admixture, W: water

Table 3.7 shows the hardened properties (Compressive strength, splitting strength and fracture energy) of all M2, SCC2, SCC3 and NC mixes.

Table 3. 7 Hardened properties of M2, SCC2, SCC3 and NC

Concrete Mechanical properties	**M2**	**SCC2**	**SCC3**	**NC**
Compressive strength, f'_c (MPa)	41	47	43	39
Splitting strength, f_t (MPa)	4.1	4.0	4.1	3.9
Fracture energy, G_f (N/m)	134	136	133	131

Chapter 4: Experimental Results and Discussion of Beam-End Specimens

4.1 General

This chapter presents the tests results and discussion of the beam-end specimens for Phase 1, which consisted of 12 beam-end specimens and Phase 2, which consisted of 24 beam-end specimens. The results of each phase will be discussed separately due to the different bonded lengths and different mass loss levels considered. The variables that for Phase 1 were two bonded lengths (250 mm and 350 mm) and two mass loss levels (5% and 10%). Only one partial depth repair concrete was used and compared to monolithic specimens. The bonded lengths and the mass loss levels in Phase 2 were 200 mm and 300 mm and 7.5% and 15%, respectively. Three partial depth repairs were used in Phase 2.

4.2 General Cracking Behaviour

Generally, the beam-end specimens failed by splitting of concrete regardless of the bonded length or mass loss level. Bond failure was expected since all bonded lengths used in this research were less than the development length specified in CSA A23.3-04. The failure process can be described in three stages of visual cracks as illustrated in Figure 4.1. At the first stage, a small longitudinal crack starts at the loaded end (in front view) and moves toward the bar in the unbonded (lead) region (top view). The second stage includes propagation of the longitudinal crack moving from the loaded end to the free end in the front view parallel to the bar accompanied by widening of the cracks. Also, at the top view of the specimen at the loaded end, the crack starts to propagate and move behind the rebar forming a V shaped crack. At the last stage where the splitting failure occurs, the cracks become wider and the longitudinal crack lengthens to the free-end. Moreover, at the same time the top V crack extends to the edge of the beam-end specimen. In the most cases, a crack perpendicular to the longitudinal crack in the front view appears at the end of the bonded length (at the free end) at the failure stage.

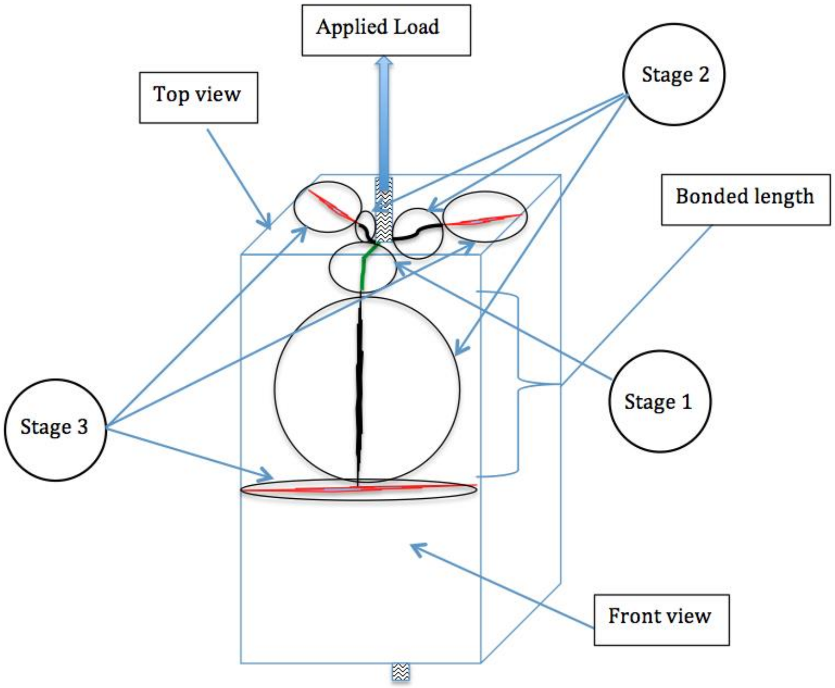

Figure 4.1 Crack initiation and propagation up to failure

4.3 Bond-Slip Response and Failure Mechanism of Beam-End Specimen

Butler (2012) divided the bond-slip response of the beam-end specimen into four stages as shown in Figure 4.2. The top view represents the circumferential tension field where an axial force was applied on the reinforcing bar. The bottom view shows the surface where the splitting crack started and propagated as the load increased. The side view illustrates the increasing of circumferential tension field along the bonded length. The first stage is the state from the beginning of applying the axial force and before the splitting crack forms. At this stage, the bond property is gained mainly by chemical adhesion and the friction between the reinforcing bar and the surrounding concrete. Adhesion prevents bars from slipping at the early stage of loading; however there is a small measured slip during this stage resulting from concrete deformation. As the load increases, the reinforcing bar starts to move relative to the concrete breaking the adhesion forces and activating the bearing forces from the mechanical interlock between the bar lugs and the surrounding concrete. This movement of the bar is accompanied by initiation of the splitting crack at the loaded end where the maximum stress exists, which was represented by

Stage 2. The mechanical interlocking between the concrete and the reinforcing bar gives the deformed bar superior bond in comparison with chemical adhesion and friction. The forces due to the bearing of the bar ribs against the concrete create the primary bond strength that inhibits the relative slip between deformed bars and surrounding concrete. At stage 3, the splitting crack propagates and the circumferential tension field resulted in widening the splitting crack increases as the axial load increases. Also, in this stage as the load increases, the reinforcing bar continues to slip until failure. In the fourth stage, the splitting crack extends suddenly to the end of the bonded length and causes a brittle failure of the beam-end accompanied by a significant increase in the bar slip. This mechanism was similar to what observed in this research.

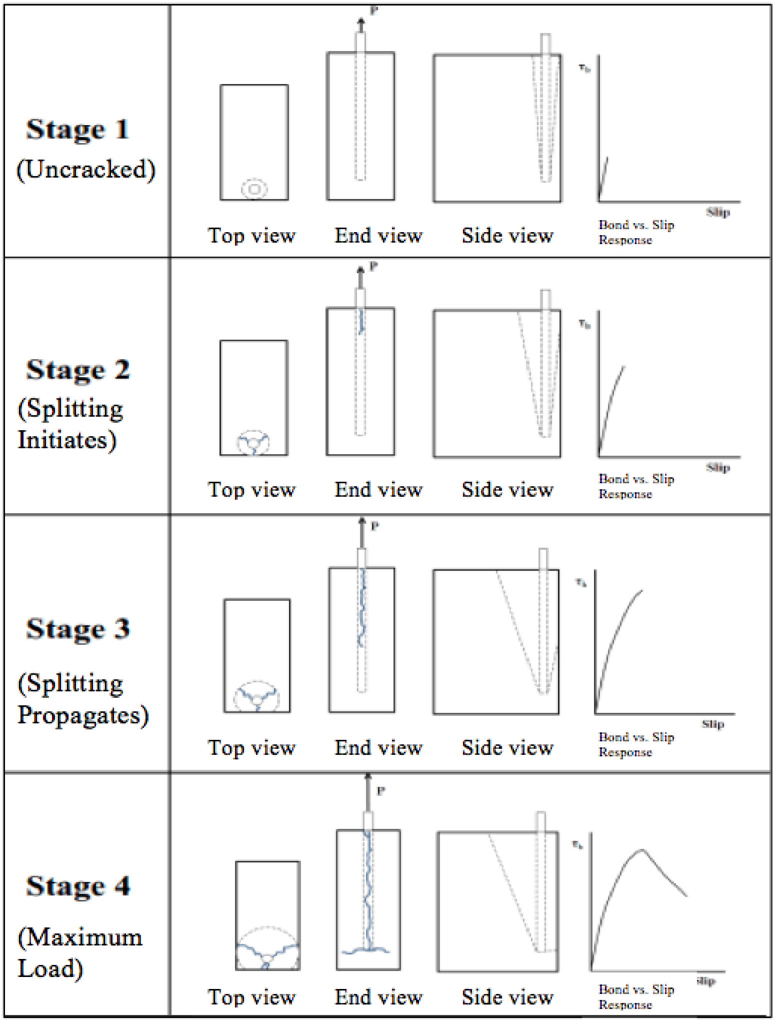

Figure 4.2 Schematic representation of stress fields and cracking of beam-end specimens (Butler, 2012)

4.4 Phase 1 Experimental Results for Beam-End Specimens

4.4.1 General Discussion of Test Results

The bar force and stress at failure, average bond strength, loaded end slip, free end slip and the failure mode are shown in Table 4.1 for all specimens. The specimen labeling system consists of four parts. The first part (BE) refers to beam-end and the second part refers to type of concrete (M1 for monolithic concrete of Phase 1 and SCC1 for the first prepackaged self-consolidating concrete). Note that the average compressive strength (f'_c) for M1 is 56.4 MPa and for SCC1 is 65.2 MPa. The third part indicates the bonded length (250 mm as a short bonded length and 350 mm as a long bonded length). The last part represents the corrosion level (C for the control specimens, 5 for the specimens with 5% corrosion level and 10 for the specimens with 10% corrosion level). The two bonded lengths 250 mm and 350 mm represent 12.5 and 17.5 bar diameters. The bar was extended out of the specimens by 75 mm for tensile loading purposes. Thus, the values of loaded end slip were corrected to account for the axial elongation of the 75 mm free length plus 50 mm of the unbonded (lead) length. The development lengths for 20M bars were estimated using CSA A23.3-04 Clause 12.2.2 as a function of the concrete cover and f'_c. The maximum ratio of bonded length, L_b, to development length, L_d, was 0.70. This indicates that splitting bond failures were expected for all specimens. The average bond strength was calculated using Equation 4.1.

$$\tau_{b(avg)} = \frac{d_b\,(\frac{T_b}{A_s})}{4L_b} = \frac{d_b\,f_s}{4L_b} \qquad \text{Equation (4.1)}$$

Where:

$\tau_{b(avg)}$: Average bond strength (MPa)

d_b: Bar diameter (mm)

T_b: Tensile force in the bar at failure (N)

A_s: Bar cross-sectional area account for actual mass loss (mm^2)

f_s: Stress in the bar at failure (MPa)

L_b: Bonded length of the bar (mm)

Table 4. 1 Summary of beam-end test results of phase 1

Specimen	Corrosion Level (%)	Actual mass loss (%)	L_b/L_d	Tensile load at failure Tb (kN)	f_s (MPa)	Average bond strength τ_b (MPa)	Adjusted Loaded-End slip at failure $*S_l$ (mm)	Failure Mode**
BE-M1-250-C	0	0	0.39	131.8	420	8.39	0.47	S
BE-SCC1-250-C		0	0.42	113.4	361	7.22	0.37	S
BE-M1-350-C		0	0.54	154.2	493	7.01	3.44	Y+S
BE-SCC1-350-C		0	0.59	133.2	424	6.06	1.80	P+S
BE-M1-250-5	5	5.1	0.42	133	446	8.69	0.39	S
BE-SCC1-250-5		6.2	0.46	116.4	395	7.65	0.31	S
BE-M1-350-5		5.5	0.59	152.6	514	7.14	2.45	N/A
BE-SCC1-350-5		4.9	0.63	138.6	464	6.47	1.58	P+S
BE-M1-250-10	10	9	0.46	135.2	473	9.02	0.33	S
BE-SCC1-250-10		12.2	0.50	120.8	438	8.21	0.27	S
BE-M1-35010		10.1	0.64	154.3	546	7.40	2.27	N/A
BE-SCC1-350-10		10.9	0.70	142.2	508	6.85	1.40	Y+S

$*S_{l,\ adj} = s_{l\text{-}measured} - (PL)/(A_bE_s)$, where L = 125 mm and E_s = 200,000 MPa.

** S: Splitting failure Y: Bar yield. P: Pullout. N/A: Not available because of bar rupture.

4.4.2 Effect of Concrete Strength and Repair Condition on Bond Strength

Because of the variation of compressive strength of the two types of concrete, the results of average bond strength have been normalized by $f'_c{}^{1/2}$ for both 250 mm and 350 mm bonded length as shown in Figure 4.3.

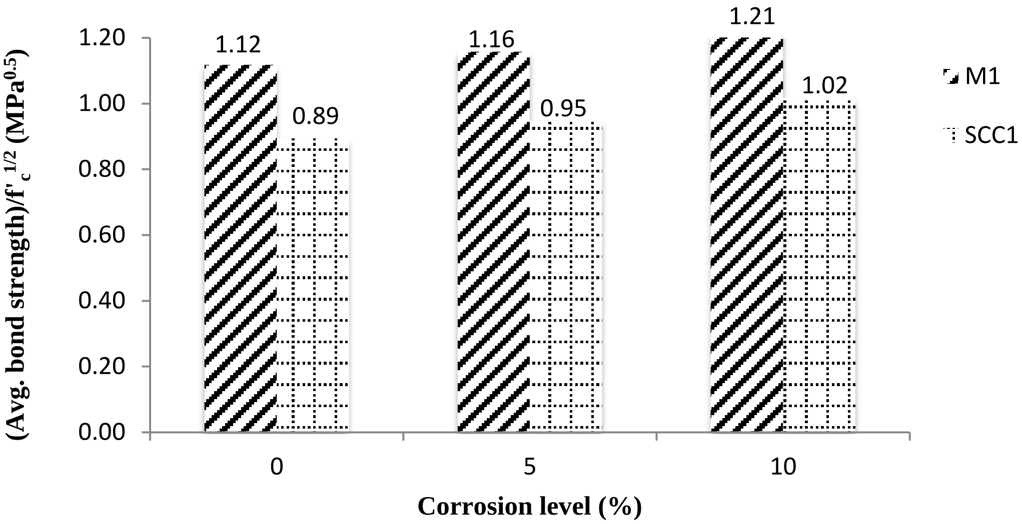

(a) 250 mm Bonded Length Specimens

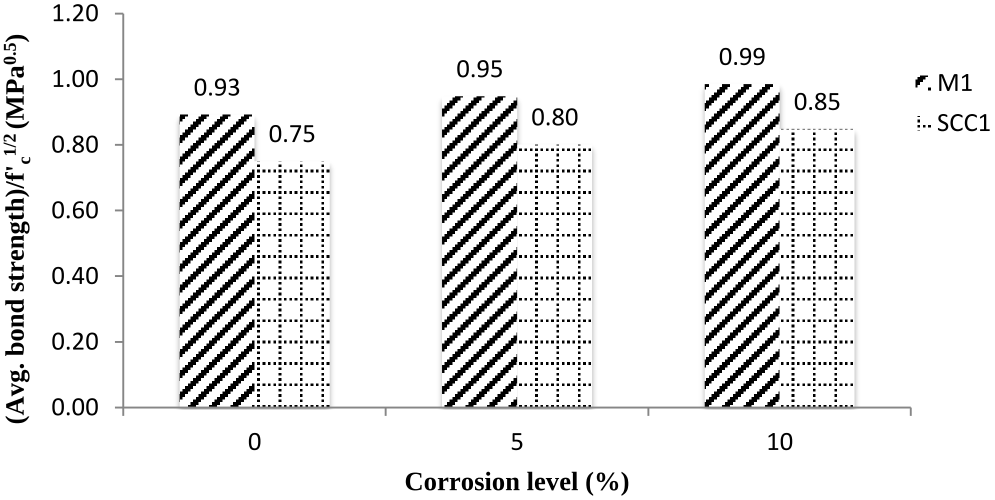

(b) 350 mm Bonded Length Specimens

Figure 4. 3 Avg. bond strength results normalized to f’$_c$$^{1/2}$

Generally, for both the 250 mm and 350 mm bonded lengths, it could be seen that the average bond strength increased slightly for the 5% and 10% corroded bars that were cleaned and repaired with new concrete (M1 or SCC1) relative to the non-corroded bars. The improvement in the average bond strength of beam-end specimens with 250 mm bonded length ranged from 4% to 9% for the bars with 5% and 10% mass loss, respectively. This increase in the average bond strength was similar to that achieved for the specimens 350 mm bonded length where it ranged from 6% to 11% for the bar with 5% and 10% corrosion level. However, the differences in normalized bond strength ($\tau_b /f'_c{}^{1/2}$) between the M1 and SCC1 were smaller for the 350 mm bonded length than for the 250 mm bonded length. This may be because by increasing the bonded length, the average bond stress between the bar and surrounding concrete decreases. Thus, the bond stresses will be distributed over a larger area leading to decrease the effect of variation of compressive strength and the effect of corrosion on the average bond strength in comparison to the shorter bonded length.

Although the compressive strength of the SCC1 was greater than the compressive strength of M1, the average bond strength of M1 was higher than that achieved by SCC1. One possible reason may be differences in the amount and the size of coarse aggregate in the two mixes, which may influence the splitting tensile strength and the fracture energy of the concrete. The M1 concrete had 19 mm maximum aggregate size and the aggregate content was about 46% by mass. However, the SCC1 mix contained less than 10% coarse aggregate by mass with an 8 mm maximum aggregate size. Resulted from that, the partial depth repair SCC1 had lower splitting tensile strength than M1.

Fracture energy is defined as the capacity of the concrete to dissipate energy as a crack opens. Generally, the bond strength mainly depends on the tensile (splitting) strength of the concrete. As a result, the bond strength is usually expressed as a function of ($f'_c{}^{1/2}$) because the tensile strength is approximately proportional to ($f'_c{}^{1/2}$). To have more accurate effect of concrete strength on bond strength, recent research has determined that the bond strength is more closely related to ($f'_c{}^{1/4}$) rather than ($f'_c{}^{1/2}$). However, the tensile strength is not the only factor that affects the bond strength of concrete. In the case of a splitting failure of reinforced concrete that is not confined with transverse reinforcement, the load at failure is governed by the tensile response of the concrete, which is represented by the tensile capacity and fracture energy. The bond capacities are improved for the concrete specimens with high fracture energies regardless of the similarity of their tensile or compressive strengths. In fact, there is no a strong relationship between the concrete compressive strength and the fracture energy. It has been found that the fracture energy increases slightly, and may decrease in some cases as the compressive strength of concrete increases, (ACI 408, 2003).

Beygi et al. (2014) reported that the fracture energy of concrete is strongly influenced by the size of coarse aggregate. As the coarse aggregate size increases, the fracture energy increases. Also, the fracture energy increases significantly with increasing coarse aggregate volume. A study on self-consolidating concrete found that increasing the volume of coarse aggregate from 30% to 60% had the most significant effect on fracture energy compared to other mechanical properties (Nikbin et al. 2014). Given the influence of the coarse aggregate on fracture energy, it can be concluded that the amount and size of the coarse aggregate will influence the splitting bond strength. Thus, the limited coarse aggregate content of the SCC1 may be limiting the average bond strength in spite of its higher compressive strength.

The second possible explanation that the M1 specimens had higher average bond strength than the SCC1 is because the bonded region of M1 was monolithic with the whole beam-end specimen. However for the specimens that were repaired with SCC1, the beam-end specimens were cast with a pocket at the repair and anchorage region to be studied. The SCC1 was placed on the substrate concrete of the beam-end specimen in the bonded region. Thus, as tension was applied to the bar, the bar was anchored in the partial depth repair which then transferred the bar force to the beam-end specimen through shear friction at the interface between the partial depth repair and the substrate concrete. This led to internal shear cracks between the main bar and the stirrups at the bottom of the partial depth repair (SCC1) pocket. This additional cracking (Figure 4.4) may have caused the longitudinal bond crack to form at a lower load level, resulting in a splitting failure and decreasing the average bond strength.

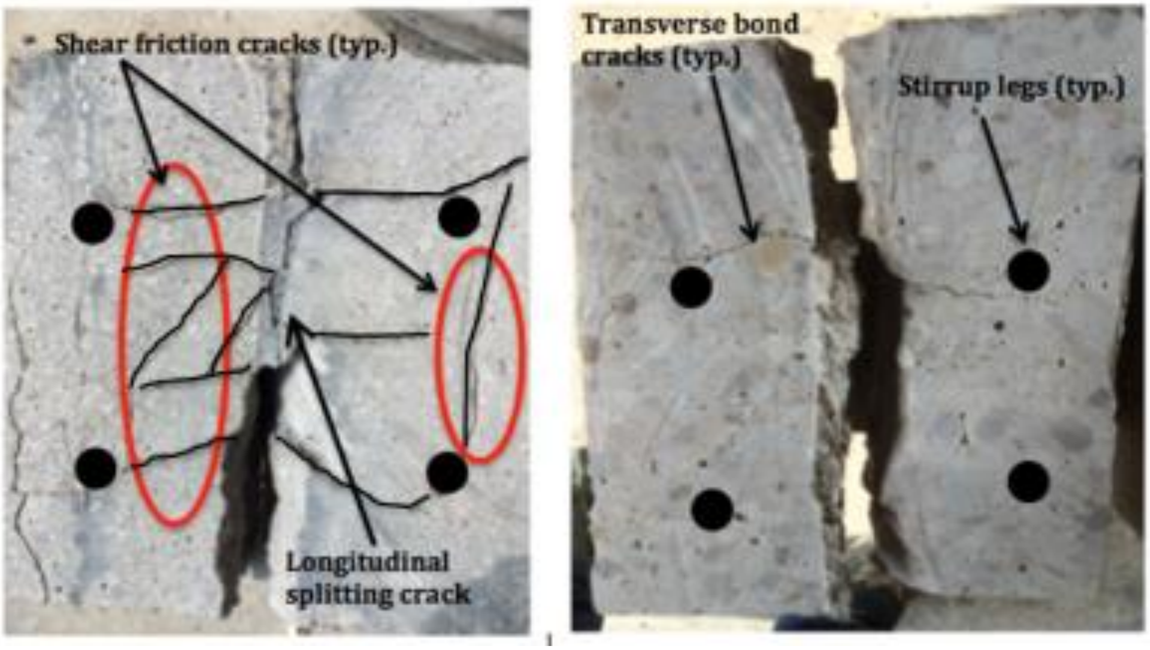

(a) SCC1 **(b) M1**

Figure 4. 4 Internal surface of bonded region after splitting failure (specimen saw-cut at level of partial repair depth for inspection)

4.4.3 Measured Bond Stress Slip Behavior

4.4.3.1 Bond Stress-Slip Behaviour for Specimens with 250 mm Bonded Length

The loaded-end bond stress-slip behaviour for the specimens with 250 mm bonded length for M1 and SCC1 is shown in Figure 4.5 (a) and Figure 4.5 (b), respectively. The slip data in Figure 4.5 were the adjusted slips after deducting the axial elongation of the extended bar. Generally, for the control, 5% and 10 % corrosion levels, the loaded end bond stress-slip curve increased nonlinearly until the maximum bond stress was achieved coinciding with splitting failure. Once the splitting failure happened, the bond stress dropped off suddenly with increasing bar slip. This sharp reduction was followed by a continued gradual decrease in bond stress as the bar continued to slip. The stiffness of the bond stress-slip curve increased as the corrosion level increased for two possible reasons. Firstly, as the corrosion level increased, the cross sectional area of the rebar decreased. It is known that as the bar size decreases, the force in the bar at bond failure decreases in proportion to the change in bar diameter, rather than in proportion to change in the bar cross-sectional area (ACI 408, 2003). Thus, as the corrosion mass loss increased, the average bond strength increased although there was only a slight difference in the force at failure. Secondly, the rebar surface for the corroded bars was rougher than for the control specimens, which was expected to improve both mechanical bond and friction properties. Subsequently, the slip of the control beam-end specimens was greater than the corroded specimens. These observations are similar to the study by Desnerck et al. (2010) who studied the bond stress-slip for various bar diameters. This research concluded that the average bond strength increases with decreasing bar diameter. However, the corresponding slip decreases with decreasing bar diameter. It was explained that because in smaller bar diameter, the amount of ribs in the bar increase and the spacing between ribs decrease which increase the surface roughness of the rebar and increasing the mechanical interlock between the concrete and the reinforcement bar, thus enhancing bond and reducing bar slip.

The bar slip at failure for the control beam-end specimen was 32% and 42% greater than the M1 specimens with 5% and 10% rebar mass loss. This trend was similar to that achieved for the specimens repaired with SCC1 where the control beam-end specimen bar slip was 28% and 66% higher than the beam-end specimens with 5% and 10% mass loss, respectively.

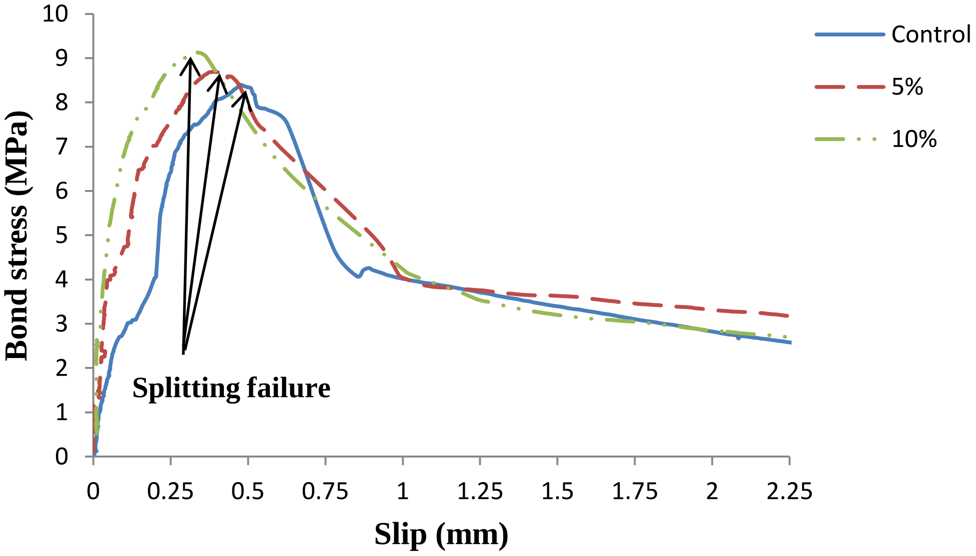

(a) Bond stress-slip of BE-M1-250

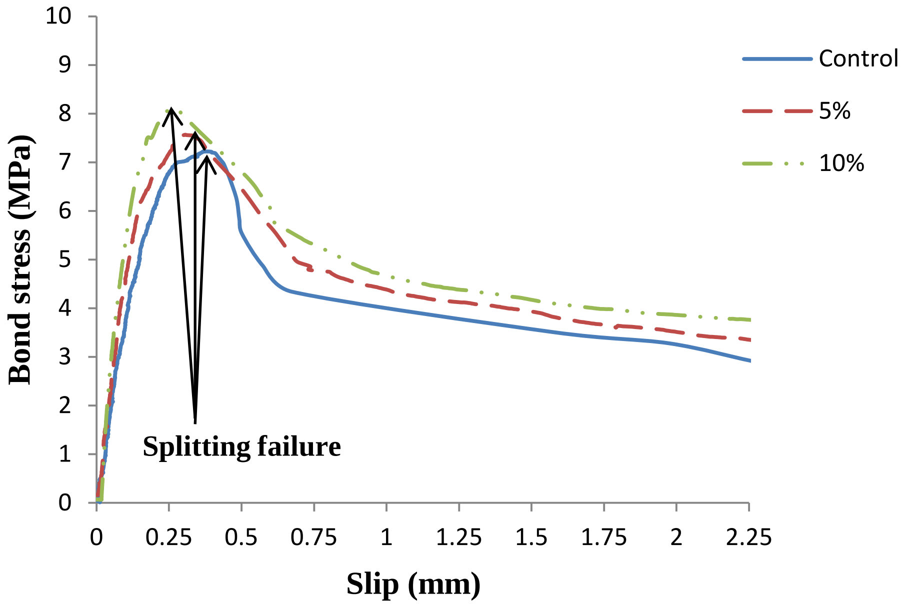

(b) Bond stress-slip of BE-SCC1-250

Figure 4. 5 Loaded-end bond-slip responses of 250 mm bonded length for (a) M1 and (b) SCC1

The free-end slip behaviour of beam-end specimens with 250 mm bonded length is shown in Figure 4.6 (a) and Figure 4.6 (b) for M1 and SCC1 respectively. The free-end slip was essentially zero prior to reaching the peak bond stress and initiation of the splitting crack. Generally, the relative magnitudes of the peak load bar slip at the (maximum bond strength) were similar to that observed for the loaded-end slip where the bar slip decreased with increasing mass loss of the bar due to corrosion.

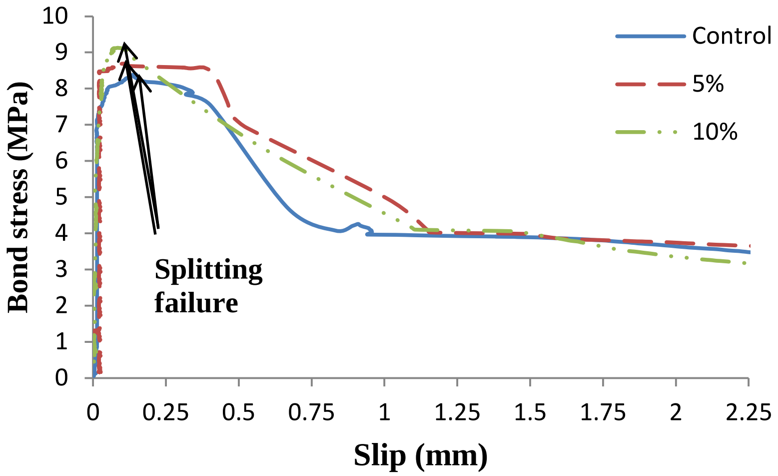

(a) Bond stress-slip of BE-M1-250

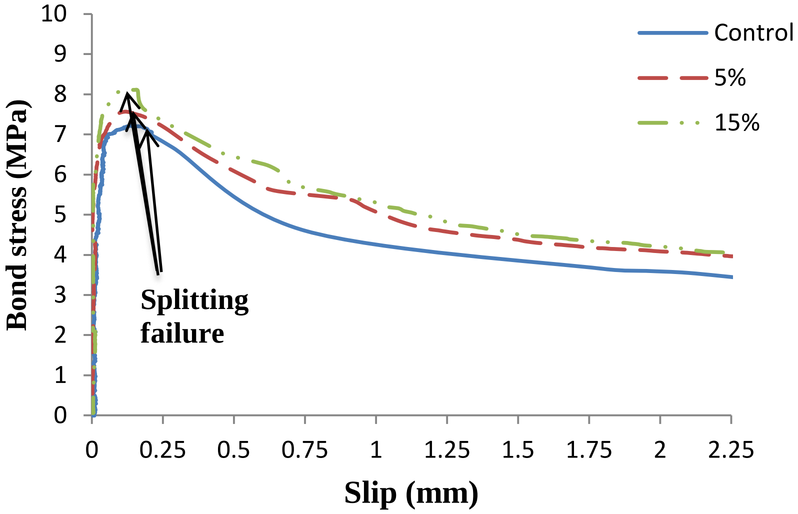

(b) Bond stress-slip of BE-SCC1-250

Figure 4. 6 Free end bond-slip responses of 250 mm bonded length for (a) M1 and (b) SCC1

4.4.3.2 Bond Stress-Slip Behaviour for Specimens with 350 mm Bonded Length

The loaded-end slip for the beam-end specimens with 350 mm bonded length (Figure 4.7) showed very different behaviour than the 250 mm bonded length specimens (Figure 4.6). The plotted slip in Figure 4.7 was the adjusted slip after deducting the axial elongation of the extended bar. The specimens with bonded length of 350 mm showed a plateau in the bond stress-slip response where the bar was responding with almost constant or slightly increasing bond stress. However, the trends in the bond stress at failure between M1 and SCC1 were similar to the beam-end specimens with 250 mm bonded length where the average bond strength and its corresponding bar slip in M1 were greater than in SCC1 (Figure 4.7 (a) and Figure 4.7 (b)). For the M1 beam-end specimens with 5% and 10% mass loss, a hole was drilled in the rebar for corrosion purposes. These two beam-end specimens experienced premature bar rupture failure through this hole and gave incomplete results. Similar to the beam-end specimens with 250 mm bonded length and repaired with SCC1, the average bond strength increased and the slip of the bar decreased with increasing corrosion mass loss in the 350 mm bonded length beam-end specimens. The bar slip at splitting failure of the control beam-end specimens increased 8% and 26% compared to the beam-end specimens with 5% and 10% rebar mass loss, respectively. The post-failure bond stress-slip curve of 250 mm and 350 mm bonded length beam-end specimens also had a different pattern. At post-failure, the 250 mm bonded length specimens tended to decrease gradually whereas the 350 mm bonded length specimens tended to decrease more rapidly. This is because the longer and wider cracks that existed in the larger bonded length in a combination with shearing off the concrete keys due to the higher bar forces provided less post-failure confinement of the bar, decreasing the residual friction in comparison to the short bonded length specimens.

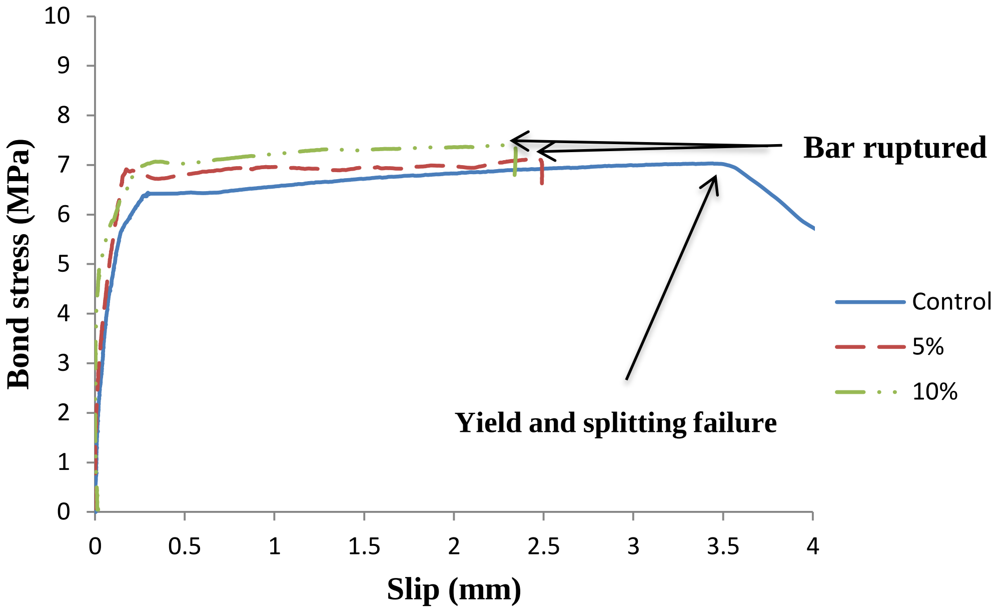

(a) Bond stress-slip of BE-M1-350

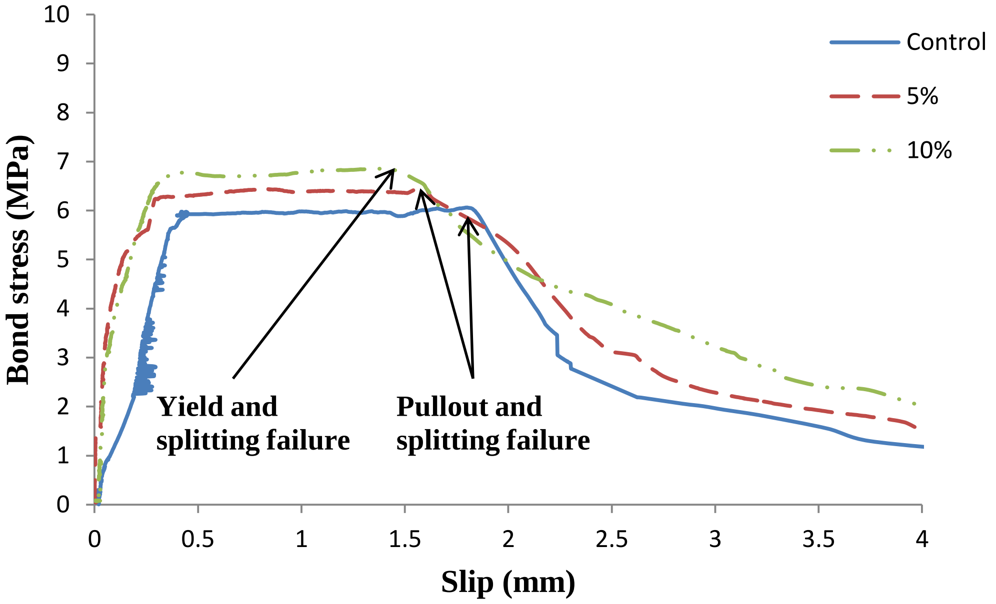

(b) Bond stress-slip of BE-SCC1-350

Figure 4.7 Loaded end-slip responses of 350 mm bonded length for (a) M1 and (b) SCC1

The free-end slip of beam-end specimens with 350 mm bonded length showed less effect of the increased bonded length in comparison to the loaded-end slip (Figure 4.8). At the beginning of the test, the free-end slip reading lagged behind the loaded-end reading until splitting failure occurred. This lag is probably because as the tensile force on the anchored bar increased, a vertical splitting crack started from the loaded-end and propagated gradually toward free-end. This splitting crack caused partial debonding of the bar before bond splitting failure occurred. Thus, the bar started to elongate within the debonded length, recorded as increased loaded-end slip while the free-end was still well anchored (free end slip essentially zero). The plateau exhibited in the loaded end slip responses (Figure 4.7) may have been caused by slip of the bar along the entire bonded length and bar elongation within the debonded length (due to the presence of the splitting crack). As well, given the magnitude of the bar force in these specimens, the plateau may also be due to bar yielding when the stress in the bar reached the bar yield stress. The occurrence of the yielding is discussed further in Section 4.4.5.

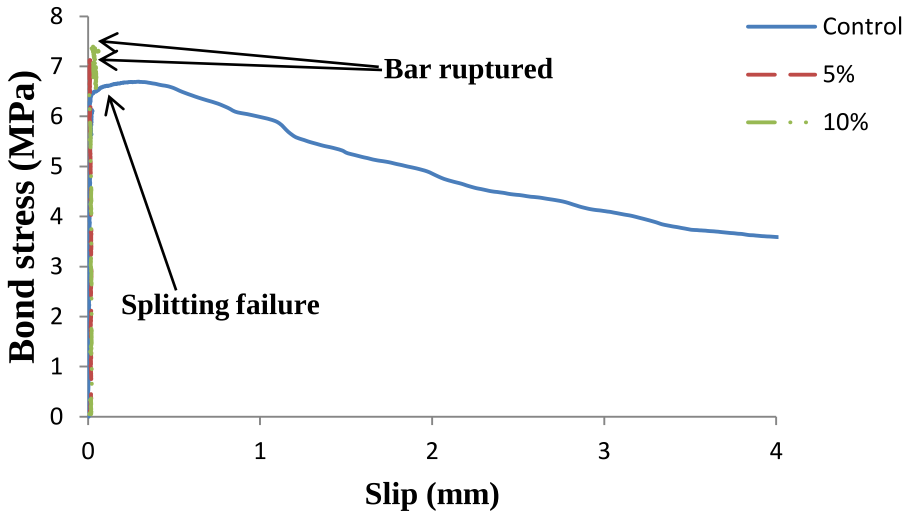

(a) Bond stress-slip of BE-M1-350

Figure 4.8 Free end bond-slip responses of 350 mm bonded length for (a) M1 and (b) SCC1

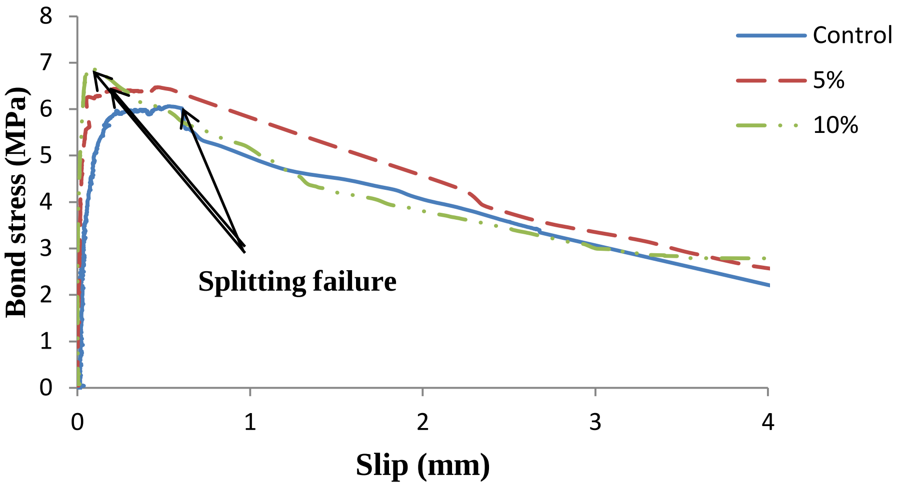

(b) Bond stress-slip of BE-SCC1-350

Figure 4.8 Free end bond-slip responses of 350 mm bonded length for (a) M1 and (b) SCC1 (Continued)

Generally, the average bond strength of the beam-end specimens with 250 mm-bonded lengths was higher than the beam-end specimens with 350 mm bonded length by 18% to 28%. Moreover, the loaded-end peak slip values at splitting failure for the 350 mm bonded length were 7 to 9 times greater than for the beam-end specimens with 250 mm bonded length. These proportions reveal that the changes in the average bond strength and peak slip values are not proportional to the increase in bonded length as suggested by (ACI 408, 2003).

4.4.4 Bond Failure Mechanism

The beam-end specimens with 250 mm bonded length had a direct splitting failure. However, the beam-end specimens with 350 mm bonded length had partial pullout or even bar yielding before splitting failure occurred. The different failure mechanisms were observed after splitting failure by examining the concrete keys at the interface between the rebar and the concrete (Figure 4.9). The specimens with 250 mm bonded length did not show any signs of shearing of the concrete keys (Figure 4.9 (a)). However, in the specimens with the 350 mm bonded length, the concrete keys were partially sheared off from either pulling out or yielding of the bar (Figure 4.9 (b)).

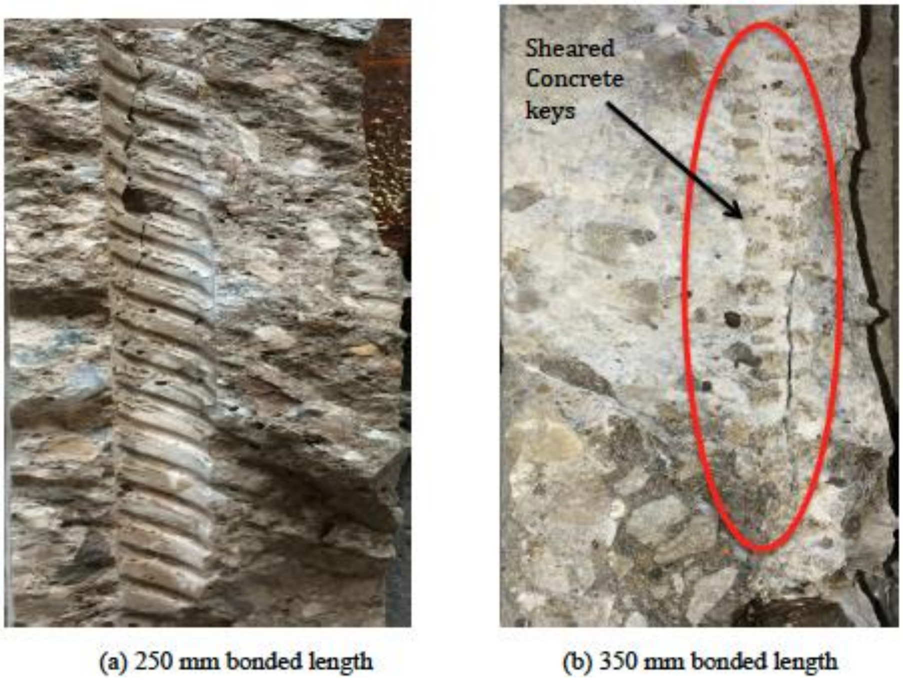

(a) 250 mm bonded length (b) 350 mm bonded length

Figure 4.9 Concrete keys inspection after splitting failure

For the specimen BE-M1-350-C, a tiny crack occurred on the surface concrete of the specimen at the loaded end at 115 kN, and the crack propagated and became wider at around 135 kN. As the specimen was carrying the load, the rebar was slipping and the concrete keys were shearing off. At failure (155 kN), the rebar was close to yielding and splitting failure occurred.

For the specimen BE-SCC1-350-C, the surface crack started at 90 kN. The crack became wider and deeper at 114 kN. The bar was slipping as the applied load increasing until around 133 kN (f_s =424 MPa), corresponding slip of around 0.5 mm. At this load (less than the bar yield strength which was around 479 MPa), the bar continued to slip by shearing off the concrete keys. After reaching maximum capacity, the specimen failed by splitting of concrete along the rebar. The specimen BE-SCC1-350-5 had similar behaviour to the control specimen. However because of the 5% mass loss of the bar, the stress on the rebar was higher. The rebar in the specimen BE-SCC1-350-10 reached its yield before reaching the bond capacity. The load and crack pattern was close to the control BE-SCC1-350-C and BE-SCC1-350-5. However, the increase in bar slip while maintaining the bond stress almost constant suggests yielding of the bar rather than pulling it out. Similar to all other specimens, BE-SCC1-350-10 finally failed by splitting failure.

4.4.5 Occurrence of Bar Yielding in Specimens with 350 mm Bonded Length

The yield strength of the reinforcing bars used in this study was 479 MPa (based on the Mill certificate from producer). The measured tensile loads at failure and associated bar stresses presented in Table 4.1 indicated that specimens BE-M1-350-C and BE-SCC1-350-10 may have experienced yielding prior to bond failure. The occurrence of yielding was also confirmed by comparing the calculated elongation of the bar to the measured elongation as it was described in Section 2.2.5.

The beam-end specimens were designed with concrete compressive strength of 35 MPa to ensure that all specimens would fail by bond failure. However, the actual concrete compressive strength was 56 MPa (from the supplier), which caused some specimens to reach to bar yield before bond failure. Thus, an examination of the bar normal stress distribution is needed for the beam-end specimens with 350 mm bonded length to determine if the specimens yielded prior to bond failure.

The normal stress distribution along the rebar was estimated considering the observed crack behaviour and based on a previous study that used strain gages on the rebar. Benmokrane et al. (1996) used six strain gages at different intervals on the rebar with 380 mm bonded length and plotted the stress distribution along the rebar with four loading levels, as shown in Figure 4.10.

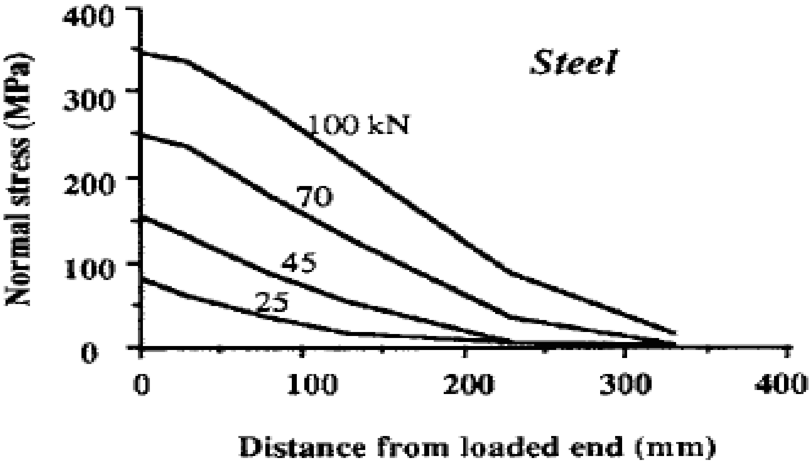

Figure 4.10 Typical tensile stress distribution of steel reinforcing bars (Benmokrane et al. 1996)

Based on a combination of the previous study and the observed crack behaviour of the current research, the estimated stress distribution along the bar length was plotted for two chosen specimens with different bonded length as shown in Figure 4.11. Generally as expected, the tensile stress decreased from the loaded end toward the free end. As the applied load was increasing, the tensile stress, and thus the corresponding bond stress was moving progressively toward the free end resulting from the bond failure at the interface of concrete and reinforcing bar. For the specimen with 350 mm bonded length, the bar stress maintains an almost constant plateau to approximately 150 mm from the loaded end before failure occurs. This represents the partially debonded region of the bar as the tensile force increased to failure. This plateau situation did not happen clearly for the specimen with 250 mm bonded length since splitting failure occurred before debonding or significant slip. It should be mentioned that the total area under the normal stress distribution should equal the calculated average bond strength at failure.

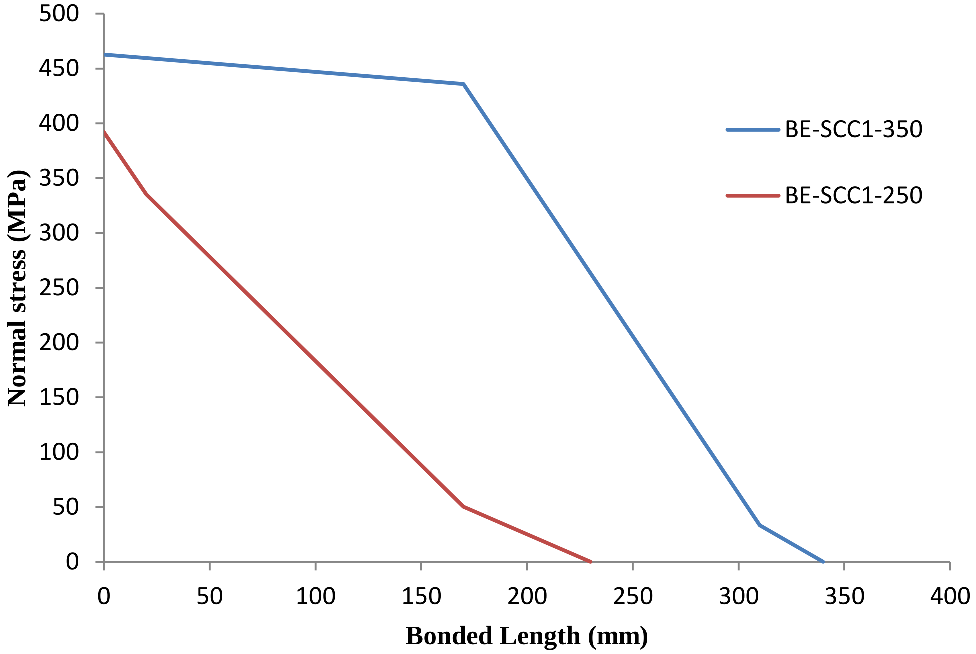

Figure 4.11 Assumed tensile stress distribution of steel reinforcing bar of beam-end specimen with 350 mm and 250 mm bonded length

Based on Equation 4.6, and considering the estimated normal stress distribution along the bar, the elongation of the bar was calculated to confirm whether the bar yielded or whether it was still elastic (Table 4.2). As the difference between the bar translation and the bar elongation plus the free end slip is close to zero, the bar still at elastic situation (not yield).

Table 4. 2 Assessment of the bar condition at failure

Specimen	**S_l (mm)**	**S_f (mm)**	**T_b (kN)**	**$S_l - S_f$ (mm)**	**Calculated Elongation δ (mm)**	**δ - ($S_l - S_f$) (mm)**	**Bar condition**
BE-M1-250-C	0.47	0.14	131.8	0.33	0.23	-0.1	Not yield
BE-SCC1-250-C	0.37	0.13	113.4	0.24	0.17	-0.07	Not yield
BE-M1-350-C	3.44	0.30	154.2	3.14	0.51	-2.63	Yield
BE-SCC1-350-C	1.80	0.61	133.2	1.19	0.53	-0.66	Not yield
BE-M1-250-5	0.39	0.12	133	0.27	0.21	-0.06	Not yield
BE-SCC1-250-5	0.31	0.11	116.4	0.20	0.18	-0.02	Not yield
BE-M1-350-5	2.45	0.01	152.6	2.44	0.48	-1.96	Rupture
BE-SCC1-350-5	1.58	0.51	138.6	1.07	0.55	-0.52	Not yield
BE-M1-250-10	0.33	0.09	135.2	0.24	0.22	-0.02	Not yield
BE-SCC1-250-10	0.27	0.07	120.8	0.20	0.21	0.01	Not yield
BE-M1-350-10	2.27	0.02	154.3	2.25	0.54	-1.71	Rupture
BE-SCC1-350-10	1.40	0.10	142.2	1.30	0.50	-0.8	Yield

Based on the calculations shown in Table 4.2, the two beam-end specimens BE-M1-350-C and BE-SCC1-350-10 were assumed to reach bar yield before the splitting failure occurred. The loaded-end slip curve of these two specimens showed a constant bond stress at a specific amount of bar slip followed by gradually increasing in bond stress until the splitting failure occurred. This pattern is slightly different than the other beam-end specimens that still in elastic situation where the bond stress maintained constant as the bar slip until failure.

4.5 Phase 2 Experimental Results for Beam-End Specimens

4.5.1 General Discussion of Test Results

Table 4.3 summarizes the Phase 2 results in terms of the average bond strength, adjusted loaded end slip, free end slip and the mode of failure for all beam-end specimens. The specimens were labeled as follows: the first part (BE) refers to beam-end and the second part refers to type of concrete (M2 for monolithic ready-mixed concrete of Phase 2, SCC2 for the second manufacture's prepackaged self-consolidating concrete, SCC3 for self-consolidating concrete that was developed at the laboratory and had the same aggregate size of the monolithic mix, and NC for normal concrete that batched at the laboratory and had exactly the same proportions as the monolithic mix but was used as a partial depth repair). The third part indicates the bonded length (200 mm and 300 mm). The last part represents the corrosion level (C for the control specimens (non-corroded), 7.5 for the specimens with 7.5% mass loss level and 15 for the specimens with 15% mass loss level). As with the beam-end specimens in Phase 1, the bar was extended out of the specimens by 75 mm for correction to the loading frame. Thus, the values of loaded end slip were adjusted to account for the axial elongation of 75 mm plus 50 mm of the unbonded (lead) length. All beam-end specimens were designed to fail at splitting bond failure based on the bonded length, concrete cover and concrete compressive strength. The average bond strength was calculated based on the stress on the bar, bonded length and the bar diameter as given previously in Equation 4.1.

Table 4. 3 Summary of beam-end specimens test results from phase 2

Specimen	Corrosion Level (%)	Actual mass loss level (%)	L_b/L_d	Tensile load at failure T_b (kN)	f_s (MPa)	Bond strength τ_b (MPa)	Adjusted Loaded-End slip at failure *S_l (mm)	Failure Mode**
BE-M2-200-C	0	0	0.31	98.8	315	7.86	0.28	S
BE-SCC2-200-C		0	0.33	87.8	279	6.99	0.27	S
BE-SCC3-200-C		0	0.32	82.9	264	6.6	0.37	S
BE-NC-200-C		0	0.30	73.9	235	5.88	0.48	S
BE-M2-300-C		0	0.47	127.0	404	6.74	0.51	S
BE-SCC2-300-C		0	0.49	118.1	376	6.27	0.48	S
BE-SCC3-300-C		0	0.48	109.6	349	5.81	0.53	S
BE-NC-300-C		0	0.45	97.5	311	5.17	0.65	S
BE-M2-200-7.5	7.5	7.4	0.34	100.2	344	8.29	0.25	S
BE-SCC2-200-7.5		7.7	0.36	91.3	315	7.56	0.24	S
BE-SCC3-200-7.5		7.5	0.35	86.3	297	7.14	0.32	S
BE-NC-200-7.5		7.5	0.33	77.8	268	6.44	0.39	S
BE-M2-300-7.5		6.8	0.51	128.1	438	7.04	0.45	S
BE-SCC2-300-7.5		7.6	0.54	119.6	412	6.6	0.40	S
BE-SCC3-300-7.5		7.9	0.52	114.1	394	6.31	0.46	S
BE-NC-300-7.5		7	0.50	100.2	343	5.51	0.53	S
BE-M2-200-15	15	15.6	0.37	101.1	381	8.76	0.21	S
BE-SCC2-200-15		13.3	0.38	93.4	343	7.98	0.21	S
BE-SCC3-200-15		16.1	0.37	88.4	335	7.68	0.28	S
BE-NC-200-15		16.6	0.36	67.7	256	5.85	0.55	Bs+S
BE-M2-300-15		17.6	0.55	124.6	482	7.28	0.74	Y+S
BE-SCC2-300-15		14.1	0.57	120.3	446	6.89	0.35	S
BE-SCC3-300-15		14.9	0.56	115.0	430	6.61	0.41	S
BE-NC-300-15		15.7	0.53	100.0	378	5.78	0.47	S

*$S_{l,\ adj} = s_{l.measured} - (PL)/(A_bE_s)$, where L = 125 mm and E_s = 200,000 MPa.
** S: Splitting failure Y: Bar yield. Bs: Bar slip.

4.5.2 Effect of Concrete Strength and Repair Condition on Bond Strength

Although the variation in concrete compressive strength amongst the four types of partial depth repair was not significant, there was a remarkable difference in the average bond strength. Figure 4.12 (a) and Figure 4.12 (b) illustrate the average bond strength normalized by $f'_c{}^{1/2}$ of the four mixes for three different corrosion levels for both bonded length of 200 mm and 300 mm, respectively.

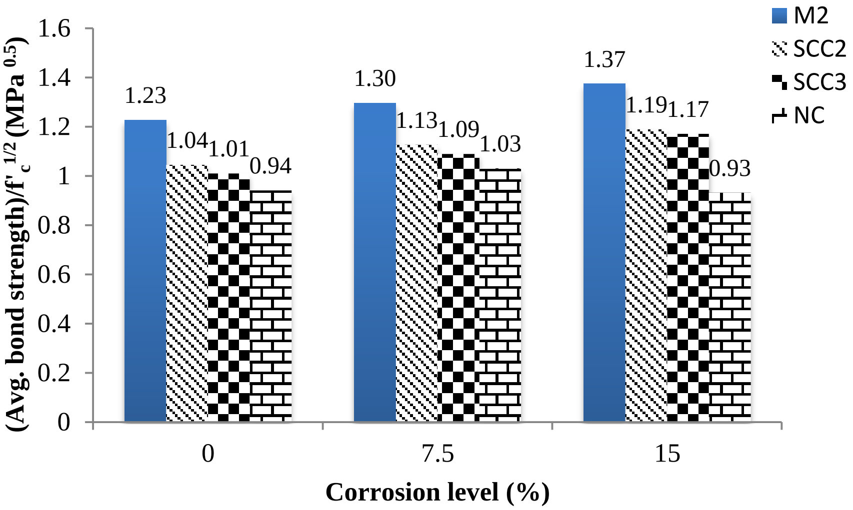

(a) 200 mm bonded length specimens

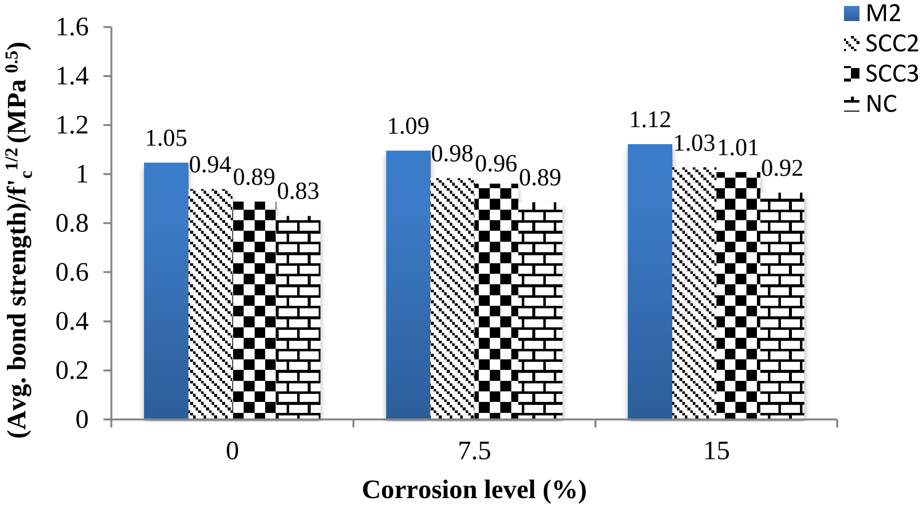

(b) 300 mm bonded length specimens

Figure 4.12 Avg. bond strength results normalized to $f'_c{}^{1/2}$

For all corrosion levels and for both bonded lengths, the highest average bond strength was observed for the monolithic (M2) beam-end specimens while the partial depth repair NC was the lowest. The partial depth repair SCC2 was considered the best mix amongst the three types of the partial depth repair in terms of improving the average bond strength. Both SCC mixes showed better bond strength than the NC. This may be related to the lower W/C ratio and higher binder content in SCC mixes which leads to reduced accumulation of bleed water underneath the reinforcing bar. Increasing the local W/C ratio underneath the bar could cause a reduction in the bond strength. Many researchers (Khayat and Feys, 2010; Zhu et al., 2004; Valcuende and Parra, 2009) have found that the top-bar effect is more marked in vibrated concrete as compared to SCC. The top-bar effect represents the differentiation in the micro strength and the elastic modulus of the interfacial transition zone (ITZ) on the top and the bottom side of the horizontal bar. This phenomenon is more pronounced for vibrated concrete than for SCC mixes. The consistent nature of SCC mixes comes from its superior flowability, resulting in a good uniformity of the ITZ around the bar, which leads to increased bond strength. The partial depth repair SCC2 was only better than SCC3 possibly due to the of silica fume in the SCC2 concrete. Previous research has shown that including silica fume in the partial depth repair affected not only the compressive strength but also considerably increased the shear bond strength at the interface surface between the substrate concrete and the partial depth repair concrete (Shin and Wan, 2011). Improving the bond between the substrate concrete and the partial depth repair concrete resulted in enhancing the bond strength of the beam-end specimen.

4.5.3 Effect of Repair Condition and Mix Properties on Shear Bond Strength

The main phenomenon that negatively affected the bond strength for beam-end specimens that were repaired with partial depth repair was the internal shear cracks at the interface between the substrate concrete and the partial depth repair concrete. This was the main reason why the average bond strength of monolithic specimen was higher than the average bond strength of beam-end specimens that were repaired with partial depth repair.

The beam-end specimens that were repaired with partial depth repair were cast with a pocket at a specified bonded region based on the required bonded length. After concrete hardening of the substrate concrete, the partial depth repair concrete was cast at the bonded region of the substrate concrete to be working as two layers. Therefore, the whole pocket of the partial depth repair region may have had a tendency to move with increased tensile force on the bar (Figure 4.13). In order to assess this, the relative movement between repair concrete and the beam-end specimen was measured as described previously and shown in Figure 3.5. The typical slip between the repair concrete and the beam-end as the load increased is shown in Figure 4.14. It can be seen that there was almost no slip recorded between the repair concrete and the substrate concrete.

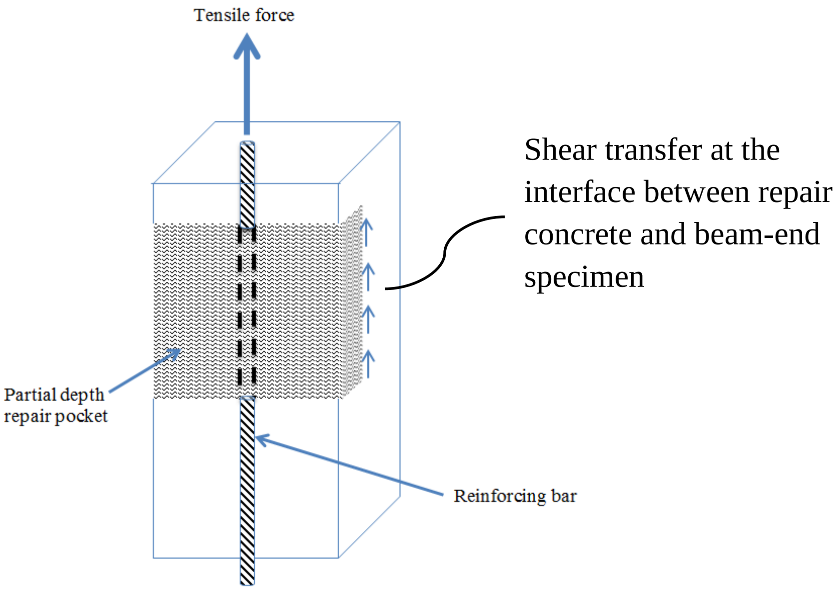

Figure 4.13 Beam-end specimen repaired with partial depth repair

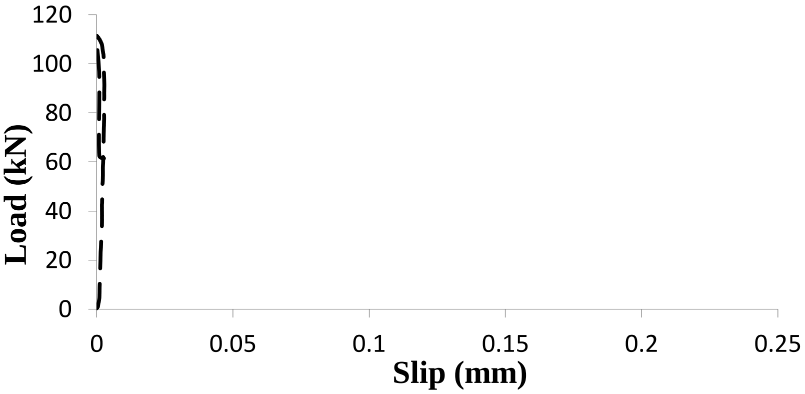

Figure 4.14 Measured slip between the repair concrete and the beam-end as the load increased

The movement of the partial depth repair pocket was resisted by the parallel transverse (shear) reinforcement that extends from the beam-end specimen into the partial depth repair, which led to internal shear cracks at the bottom of the pocket at the interface of the substrate concrete and the partial depth repair concrete and within the repair concrete. The internal shear cracks are associated with mechanism of shear friction to transfer shear between the repair concrete and substrate concrete. The presence of those shear cracks in the repair concrete are interacting with the state of stress from bond (hoop stress) and may have caused the longitudinal bond splitting crack to occur at a lower load level, resulting in a decrease in the average bond strength. On the other hand, this scenario did not exist in the monolithic beam-end specimens where the whole beam-end specimen including the bonded region were cast together as one cast to be working as one layer. Figure 4.15 shows the shear crack pattern at the bottom interface of the bonded region for the four concrete mixes.

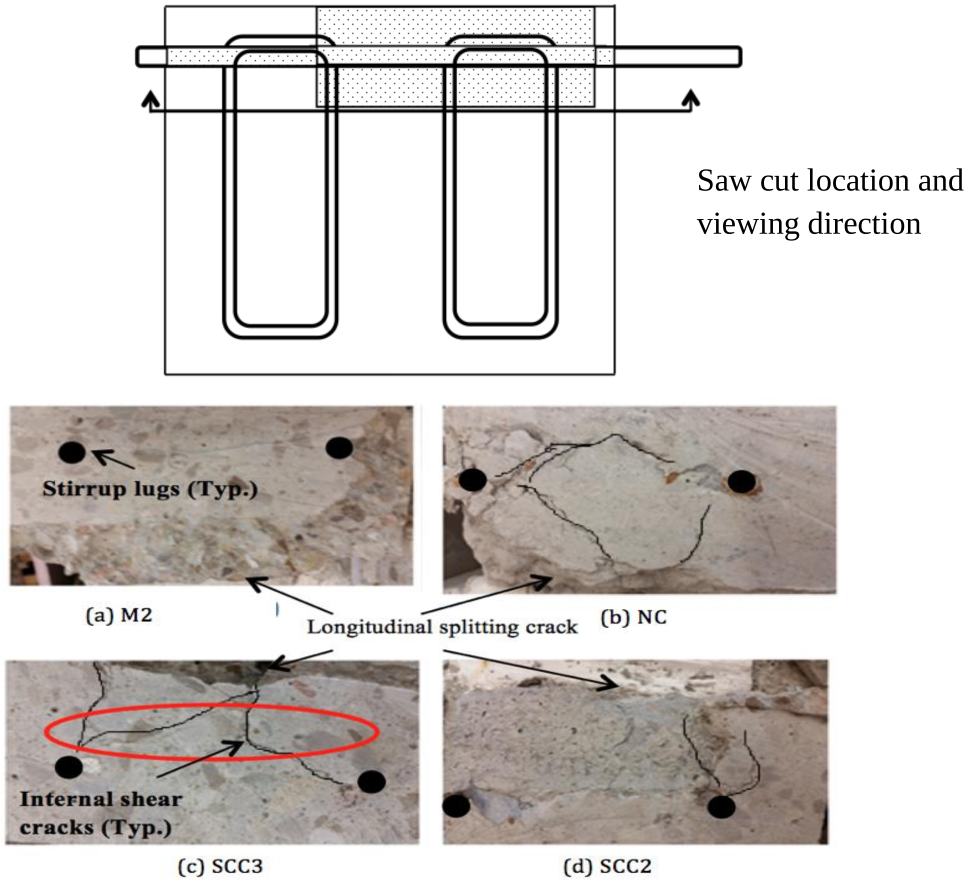

Saw cut location and viewing direction

Figure 4.15 The bottom interface of the bonded region after splitting failure and cutting off the specimens for inspection

The monolithic concrete M2 showed almost no shear cracks at the internal surface of the bonding region and this might be explained because the entire beam-end specimen was behaving as one part. This property was the main reason why the average bond strength of M2 specimens higher than the specimens that use partial depth repair. The internal shear cracks in SCC2 were limited compared to the NC and SCC3 concretes. This indicated an improved bond between SCC2 and substrate concrete that might be mainly due to the inclusion of bonding agent and silica fume in SCC2. Thus, SCC2 was the best type of partial depth repair that enhanced the average bond strength before splitting failure occurred. The partial depth repair SCC3 to some extent showed fewer internal shear cracks compared to NC. One reason can be because SCC3 had a higher compressive strength a slightly higher splitting tensile strength than NC. Also, high flowability and low water-to-cement ratio in SCC3 compared to NC might be a reason to improve the bond at the interface between the substrate concrete and the partial depth repair concrete, thus decrease the internal shear cracks. Increasing the flowability resulted in increasing the ability to fill voids properly, which leaded to enhance the bond strength between the substrate concrete and the partial depth repair concrete.

4.5.4 Bond Stress-Slip Behaviour for Specimens with 200 mm Bonded Length

The overall behavior of the average bond stress-slip could be explained as the curve was increasing nonlinearly until the peak point was achieved, which represented the point of splitting failure. A sudden load drop (and reduction in the average bond stress) followed the splitting failure. These sudden drops were followed by a slight decreased in bond stress and increased in the bar slip. All beam-end specimens with 200 mm bonded length demonstrated this behavior pattern for the different corrosion levels and different types of partial depth repair investigated (Figure 4.16). The plotted slip in Figure 4.16 was the adjusted slip after deducting the axial elongation of the extended bar. Generally, as the corrosion level increased, the average bond strength of the cleaned corroded rebar increased and the corresponding slip decreased. This pattern was similar to that observed in Phase 1 (the same reasons and discussion in the beam-end specimens in Phase 1).

The monolithic beam-end specimens (M2) and the specimens that repaired with partial depth repair SCC2 showed a sharp drop in the bond stress-slip curve at failure (Figure 4.16 (a) and Figure 4.16 (b), respectively). However, the partial depth repair concretes SCC3 and NC had a smooth decreasing in the bond stress-slip curve at failure ((Figure 4.16 (c) and Figure 4.16 (d), respectively). The monolithic specimens considered the typical and the reference shape of the bond stress-slip curve since there was not internal shear cracks where the whole beam-end specimen including the bonded region were cast together as one cast to be working as one layer. Since the SCC2 had bond stress-slip behavior at failure similar to M2, it was an evidence that it had better bond at the interface between the substrate concrete and the repair concrete compared to the other partial depth repair materials SCC3 and NC. That might be because SCC2 had higher compressive strength than SCC3 and NC. Also, the partial depth repair materials SCC2 included a bonding agent and silica fume, which could be an important reason in improving the bond at the interface bonded zone; thus enhancing the bond strength of the beam-end specimen. As the bond at the interface between the substrate concrete and the repair materials increased, the shear resistance between the two layers of concretes increased. Thus, the internal shear cracks at the interface between the substrate concrete and the partial depth repair concrete decreased resulted in improving the bond strength of the beam-end specimen. The smooth decreasing in bond stress-slip curve of the partial depth repair SCC3 and NC could explain that they had lower bond at the interface between the substrate concrete and the repair materials than SCC2. The smooth behavior in SCC3 and NC can be explained by as the bar force increased, internal shear cracks at the interface bonded region occurred and propagated as the bar slip increased leading to gradual failure behavior compared to the sudden failure in M2 and SCC2.

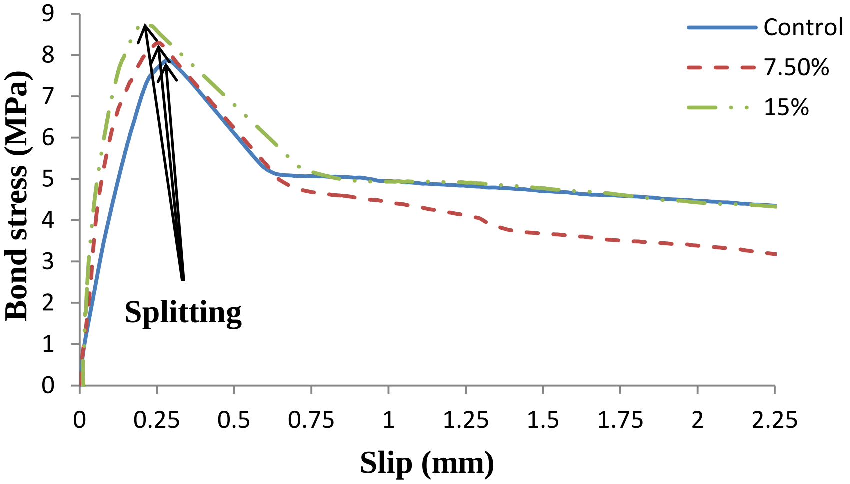

(a) Bond stress-slip of BE-M2-200

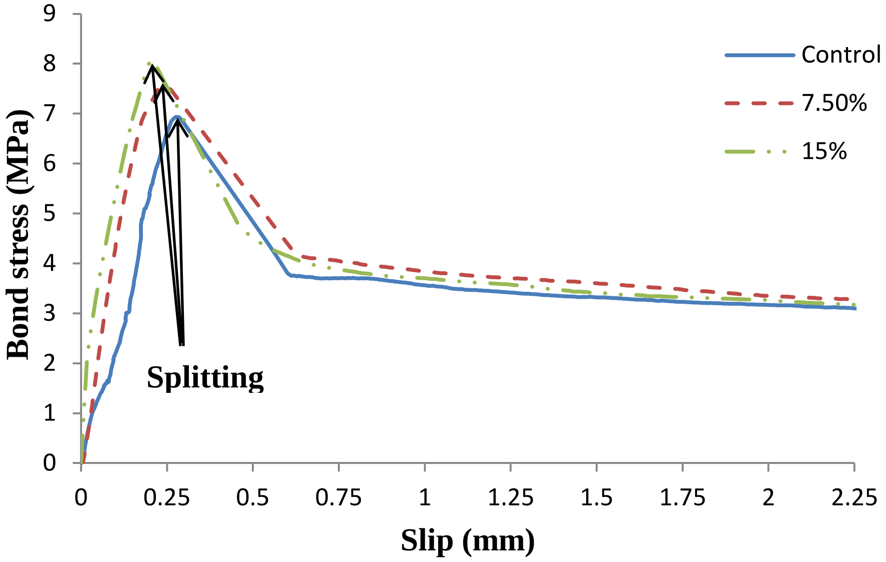

(b) Bond stress-slip of BE-SCC2-200

Figure 4.16 Bond stress-slip responses of 200 mm bonded length for (a) M2, (b) SCC2, (c) SCC3 and (b) NC

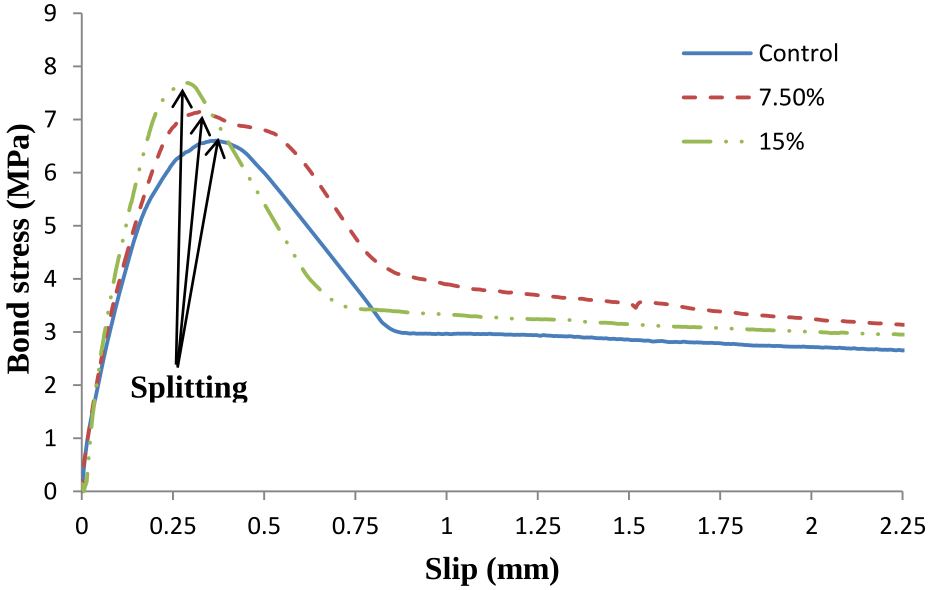

(c) Bond stress-slip of BE-SCC3-200

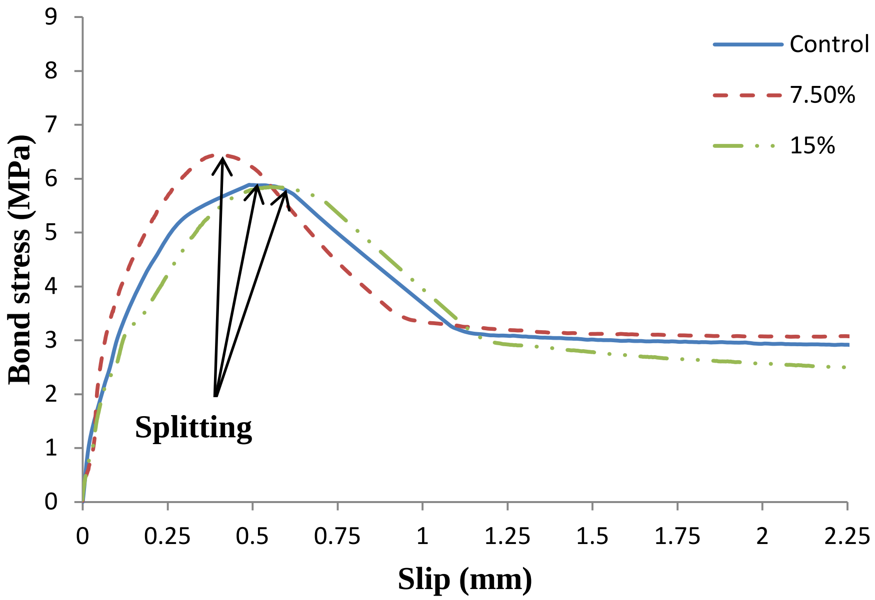

(d) Bond stress-slip of BE-NC-200

Figure 4.16 Bond stress-slip responses of 200 mm bonded length for (a) M2, (b) SCC2, (c) SCC3 and (b) NC (continued)

The beam-end specimen BE-NC-200-15 was the only specimen that had a different bond stress-slip pattern than the other specimens with 200 mm bonded length relative to the control and 7.5% mass loss level of the same type of concrete. Figure 4.16 (d) showed that the specimen BE-NC-200-15 had lower average bond strength and higher slip compared to the specimens BE-NC-200-7.5 and BE-NC-200-C. This might be explained due to the corrosion of the bar on this specimen being concentrated on the ribs of the bar which resulted in almost eliminating the ribs of the bar and decreasing the mechanical interlock between the bar and the surrounding concrete. Consequently, the bar tended to pullout easily before splitting failure occurred. The severe corrosion of the bar ribs was only observed in BE-NC-200-15. As well, its mass loss level was 16.68% rather than the 15% value for the other specimens with the same bonded length as shown in Table 4.3. Due to the non-typical corrosion and the inconsistent average bond strength results for this specimen, it was excluded from further analysis.

4.5.5 Bond Stress-Slip Behaviour for Specimens with 300 mm Bonded Length

Generally, the average bond stress-slip behaviour of the beam-end specimens with 300 mm bonded length was similar to the beam-end specimens with 200 mm bonded length. The average bond stress-slip curve increased nonlinearly until the maximum bond stress was achieved. After splitting failure, the load dropped off suddenly, followed by gradual decrease in the load and higher increase in the bar slip (Figure 4.17). The beam-end specimen BE-M2-300-15 had a different pattern than the other beam-end specimens with 300 mm bonded length (Figure 4.17 (a)). Once the average bond stress-slip curve reached the peak, the reinforcing bar was slipping with almost constant (plateau) bond stress before splitting failure occurred. This plateau might be due to the rebar yielding ahead of splitting failure where the stress in the bar was 482 MPa exceeded the yield strength of the reinforcing bars used in this study was 479 MPa (based on the Mill certificate from producer).

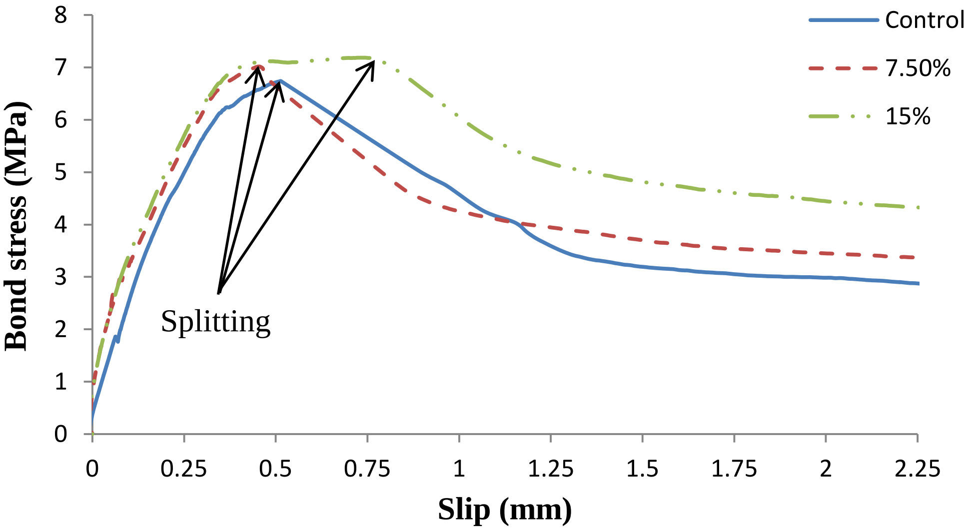

(a) Bond stress-slip of BE-M2-300

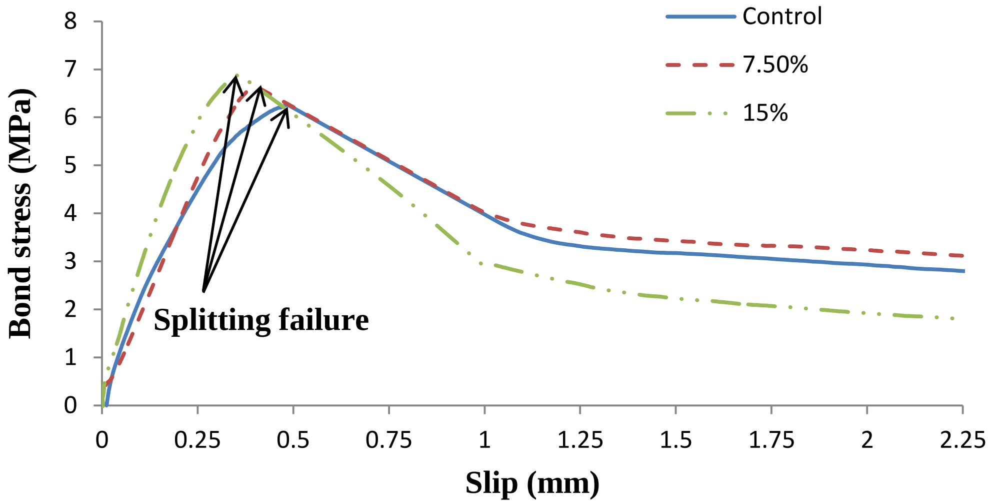

(b) Bond stress-slip of BE-SCC2-300

Figure 4.17 Bond stress-slip responses of 300 mm bonded length for (a) M2, (b) SCC2, (c) SCC3 and (b) NC

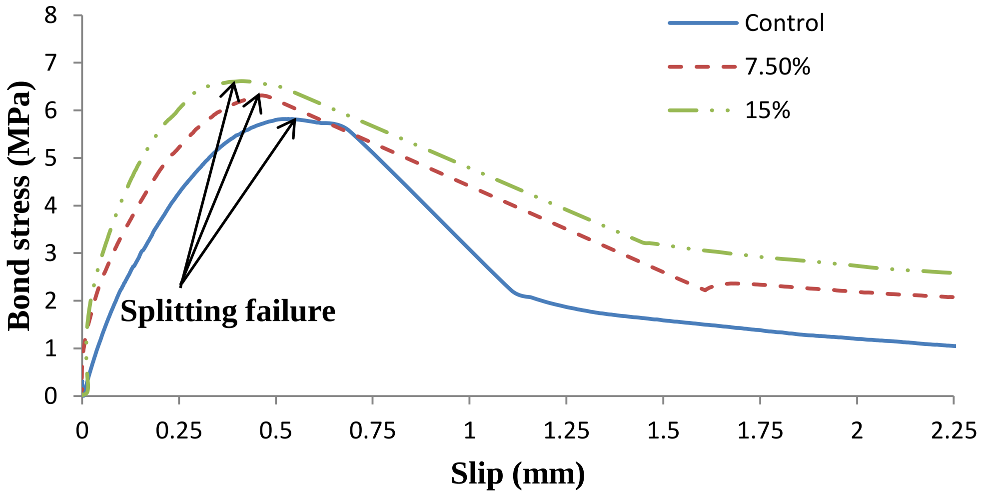

(c) Bond stress-slip of BE-SCC3-300

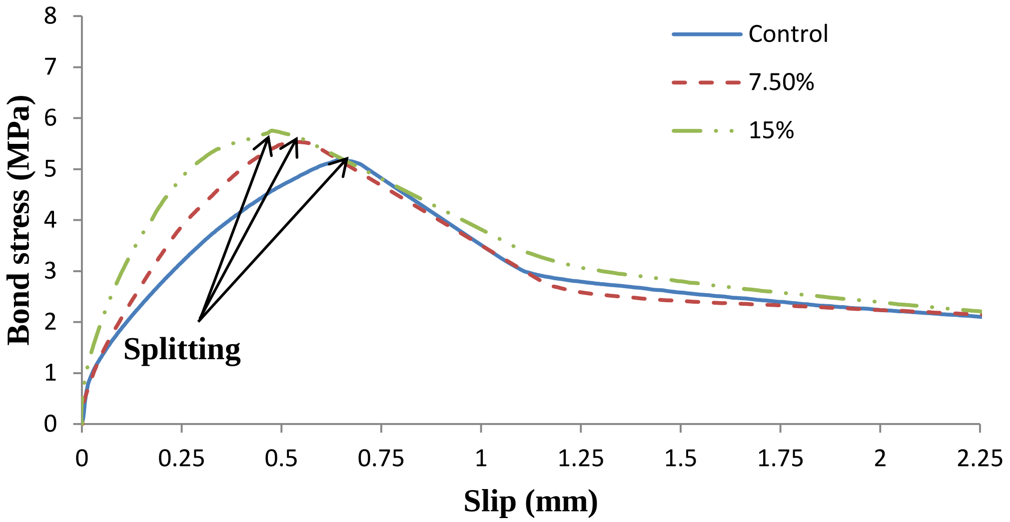

(d) Bond stress-slip of BE-NC-300

Figure 4.17 Bond stress-slip responses of 300 mm bonded length for (a) M2, (b) SCC2, (c) SCC3 and (b) NC (continued)

It can be noticed from Figure 4.16 and Figure 4.17 that the post-failure bond stress-slip curve of 200 mm and 300 mm bonded length beam-end specimens had a different pattern. At post-failure and after the sudden drop in the load, the beam-end specimens with 200 mm bonded length tended to be constant or decrease gradually. However, the 300 mm bonded length beam-end specimens tended to decrease more rapidly. This is because the longer and wider cracks that existed in the larger bonded length in a combination with shearing off of the concrete keys due to the higher bar forces, provided less post-failure confinement of the bar, decreasing the residual friction in comparison to the beam-end specimens with 200 mm bonded length.

4.6 Summary of this Chapter

For the same bonded length and the same type of the partial depth repair, the bond strength increased with increasing the corrosion level. As the bonded length increased, the bond strength decreased and the corresponding bar slip increased. However, the change in bond strength and the corresponding slip were not proportional to the change in bonded length. The beam-end specimens with 200 mm, 250 mm and 300 mm bonded length failed by splitting bond failure. However, the beam-end specimens with 350 mm bonded length, the failure mode was combined between pullout and splitting failure, or bar yield and splitting failure. Although M1 had lower compressive strength than SCC1, it had better bond. This may be due to two factors. First, the quantity and the size of the coarse aggregate in M1 mix was greater than it in SCC1, which increased the splitting tensile strength of M1, which then increased the average bond strength. Second, the internal shear cracks at the interface between the repair concrete (SCC1) and the substrate concrete and within the repair concrete decreased the average bond strength of SCC1.

For the other types of repair concrete, which have a similar proportion of coarse aggregate to the monolithic specimens, the monolithic beam-end specimens had also higher bond strength than all types of partial depth repair concretes for all bar mass loss levels. That was because of the effect of the internal shear cracks in the beam-end specimens that were repaired with partial depth repair concrete. The high flowability in the SCC repair concretes compared to NC may have improved the bond at the interface between the substrate concrete and the partial depth repair concrete, thus reducing the occurrence of the internal shear cracks. Increasing the flowability resulted in increasing the ability to fill voids properly, which leaded to enhance the bond strength between the substrate concrete and the partial depth repair concrete. Among all partial depth repair concretes, all SCC mixes showed better bonding than the NC. The partial depth repair concrete SCC2 had higher average bond strength than SCC3.

Chapter 5: Lap Splice Beam Specimen Experimental Program

5.1 General

The lap splice beam test series involved 24 lap splice beams with dimensions of 250 mm W x 350 mm H x 2200 mm L. The purpose of this study was to evaluate the effect of the transverse reinforcement by stirrups and fiber reinforced polymer (FRP) sheet on the bond strength of cleaned corroded bars lap spliced in a beam and repaired with a partial depth repair. Splitting crack propagation was monitored as the load was applied. Also, the slip of the spliced bar was measured using linear variable differential transformers (LVDTs). All of the lab splice beams were designed to fail by bond failure.

5.2 Test Program

Twenty-four lap splice beams were cast to study the bond behavior of cleaned corroded spliced bars repaired with partial depth repair with and without transverse reinforcement or FRP sheets. Two corrosion levels were considered (7.5% and 15% mass loss) and the results of their tests were compared with those for non-corroded reinforcement. The splice length was the same for all of the beams; a 300 mm splice length and a clear cover of 25 mm were used. Based on the superior performance observed during the beam-end specimen experiments, the commercial prepackaged self-consolidating concrete extended with 50% of 13 mm coarse aggregate (SCC2) was used as the main partial depth repair for all lap splice beams. For the purposes of this study, this concrete will be re-designated as SCC50. Three lap splice beams repaired with the same commercial prepackaged self-consolidating concrete without coarse aggregate (SCC0) were also included to study the effect of coarse aggregate on bond behavior. Test results for the partial depth repaired beams were compared with test results for monolithic lap splice beams. Transverse reinforcement or FRP sheets were used as confinement for both monolithic beams and the beams repaired with a partial depth repair. Figure 5.1 shows the test matrix of variables used for all lab splice beams.

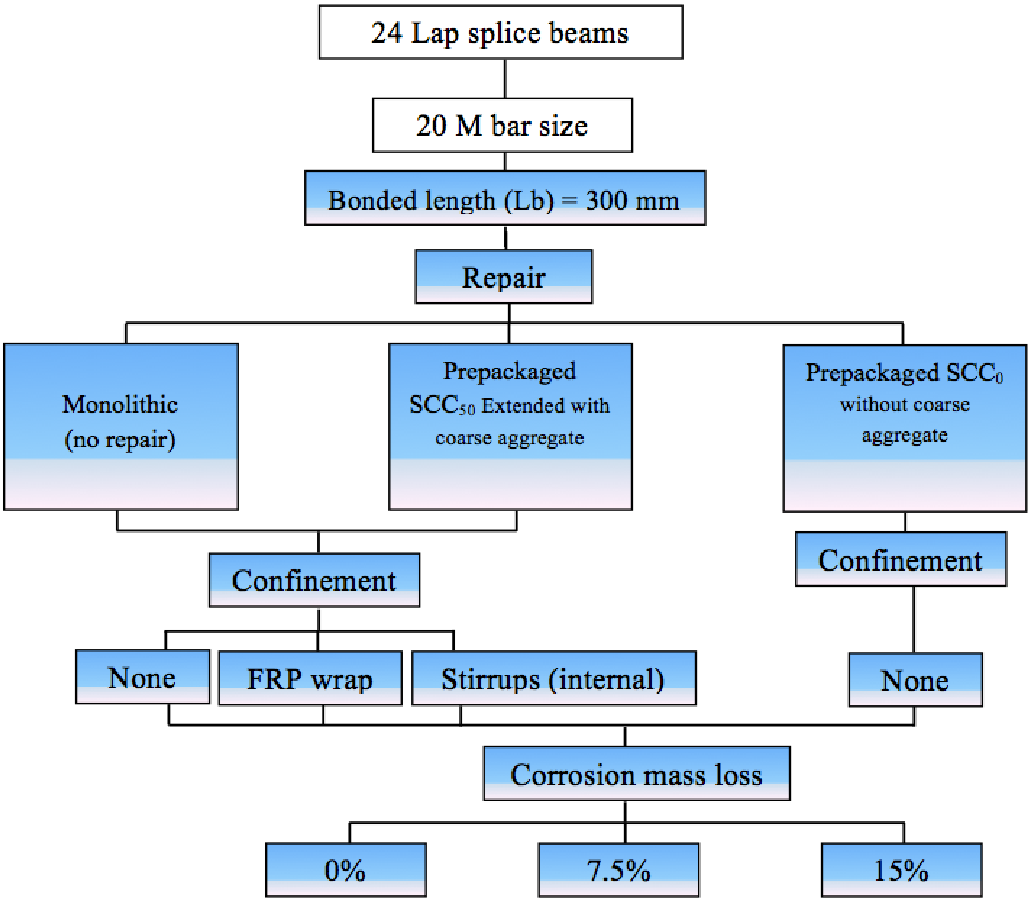

Figure 5.1 Test matrix of the lap splice beams

Given the broad scope of experimental parameters and the size of the test specimens, it was not practical to include replicate specimens. This is not uncommon in large scale structural experimental programs. Since the replicates were not used, care was taken to examine trends in the experimental data to identify any possible inconsistent results. In the rare event that inconsistent data were observed, individual data points were removed from further analysis, but only if a clear reason leading to the outlier result could be determined (e.g, obvious experimental error, non-typical experimental condition)

5.3 Test Specimen

Twenty-four lap splice beams were cast and tested statically under four-point loading with an 1800 mm clear span length (600 mm constant moment region and 600 mm shear spans). All of the lap splice beams had the same dimensions, a rectangular cross section of 250 mm x 350 mm and a total length of 2200 mm. The lap splice length was 300 mm. The beams were designed to fail by bond splitting before the reinforcing bar reached its yield strength (flexural failure). Each beam was reinforced for flexure with two 20M steel bars spliced at midspan. In addition, all beams were also reinforced with two continuous 10M steel bars at the top (compression zone) of the beam. To avoid a shear failure, each beam was provided with 10M stirrups as transverse reinforcement in the shear spans spaced at 100 mm center to center (Figure 5.2).

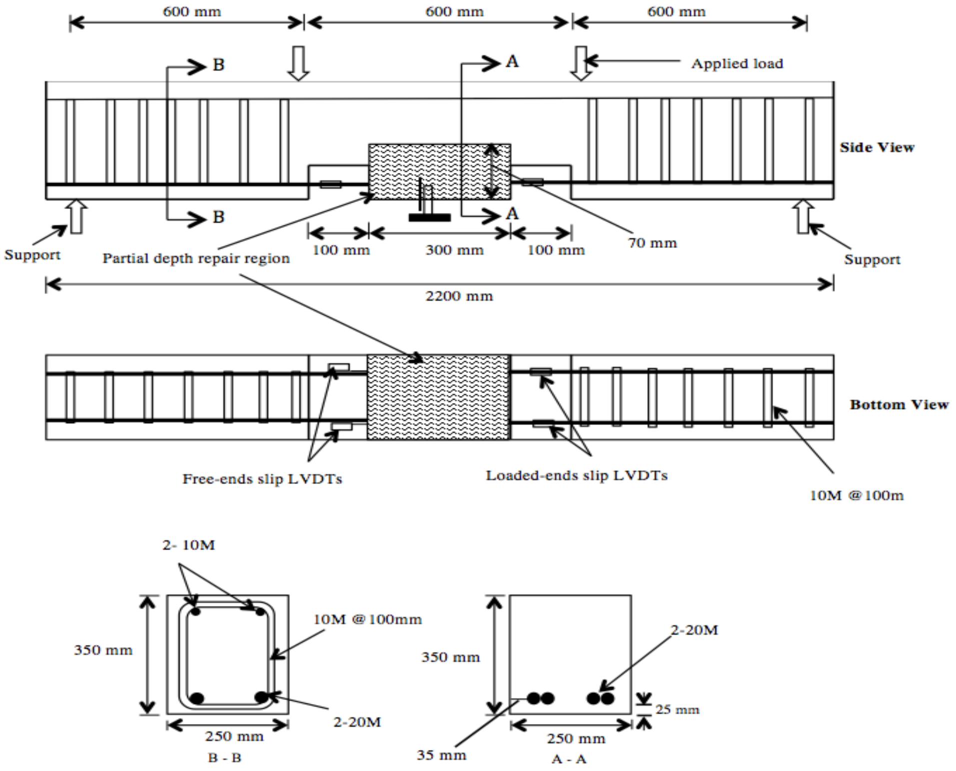

Figure 5.2 The cross section and reinforcement details of the lap splice beam

For the beams that were repaired with a partial depth repair, a pocket was designed for the repair purposes, with dimensions of 300 mm in length, 250 mm in width and 70 mm in depth. The concrete cover for all beams was 25 mm. A 25 mm clearance was kept under the spliced bars to meet the minimum clearance reinforcement of 19 mm or 6 mm larger than the maximum coarse aggregate size in the partial depth repair material (ACI 364, 2014).

All of the beams were fabricated with two notches with dimensions of 100 mm X 50 mm at the bottom of the beam that exposed the flexural reinforcing bars. The two notches were placed at the two ends of the lap spliced region to facilitate measurement of the bond stress-slip behaviour. Five linear variable differential transformers (LVDTs) were used: two to measure the loaded end slip, two to measure the free end slip and one to measure the deflection of the beam. A total of 10 electrical resistance strain gauges were used on the spliced bars for each beam to measure the strain distribution along the spliced length. Two strain gauges were fixed on each bar at the lap splice zone at distances of 50 mm and 225 mm from the beginning of the splice zone. Additionally, one strain gauge was placed on each side of the splice zone on the exposed reinforcing bar at the notches. Figure 5.3 shows the strain gauge layout.

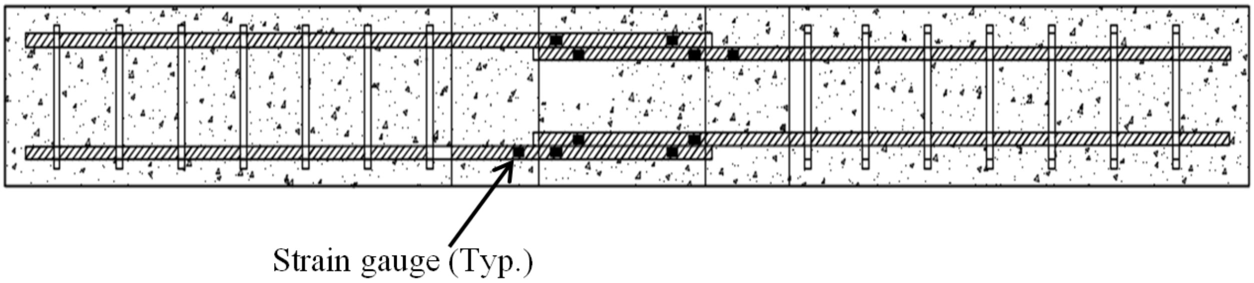

Figure 5.3 Strain gauge layout

Six lap splice beams were confined within the splice length with internal transverse reinforcement (stirrups) and six were wrapped with carbon fiber reinforced polymer (CFRP) sheets. For the first condition, two non-corroded 10M stirrups were placed at spacing of 150 mm at the spliced region. For the wrapped condition, the CFRP sheet was U-wrapped in a single layer of 950 mm length and 300 mm width to confine the lap splice zone. For each type of confinement, three beams were monolithic at different mass loss levels (control, 7.5% and 15% mass loss) and three beams were repaired with a partial depth repair concrete at different mass loss levels (control, 7.5% and 15% mass loss).

5.4 Test Procedure

All of the beam lap splice beams were simply supported with a 1800 mm span length and tested statically under four point loading until failure. The load was applied to the beam through a steel spreader beam connected to the actuator. The steel beam then transferred the load to two locations on the top of the beam to produce a constant moment region in the middle region of the lap splice beam. The test frame was servo-controlled with a capacity of 500 kN. Tests were run in displacement control at rate of 0.3mm/min to simulate the procedure that was used in the beam-end specimens. The displacement at the center of the lap splice beam was recorded as the load was applied until failure. Figure 5.4 shows the lap splice beam installed in the test frame.

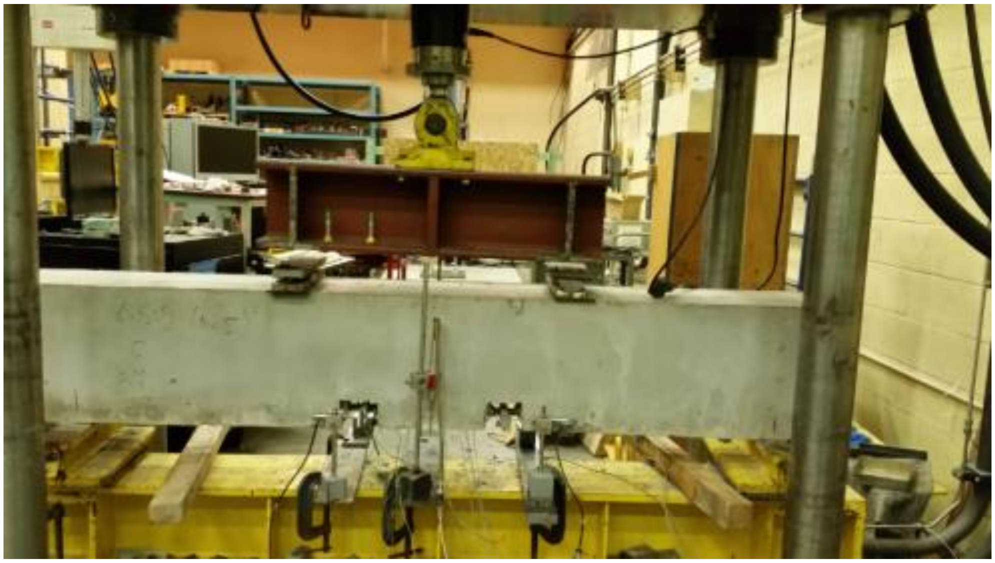

Figure 5.4 Lap splice beam installed in the test frame

5.5 Specimen Fabrication

The lap spliced bars that needed to be corroded were cast first into small concrete prisms with dimensions of 100 mm in depth, 100 mm in width and 300 mm in length, which was the lap splice length. To accelerate the corrosion rate, the concrete used to cast those prisms contained salt equal to 3.8% of the cement mass, which was equivalent to 2.3% of chloride. The prisms were kept in a chamber subjected continuously to a 100% humidity to facilitate the corrosion reaction. Also, power supplies were used to accelerate the corrosion through an impressed current. The prisms were divided into two groups: 7.5% and 15% mass loss, and the specimens of each group to be corroded to a given level were connected in series to ensure a constant current. Every prism was cast with one reinforcing bar (anode) and one stainless steel bar (cathode). The technique of corrosion acceleration and mass loss measurement was the same technique used for the beam-end specimens. Figures 5.5 and 5.6 show the corrosion induced cracking and the effect of corrosion products at the interface between the rebar and the surrounding concrete, respectively.

Figure 5.5 Corrosion-induced cracking of the concrete prism

Figure 5.6 Corrosion products at the interface between the rebar and the concrete

For all the of lap splice beams, two blocks of high-density foam were placed in the constant moment region at the ends of the spliced region to form notches to allow measurement of the slip of the bars (Figure 5.7 (a)). For the lap splice beams that were repaired with a partial depth repair, high-density foam was also used to isolate the patch region during the main cast (Figure 5.7 (b))

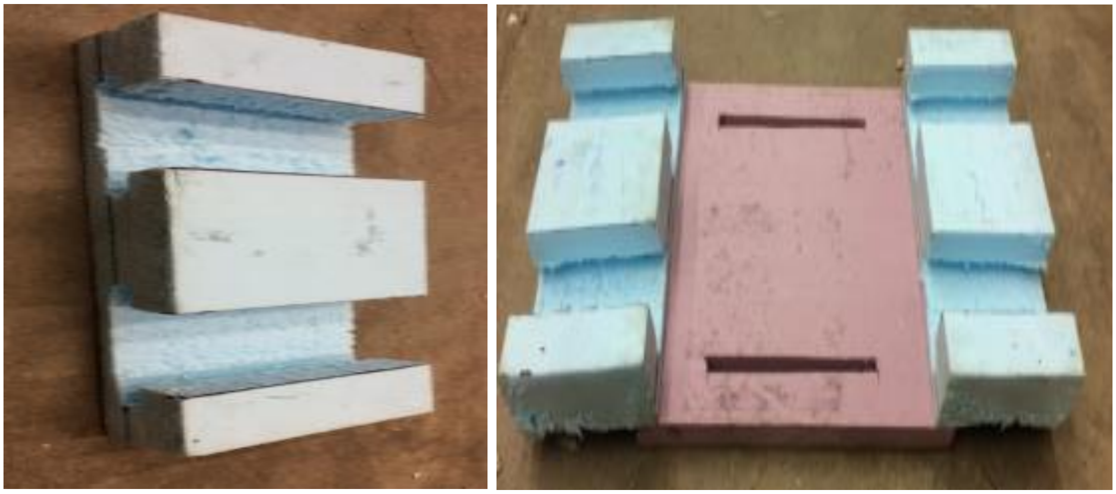

(a) To form notches (b) To form partial depth repair

Figure 5.7 High-density foam blocking

The 24 lap splice beams were cast as two sets due to the limited number of the forms and space constraints in the lab; each set was cast into twelve forms. Figure 5.8 shows the reinforcement cages placed inside the formwork.

Figure 5.8 Reinforcement cages placed inside the formwork

The lap splice beams were cast using ready-mix concrete with a specified compressive strength of 35 MPa. The concrete was cast in two layers to ensure that each layer was vibrated adequately to ensure proper consolidation and avoid segregation. Once the concrete was placed, the top surface of the concrete was finished by troweling. After finishing, two anchorages were placed on top of each beam for lifting and movement purposes. Wet burlap was used to cure the concrete surface for 10 days to minimized concrete shrinkage and cracking. Figure 5.9 shows concrete placement, surface finishing and concrete curing.

Concrete placement

Surface finishing

Concrete curing (burlap and plastic)

Figure 5.9 Concrete placement and curing process

After 28 days of curing, the high-density foam used to form the repair pocket was removed and the surface of the substrate concrete was roughened using a needle peener (Figure 5.10). Before placing the partial depth repair concrete, the strain gauges were applied on the spliced bars (Figure 5.11).

Figure 5.10 Roughening the substrate concrete with needle peener

Figure 5.11 The splice region to be repaired with partial depth repair

5.6 Material Properties

The 20M deformed reinforcing bar had 479 MPa yield strength and 612 MPa ultimate tensile strength, as provided from the supplier. The partial depth repair material was the same commercial prepackaged concrete (SCC2) used in the beam-end specimens (see Table 3.1 for specified properties). The repair material had a rapid strength gain, a fast turnover of repair area and a flowable consistency. The CFRP wrapping sheet was SikaWrap Hex 103C with a weight of 610 g/m^2. Two types of epoxies were used for the SikaWrap Hex 103C installation; Sikadur 330 and Sikadur 300. Prior to placing the CFRP, the concrete surface was sealed with Sikadur 330 and the CFRP sheets was saturated manually by hand with Sikadur 300. The properties of CFRP sheets and the two epoxies are shown in Table 5.1 and Table 5.2, respectively.

Table 5.1 SikaWrap Hex 103C Properties (provided by manufacture)

Property	Typical properties of SikaWrap Hex 103C	Cured laminated properties of SikaWrap Hex 103C
Tensile strength (MPa)	3,7	1,055
Tensile Modulus (MPa)	234,500	64,828
Elongation (%)	1.5	0.89
Thickness (mm)	0.34	1.016

Table 5.2 Sikadur 330 and Sikadur 300 properties (provided by manufacture)

Property	Sikadur 330	Sikadur 300
Tensile strength (MPa)	30	55
Tensile Modulus (MPa)	4,500	1,724
Flexural Modulus (MPa)	3,800	3,450
Elongation (%)	0.9	3

Table 5.3 Material properties for 20M reinforcing steel test bar (Mill certificate)

Material Property	Value
Yield Strength	479 (MPa)
Tensile Strength (Ultimate)	603 (MPa)
Elongation	17.5 (%)

5.7 Properties of the Monolithic Concrete and the Partial Depth Repair Concretes

The partial depth repair materials SCC50 and SCC0 were commercial prepackaged self-consolidating concrete with the same properties except that the SCC50 was extended with 50% of 13 mm coarse aggregate while the SCC0 had no coarse aggregate. It should be mentioned that SCC50 was the same partial depth repair material labeled as SCC2 that was used in Phase 2 testing of the beam-end specimens and gave the best average bond strength comparing to the other partial depth repairs. Also, the mixture proportions of the concrete used for monolithic lap splice beams had the same properties as M2 of the beam-end specimens (Phase 2). Table 5.4 shows the proportions for the monolithic concrete. Table 5.5 shows the hardened properties (Compressive strength, splitting strength and fracture energy) of the M1, M2, SCC50 and SCC0 concretes.

Table 5.4 Mixture properties design for the monolithic concrete

Concrete type	CA* (kg/m^3)	FA* (kg/m^3)	Cement (kg/m^3)	WR* (%C)	AEA* (%C)	W* (kg/m^3)	W/C	CA%
M1 and M2	1110	865	280	0.29	0.003	155	0.55	46

CA: coarse aggregate (19 mm), FA: fine aggregate, WR: water reducer, AEA: air entrained admixture, W: water

Table 5. 5 Hardened properties of M1, M2, SCC50 and SCC0 concretes

Concrete Mechanical properties	M1	M2	SCC50	SCC0
Compressive strength, f'_c (MPa)	42	38	48	55
Splitting strength, f_t (MPa)	4.1	4.0	4.1	3.7
Fracture energy, G_f (N/m)	135	135	137	124

Chapter 6: Experimental Results and Discussion of Lap Splice Beams

6.1 General

This chapter presents and discusses the test results of 24 lap splice beams to analyze the bond behaviour of beams with cleaned corroded bars rehabilitated by partial depth repair concrete. Two bar mass loss levels were considered (7.5% and 15% mass loss level) and the results were compared with those of non-corroded bars. A commercial prepackaged self-consolidating concrete extended with 50% of 13 mm coarse aggregate (SCC50) was used as main partial depth repairs and their test results were compared with those of a monolithic beams. Three other lap splice beams were repaired with the same commercial prepackaged self-consolidating concrete but without coarse aggregate (SCC0) to study the effect of coarse aggregate and the lack of it on bond behavior. Six beams were confined with transverse internal reinforcement (stirrups) and six beams were confined externally with FRP sheets. The 24 lap splice beams were cast as two sets because of a limited number of forms; each set was cast into the twelve available forms. Each set had three unconfined monolithic beams with control, 7.5% and 15% mass loss level. Test results from these beams were used as references for the test results of other beams in the same set. The monolithic mixes for the first set and the second set, which came from separate ready mix loads, were labeled by M1 and M2, respectively. Both monolithic mixes had the same mixture proportions.

6.2 Mode of Failure and Cracking Pattern

All of the lap splice beams failed by a splitting bond failure (as intended). The first flexural crack in the beams occurred at the upper corners of the notches at the end of the lap spliced region and still within the constant moment region. As the applied load increased, more flexural cracks developed in the spliced zone together with longitudinal cracks along the lap spliced bars. The longitudinal splitting cracks occurred on the bottom face of the beam from both ends of the splice region (Figure 6.1).

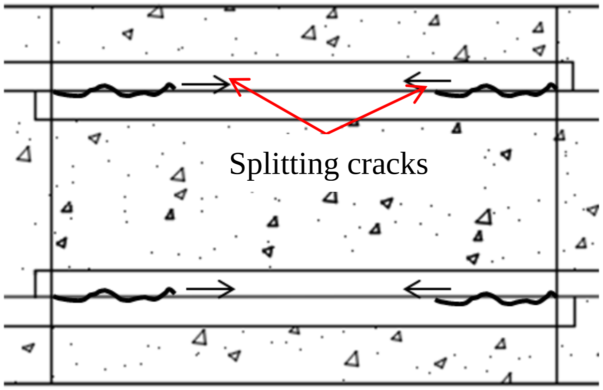

Figure 6.1 Initiation of splitting cracks on the bottom face of the beam

The unconfined beams had a sudden brittle failure associated with loud sound resulting from the splitting of the final length of the concrete cover. The bottom face cracks in the unconfined beams formed V shape (Figure 6.2). Sizable chunks of concrete were formed and in some cases spalled off from the concrete cover at failure because of the absence of confinement.

Figure 6.2 Bottom face bond splitting cracks for an unconfined beam

The mode of failure was different for the beams confined with internal transverse reinforcement and FRP sheets. The confined beams had a more ductile mode of failure compared to the unconfined beams in which the confinement delayed the splitting of the concrete cover.

Unlike the unconfined beams, the concrete cover did not spall off in the beams confined with transverse reinforcement or FRP sheet; the stirrups or FRP sheets held the concrete cover in place after splitting occurred. The confined beams experienced an increase in the ultimate load, corresponding deflection at failure and flexural crack width compared to the unconfined beams. Extensive flexural and splitting cracks formed in the bottom cover in the spliced region of the beams confined with transverse reinforcement (Figure 6.3).

Figure 6.3 Bottom face cracks of beam confined with internal transverse reinforcement

The transverse confinement considerably reduced the widening of the splitting cracks as the load increased and produced smaller pieces of concrete than those of the unconfined beams. For the beams confined with FRP sheet, the crack pattern could not be monitored during testing since the cracks did not penetrate the FRP sheet. At failure, both the unconfined beams and the beams confined with transverse reinforcement formed horizontal splitting cracks on the side of the spliced zone along the lap spliced bars. After the test, when the FRP sheets were removed for inspection it was found that the failure produced smaller pieces of concrete compared to unconfined beams and beams confined with transverse reinforcement (Figure 6.4).

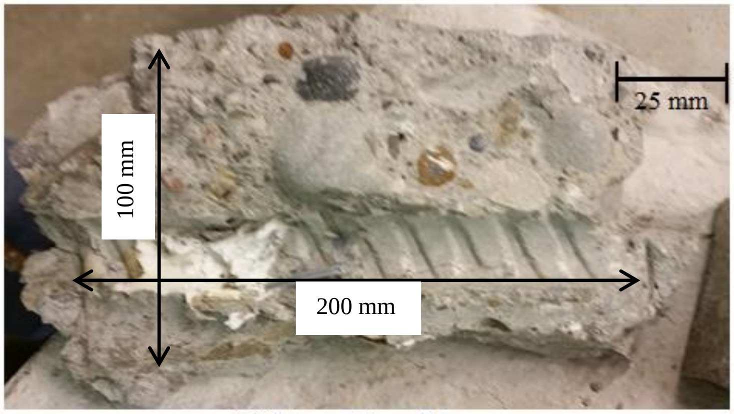

(a) Unconfined beam

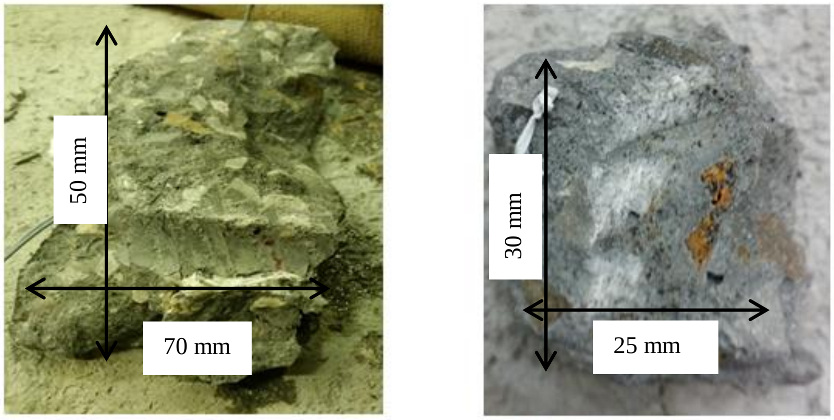

(b) Beam repaired with transverse reinforcement

(c) Beam repaired with FRP sheet

Figure 6.4 Pieces of concrete of (a) unconfined beam, (b) beam confined with transverse reinforcement (c) beam confined with FRP sheet

6.3 Summary of Lap Splice Beam Test Results

Table 6.1 shows a summary of all lap splice beams test results including the load at failure, the average bond strength at failure, the loaded end slip and the failure mode. The lap splice beams were labeled as follows: the first part (LS) refers to lap splice and the second part refers to type of concrete (M1 and M2 for monolithic concrete of the first set and the second set, respectively), SCC50 for commercial prepackaged self-consolidating concrete extended with 50% of 13 mm coarse aggregate and SCC0 for the prepackaged self-consolidating concrete without the addition of a coarse aggregate. The third part refers to the confinement condition (UN for the unconfined beams, T for the beams confined with transverse reinforcement and F for the beams confined with FRP sheets). The last part represents the corrosion level (C for the control specimens (non-corroded), 7.5 for the specimens with a 7.5% mass loss level and 15 for the specimens with a 15% mass loss level). The splice length and the concrete cover for all beams were fixed as 300 mm and 25 mm, respectively.

Based on the splice length, the concrete cover, the mass loss level and the confinement condition, all lap splice beams were designed to fail by a splitting failure. The average bond strength was calculated using Equation 6.1

$$\tau_b = \frac{d_b\, f_s}{4L_s} \qquad \text{Equation (6.1)}$$

Where:

τ_b: The average bond strength (MPa)

d_b: The bar diameter account for actual mass loss (mm)

f_s: Steel stress at failure (MPa)

L_s: The splice length (mm) = 300 mm

Table 6.1 Summary of lap splice beams test results

Specimen	Corrosion Level (%)	Load on beam at failure (kN)	f_s (MPa)	Bond strength τ_b (MPa)	Bar slip at failure (mm)	Failure Mode*
LS-M1-UN-C	0	172.3	269	4.42	1.30	S
LS-M2-T-C		191.8	298	4.90	1.62	S
LS-M1-F-C		231.0	361	5.91	2.04	S
LS-SCC50-UN-C		186.4	291	4.78	1.44	S
LS-SCC50-T-C		213.2	333	5.51	1.97	S
LS-SCC50-F-C		250.2	391	6.41	2.52	S
LS-M2-UN-C		166.3	260	4.22	1.03	S
LS-SCC0-UN-C		157.0	245	4.02	0.83	S
LS-M1-UN-7.5	7.5	173.9	294	4.63	1.41	S
LS-M2-T-7.5		200.0	338	5.32	1.97	S
LS-M1-F-7.5		245.0	414	6.51	2.42	S
LS-SCC50-UN-7.5		192.5	325	5.13	1.59	S
LS-SCC50-T-7.5		222.6	376	5.93	2.42	S
LS-SCC50-F-7.5		261.7	442	6.97	2.81	S
LS-M2-UN-7.5		163.1	275	4.35	1.19	S
LS-SCC0-UN-7.5		156.4	264	4.16	0.92	S
LS-M1-UN-15	15	176.8	324	4.91	1.52	S
LS-M2-T-15		204.0	376	5.65	2.29	S
LS-M1-F-15		258.1	473	7.16	2.93	S
LS-SCC50-UN-15		191.8	352	5.32	1.71	S
LS-SCC50-T-15		229.3	420	6.36	2.76	S
LS-SCC50-F-15		285.7	524	7.93	6.25	Y+S
LS-M2-UN-15		165.0	303	4.58	1.32	S
LS-SCC0-UN-15		155.8	286	4.32	1.09	S

* S: Splitting failure Y: Bar yield.

6.4 Effect of Concrete Properties and Repair Condition on Bond Strength

Figure 6.5 shows the average bond strengths normalized by $f'_c{}^{1/2}$ of the monolithic mixes (M1 and M2) and partial depth repair concretes (SCC50 and SCC0) at different mass loss levels. In contrast to the beam-end specimens, the lap splice beams repaired with the partial depth repair SCC50 material had similar or almost higher normalized average bond strengths than the monolithic beams. Unlike the beam end specimens, there is no shear in the splice region and the shear cracking along the boundary between the beam and repair material is absent. Thus, the variables that affected the average bond strength were the concrete strength and the amount of the coarse aggregate in the concrete mix.

The partial depth repair material SCC0 had the highest compressive strength of the mixes; but had the lowest normalized average bond strength. Table 5.5 shows that the absence of the coarse aggregate in SCC0 led to a decrease in the splitting strength and fracture energy relative to the compressive strength, which has been reported previously by others (Beygi et al. 2014; Nikbin et al. 2014). The reduced tensile properties (f_t and G_f) of SCC0 likely reduced the average bond strength in spite of the high compressive strength.

The monolithic concrete (M1 and M2) and the partial depth repair SCC50 had a similar proportions of coarse aggregate with 46% and 50% (by weight), respectively. The partial depth repair SCC50 had a higher strength than the monolithic concrete presumably due to the inclusion of silica fume and a lower water-to-binder ratio in the SCC50 material, which may have improved the bond properties as reported by (Chan and Chu, 2004)

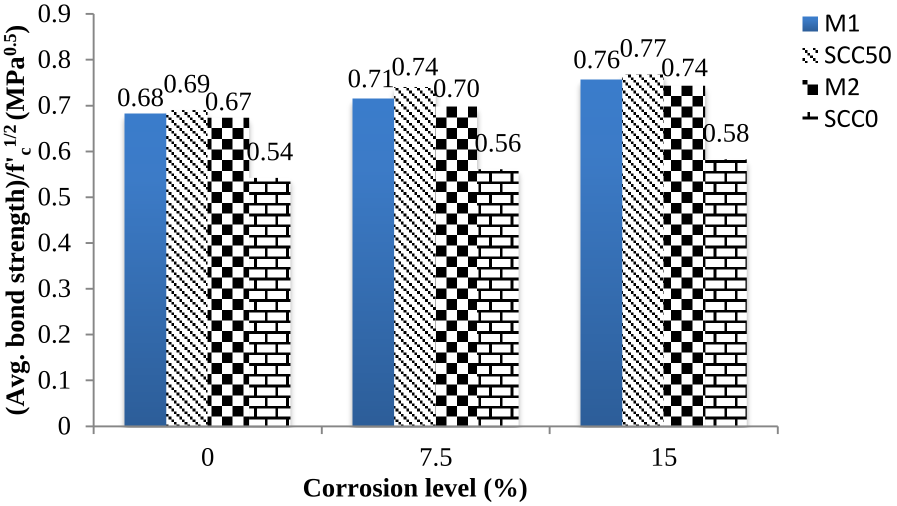

Figure 6.5 Avg. bond strength normalized by $f'^{1/2}_c$

6.5 Lap Splice Beam Load-Deflection Behavior

6.5.1 Effect of Partial Depth Repair with and without FRP Wrapping

The load deflection curves for the lap splice beams; monolithic specimens (M1) and partial depth repaired specimens (SCC50) with and without FRP wrapping (F) are shown in Figures 6.6 (a), 6.6(b) and 6.6 (c) for the control beam and the 7.5% rebar mass loss and 15% rebar mass loss beams, respectively.

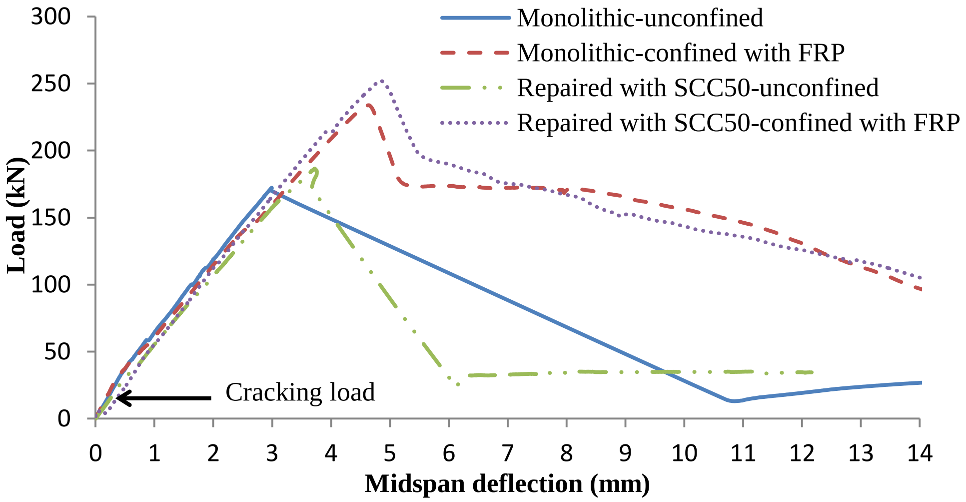

(a) Control beams

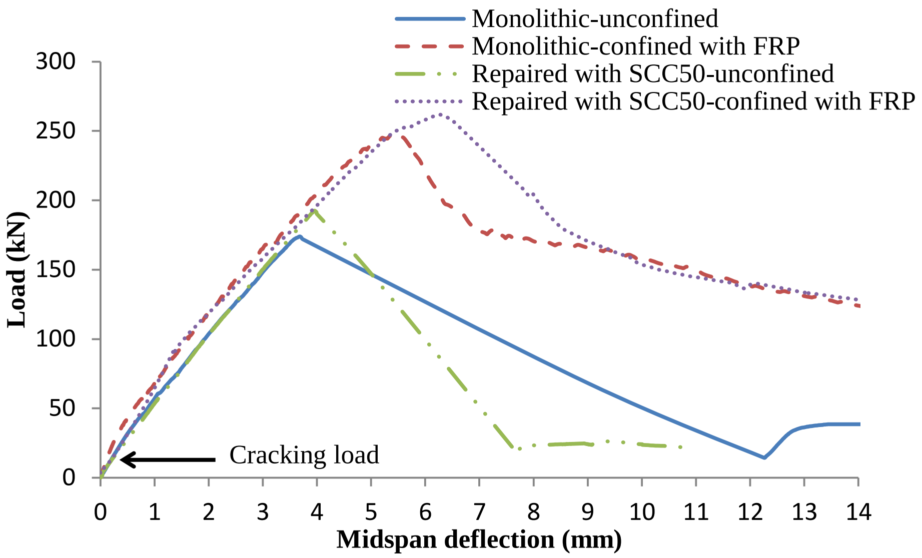

(b) Beams with 7.5% mass loss

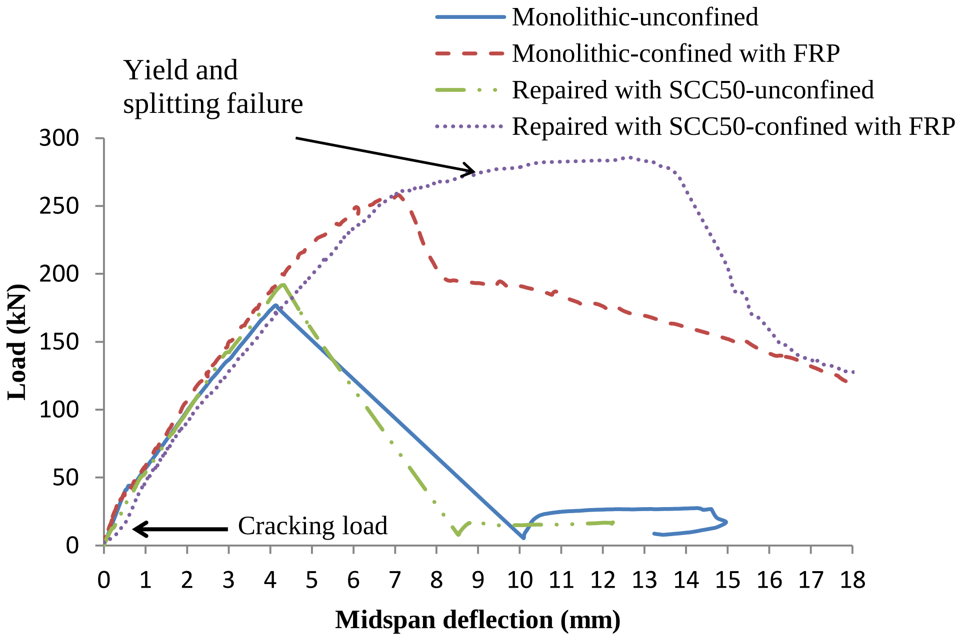

(c) Beams with 15% mass loss

Figure 6.6 Load-deflection curves of monolithic beams and beams repaired with partial depth repair SCC50 with and without FRP confinement

The beams confined with FRP sheets experienced an increase in the ultimate load and the corresponding deflection at failure compared to the unconfined beams. The beams wrapped with FRP sheets had a higher maximum load and corresponding deflection than the unwrapped beams by 55% and 191%, respectively. The load deflection curves increased linearly after initial flexural cracking until the maximum load was achieved coincident with a bond splitting failure. After the splitting failure, the load deflection behavior of the unconfined beams was different than the beams confined with FRP sheets. The splitting failure of unconfined beams was accompanied by a sudden drop of the load and increase in deflection. However, the beams confined with FRP sheets had a more ductile post-failure behaviour in which the load dropped gradually as the deflection increased. This is attributed to the FRP sheets limiting the bond crack widths and preventing spalling of the concrete cover. The partial depth repair was able to restore and even increase the capacity of the repaired beams, which had a higher maximum load at failure than the monolithic beams. The beam LS-SCC50-15-F failed by bar yielding followed by a splitting failure (the stress on the bar exceeded the manufactured reported yield strength (479 MPa) before the splitting failure occurred. As the bar was yielding, the deflection of the beam was increasing considerably resulting from the bar elongation with only a slight increased in the applied load until failure. Except for this beam, all of the other beams failed by a splitting bond failure. The rebond state (constant or slight increase in bond after failure) in the unconfined beams could be from the residual friction between the reinforcing bar and the surrounding concrete where the concrete keys did not shear off unlike the confined beams.

6.5.2 Effect of Partial Depth Repair with and without internal Transverse reinforcement

The load deflection curves for the lap splice beams of monolithic specimens (M2) and partial depth repaired beams SCC50 with and without transverse reinforcement (T) are shown in Figure 6.7 (a), 6.7 (b) and 6.7 (c) for the control beam and for the 7.5% and 15% rebar mass loss beams, respectively.

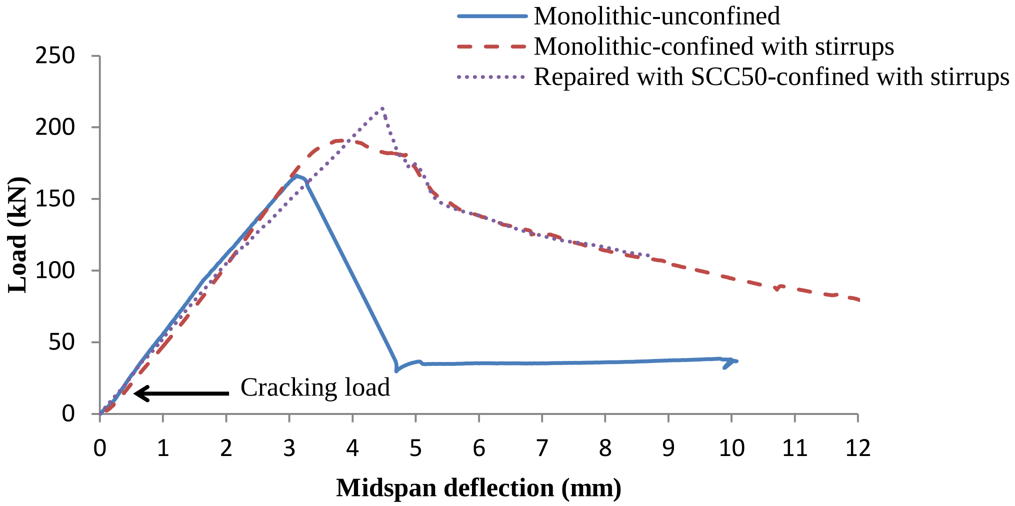

(a) Control beams

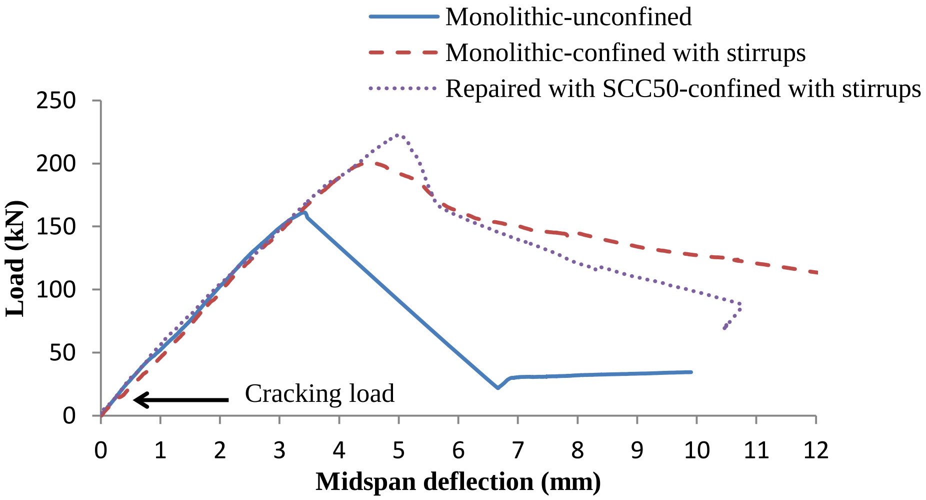

(b) Beams with 7.5% mass loss

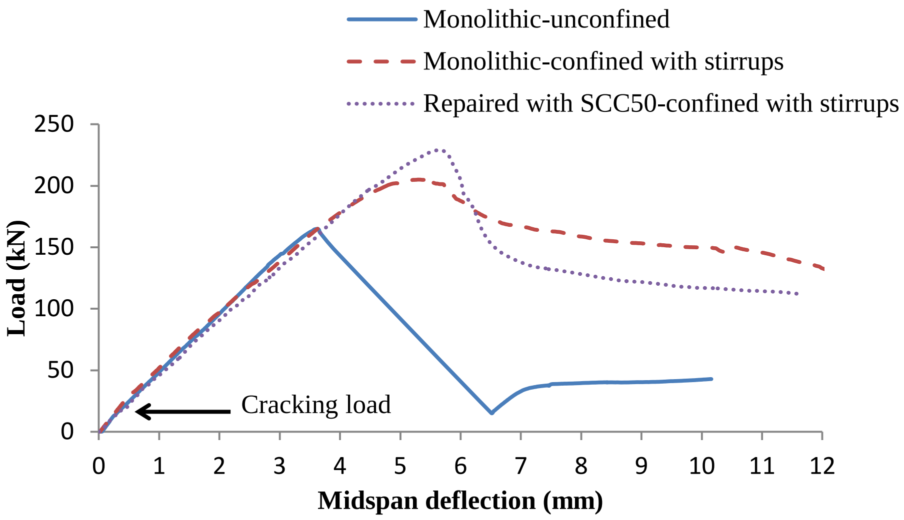

(c) Beams with 15% mass loss

Figure 6.7 Load-deflection curves of monolithic beams and beams repaired with partial depth repair SCC50 with and without transverse reinforcement

Confining the beams with transverse reinforcement increased both the maximum load and the corresponding deflection at failure compared to the unconfined beams. The ultimate load at failure and the corresponding deflection increased by 36% and 64% compared to the unconfined beams, respectively. A minor reduction in stiffness was observed due to coincide with formation of flexural cracking at the notches in the beam at the load level shown in Figure 6.6 and Figure 6.7. The number of cracks and the stiffness loss was small. The occurrence of cracking at the notches was due to their location in the constant moment region of the beam and the reduced cross-section at the notch locations. After the initial flexural cracking load, all of the load-deflection curves increased linearly until the maximum load was achieved. After the maximum load, the transverse reinforcement improved the ductility at failure and the post maximum load strength of the confined beams, but the unconfined beams had a brittle failure in which the load dropped suddenly during the splitting bond failure. The partial depth repair with 50% of coarse aggregate gave these beams a greater capacity than the monolithic beams. The beams confined with FRP sheets had a higher ultimate load and corresponding deflection than the beams confined with transverse reinforcement (stirrups). Figure 6.8 shows a comparison of the typical load-deflection response of the monolithic lap splice beams confined with stirrups or FRP sheets at different mass loss levels (control, 7.5% and 15% mass loss level). The FRP sheets confinement considerably delayed the splitting failure compared to the lap splice beams confined with stirrups. This is likely because the FRP sheets (as external confinement) confined all of the concrete around the spliced bar in the lap splice area (uniform confinement); however the stirrups (as internal confinement) confined particular area of concrete around the spliced bars (discrete confinement) (Figure 6.9). At failure, the lap splice beams confined with stirrups showed a gentle drop in the load compared to the beams confined with FRP sheet. That could be because the advantage of the mechanical interlock between the stirrups and the rebar.

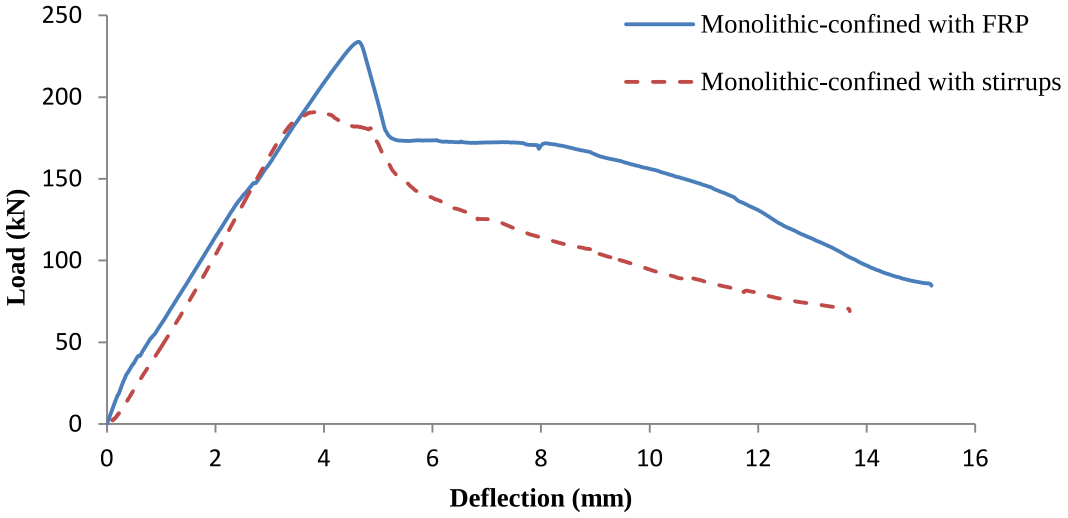

(a) Control beams

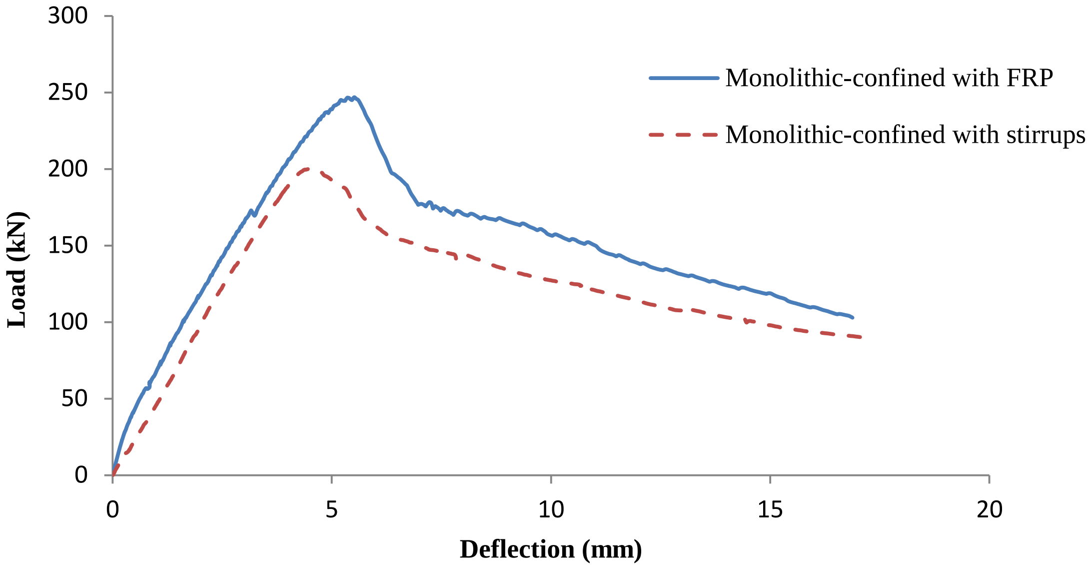

(b) Beams with 7.5% mass loss

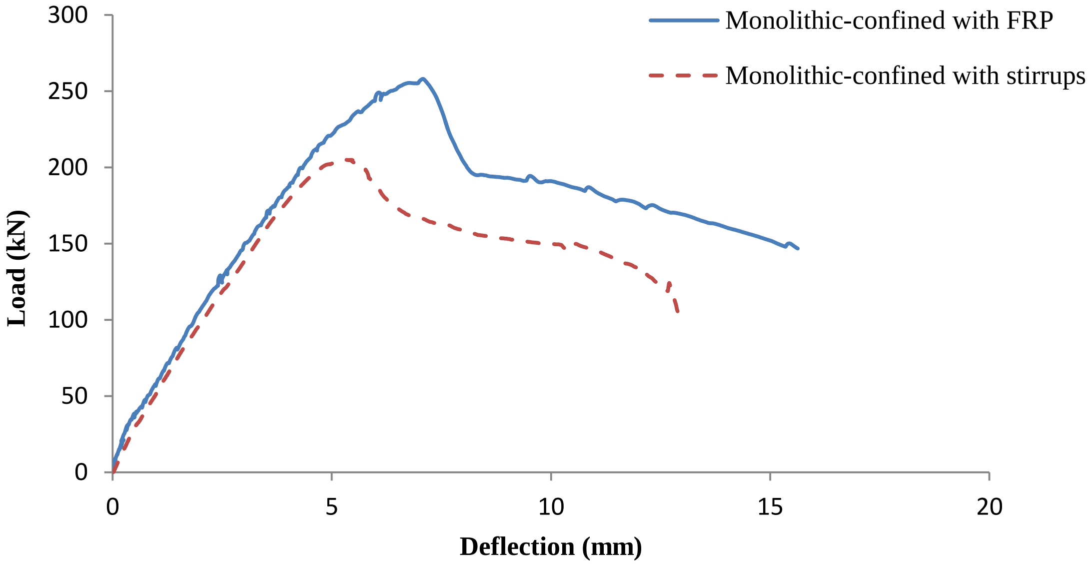

(c) Beams with 15% mass loss

Figure 6. 8 Typical load-deflection response of the monolithic beams confined with stirrups or FRP sheets

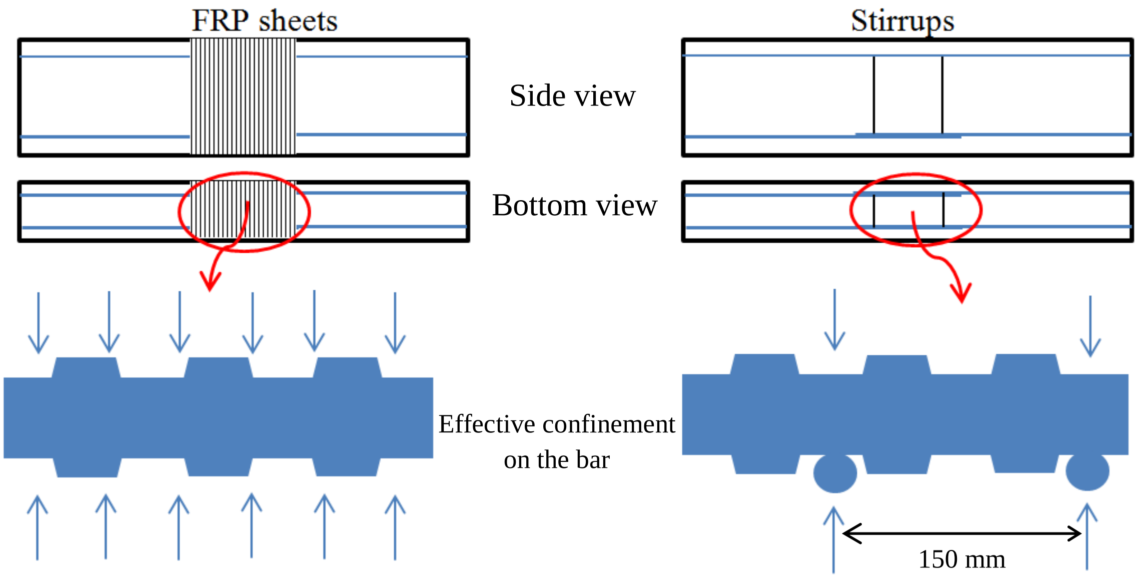

Figure 6.9 Schematic comparison of FRP sheet and stirrup confinement

6.5.3 Effect of Corrosion on Load-Deflection Response

Figure 6.10 shows typical load deflection curves of beams with different levels of mass loss. The beams in the same mass loss category had almost the same stiffness. However, the stiffness decreased slightly with increased reinforcing bar mass loss. As the bar mass loss increased, the total cross sectional area of the bars decreased, reducing the effective stiffness of the beam, thereby increasing the mid-span deflection. In spite of the minor difference in load at failure, the average bond strength increased as the mass loss increased as shown in Figure 6.11 due to the reduction in bar area and diameter (see Section 4.6.4.2 for more discussion).

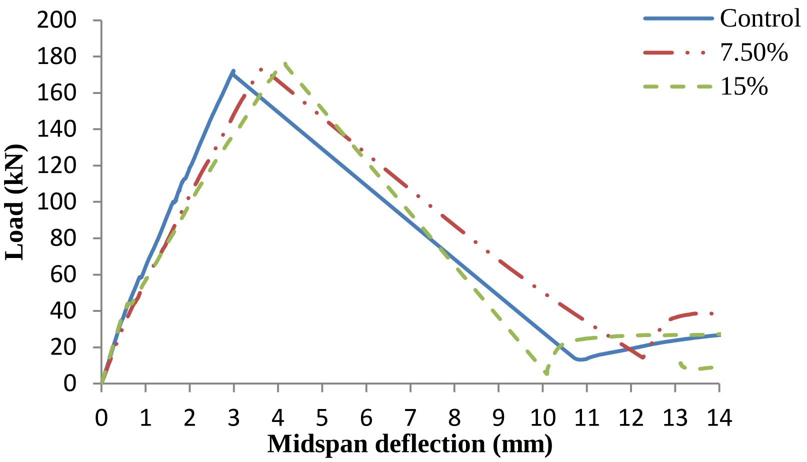

Figure 6. 10 Typical load deflection curve of monolithic unconfined lap splice beams with different levels of mass loss

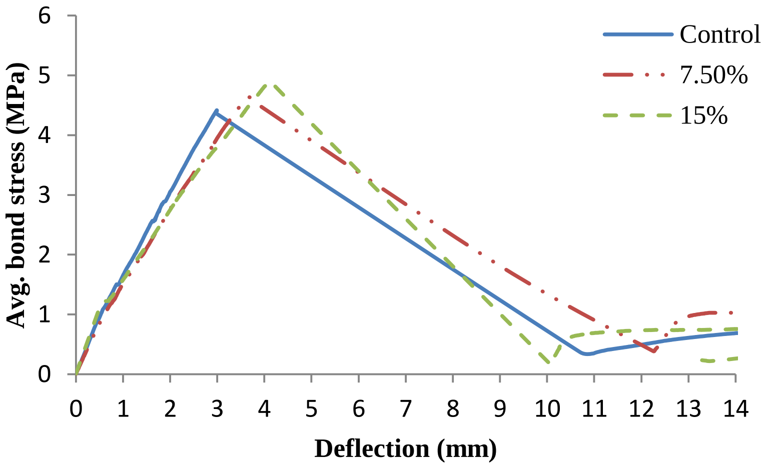

Figure 6.11 Typical Avg. bond stress versus deflection curve of monolithic unconfined lap splice beams with different levels of mass loss

6.5.4 Effect of Coarse Aggregate in Repair Concrete on Load-Deflection Response

Two types of partial depth repair concrete were used, SCC with 50% and 0% content of coarse aggregate, to evaluate the effect of coarse aggregate on bond behaviour. Figure 6.12 illustrates the load deflection curves for the unconfined beams repaired with SCC50 and SCC0 at different mass loss levels. The unconfined beams with the partial depth repair without coarse aggregate (SCC0) showed lower ultimate load and corresponding deflection than the beams repaired with SCC50. Because all beams failed by splitting bond failure, the beams that repaired with SCC50 had higher bond strength than the beams repaired with SCC0. That could be explaining the higher bond strength for the SCC50 beams is likely due to higher splitting tensile strength and fracture energy measured for SCC50 compared to SCC0. The absence of coarse aggregate in SCC0 decreased the fracture energy of SCC0 compared to SCC50. This reduced the bond strength of SCC0 even though the compressive strength of SCC0 was higher than SCC50. As a result, the reduced fracture energy of SCC0 decreased the failure load and deflection of the beam compared to the beams repaired with SCC50.

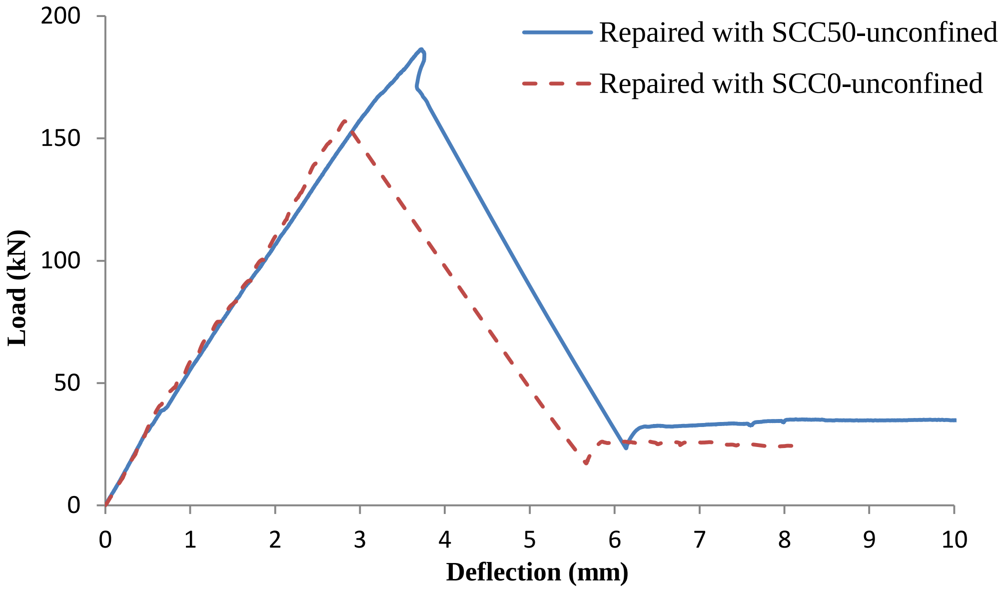

(a) Control beams

Figure 6.12 Load deflection curves of the unconfined beams repaired with SCC50 and SCC0

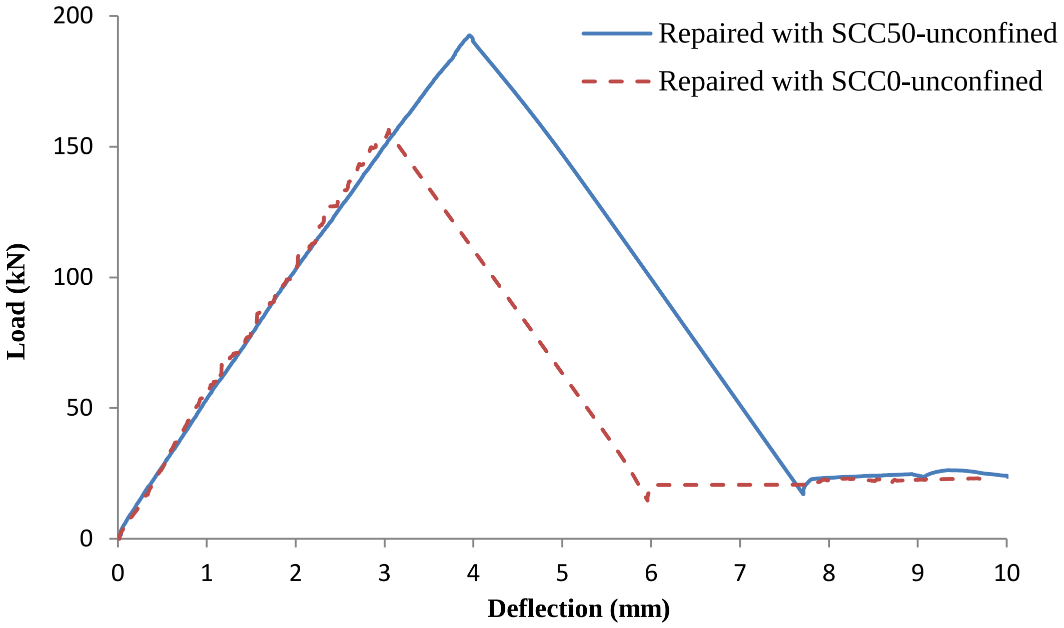

(b) Beams with 7.5% mass loss

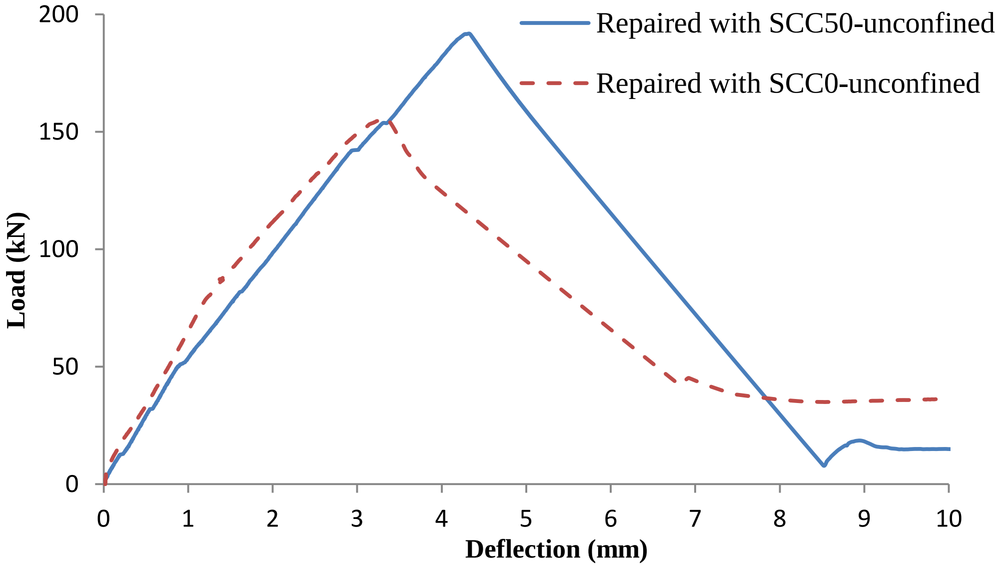

(c) Beams with 15% mass loss

Figure 6.12 Load deflection curves of the unconfined beams repaired with SCC50 and SCC0 (continued)

6.6 Bond Stress versus Slip Response

The typical bond stress versus slip response for the control monolithic beams (M1 and M2) partial depth repaired specimens (SCC50 and SCC0) with and without FRP wrapping (F) and with and without stirrups (T) are shown in Figures 6.13 and Figure 6.14, respectively. The beams confined with FRP sheets and with stirrups had higher values of bond strength and slip at maximum load than the unconfined beams. The confined beams experienced a later start and slower growth of the splitting cracks. The bond strength of beams repaired with FRP sheets was higher than that of the beams confined with transverse reinforcement. The transverse reinforcement increased the average bond strength and the corresponding slip by (15% - 29%) and (32% - 62%) compared to the unwrapped beams, respectively. However, the beams confined with FRP sheets showed an increase in the bond strength and the corresponding slip by (34 - 49%) and (56 - 260%) compared to the unconfined beams, respectively. In all cases, with and without confinement, the partial depth repair with the SCC50 had a higher bond strength than the monolithic specimens. Although the concrete used in the partial depth repair without coarse aggregate had a higher compressive strength than the partial depth repair with a 50% coarse aggregate content, the beams repaired with a partial depth repair with a 50% coarse aggregate content had a higher bond strength. The absence of coarse aggregate affected both the splitting tensile strength and the fracture energy, both of which have a direct effect on bond strength.

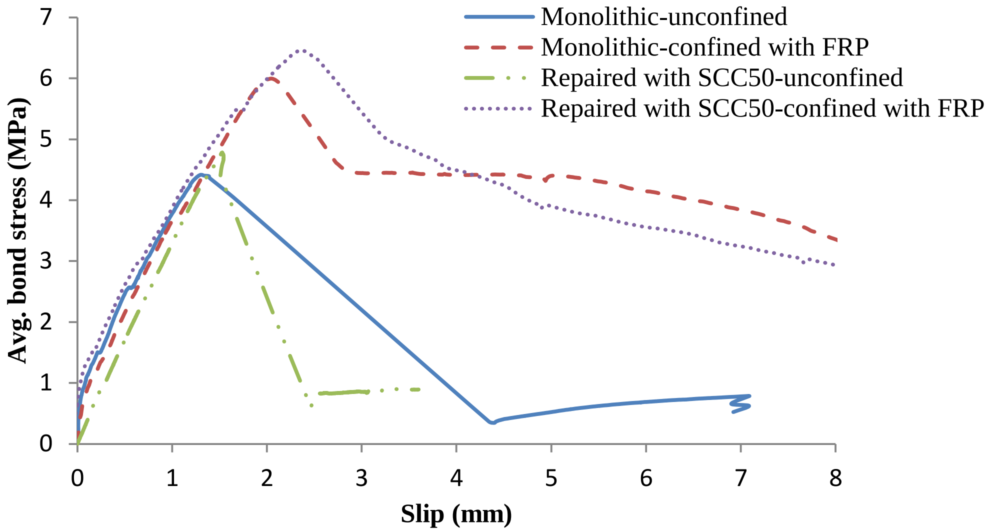

Figure 6.13 Avg. bond stress versus slip for unconfined beams and beams wrapped with FRP

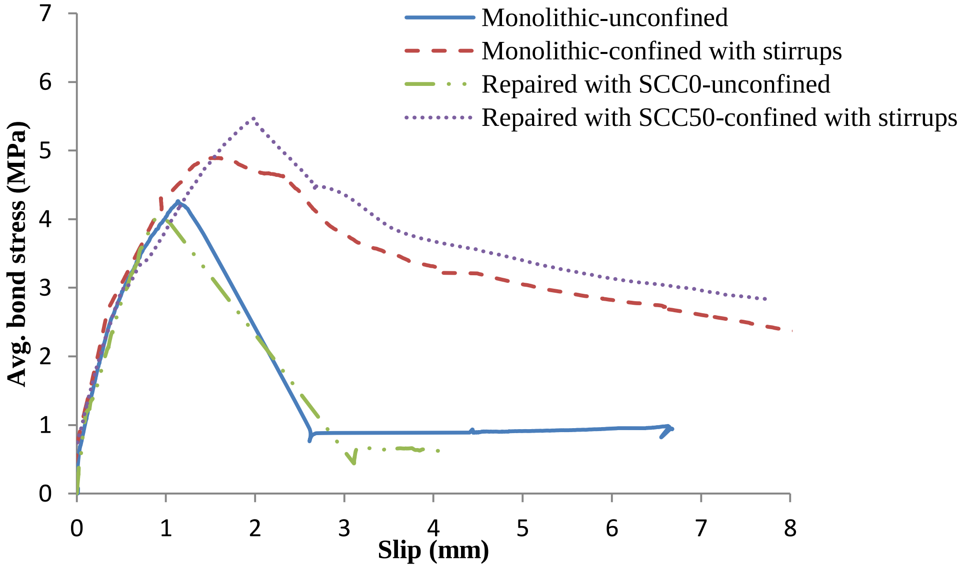

Figure 6.14 Avg. bond stress versus slip for unconfined beams and beams with internal transverse reinforcement

The typical bond stress-slip curve of beams confined with FRP sheets for the control beam and the 7.5% and 15% mass loss beams are shown in Figure 6.15. The bond strength and the corresponding slip increased with increasing rebar mass loss. The reason was that the cross sectional area of the bars decreased with increased the corrosion level; thus, the force on the bar at bond failure decreases more slowly than decreasing the area of the bar (ACI 408, 2003).

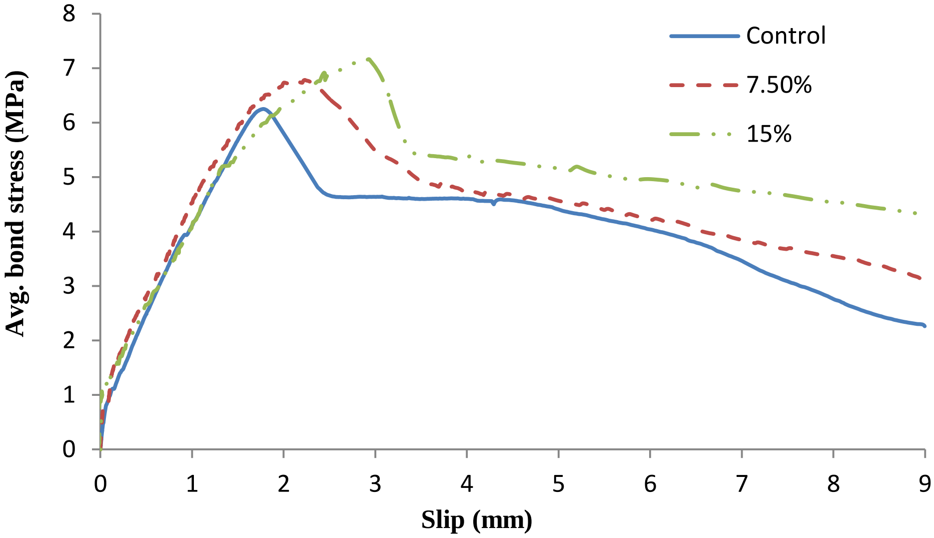

Figure 6.15 Avg. bond stress versus slip for beams wrapped with FRP with different rebar mass loss

6.7 Summary of this Chapter

All of the unconfined beams and the beams confined with stirrups or FRP sheets failed by splitting bond failure. The beams confined with stirrups or FRP sheets had more ductile failure than the unconfined beams. At failure, the lap splice beams confined with transverse reinforcement or FRP sheets produced smaller chunks of concrete than those of the unconfined beams. Also, the beams confined with FRP sheets produced smaller chunks of concrete compared to beams confined with transverse reinforcement.

The average bond strength increased with increasing bar mass loss level. Repairing the beams with partial depth repair SCC50 concrete enhanced the average bond strength compared to the monolithic beams. Although the partial depth repair concrete SCC0 had higher compressive strength than SCC50; it had lower average bond strength. That because the absence of the coarse aggregate in SCC0 led to a decrease splitting strength and fracture energy; thus led to decrease the average bond strength.

The beams confined with stirrups or FRP sheets delayed the bond failure compared to the unconfined beams. The ultimate load at failure of the beams confined with stirrups or with FRP sheets increased by 36% and 49%, respectively compared to the unconfined beams. The beams confined with FRP sheets had a higher ultimate load and corresponding deflection than the beams confined with transverse reinforcement.

Chapter 7: Bond Strength Prediction and the Effect of Bar Mass Loss

7.1 Introduction

The general results for the beam-end specimens and the lap splice beams showed that the average bond strength increased with increasing corrosion mass loss level of the cleaned reinforcing bar. This conclusion was observed for all of the concrete types and for different bonded lengths. This chapter presents an in-depth discussion of factors affecting bond strength in the experimental results, and presents models to predict the average bond strength as the mass loss level increased for the beam-end specimens and the lap-splice beams. The type of confinement (stirrups and FRP sheets) was taken into account in the average bond strength prediction as the mass loss increased.

7.2 Beam-End Specimens

7.2.1 General

The bond between the steel and the concrete is an important property that should be taken into account in order to design reinforcement concrete (RC) member. The bond stress distribution along a reinforcing bar changes as the splitting crack progresses. In the current study of beam-end specimens repaired with partial depth repair, the bond between the substrate concrete and the new concrete also affects the overall performance of the bond.

A partial depth repair technique was used to repair a RC member that had a 20M cleaned corroded reinforcing bar after different mass loss levels (control, 5%, 7.5%, 10% and 15%). Four types of concrete were used for partial depth repair and compared to a monolithic beam-end specimen to study the effect of different parameters such as aggregate size, aggregate content, the use of silica fume and of a bonding agent. Table 7.1 describes all of the repair concretes used including the monolithic mix and gives their compressive strengths. Because the 36 beam-end specimens were cast into two phases (12 beam-end specimens for the first phase and 24 beam-end specimens for the second phase), their two different monolithic mixes will be denoted as M1 and M2. The expressions SCC1 and SCC2 refer to two types of commercial prepackaged self-compacting concrete used for partial depth repair. SCC3 is a self-compacting concrete that was developed and batched in the laboratory. The normal concrete (NC) used for repair was also batched in the laboratory and had exactly the same proportions as the monolithic concrete.

Four bonded lengths were used: 250 mm and 350 mm in the first phase and 200 mm and 300 mm in the second phase. The bonded lengths in the first phase were chosen based on calculations of the lengths required for the beam-end specimens to fail in a splitting bond mode. Based on the results of the first phase, the bonded lengths were decreased in the second phase to avoid the risk of bar yield or bar rupture.

Table 7.1 Concrete types and characteristics for beam-end

<table>
<tr><th colspan="6">Phase 1</th></tr>
<tr><th>Mix</th><th>Coarse aggregate size (mm)</th><th>Coarse aggregate proportion (%)</th><th>Silica Fume</th><th>Bonding agent</th><th>Compressive strength (MPa)</th></tr>
<tr><td>M1</td><td>19</td><td>46</td><td>NO</td><td>-</td><td>55</td></tr>
<tr><td>SCC1</td><td>8</td><td>10</td><td>YES</td><td>YES</td><td>65</td></tr>
<tr><th colspan="6">Phase 2</th></tr>
<tr><th>Mix</th><th>Coarse aggregate size (mm)</th><th>Coarse aggregate proportion (%)</th><th>Silica Fume</th><th>Bonding agent</th><th>Compressive strength (MPa)</th></tr>
<tr><td>M2</td><td>19</td><td>46</td><td>NO</td><td>-</td><td>41</td></tr>
<tr><td>SCC2</td><td>13</td><td>50</td><td>YES</td><td>YES</td><td>47</td></tr>
<tr><td>SCC3</td><td>19</td><td>40</td><td>NO</td><td>NO</td><td>43</td></tr>
<tr><td>NC</td><td>19</td><td>46</td><td>NO</td><td>NO</td><td>39</td></tr>
</table>

7.2.2 Bond Stress Distribution along the Bonded Length

The beam-end specimen represents a condition of anchorage bond for a reinforcing bar. The tensile stress in the reinforcing bar decreases over the bonded length with distance from the loaded end. As the applied force in the bar increases, the tensile stress distribution in the bar, and the corresponding bond stress change and move progressively toward the free end as the bond splitting cracks forms at the interface of the concrete and the reinforcing bar and progresses from the loaded end. Figure 7.1 shows changes in the bond stress distribution as the splitting crack length increases, which was divided into three stages (A, B and C as shown). In stage A, the splitting crack has not yet formed and there is no slip between the steel and the concrete (just before initiation the splitting crack). In stage B, where the remaining bonded length was still adequate to develop more bar force, the load has increased until the maximum local bond stress was reached, followed by propagating the splitting crack length. In the cracked region, only a residual bond stress remains along the splitting crack length. In stage C (immediately before splitting bond failure occurred), the beam-end specimen reaches the maximum bond force and the specimen cannot carry any further load. As the load is increased, a splitting bond failure occurs because the remaining bonded length (uncracked region) is not sufficient to develop further increases in bar force.

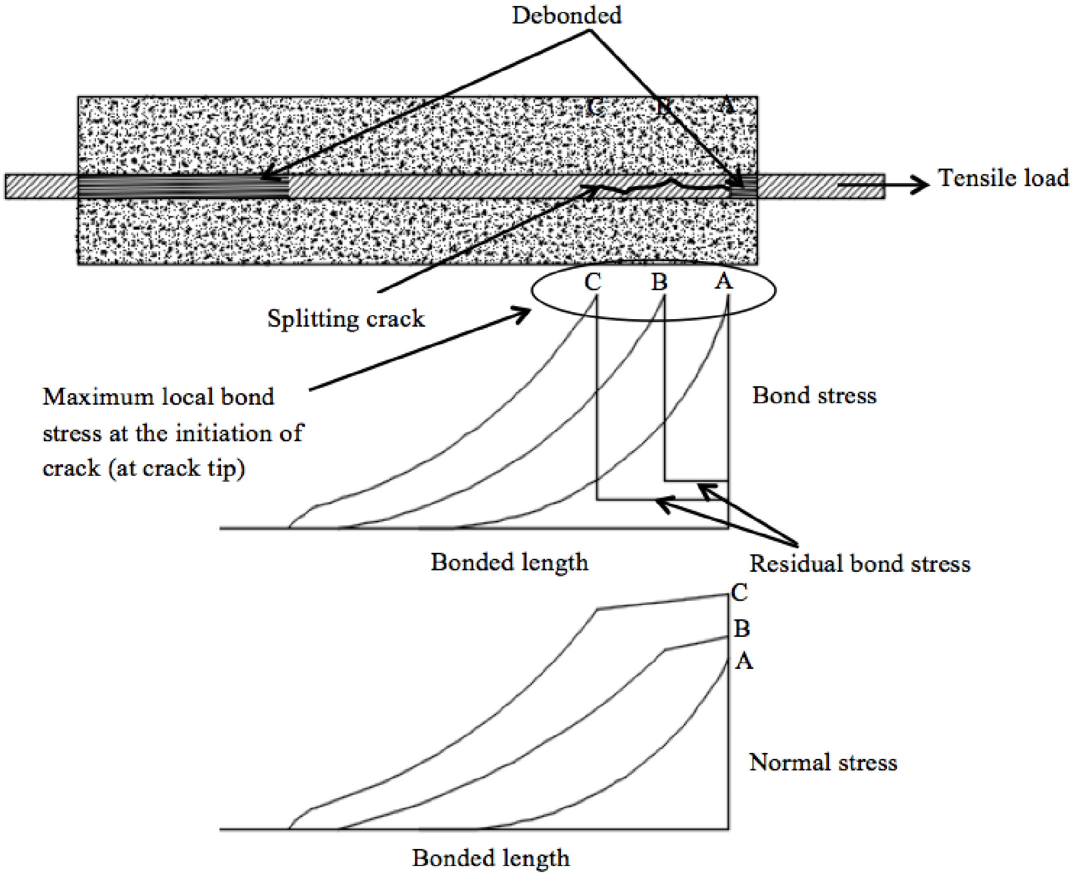

Figure 7.1 Bond stress distributions in beam-end specimen as the splitting crack propagates

7.2.3 Comparison of Bond Strength Test Results to the Predicted Bond Strength

The bond between the reinforcing bar and the surrounding concrete is influenced by concrete properties (strength properties and the concrete cover), reinforcing bar properties (bar diameter and the depth of the lugs) and the confinement (transverse reinforcement or FRP sheet). The total average bond strength can be calculated as a follows:

$$\tau_t = \tau_{concrete} + \tau_{confinement} \qquad \text{Equation (7.1)}$$

Where:

τ_t: Total bond strength (MPa)

$\tau_{concrete}$: Contribution of concrete to the bond strength (MPa)

$\tau_{confinement}$: Contribution of confinement to the bond strength (MPa)

In the current study, the beam-end specimens were not confined with transverse reinforcement or with FRP sheet; thus the contribution of confinement to the bond strength was zero. Therefore, the bond strength of the embedded bar in the concrete in the current study was limited to the concrete contribution, which involves adhesion, friction and mechanical interlock between the reinforcing bar and the surrounding concrete.

The average measured bond strength of the tested beam-end specimens was calculated from equilibrium considerations:

$$\tau_{avg} = \frac{d_b * f_s}{4 l_b} \qquad \text{Equation (7.2)}$$

Where:

τ_{avg}: The average bond strength at failure (MPa)

d_b: Bar diameter (mm)

f_s: Maximum stress in the bar at failure (MPa)

l_b: Bonded length (mm)

The average bond strength at zero mass loss can be predicted using the bond equation from ACI 408-03 as follows:

$$\tau_{avg(M_o)} = u = \left[0.10 + \frac{c}{4d_b} + \frac{4.15d_b}{l_d}\right]\sqrt{f'_c} \qquad \text{Equation (7.3)}$$

Where:

$\tau_{avg(M_o)}$: Predicted average bond strength at failure (zero mass loss) (MPa)

c: Concrete clear cover (mm)

d_b: Bar diameter (mm)

l_d: Bonded length (mm)

f'_c: Concrete compressive strength (MPa)

There are variety of predictive equations in published literature proposed to predict the average bond strength. Several of these equations were used to predict the bond strength of the beam-end specimens in the current study, and were found to produce similar results. The ACI 408-03 equation was chosen for the purposes of the current study since this was the same equation that used for the lap splice beams confined with FRP sheets which was developed by Hamad et al. (2004). Table 7.2 shows the difference between predicted bond strength from ACI 408 equation and the actual bond strength results of non-corroded bars embedded in beams-end specimens.

Table 7.2 Comparison of actual bond strength results of uncorroded beam-end specimens and predicted bond from ACI 408 equation

Specimen	Actual bond strength results (MPa)	Predicted bond strength from ACI (MPa)	Difference between prediction and actual results (%)
BE-M1-250-C	8.39	5.60	-33
BE-SCC1-250-C	7.22	6.04	-16
BE-M1-350-C	6.70	4.88	-27
BE-SCC1-350-C	6.06	5.26	-13
BE-M2-200-C	7.86	5.33	-32
BE-SCC2-200-C	6.99	5.58	-20
BE-SCC3-200-C	6.6	5.46	-17
BE-NC-200-C	5.88	5.20	-12
BE-M2-300-C	6.74	4.43	-34
BE-SCC2-300-C	6.29	4.65	-26
BE-SCC3-300-C	5.81	4.54	-22
BE-NC-300-C	5.13	4.32	-16

Based on Table 7.2, it can be noticed that the ACI 408 equation was conservative and under-estimated the bond strengths by up to 33% compared to the actual bond strength results of the beam-end specimens. That might be because the ACI 408 equation (Equation 7.3) was created based on data from development and lap splice beams. It has been shown that for the same bonded length and the same confinement, the beam-end specimens provided higher bond strength than the lap splice beams (El-Hacha et al. 2006). That was explained because of the deflection in the lap splice beams, which forced the spliced bars to apply additional outward pressure on the concrete cover causing a premature failure of the splice and resulting in reduced bond strength compared to the beams-end specimens. However, based on previous research was by Turk et al. (2009), this difference between the beam-end results and the ACI 408 equation is considered to be acceptable since concrete is a nonhomogeneous material and the bond behavior is complicated and is sensitive to the concrete properties.

It can be noticed that for the same bonded length, the monolithic beam-end specimens had a higher actual bond strength than all types of the partial depth repair concrete, regardless of the compressive strength of concrete. This is likely because of interface between the partial depth repair concrete and the substrate concrete, which led to increased cracking that, may have decreased the bond strength of the beam-end specimen repaired with partial depth repair concrete. However, this trend was not the same in the predicted bond strength where the bond stress depends mainly on the square root of the compressive strength of concrete for the same conditions of the bonded length and the bar diameter. Thus, the prediction equation showed that the beam-end specimens with higher compressive strength had higher bond strength because it does not take into account the effect of the internal shear cracks in case of the partial depth repair.

7.2.4 Effect of Partial Depth Repair on Bond Performance

The average bond strength at failure decreased with increasing bonded length for both the monolithic beams-end specimens and the specimens repaired with a partial depth repair, which was expected from the literature review. Figure 7.2 shows the relationship between the normalized average bond strength and the bonded length for different mass loss levels. The average bond strength results were normalized by $f'_c{}^{1/2}$ to indirectly take into account the effect of the concrete tensile strength on the bond failure stress. For all bonded lengths and mass loss levels (up to 15%), the monolithic beam-end specimens had a higher normalized average bond strength than any of the beam-end specimens repaired with a partial depth repair. However, the difference in strength between the monolithic beam-end specimens and the specimens repaired with a partial depth repair decreased as the bonded length increased (Figure 7.2). It is expected that at a certain bonded length, the partial depth repair could have a similar or even higher bond strength than the monolithic specimens if an appropriate partial depth repair concrete is used (see Section 4.6.1). That may be because with increasing the bonded length, the area to be repaired will increase resulting in increasing the bond between the repair concrete and the substrate concrete, thus increasing the shear resistance between the two layers of concretes. However, supplementary research is needed for more beam-end specimens with larger bonded length to support this expectation.

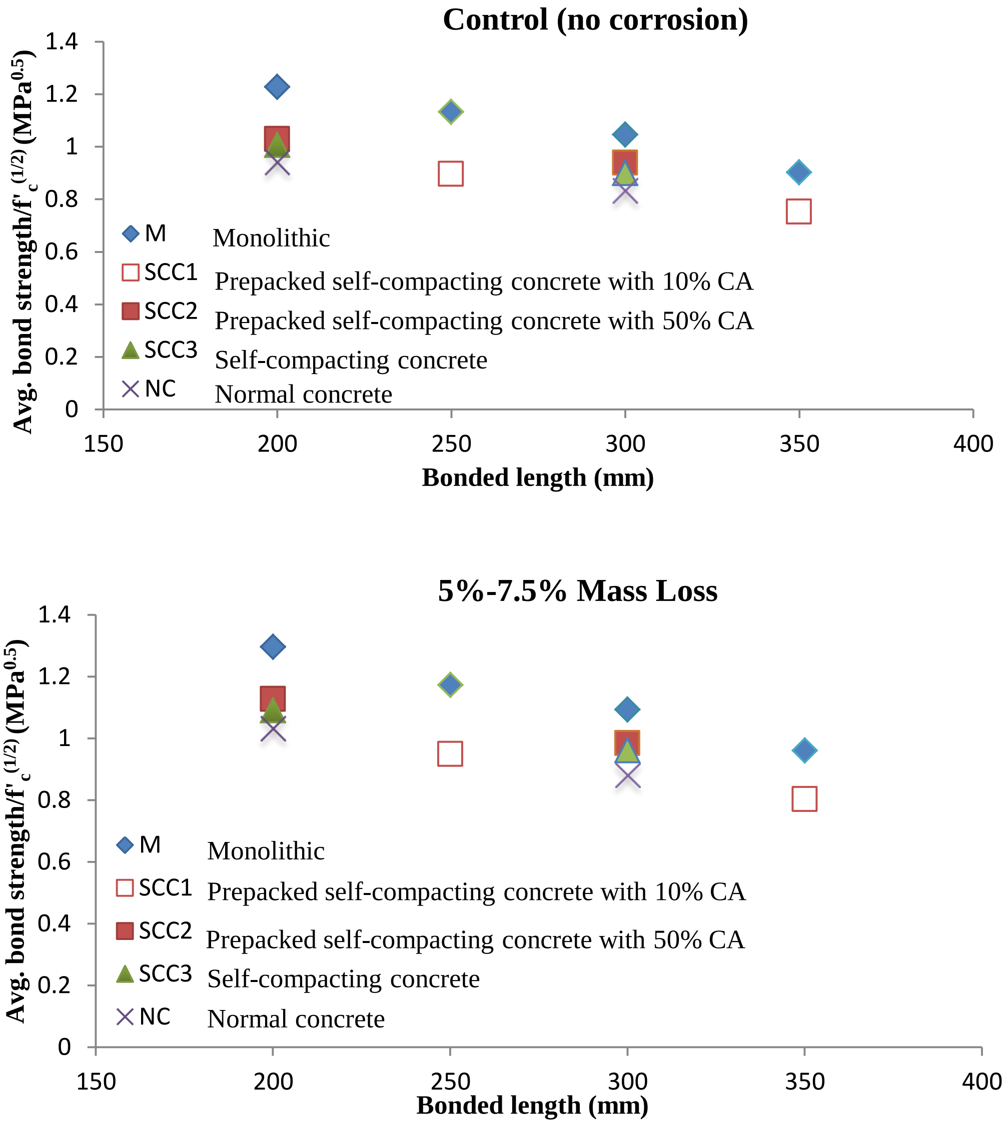

Figure 7.2 Normalized average bond strength at bonded lengths 200, 250, 300 and 350 mm

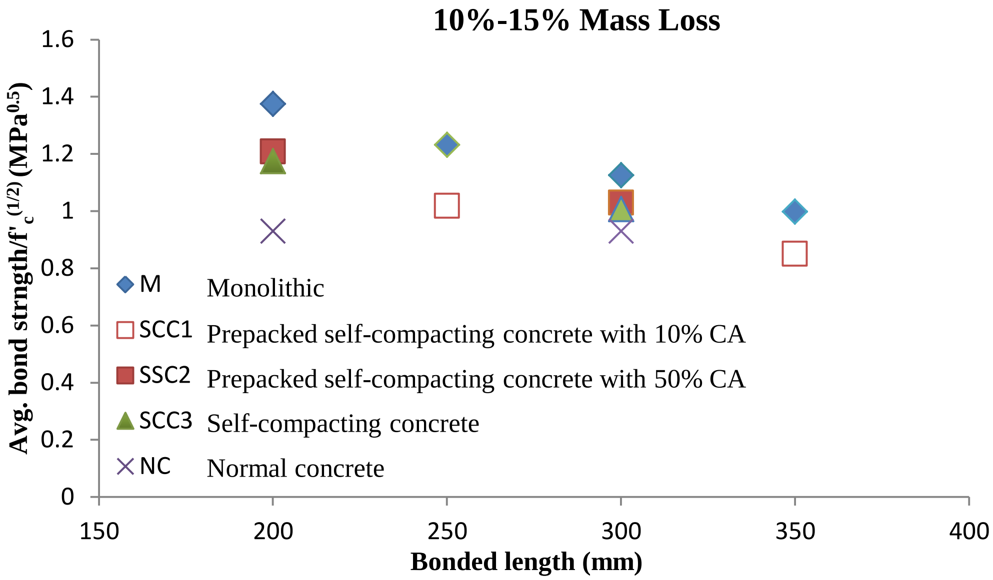

Figure 7.2 Normalized average bond strength at bonded lengths 200, 250, 300 and 350 mm (continued)

7.2.5 Effect of the Partial Depth Repair on the Average Bond Strength versus Slip at Failure for Different Mass Loss Levels

Figure 7.3 (a) and Figure 7.3 (b) show the typical normalized average bond strength versus bar slip at failure for Phase 1 (control, 5% and 10% mass loss) and Phase 2 (control, 7.5% and 15% mass loss), respectively. The monolithic beam-end specimens had higher normalized average bond strengths and greater slip values at failure than the beam-end specimens that were repaired with a partial depth repair SCC1 and SCC2, even though the compressive strength of the concrete used in the repair (SCC1 and SCC2) was higher than that of the monolithic concrete. Also the beam-end specimens repaired with partial depth repair concrete (SCC3 and NC) with a lower compressive than the monolithic specimens had a lower average bond strength than the monolithic beam-end specimens but higher but slip values. The reduced slip at failure for the repaired beams with SCC1 and SCC2 may be due an increased adhesion between the materials in the repair concrete such as silica fume and their bonding agent and the reinforcing bars. Also, including silica fume and bonding agent in the partial depth repair SCC1 and SCC2 may enhance the bond between the substrate concrete and the repair concrete (see Section 4.7.5).

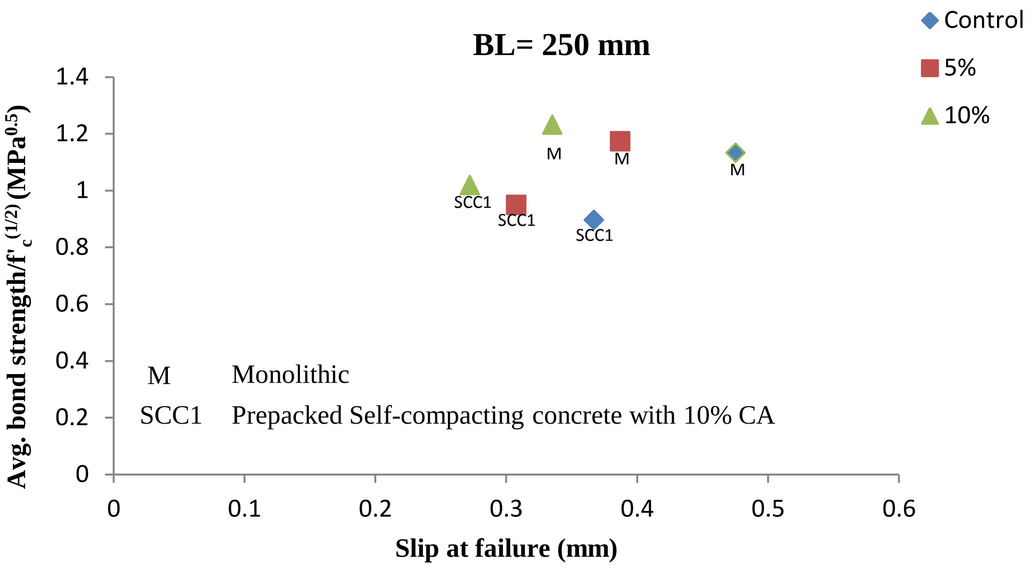

(a) Beam-end slip at failure results from Phase 1 specimens (control, 5% and 10% mass loss)

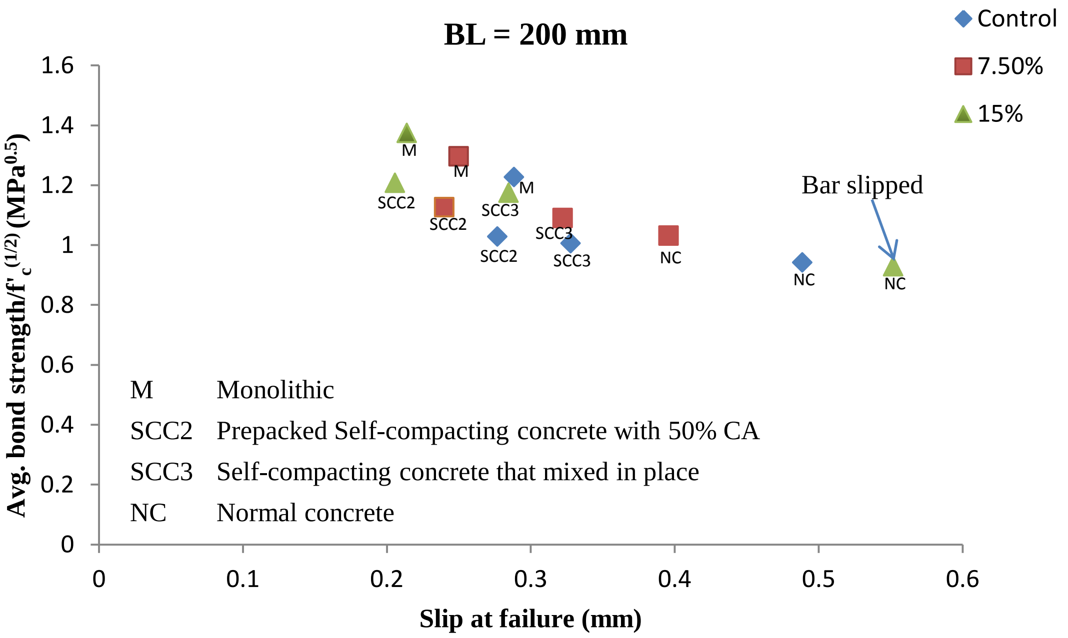

(b) Beam-end slip at failure results for Phase 2 specimens (control, 7.5% and 15% mass loss)

Figure 7.3 Typical normalized average bond strength versus bar slip at failure

7.2.6 Average Bond Strength Prediction Based on the Mass Loss Level

The previous average bond strength results and predictions presented in Section 7.2.3 and Table 7.2 were for uncorroded specimens. In order to calculate the average bond strength for the corroded specimens, the bar diameter was calculated from the reduced bar area after the mass loss assuming a uniform reduction in equal to the mass loss as follows:

$$A_{(M_l)} = A_{org} - A_{org}\,\frac{M_l}{100} \qquad \text{Equation (7.4)}$$

Where:

$A_{(Ml)}$: Area of the reinforcing bar at (M_l) mass loss (mm^2)

A_{org}: Original area of the bar before corrosion (mm^2)

M_l: Mass loss level (%)

Therefore, the reduced diameter of the corroded bar can be approximated as:

$$A_{(M_l)} = \frac{\pi d_{b(M_l)}^2}{4} \;\rightarrow\; d_{b(x)} = \sqrt{\frac{4 * A_{(M_l)}}{\pi}} \qquad \text{Equation (7.5)}$$

Where:

$d_{b(Ml)}$: Bar diameter at (M_l) mass loss level (mm)

It was found from the results of the beam-end specimens that the average bond strength of the cleaned corroded rebar increased with increasing the mass loss level as long as the beam-end specimens failed by a splitting bond failure. Two reasons for this may be suggested. Firstly, it is known that as the bar size decreases, the bond force at failure decreases more slowly than the reduction in bar cross-sectional area (ACI 408, 2003). Thus, as the mass loss increases, the bond strength will increase since there was only a slight difference in the bar force at failure.

Secondly, as the mass loss increases, the surface of the reinforcing bar becomes rougher which improves both the mechanical interlock and the friction between the reinforcing bar and the surrounding concrete. This behaviour was a similar to that observed by Desnerck et al. (2010) who studied the effect of the variation in bar diameter on average bond strength and concluded that the average bond strength increased with decreasing the bar diameter. They explained that for a smaller bar diameter, the relative size of the bar ribs increases and the spacing between ribs decreases increasing the mechanical interlock between the concrete and the reinforcement bar, and thus enhancing the bond. However, they did not give an equation to predict the change in average bond strength of cleaned corroded rebar with increasing the mass loss level.

The normalized average bond strength is plotted as a function of mass loss for each bonded length and repair type in Figure 7.4. These results show an approximately linear increase in bond strength as a function of mass loss level. For each bonded length, the normalized average bond strength versus mass loss level showed an excellent linear correlation with R^2 values ranging from 1 to 0.98.

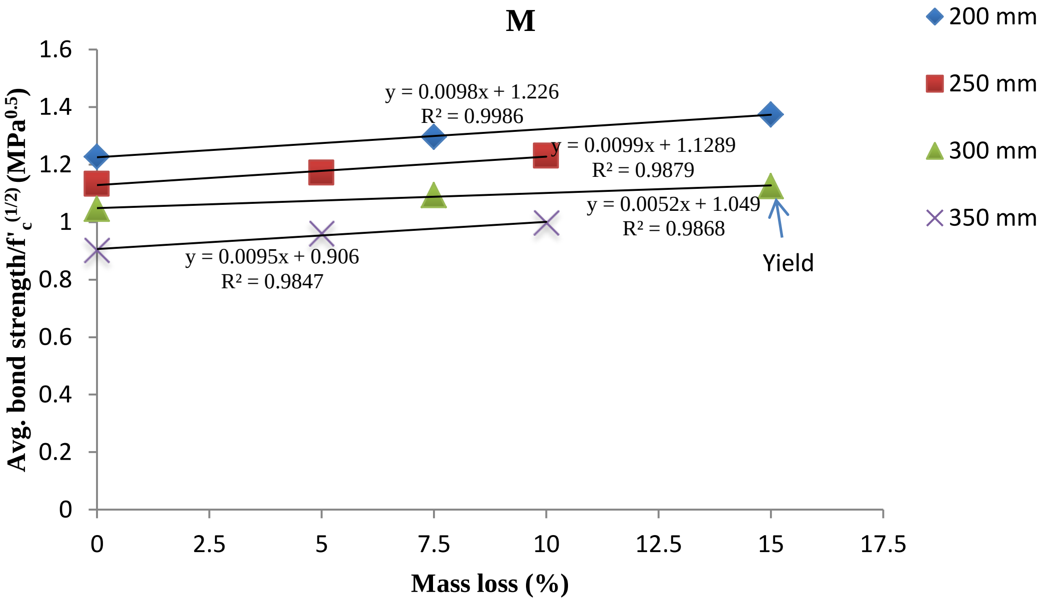

Figure 7.4 Normalized Average bond strength as the mass loss increased

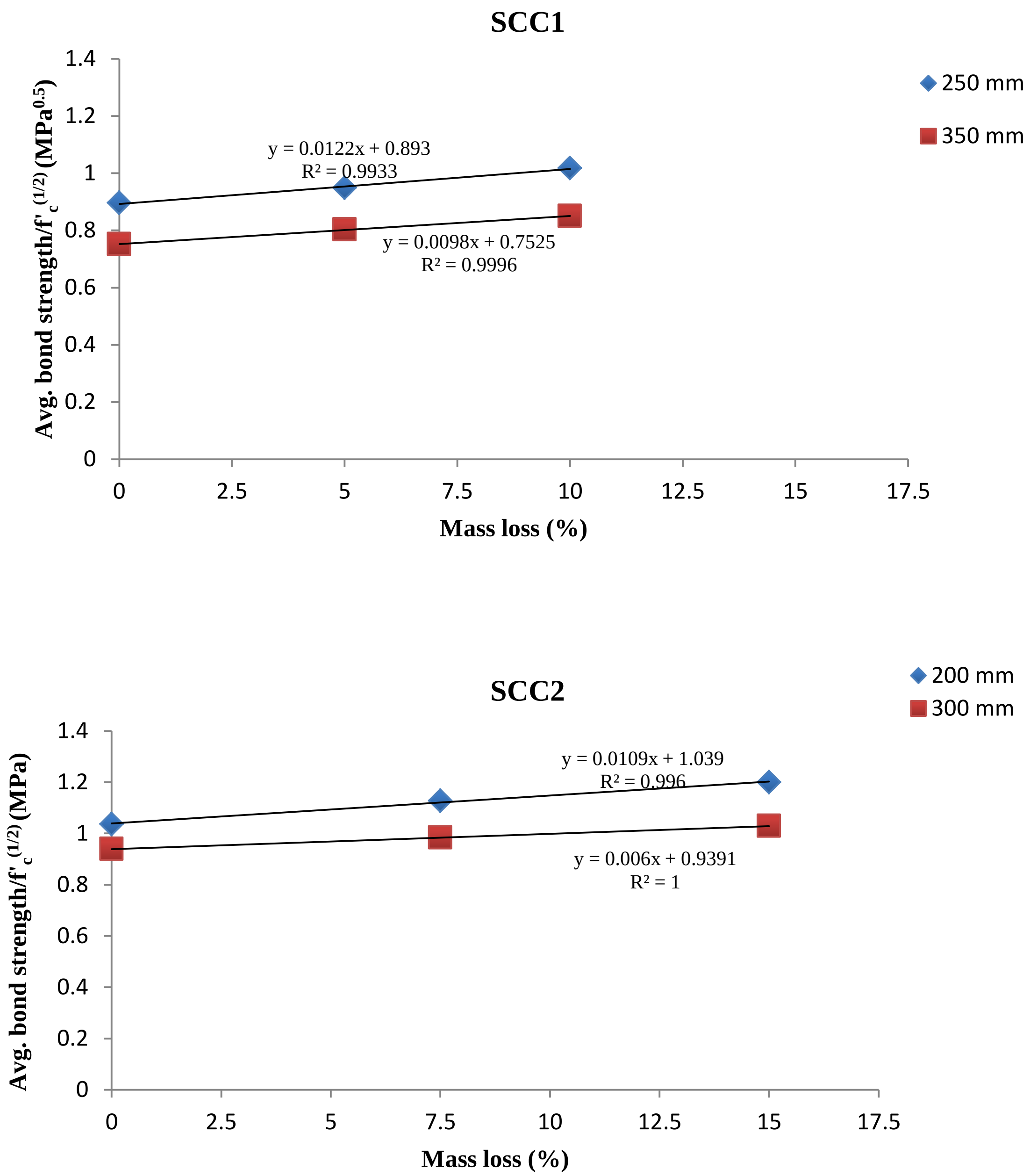

Figure 7.4 Normalized Average bond strength as the mass loss increased (continued)

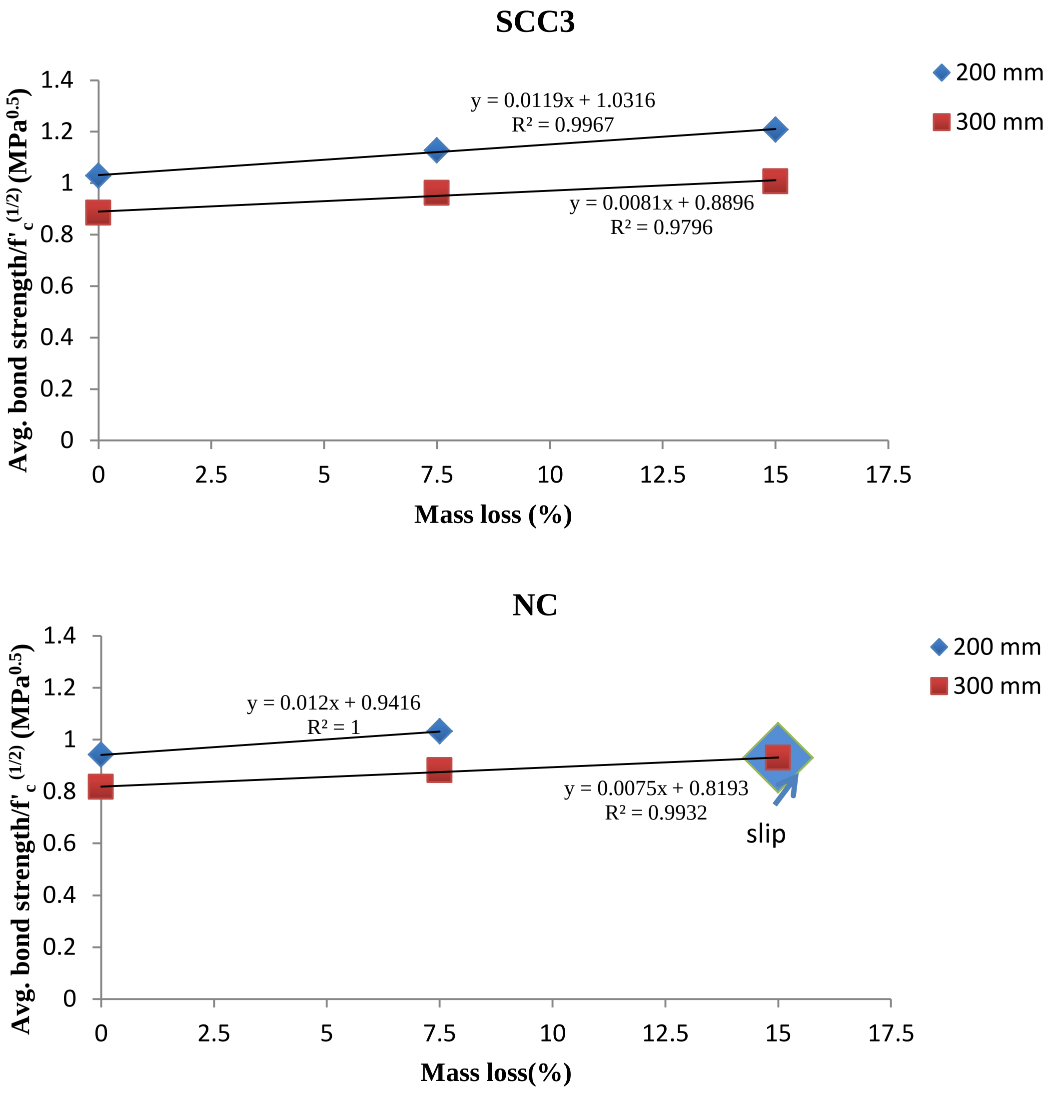

Figure 7.4 Normalized Average bond strength as the mass loss increased (continued)

The slopes of the linear relationships between mass loss level and average bond strength, termed β in this analysis, are summarized in Table 7.3 for all concrete types and bonded lengths. Note that the results for the NC partial depth repaired beam with a 15% mass loss and 200 mm bonded length was excluded because the bar so severely corroded that the bar ribs were eliminated together with the mechanical interlock. Although the variation of the slope of the normalized average bond strength versus mass loss level was small with standard deviation of only 0.002, the coefficient of variation was fairly high which might be because of the varying of bonded length (Table 7.3).

Table 7.3 Variation of the slope of bond strength of beam-end specimens as a function of mass loss

Specimens	Bonded length (mm)	R^2	Slope of linear relationship between bond strength and mass loss (β)	Average of β values	Standard deviation β values	C.O.V (%)
M	200	0.99	0.0098	0.0094	0.002	21.2
	250	0.98	0.0099			
	300	0.98	0.0052			
	350	0.98	0.0095			
SCC1	250	0.99	0.0122			
	350	0.99	0.0098			
SCC2	200	0.99	0.011			
	300	1	0.006			
SCC3	200	0.99	0.0119			
	300	0.98	0.0081			
NC	200	1	0.0120			
	300	1	0.0075			

From Table 7.3, it can be seen that β had different values for the same concrete type as the bonded length changed which indicated that there might be inter-related effect of mass loss and the changing the bonded length. Also, for the same bonded length, the β values were varying with the presence the partial depth repair concrete compared with monolithic specimens. This might be an indication that there was an inter-related effect of the mass loss and the presence of the repair concrete.

All of the experimental normalized average bond strength results were plotted and compared with the predicted results (Equation 7.3 proposed by ACI 408) for different bonded lengths (200 mm, 250 mm, 300 mm and 350 mm) as shown in Figure 7.5. Note that the effect of mass loss was accounted for in Equation 7.3 by adjusting the bar diameter using Equation 7.5.

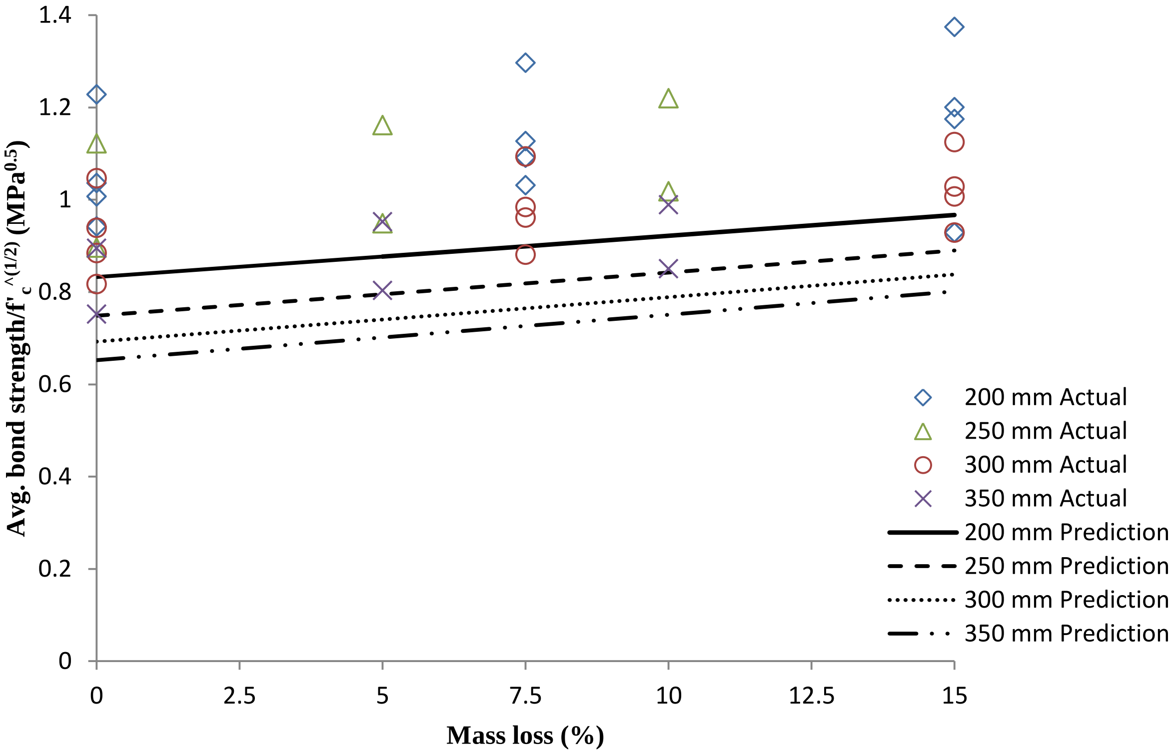

Figure 7.5 Comparison between the experimental normalized average bond strength and bond strength predicted by ACI 408 equation

From Figure 7.5, it can be noticed that the results of the normalized average bond strength predicted by ACI 408 were not consistent with the experimental normalized average bond strength results. Generally, the ACI 408 equation under-estimated the normalized average bond strength. That could be because the ACI 408 equation was developed based on lap splice beams rather than beam-end specimens (see Section 7.2.3). As well, there could be inter-related effects of mass loss and the other factors that affect bond strength (such as bonded length and presence of partial depth repair). Based on these observations, a statistical analysis was done to determine whether there was a significant effect of changing bonded length on the normalized average bond strength as the mass loss increased. Following the statistical analysis, a linear regression model was developed to predict the normalized average bond strength of clean corroded rebar embedded in beam-end concrete member.

7.2.7 Statistical Significance of Bonded Length and Mass Loss on Bond Strength

A statistical analysis was conducted to determine whether changes in bonded length had a statically significant effect on bond strength as the mass loss increased. Analysis of variance (ANOVA) was used to calculate F_{stat} based on the results shown in Table 7.3, and was compared it with F_{crit} at significant level of 5%. The following assumptions were carried out:

- Null hypothesis: There is no interaction between the mass loss and bonded length affecting on the bond strength.
- Alternative hypothesis: There is a significant effect of changing the bonded length as the mass loss increased on the bond strength
- Level of significance: 5% ($\alpha = 0.05$)
- F_{crit}: The critical value of F at the lowest level of significant (i.e., $\alpha = 0.05$) for specific degree of freedom
- Criterion: If $F_{stat} > F_{crit}$, then reject the null hypothesis where the alternative hypothesis is correct

The statistical parameters that calculated for the ANOVA to examine if varying the bonded length and mass loss level had a significant interactive effect on the normalized average bond strength are summarized in Table 7.4

Table 7.4 Summary of parameters values calculated by ANOVA

Source of Variation	*SS*	*df*	*MS*	*F-stat*	*p-value*	*F-crit*
Between Groups	0.00005	3	0.00002	11.31237	0.003	4.06618
Within Groups	0.00001	8	1.39469E-6			
Total	0.00006	11				

Based on the ANOVA presented in Table 7.4, the value of F_{stat} was greater than F_{crit}, which indicated that the null hypothesis was rejected and that changes in the bonded length have a significant interaction with mass loss on the normalized average bond strength. Sample of calculations for the statistical parameters for ANOVA are presented in Appendix B. Given the inter-related effect of bonded length and mass loss on bond strength, it is not possible to add a simple modification to the ACI 408 equation (Equation 7.3) to account for mass loss. Instead, a multiple regression analysis was performed.

7.2.8 Predictive Experimental Bond Equation for Cleaned Corroded Bar Repaired with Partial Depth Repair

Based on the limited data set (36 beam-end specimens) with three different variables (mass loss level, bonded length and the partial depth repair), it was not practical to develop a design equation to predict the average bond strength of cleaned corroded bar embedded in concrete member. Instead, a model was developed using regression analysis to illustrate the effect of each variable on the bond strength of cleaned corroded rebar.

Based on the results in Table 7.3 and the discussion in Section 7.2.7, a multiple linear regression analysis was conducted to predict the effect of the independent variables of mass loss level, bonded length and the repair condition (Monolithic or partial depth repair) on the normalized average bond strength. The beta coefficients (β_i) of the regression line were used to evaluate influence of each independent variable on the dependent variable (normalized average bond strength). The multiple linear regression analysis was conducted at a confidence level of 95%. Based on the experimental data, a linear regression model was developed and the main model statistics and parameter estimates are summarized in Table 7.5. The parameters X_1, X_2 and X_3 represent the variables of bonded length (L_b), mass loss level (M_l) and partial depth repair concrete (P), respectively. The variable X_3 was set to be 0 for the monolithic beam-end specimens and 1 for the beam-end specimens repaired with partial depth repair concrete.

Table 7.5 Summary of developed regression model and the associated parameters

Regression statistics

Y	**X_1**	**X_2**	**X_3**	**Adjusted R^{2*}**	**F-stat**	**P-value**
$\frac{\tau_{avg}}{\sqrt{f'c}}$	L_b	M_l	P	0.925	140.7	0

Parameter Estimates and Statistics

	X_1			**X_2**			**X_3**		
Intercept**	**β$_1$**	**t-stat**	**P-value**	**β$_2$**	**t-stat**	**P-value**	**β$_3$**	**t-stat**	**P-value**
1.55895	-0.00179	-14.78	0.0000	0.00976	8.17	3.157E-9	-0.17766	-12.68	0.0000

*Modification of the normal coefficient of determination that provides adjustment for the degrees of freedom
**The intercept value was found to be statistically significant

From Table 7.5, it can be noticed that the p-value of all variables are less than the significant level of 0.05, which provided strong evidence that all three variables were considered as significant parameters in the regression model. The linear regression model can be represented by the following equation:

$$\frac{\tau_{avg\ (M_l)}}{\sqrt{f'c}} = 1.55895 - 0.00179L_b + 0.00976M_l - 0.17766P \qquad \text{Equation (7.6)}$$

Where:

$\tau_{avg\ (M_l)}$: Average bond strength at (M_l) mass loss level (MPa)

f'_c: Concrete compressive strength (MPa)

M_l: Mass loss level (%)

L_b: Bonded length (mm)

P : Factor refer to the situation of partial depth repair, where

P = 1 for the beam-end specimen repaired with partial depth repair concrete, and

P = 0 for the monolithic beam-end specimen

β_1: Beta coefficients of bonded length $\left(\frac{MPa^{0.5}}{mm}\right)$

β_2: Beta coefficients of mass loss level $\left(\frac{MPa^{0.5}}{\%}\right)$

β_3: Beta coefficients of presence of repair concrete ($MPa^{0.5}$)

The normalized average bond strength experimental results was plotted versus the predicted normalized average bond strength results to assess the accuracy of the regression model to predicts the experimental normalized average bond strength (Figure 7.6). The ratio of the experimental to the prediction results were computed, then the average, the standard deviation and the coefficient of variation correlated with all results of test to prediction ratio were also calculated (Table 7.6).

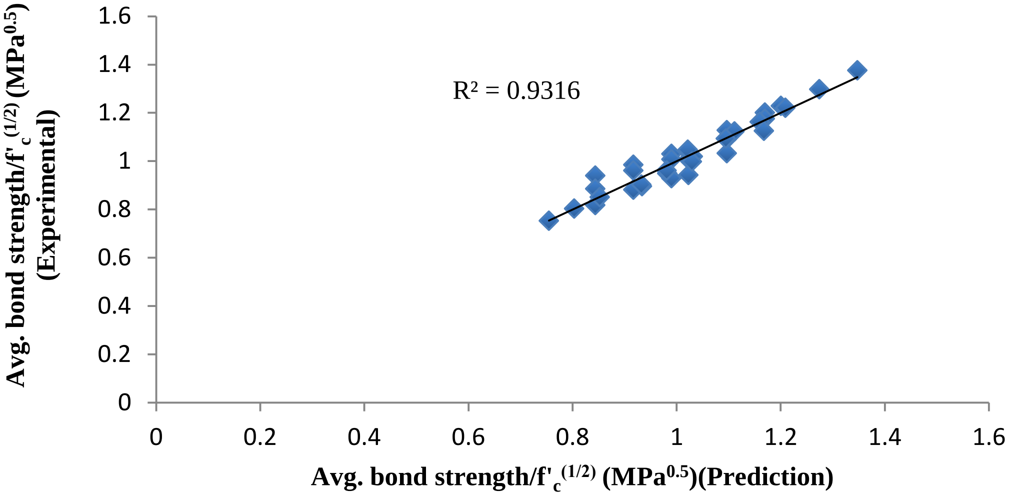

Figure 7.6 Experimental normalized average bond strength versus predicted normalized average bond strength based on regression model

Table 7.6 Parameters computed from experimental-predicted ratio

	R^2	**S.D**	**Average**	**C.O.V**
$\dfrac{\dfrac{\tau_{avg\,(M_l)}}{\sqrt{f'c}}\ (experimental)}{\dfrac{\tau_{avg\,(M_l)}}{\sqrt{f'c}}\ (predicted)}$	0.93	0.038	0.999	0.038

From Figure (7.6) and Table (7.6), it can be seen that the low values of standard deviation and coefficient of variation with 0.038 and with relatively high R^2 of 0.93 is an indication of a good consistency between the experimental and prediction results. Based on that, the regression model provided and accurate prediction of the normalized average bond strength. It should be mentioned that the regression model that represented in Equation 7.6 was not a modification to the ACI 408 equation (Equation 7.3) to predict the average bond strength accounting for mass loss. However, it gives an indication of the effect of mass loss, bonded length and the presence of the partial depth repair on the normalized average bond strength.

7.3 Lap Splice Beams

7.3.1 Comparing Bond Strength Test Results to Predicted Bond Strength

The bond strength of the spliced bars in the concrete beams in the current study was divided into three categories: bond strength of the unconfined beams, bond strength of the beams confined with internal transverse reinforcement and the bond strength of the beams confined with FRP sheets. The bond strength of the unconfined beams was represented by only the contribution of concrete in the bond behaviour. However, the bond strength of the beams confined by transverse reinforcement or by FRP sheets was represented by the contributions of the concrete and the type of the confinement. In general, the average bond strength of the tested lap splice beams was calculated through Equation 7.2. The average bond strength at zero mass loss can be predicted from bond equation of ACI 408-03 including the effects of confinement as follows:

$$\tau_{avg(M_o)} = u = \left[0.10 + \frac{C}{4d_b} + \frac{4.2d_b}{l_d} + K\right]\sqrt{f'_c} \qquad \text{Equation (7.7)}$$

Where:

$\tau_{avg(M_o)}$: Predicted average bond strength at failure at zero mass loss (MPa)

c: Concrete cover (mm)

d_b: Bar diameter (mm)

l_d: Bonded length (mm)

f'_c: Concrete compressive strength (MPa)

K: Confinement coefficient (MPa$^{0.5}$)

Where

K = 0 For unconfined beam

$$K = K_{tr,s} = \frac{A_{tr}\, f_{yt}}{41.5 s n d_b} \qquad \text{Equation (7.8)}$$

For the beam confined with transverse internal reinforcement (ACI 408-03)

Where:

A_{tr}: Area of transverse reinforcement (mm^2)

f_{yt}: Yield strength of transverse reinforcement (MPa)

s: Spacing of transverse reinforcement (mm)

n: Number of developed bars

$\frac{1}{41.5}$: Constant coefficient ($MPa^{-0.5}$)

$$K = K_{tr,frp} = \frac{C_1 A_{tr,f}\, f_{fe}}{d_b n_b s_f} \leq 0.25 \qquad \text{Equation (7.9)}$$

For the beam confined with FRP sheets as proposed by Hamad et al. (2004)

Where:

C_1 = proportionality constant = $\frac{1}{16.6}$ ($MPa^{-0.5}$)

$A_{tr,f}$: Area of FRP sheets (mm^2)

f_{fe}: Effective stress in the FRP laminate (MPa)

n_b: Number of spliced bars

s_f: Width of FRP sheets along length of beam (mm)

The Effective stress in the FRP laminate can be calculated by following equation:

$$f_{fe} = R\, f_{fu} \qquad \text{Equation (7.10)}$$

Where:

f_{fu}: Ultimate strength of FRP sheets (MPa)

R is the stress reduction factor and can be calculated as follows:

$$R = \frac{k_1 k_2 l_e}{11{,}900\varepsilon_{fu}} \le \frac{0.004}{\varepsilon_{fu}} \qquad \text{Equation (7.11)}$$

Where

l_e: Effective bond strength length (mm)

k_1 and k_2: coefficients to account for concrete strength and sheet layout, respectively

ε_{fu}: Ultimate strain of FRP sheets

The effective bond strength length and the coefficients k_1 and k_2 can be calculated by Equation 7.9, Equation 7.10 and 7.11, respectively.

$$l_e = \frac{23{,}300}{(n t_f E_f)^{0.58}} \qquad \text{Equation (7.12)}$$

$$k_1 = \left(\frac{f'_c}{27}\right)^{\frac{2}{3}} \qquad \text{Equation (7.13)}$$

$$k_2 = \left(\frac{d_f - l_e}{d_f}\right) \qquad \text{Equation (7.14)}$$

Where

n: Number of FRP sheets

t_f: Thickness of FRP sheets (mm)

E_f: Modulus of elasticity of FRP sheets (MPa)

d_f: Depth of FRP sheets on side of the beam (mm)

A comparison of the actual bond strength results for the non-corroded lap splice beams and the predicted bond from the ACI 408 equation (Equation 7.7) is shown in Table 7.7.

Table 7.7 Comparison of the actual bond strength results of lap splice beams and predicted bond strength from ACI 408 equation

Specimen	Actual bond strength results (MPa)	Predicted bond strength from ACI (MPa)	Difference between prediction and actual results (%)
LS-M1-UN-C	4.42	4.47	1
LS-M2-T-C	4.90	4.91	0
LS-M1-F-C	5.91	6.09	3
LS-SCC50-UN-C	4.78	4.77	0
LS-SCC50-T-C	5.51	5.52	0
LS-SCC50-F-C	6.4	6.51	2
LS-M2-UN-C	4.22	4.25	1
LS-SCC0-UN-C	4.02	5.02	25

From Table 7.7, it can be seen clearly that the average bond strength results for the lap splice beams were closer to the prediction equation in ACI 408 than the beam-end specimens. The maximum difference between the actual and the predicted bond strength was 13% except for the lap splice specimen LS-SCC0-UN-C that reached to 25%. That was because the partial depth repair SCC0 had high compressive strength (53 MPa); however it had low splitting tensile strength because of the absence of coarse aggregate. The ACI 408 prediction equation indirectly considers f_t as a function of square root of f'_c; however it would be better to directly consider f_t which is sensitive to coarse aggregate type, size and amount.

7.3.2 Comparison between Experimental and Predicted Bond Strength as the Mass Loss Increased

The difference between the experimental and the predicted average bond strength as the mass loss increased is shown in Table 7.8. It can be seen that the difference between the experimental and the predicted average bond strength increased as the mass loss level increased. This may be because the prediction equation only accounted for changing the bar diameter as the mass loss increased without taking into account the effect of the friction and the mechanical bond from the corrosion pits which may have increased the bond strength. For 0% corrosion, the predicted average bond strength was very close to the measured values. However, with increasing the mass loss level, the predicted bond strength results became more conservative compared to the experimental results especially for 15% mass loss level.

Table 7. 8 Experimental and predicted average bond strength results as the mass loss increase

Specimen	Mass loss level (%)	Experimental bond strength (MPa)	Prediction bond strength (MPa)	Difference between prediction and actual results (%)
LS-M1-UN-C	0	4.42	4.47	-1.05
LS-M2-T-C		4.9	4.91	-0.18
LS-M1-F-C		5.91	6.09	-2.99
LS-SCC50-UN-C		4.78	4.77	0.11
LS-SCC50-T-C		5.51	5.52	-0.13
LS-SCC50-F-C		6.4	6.51	-1.67
LS-M2-UN-C		4.22	4.25	-0.67
LS-SCC0-UN-C		4.02	5.02	-24.81
LS-M1-UN-7.5	7.5	4.63	4.48	3.14
LS-M2-T-7.5		5.22	4.96	6.71
LS-M1-F-7.5		6.51	6.10	6.23
LS-SCC50-UN-7.5		5.13	4.79	6.55
LS-SCC50-T-7.5		5.93	5.58	5.94
LS-SCC50-F-7.5		6.97	6.53	6.37
LS-M2-UN-7.5		4.35	4.27	1.94
LS-SCC0-UN-7.5		4.16	5.04	-21.09
LS-M1-UN-15	15	4.91	4.51	8.24
LS-M2-T-15		5.65	5.01	11.30
LS-M1-F-15		7.16	6.13	14.45
LS-SCC50-UN-15		5.32	4.82	9.47
LS-SCC50-T-15		6.36	5.63	11.44
LS-SCC50-F-15		7.93	6.55	17.42
LS-M2-UN-15		4.58	4.29	6.43
LS-SCC0-UN-15		4.32	5.06	-17.15

Table 7.9 summarizes the increase in the average bond strength due to confinement as the mass loss increased for the experimental and the predicted results. Generally for all mass loss levels, the predicted bond strength showed an almost constant increase in bond strength due to confinement (stirrups or FRP sheets) compared to the unconfined beams. However, the experimental results showed that as the mass loss increased, the increase in bond strength due to confinement was more pronounced for the beams confined with FRP sheets.

Figure 7.7 clarifies the increase in bond strength due to stirrups and FRP sheets confinement as the mass loss increased. It can be seen that the beams confined by FRP sheets showed a more significant increase in bond stress as the mass loss increased than the beams confined with stirrups. The increased bond strength may be because the FRP sheets confined the entire spliced region, so it had a uniform confinement acting along the spliced bars that may have enhanced the friction and the mechanical bond from the corrosion pits. The enhancement in bond strength due to confinement also depends on the properties of the system (FRP sheets of stirrups). This can be illustrated from the predicted bond strength for confined beams using Equation 7.7 with K for FRP sheets and stirrups. The predicted values reported in Table 7.9 show that the beams repaired with FRP sheets is expected to improve the average bond strength relative to the unconfined beams more than double in comparison to the beams with stirrups (36% increase versus 16% increase).

Table 7. 9 Increasing in bond strength due to confinement for experimental and predicted results

		Experimental bond strength			**Predicted bond strength**		
		Mass loss level (%)			**Mass loss level (%)**		
Concrete	**Confinement**	0	7.5	15	0	7.5	15
SCC50	**Unconfined (MPa)**	4.78	5.13	5.32	4.77	4.79	4.82
	Stirrups (MPa)	5.51	5.93	6.36	5.52	5.57	5.63
	FRP sheets (MPa)	6.4	6.97	7.93	6.51	6.53	6.55
		Increase in bond strength due to confinement (%)			Increase in bond strength due to confinement (%)		
	Due to stirrups	15.3	15.6	19.6	15.6	16.4	16.9
	Due to FRP sheets	33.9	35.9	49.1	36.3	36.1	35.9
		Mass loss level (%)			Mass loss level (%)		
Concrete	**Confinement**	0	7.5	15	0	7.5	15
M1	**Unconfined (MPa)**	4.4	4.6	4.9	4.5	4.5	4.5
	FRP sheets (MPa)	5.9	6.5	7.2	6.1	6.1	6.1
		Increase in bond strength due to confinement (%)			Increase in bond strength due to confinement (%)		
	Due to FRP sheets	33.71	40.60	45.82	36.28	36.13	35.96
		Mass loss level (%)			Mass loss level (%)		
Concrete	**Confinement**	0	7.5	15	0	7.5	15
M2	**Unconfined (MPa)**	4.2	4.4	4.6	4.3	4.3	4.3
	Stirrups (MPa)	4.9	5.2	5.7	4.9	4.9	5.0
		Increase in bond strength due to confinement (%)			Increase in bond strength due to confinement (%)		
	Due to stirrups	16.1	20.3	23.4	15.6	16.4	16.9

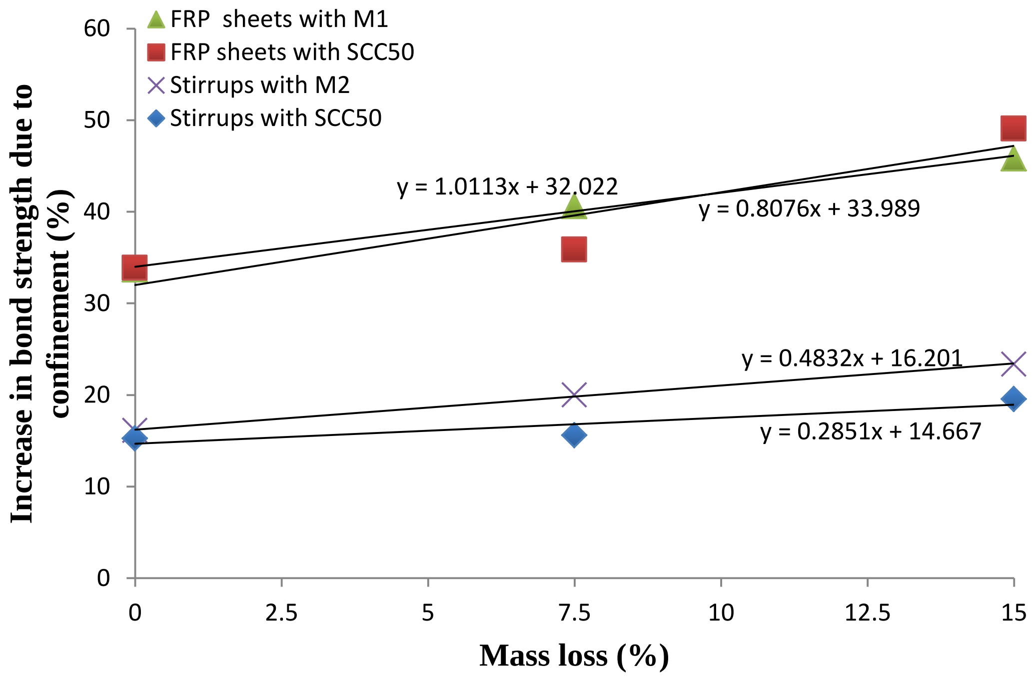

Figure 7. 7 Increase in bond strength due to confinement as the mass loss increased

7.3.3 Predicted Average Bond Strength as the Mass Loss Increased

From the results of the lap splice beams, it was found that the average bond strength of the cleaned corroded bars increased with increasing mass loss level. The rate of increase of the average bond strength as the mass loss level increased in the unconfined beams was lower than the rate of increase in the confined beams. The FRP sheets confinement had the largest effect on increasing the average bond strength as the mass loss increased. The current study has calibrated an average bond strength equation based on the mass loss level and based on the type of the confinement.

The calibrated equation for the beam-end specimens (Equation 7.6) could not be used for the unconfined lap splice beams because the beam-end specimens and the lap splice beams have a different bond mechanism (anchorage bond versus splice bond) and because of the effect of the deflection on the bond strength in the lap splice beams (see Section 7.2.3). Also, for the lap splice beams that were repaired with partial depth repair concrete, there was no shear effect at the interface between the substrate concrete and the repair concrete where it remarkably affected the bond in the beam-end specimens. The current study has calibrated the average bond strength of the lap splice beams as the mass loss level increased. Figure 7.8 shows the increase of the normalized average bond strength of the lap splice beams as a function of increasing mass loss level for all of the repair concrete types.

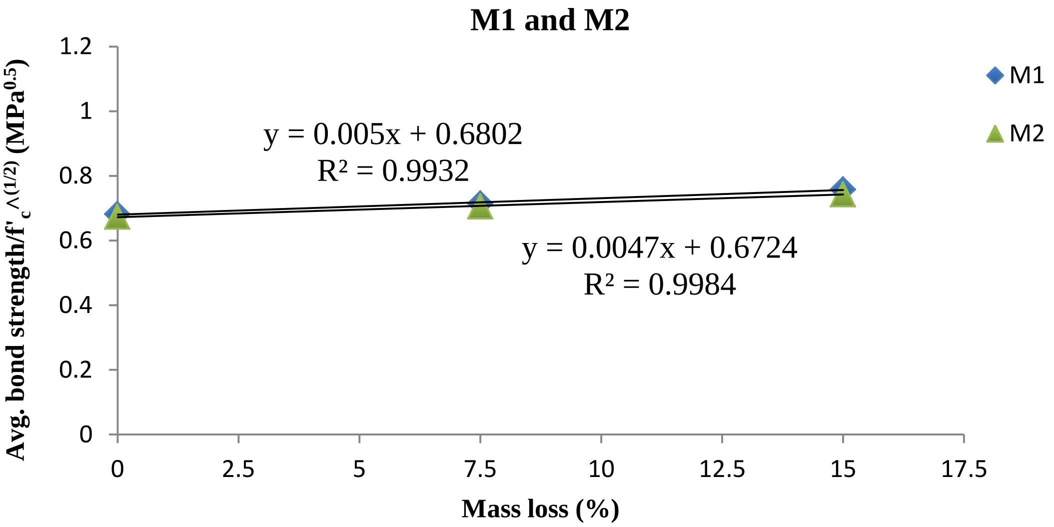

Figure 7.8 Normalized Average bond strength as the mass loss increased

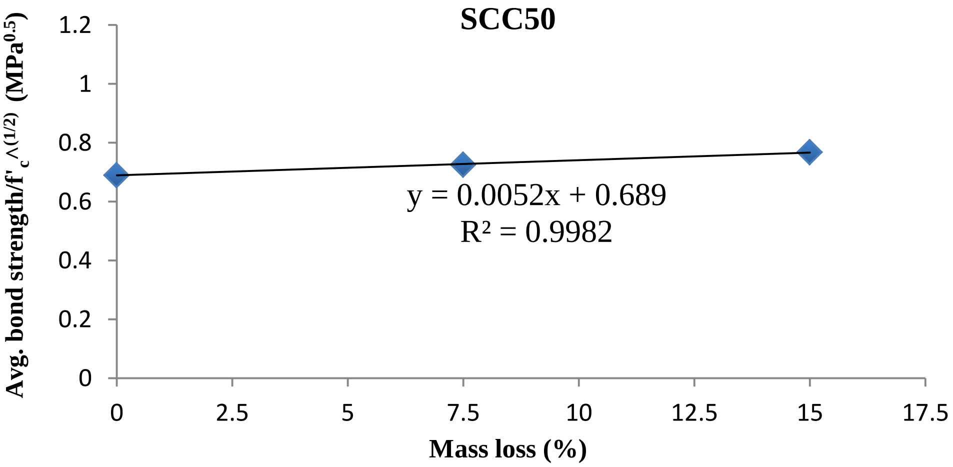

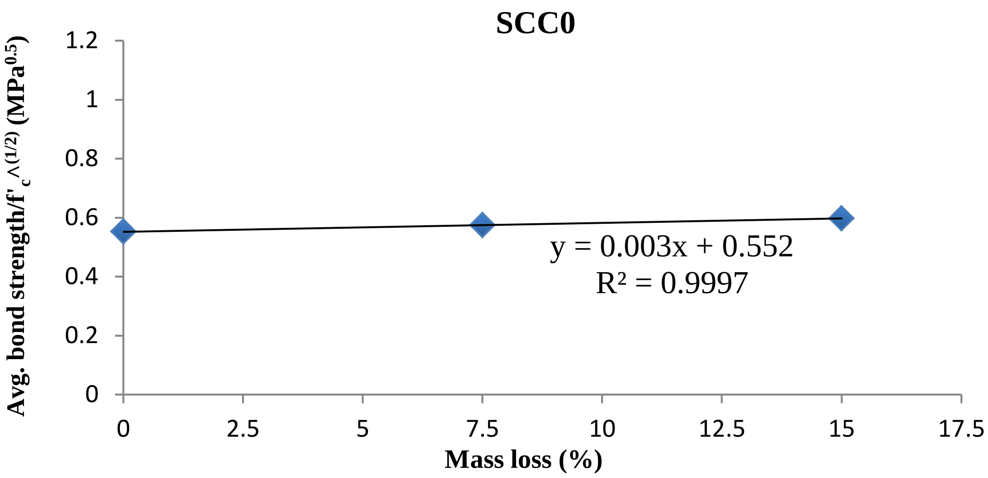

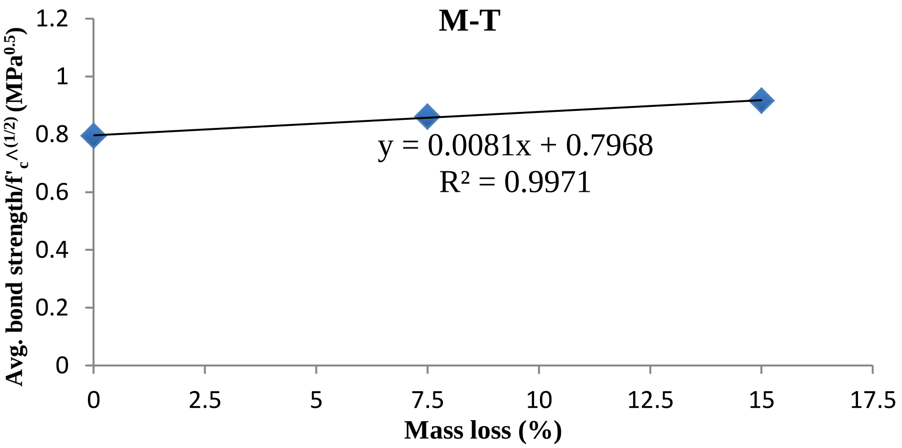

Figure 7.8 Normalized Average bond strength as a function of mass loss increased (continued)

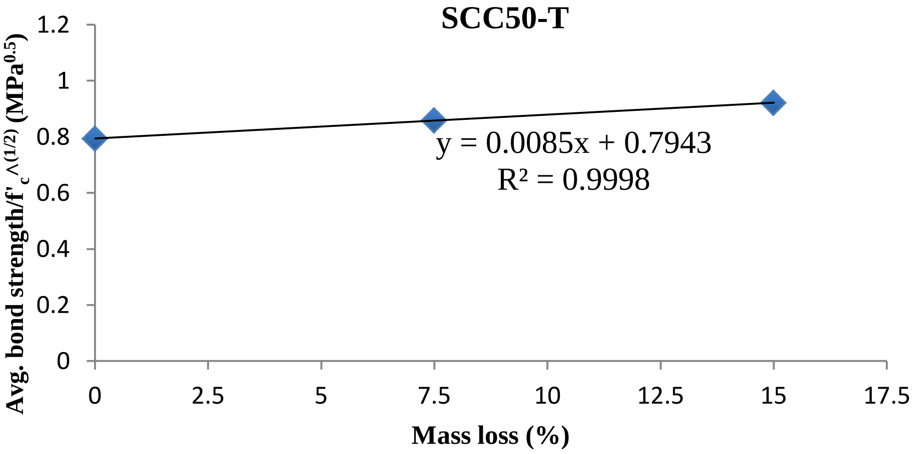

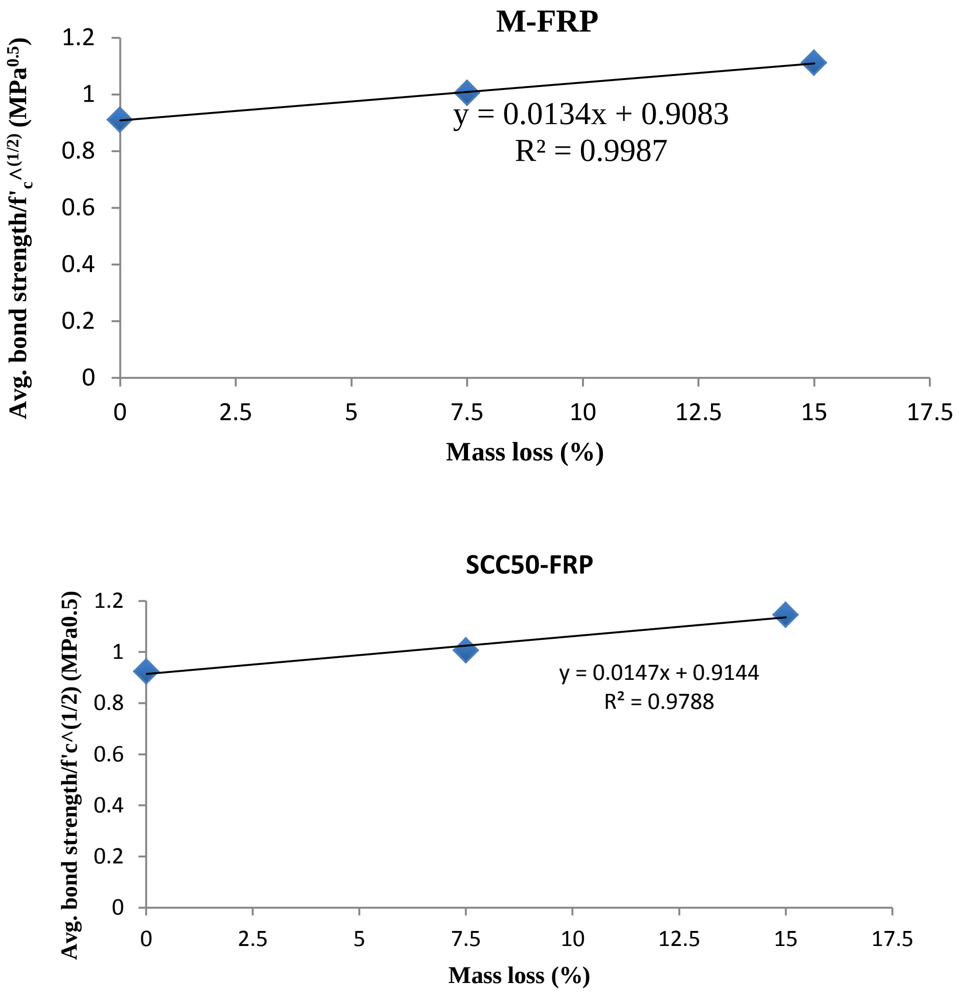

Figure 7.8 Normalized Average bond strength as a function of mass loss increased (continued)

For each type of concrete, the normalized average bond strength versus mass loss level showed an excellent linear correlation with minimum R^2 of 0.98. Table 7.10 shows the standard deviation, coefficient of variation and the average slopes of the normalized average bond strength versus mass loss level for the unconfined lap splice beams, the beams confined with transverse reinforcement (stirrups) and the beams confined with FRP sheets.

Table 7.10 Variation of the slope of increasing the bond strength as the mass loss increased

Specimens	R^2	Slope of linear relationship between bond strength and mass loss (β)	Average slope	Standard deviation of slopes	C.O.V (%)
M1	0.99	0.0050	0.0045	0.0010	22.2
M2	0.99	0.0047			
SCC50	0.99	0.0052			
SCC0	0.99	0.0030			
M-T	0.99	0.0081	0.0083	0.0002	2.4
SCC50-T	0.99	0.0085			
M-FRP	0.99	0.0134	0.0141	0.0009	6.3
SCC50-FRP	0.98	0.0147			

From Table 7.10, it can be seen that the lap splice beams confined with stirrups or FRP sheets had a low standard deviation and coefficient of variation between the monolithic beams and the beams repaired with partial depth repair concrete. However, the unconfined lap splice beams had a fairly high coefficient of variation of 22.2%. That was only because of the partial depth repair without coarse aggregate SCC0 that showed a lower value of β comparing to the other types of concrete. Further research should be done to study the effect of coarse aggregate size and content of the bond strength of concrete as the mass loss increasing.

The calibrated equations depended on the best-fit line of the bond strength versus mass loss plot for each confinement situation. The slope of each best-fit line was set equal to the average line slopes of each type of confinement separately. The calibrated normalized average bond strength equations of the unconfined lap splice beams, the beams confined with transverse reinforcement (stirrups) and the beams confined with FRP sheets are given by Equation 7.12, Equation 7.13 and Equation 7.14, respectively.

$$\frac{\tau_{avg\,(M_l)}}{\sqrt{f'c}} = 0.0045M_l + \left(\frac{\tau_{avg(M_0)}}{\sqrt{f'c}}\right) \qquad \text{Equation (7.12)}$$

Thus

$$\tau_{avg\,(M_l)} = \left[0.10 + \frac{C}{4d_b} + \frac{4.2d_b}{l_d} + 0.0045M_l\right]\sqrt{f'_c}$$

$$\frac{\tau_{avg\,(M_l)}}{\sqrt{f'c}} = 0.0083M_l + \left(\frac{\tau_{avg(M_0)}}{\sqrt{f'c}}\right) \qquad \text{Equation (7.13)}$$

Thus

$$\tau_{avg\,(M_l)} = \left[0.10 + \frac{C}{4d_b} + \frac{4.2d_b}{l_d} + K_{tr,s} + 0.0083M_l\right]\sqrt{f'_c}$$

$$\frac{\tau_{avg\,(M_l)}}{\sqrt{f'c}} = 0.0141M_l + \left(\frac{\tau_{avg(M_0)}}{\sqrt{f'c}}\right) \qquad \text{Equation (7.14)}$$

Thus

$$\tau_{avg\,(M_l)} = \left[0.10 + \frac{C}{4d_b} + \frac{4.2d_b}{l_d} + K_{tr,frp} + 0.0141M_l\right]\sqrt{f'_c}$$

Where:

$\tau_{avg\,(M_l)}$: Average bond strength at (M_l) mass loss level (MPa)

f'_c: Concrete compressive strength (MPa)

M_l: Mass loss level (%)

$K_{tr,s}$ and $k_{tr,f}$ are calculated from Equation 7.8 and Equation 8.9, respectively

$\tau_{avg(M_0)}$: Average bond strength at zero mass loss level (control) (MPa)

The experimental normalized average bond strength results for the lap splice beams were compared with the predicted results using the ACI 408 equation (Equation 7.7) and modified to account for the effect of mass loss depending on the confinement type (Equation 7.12, 7.13 and 7.14) as shown in Figure 7.9.

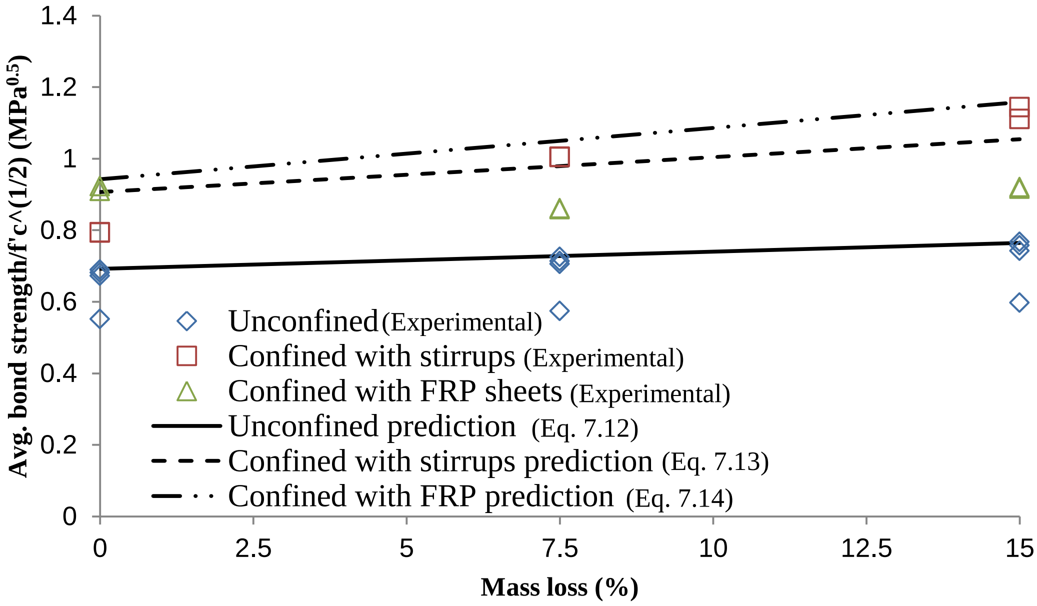

Figure 7.9 Comparison between the experimental normalized average bond strength and predicted by ACI 408 equation

Based on Figure 7.9, it can be noticed that the predicted results using the modified ACI 408 equation (Equation 7.7) are fairly close to the experimental normalized average bond strength results. This indicated that the experimental and the predicted results of the normalized average bond strength were consistency. It should be mentioned that based on limited data of specimens (24 lap splice beams), the developed equations (Equation 7.12, Equation 7.13 and Equation 7.14) are valid only for a bonded length of 300 mm. More research is needed for different bonded lengths to determine whether there in an effect of changing the bonded length on the normalized average bond strength as the mass loss increased in lap splice beams.

Chapter 8: Bond Stress Distribution in Lap Splice Beams

8.1 Mode of Failure in Lap Splice Beams

As described previously in Section 6.2, a splitting bond failure was the main mode of failure for all of the unconfined beams, as well as the beams confined with internal transverse reinforcement or FRP sheet. A horizontal splitting crack initiated on the bottom face of the beam at the beginning of the splice region from both sides causing partial debonding of the reinforcing bar from the surrounding concrete. As the load increased, the splitting cracks in the unconfined beams progressively moved towards each other until a bond-splitting failure occurred with an uncracked length of approximately 80 mm between the crack tips. The crack widths of the unconfined beams were greater than those of the confined beams. For the confined beams, the horizontal splitting cracks extended to intersect each other before failure occurred. The fully cracked beam continued to resist further increases in load before final failure, demonstrating greater ductility than that shown by the unconfined beam.

8.2 Splitting Crack Propagation Behavior

From the initiation of loading up to a load of about 80kN, only flexural cracks appeared at the ends of the of the lap splice region and within the constant moment region for all confined and unconfined beams; no horizontal splitting cracks were observed up to that load. As the load increased, a horizontal splitting crack occurred at both lap splice ends on the bottom face of the beam. For the unconfined beams, splitting cracks parallel to the spliced bars initially formed to a 25 mm crack length. The beams with internal transverse reinforcement or external fiber strengthening, the confinement from the transverse reinforcement delayed the occurrence of a splitting crack until a load of about 105kN. For both the unconfined and confined beams, the splitting cracks stabilized after their initiation until the load increased such that further cracking was initiated; then the splitting crack steadily increased in length with increasing load as shown in Figure 8.1. As the load increased further, the horizontal splitting cracks in the unconfined beams propagated at both ends of the lap splice until failure. The last measured splitting crack length for the unconfined beams before failure was 110 mm at which point the beam failed suddenly (Figure 8.1). However, for the lap splice beams confined with transverse reinforcement, the splitting crack length progressed over the full length of the spliced region before the failure of the beam (Figure 8.1). The splitting crack initiation and propagation increased almost linearly with increasing load (Figure 8.1). For the beams confined with FRP sheet, the crack pattern was covered by the sheet and thus was not visible. It is assumed that the propagation of the splitting crack for the beams confined with FRP sheets was similar to that of the beams confined with transverse reinforcement.

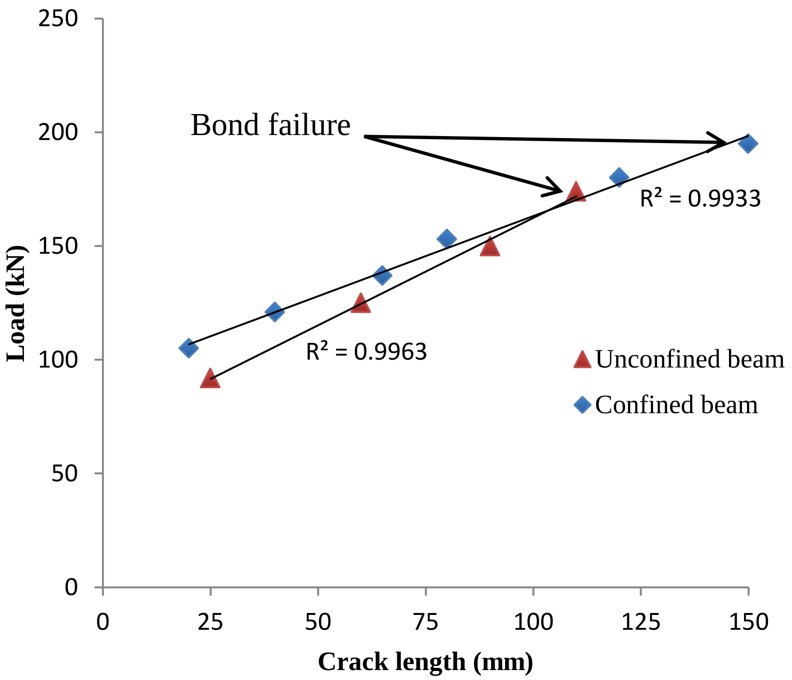

Figure 8.1 Load versus splitting crack propagation

8.3 Residual Bond Stress Behaviour as the Splitting Crack Propagated in the Unconfined Beams

Once the horizontal splitting crack started to propagate along the lap splice bars in the unconfined beam, the bond between the reinforcing bar and the surrounding concrete deteriorated in the cracked region. However, there was still a residual bond stress resulting from the friction between the reinforcing bar and the concrete. As the load increased, the splitting crack increased in length accompanied by an increase in the crack width which was greatest at the beginning of the crack and decreased as the crack tip was approached. As the width of the splitting crack increased, the friction between the reinforcing bar and the surrounding concrete decreased, resulting in a decrease of the residual bond stress. The tensile stresses in the concrete around the bars continued to increase with increasing load and at a crack length of 110 mm the stresses were great enough to cause lateral splitting and a sudden failure. Figure 8.2 shows the normal stress in the bar at strain gauge locations and the center of the splice as determined by strain gauge readings and symmetry (midpoint of splice) as the crack propagated in a typical unconfined beam. The average residual bond stress between the two strain gauge locations at the end of the splice was calculated from the difference in normal force between the two strain gauge locations as given by Equation 8.1. This residual bond stress decreased linearly as the splitting crack length increased as shown in Figure 8.3 for a typical beam.

$$\tau_r = \frac{d_b \left(f_{s\,(o)} - f_{s\,(L_c)}\right)}{4L_c} \qquad \text{Equation (8.1)}$$

Where:

τ_r: Residual bond stress at crack length, L_c (MPa)

d_b: Bar diameter (mm)

$f_{s(o)}$: Normal stress at the beginning of the lap splice (MPa)

$f_{s(Lc)}$: Normal stress at the crack tip (MPa)

L_c: Length of the splitting crack (mm)

The normal stress at the crack tip $f_{s(Lc)}$ was measured through a linear interpolation between the strain gauges from 0 to 50 mm if the crack length less than 50 mm. When the crack length was longer than 50 mm, $f_{s(Lc)}$ was calculated by linear extrapolation using the strain gauges placed in 0 and 50 mm of the beginning of the splice region (as shown in Figure 8.2 by tangents). Examination of the failed beams showed undamaged concrete keys above the bars in the beams, indicating that failure was by lateral splitting of the concrete without partial pullout that would have damaged the shear keys.

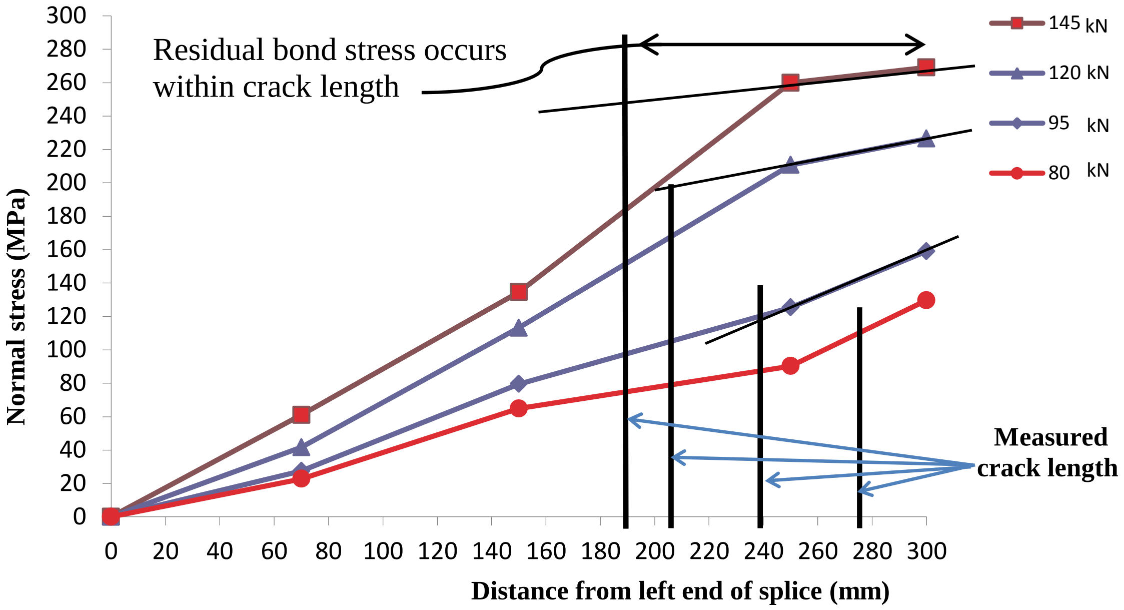

Figure 8.2 Bar normal stress distribution along splice length for unconfined beam specimen (LS-M1-UN-C)

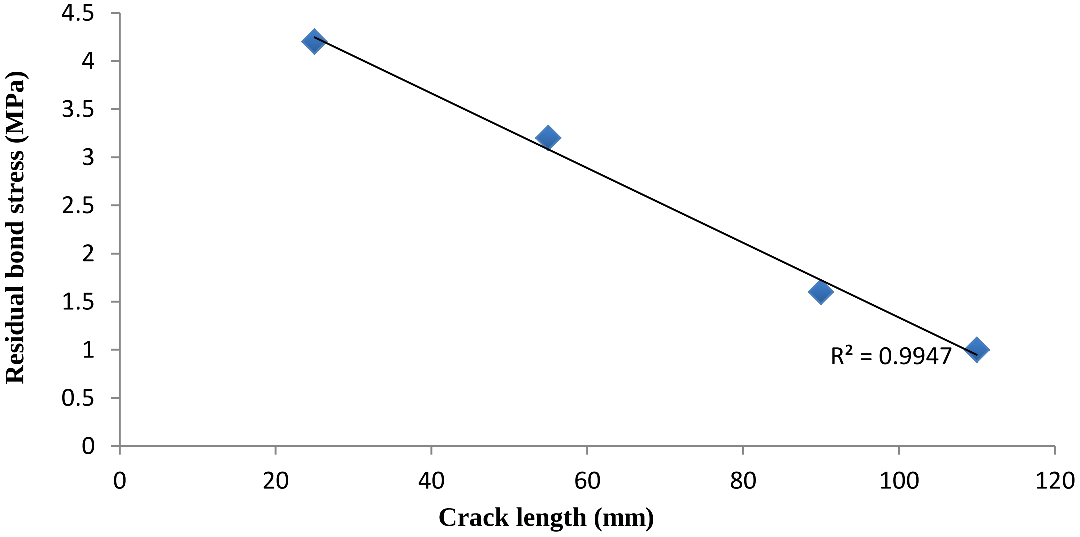

Figure 8.3 Variation of residual bond stress with splitting crack length for unconfined beam specimen (LS-M1-UN-C)

8.4 Residual Bond Stress Behaviour as the Splitting Crack Propagated in the Confined Beams

The behaviour of the residual bond stress distribution along the lap splice of beams that were confined with transverse reinforcement was divided into two stages, one before the splitting cracks had joined to produce a fully cracked beam, and the other after the beam was fully cracked. The residual bond stress of the confined beam in the first stage was similar to that of the unconfined beams. Again, the residual stress was calculated from the two strain gauges at the end of the splice decreased linearly as the crack length increased as the splitting cracks advanced. However, the residual bond stress values for the confined beams were higher than those of the unconfined beams. The increased bond stresses are attributed to the confinement of the splice region due to the transverse reinforcement or FRP wrapping, which held the bar against the concrete above the bar and maintained the bar lugs in place between the concrete keys between the lugs. At a crack length of 120 mm, the splitting cracks extended abruptly to the full length of the splice, but the confining action maintained the concrete cover in place and failure did not occur. The normal stress on the bar as the load increased and the residual bond stress values between the first two strain gauge locations calculated from Equation 8.1 are shown in Figures 8.4 and 8.5, respectively.

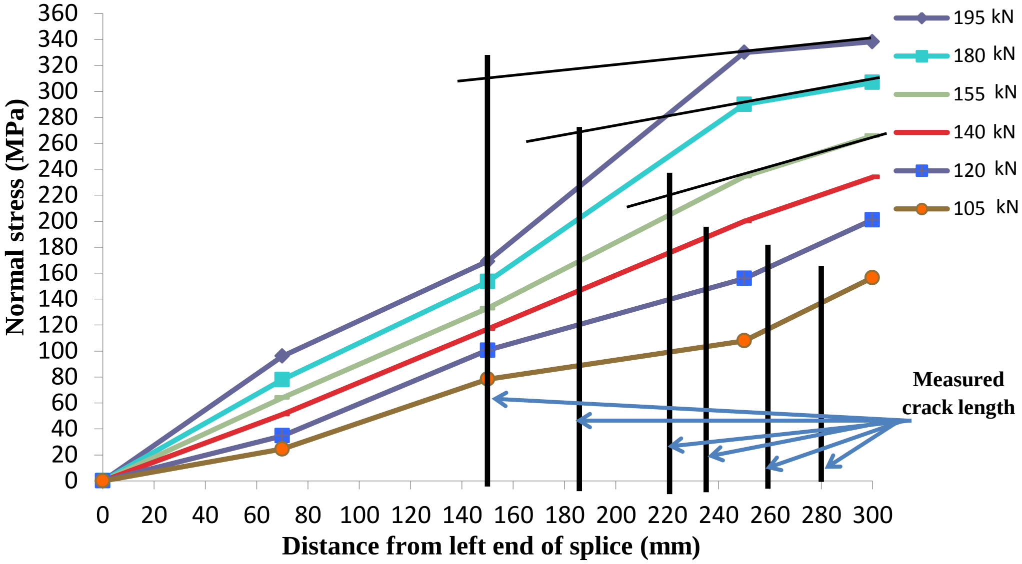

Figure 8.4 Bar normal stress distribution along splice length for confined beam specimen (LS-M2-T-C)

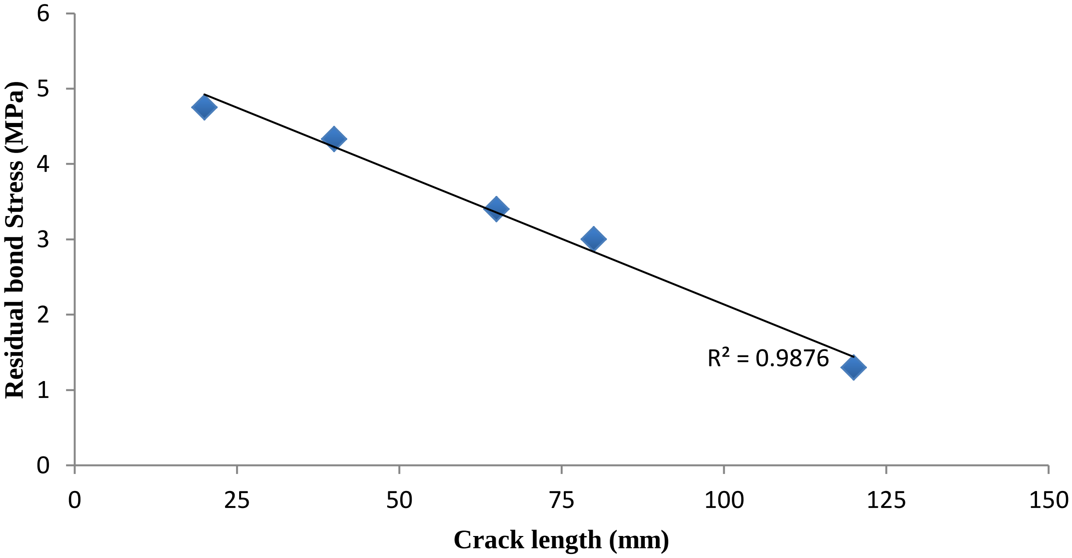

Figure 8.5 Variation of residual bond stress with splitting crack length in the first stage for confined beams specimen (LS-M2-T-C)

In the second stage, although the splitting crack extended the whole splice length the beam was able to carry more load before failure because the lugs on the bars remained in contact with the concrete keys and transferred the bond forces to the concrete. A possible shape of the residual bond stress distribution of the second stage is shown in Figure 8.6. Based on this assumed shape of the residual bond stress, and because of limited data that could be taken from strain gauges, a schematic shape of the bar normal stress is shown in Figure (8.7). The values of the residual bond stress near the end of the splice were calculated from measurements of force change between the first two strain gauges and were found to be small. Equilibrium requires that the bond force along the length of the splice reduce the axial force in a bar to zero at the end of the bar. The low values of bond stress at the end of the splice indicate that in this region, the steel lugs on the bar were not firmly held in place in the concrete keys, while the higher bond stresses required in the central region of the splice to satisfy equilibrium indicate that most of the bond force originates in the central region of the splice. In this region, the forces between the bar lugs and the concrete are high indicating that the transverse reinforcement held the bar firmly in place between the concrete lugs. The observation that the splitting crack was wider at the beginning of the splice region and narrower at the middle of the splice region (Figure 8.8) is consistent with a lower restraint on the bar near the ends of the splice.

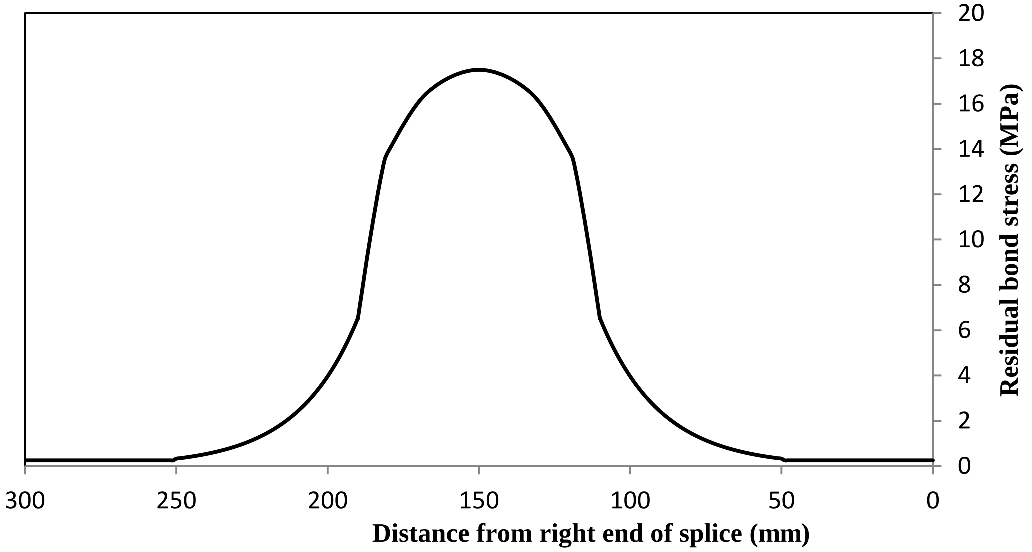

Figure 8.6 Assumed variation of residual bond stress with splitting crack length in the second stage for confined beams

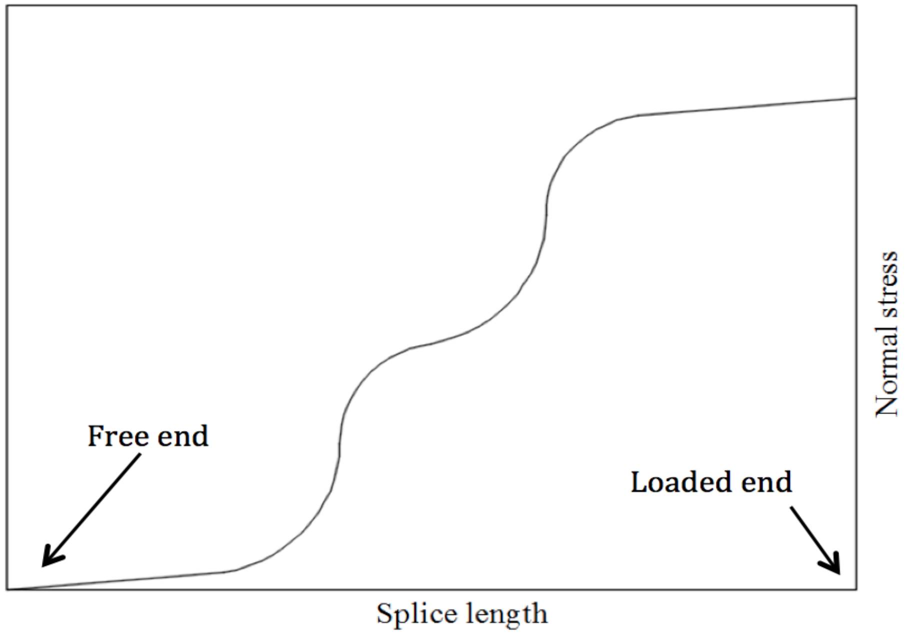

Figure 8.7 A possible bar normal stress distribution based on the assumed residual bond stress distribution

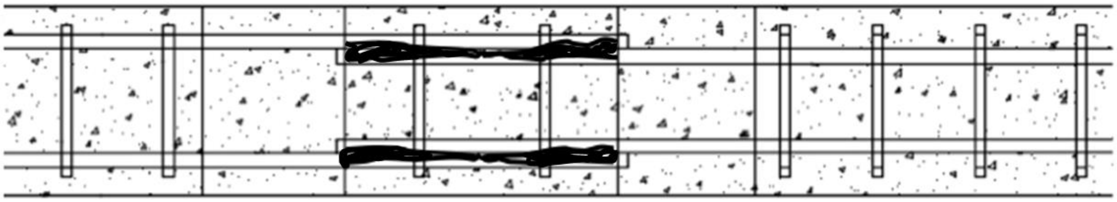

Figure 8. 8 Schematic crack width pattern along the splice length for confined beam

8.5 Bar Force Distributions and Bond Stress Distributions Observed in Previous Research

The bar force distribution, the bond stress distribution and the propagation of debonding in a beam anchorage specimen prestressed with FRP bars and repaired with a near surface mounted FRP bar was studied by Wahab et al. (2015). The bonded length and the number of strain gauges applied to the FRP bar were sufficient to describe the force distribution and the bond stress distribution along the bonded length. It was found that the bond stress varied exponentially along the bonded length. The bond stress distribution had two states; fully bonded before the initiation of a splitting crack and partially bonded after the splitting crack had initiated. The bond stress was divided into two regions; one behind the splitting crack tip and the other ahead of the crack tip as shown in Figure 8.9.

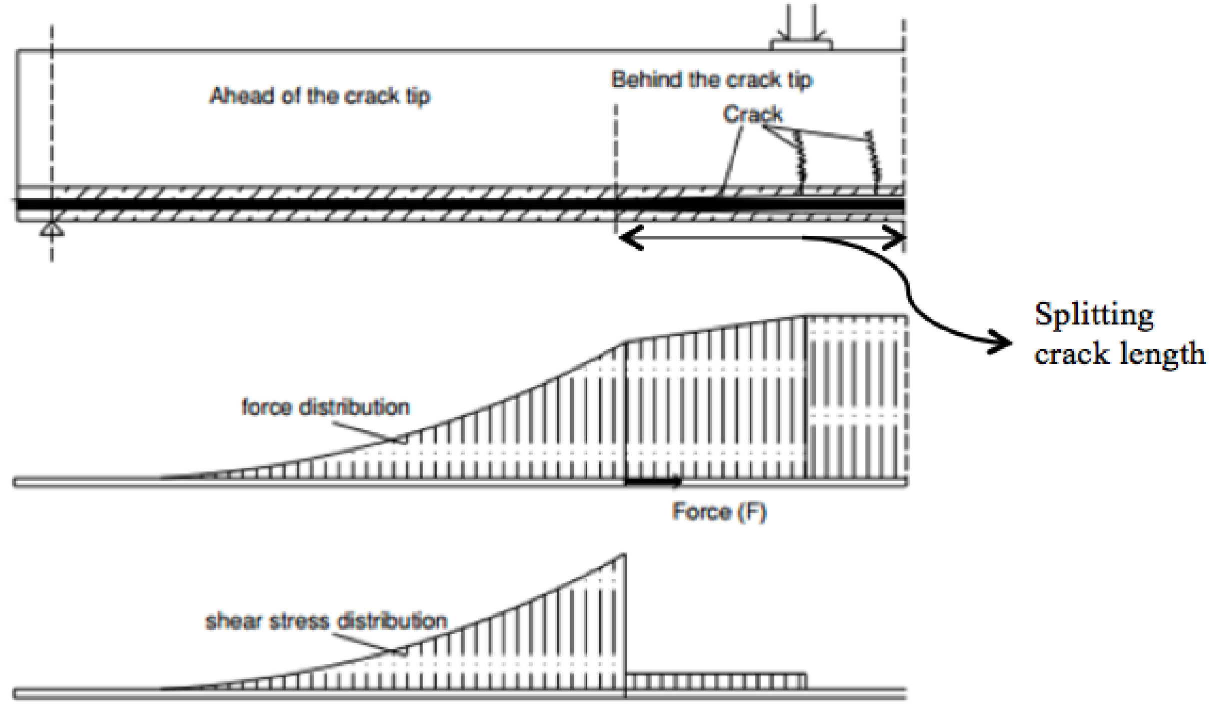

(a) Partially debonded

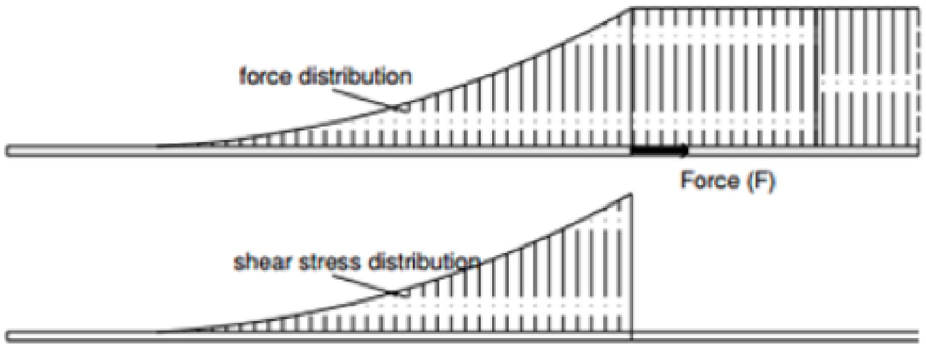

(b) Fully debonded

Figure 8.9 Force and shear stress distribution in the cases of (a) Partially debonded and (b) Fully debonded (Wahab et al. 2015)

Based on Wahab et al. (2015), the exponential curve of the force distribution is expressed by Equation 8.2 as follows:

$$F(x) = F\ exp^{(-c*x)}$$ Equation (8.2)

Where:

F(x): The normal force in the bar at a distance (x) (kN)
F: The force in the bar at the splitting crack tip (kN)
c: Constant depends on the bar texture and beam configuration
x: The distance from the crack tip (mm)

It was found that the value of c value changed from one beam to another based on the beam configuration; however it was constant for each beam configuration for all loads until failure.

Based on the model of Wahab et al. (2015), it was assumed that the bond stress distribution along the splice length ahead of the splitting crack can be described by the following equation:

$$\tau(x) = \tau_0\ exp^{(-c*x)}$$ Equation (8.3)

Where:

$\tau_{(x)}$**:** The bond stress along the splice length at distance (x) (MPa)
τ_0**:** The peak bond stress at the crack tip (MPa)
c: A constant that depends on crack length and beam confinement
x: The distance from the crack tip within the uncracked length (mm)

Based on equilibrium and using Equation 8.2 and 8.3, it can be shown that

$$\tau_o = \frac{-cF}{\pi d_b}$$ Equation (8.4)

Figure 8.10 shows the a idealized force distribution and the corresponding bond stress distribution ahead of splitting crack in an RC member. The bond force is the rate of change in the axial force so the bond stress at a point is proportional to slope of force diagram. As the force increases, the τ_o values increase based on constant value of c and increasing bar force. As the bar force increases further, a splitting crack occurs as the circumferential stresses around the bar exceed the cracking strength of the concrete. After cracking initiates, the maximum local bond stress at the crack tip will remain constant at τ_{omax} and the stress distribution ahead of the crack and c will change so that the sum of the bond forces over the length of the lap splice equal the applied force in the bar.

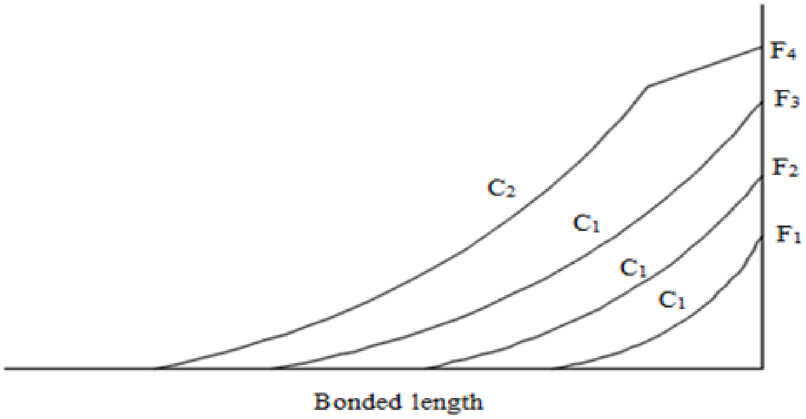

Force distribution along the bonded length

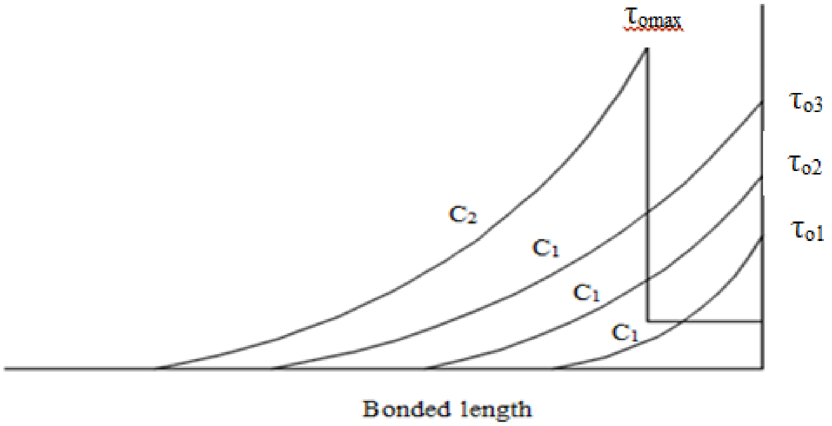

Bond stress distribution along the bonded length

Figure 8.10 Assumed bar force distributions and the corresponding bond stress distribution ahead of splitting crack of RC member

8.6 Suggested Normal Stress Distribution and Bond Stress Distribution Associated with Crack Propagation Observed in the Current Study

Previous research on a lap splice beam with numerous strain gauges on the spliced bars obtained a normal stress distribution in the lap spliced bars. Figure 8.11 shows the normal stress distribution shape of the lap spliced bars along the splice length (Tepfers, 1973; Kluge and Tuma, 1945). In the present investigation, only two strain gauges were applied on the spliced region to avoid the effect of the strain gauges on the bond strength. Because of that, the normal stress distribution in the lap spliced bars was assumed to follow the behaviour found in the previous research (Figure 8.12).

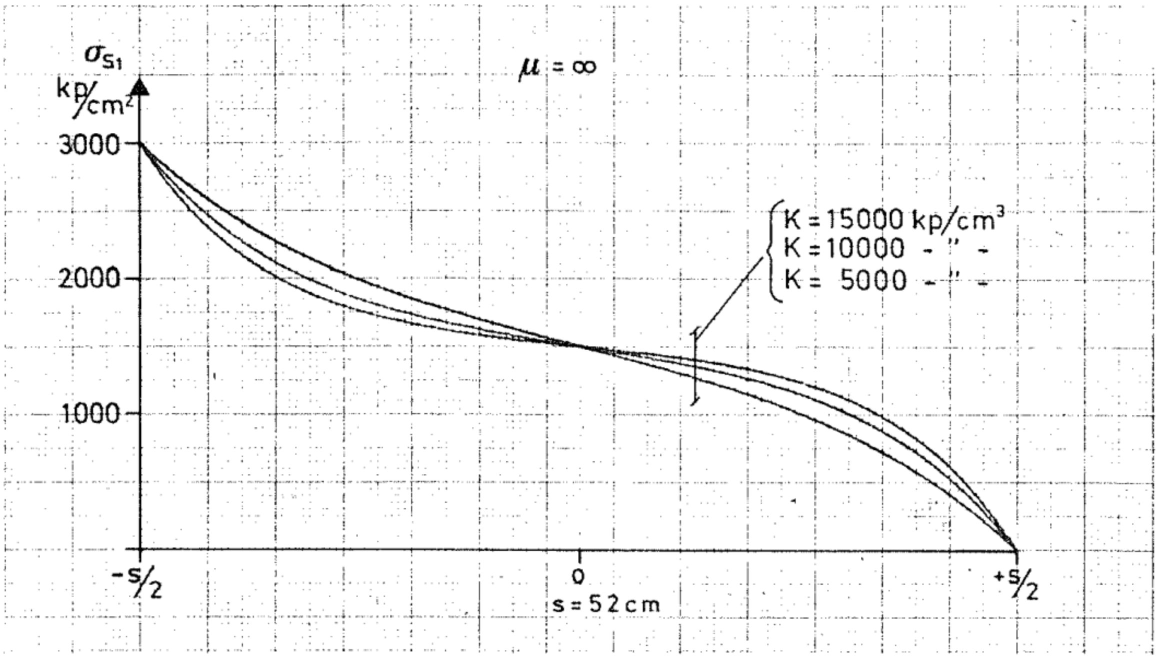

Figure 8.11 Normal stress distribution shape of spliced bar that observed from previous research (Tepfers, 1973)

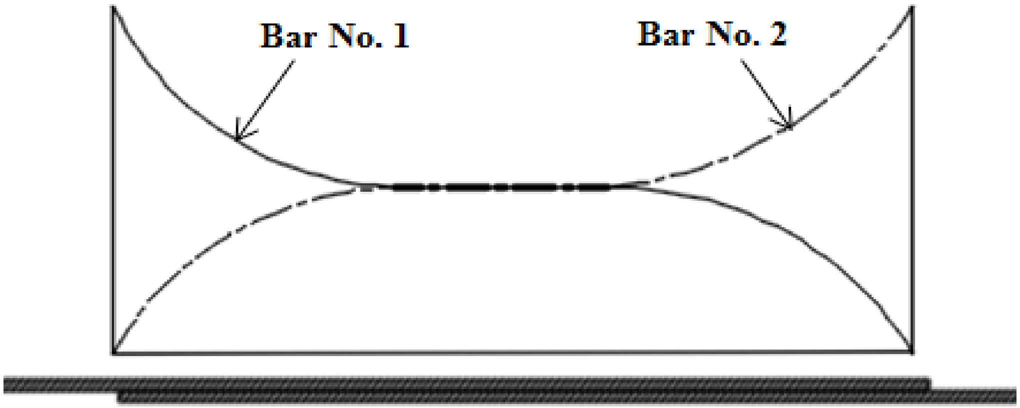

Figure 8.12 Schematic of normal stress distribution in lap splice beams

The normal stress distribution and the bond stress distribution for the beams in the present study are shown in Figure 8.13. The normal stress distribution is described by straight lines unlike the previous model of Wahab et al. (2015) who had enough strain gauges along the bonded length to describe the shape of the distribution. Since the splice length in the current study was short, only two strain gauges were applied to each bar in the spliced region to decrease the effect of the strain gauge applications on the bond strength. An extra strain gauge was applied outside of the spliced region on the bar in the constant moment region to monitor the initiation of the splitting crack. This strain gauge recorded the maximum stress in the bar since it was applied at the beginning of the spliced region. When the splitting crack reached 50 mm in length (the location of the second strain gauge) the strain gauge reading jumped suddenly and the difference between the first two strain gauge readings decreased. The splitting crack was monitored and marked at various lengths and the corresponding load was recorded. The normal stress distribution is expected to vary exponentially along the splice length; however it was described by straight lines between strain gauges locations since there were not enough strain gauges to derive the exponential shape. However the bond stress distribution is described by the expected exponential shape. Before the initiation of the splitting crack (Figure 8.13 (a)), the tensile forces in the beam were carried by both the reinforcing bar and the concrete. After a splitting crack formed, bond stresses and the rate of change in the force in the steel bar behind the crack decreases and the slope of the steel bar force versus distance from the end of the splice curve decreases as shown in Figure 8.13 (b). If there is a uniform residual bond stress in the cracked region, the steel force curve will have a linear slope and there will be a residual bond stress as shown in Figure 8.13 (b). If debonding was complete within the crack length, there would be no bond stress in the debonded region and the steel force curve would be constant.

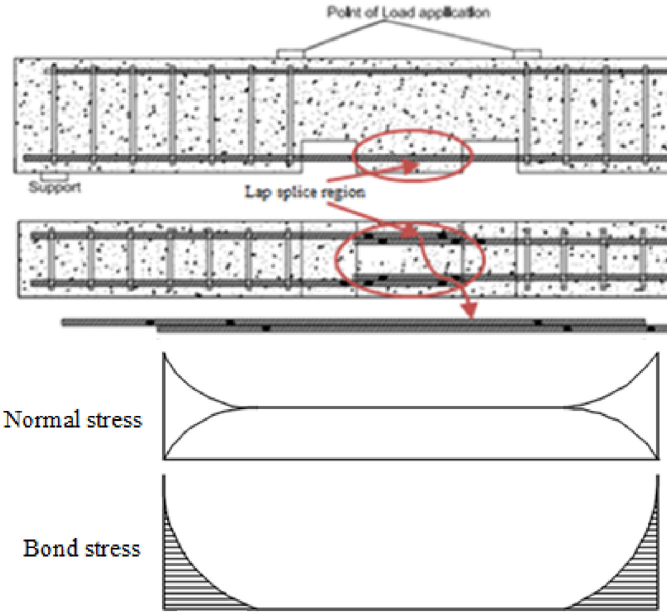

(a) Before splitting crack (Fully bonded)

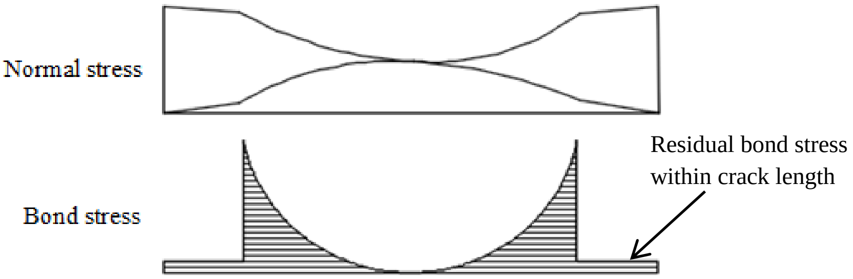

(b) After splitting crack (Partially bonded)

Figure 8.13 Assumed normal stress and bond stress distribution before and after a splitting crack occurs

The exponential curve equation for the bar force distribution proposed by Wahab et al. (2015) can be adapted for lap splice beams prior to formation of the splitting cracking as follows:

From 0 to $\boldsymbol{\frac{l_s}{2}}$

$$F(x) = \frac{F + F\ exp^{(-cx)}}{2} \qquad 0 \le x \le \frac{l_s}{2} \qquad \text{Equation (8.5)}$$

From $\boldsymbol{\frac{l_s}{2}}$ ***to*** $\boldsymbol{l_s}$

$$F(x) = \frac{F - F\ exp^{-c*(L_S - x)}}{2} \qquad \frac{l_S}{2} < x \le l_s \qquad \text{Equation (8.6)}$$

Where

F(x): Normal force in the bar at a distance (x) (kN)
F: Force in the bar at the beginning of splice length (kN)
c: Constant depends on the bar texture and beam configuration

Once the splitting crack occurs, the force distribution can be written as:

For x from 0 to L_c

$$F(x) = F - \tau_r \pi d_b x \qquad \text{Equation (8.7)}$$

For x from L_c to $L_s/2$

$$F(x) = \frac{F}{2} + (\frac{F}{2} - \ \tau_r \pi d_b L_c) exp^{(-c(x - L_c))} \qquad \text{Equation (8.8)}$$

For x from $L_s/2$ to crack tip (L_s – L_c)

$$F(x) = \frac{F}{2} - (\frac{F}{2} - \ \tau_r \pi d_b L_c) exp^{(-c(L_S - x))} \qquad \text{Equation (8.9)}$$

For x crack tip L_s

$$F(x) = \tau_r \pi d_b L_c - \tau_r \pi d_b (x - (L_s - L_c)) \qquad \text{Equation (8.10)}$$

The shape of the bond stress distribution along the lap splice beam immediately prior of of the splitting crack can be described by the following equations:

From 0 to $\boldsymbol{\frac{l_s}{2}}$

$$\tau(x) = \tau_{o,max} exp^{-c*x} \qquad \text{Equation (8.11)}$$

Where

x: Distance loaded end of the bar, $(0 \leq x \leq \frac{l_s}{2})$

From $\boldsymbol{\frac{l_s}{2}}$ ***to*** $\boldsymbol{l_s}$

$$\tau(x) = \tau_{o,max} exp^{-c*(Ls - x)} \qquad \text{Equation (8.12)}$$

Where

x: Distance loaded end of the bar, $(\frac{l_s}{2} < x \leq l_s)$

Based on equilibrium, $\tau_{o,max}$ can be shown as

$$\tau_b = \frac{\Delta F}{\pi d_b \Delta x} = \frac{1}{\pi d_b} \frac{dF}{dx}$$

$$\frac{dF}{dx} = \frac{-cFexp^{-cx}}{2}$$

$$\tau_b = \frac{-cF}{2\pi d_b} exp^{-cx}$$

$$\tau_{o,max} = \frac{-cF}{2\pi d_b} \qquad \text{Equation (8.13)}$$

After splitting crack occurs, the bond stress along the cracked length equal to the residual bond stress

For x from 0 to L$_c$

$$\tau(x) = \tau_r \qquad \text{Equation (8.14)}$$

For x from L_c to $L_s/2$

$$\tau(x) = \frac{-c}{\pi d_b}(\frac{F}{2} - \tau_r \pi d_b L_c) exp^{(-c(x-L_c))}$$ Equation (8.15)

For x from $L_s/2$ to crack tip

$$\tau(x) = \frac{-c}{\pi d_b}(\frac{F}{2} - \tau_r \pi d_b L_c) exp^{(-c(L_s-x))}$$ Equation (8.16)

For x from crack tip to L_s

$$\tau(x) = \tau_r$$ Equation (8.17)

8.7 Bond Stress Distribution during Splitting Crack Propagation Observed from the Results of the Current Study

There were three factors that were taken into account to calibrate the model describing the bond stress behaviour as the load increased monotonically until failure, which are:

- The equilibrium of bond force and bar force at each load level.
- Measured splitting crack length versus load data.
- The normal stress distribution in the bar that was derived from the strain gauge readings.

Figure 8.14 shows the assumed variation of the bond stress distribution shape as the crack propagated with increasing load until failure. To draw the bond stress distributions of Figure 8.14, the equilibrium bond force at each crack length was calculated. During each the test, the length of the propagating crack was measured and the corresponding loads were recorded.

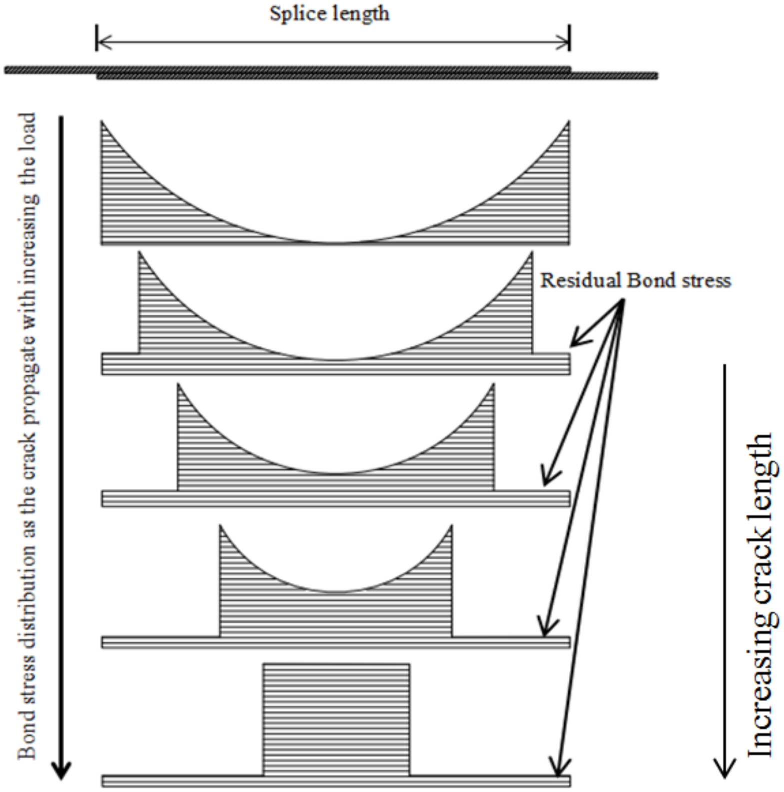

Figure 8.14 Assumed progression of bond stress distribution shape as the bond splitting crack propagates

Figure 8.14 shows the evolution of bond stress distribution shapes from the initiation of the splitting crack until failure. Before formation of the splitting crack, no residual bond stress appeared in the bond stress distribution along the splice length. When the circumferential tensile stress around the bar reached the cracking stress of the concrete, a splitting crack formed and the residual bond stress was developed along the crack length. As the splitting crack length increased, the crack width increased, decreasing the value of the residual bond stress. The exponential shapes of the bond stress versus distance along the splice from the location of the crack at each of the crack locations were maintained as the crack advanced but the distribution became flatter. This was attributed to increasing slip as the average bond stress increases. This slip redistributed the bond stresses to a more uniform distribution until at failure the bond stress is almost constant. Figure 8.15 shows the summation of the bond stress distribution as the crack propagating.

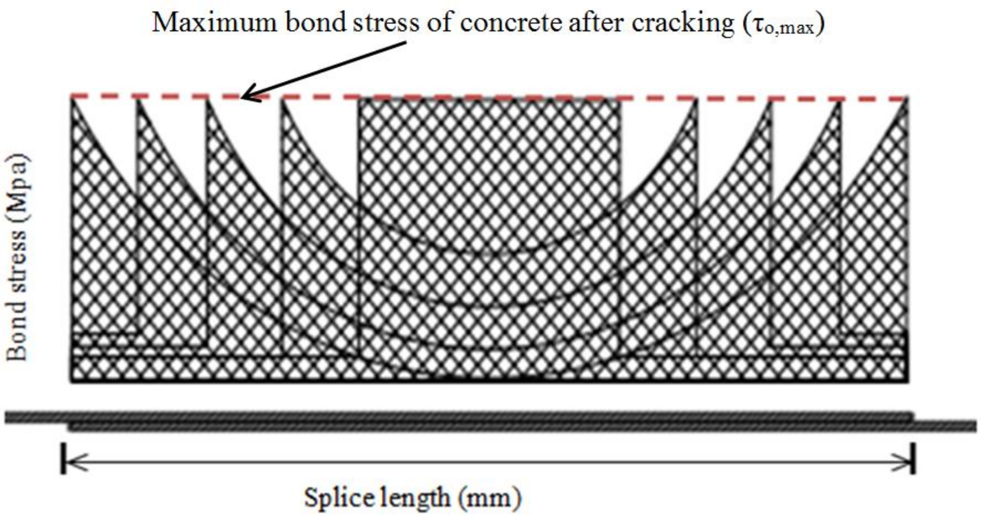

Figure 8.15 Summation of the bond stress distribution and the crack pattern

The exponential bond equation (Equation 8.10) has two unknowns, $\tau_{o,max}$ and c. To solve this equation, either $\tau_{o,max}$ or c should be known to be able to estimate the other unknown value and then to draw the bond stress distribution.

To do that, the load that caused the initial splitting crack was recorded. At this load the maximum local bond stress is equal to $\tau_{o,max}$ and it is function of the concrete cracking stress. It was found that the maximum bond stress is at the splice loaded ends and the splitting crack started and propagated when the ultimate concrete tensile strength was exceeded (Tepfers, 1973). Since $\tau_{o,max}$ is function of the cracking strength of concrete, the value of $\tau_{o,max}$ was assumed to be constant because it is related to a concrete property which is expected to be constant over the whole splice length. At the same time, the value of c was now expected to be varying after formation of the splitting crack. To calculate the value of $\tau_{o,max,}$ two equilibrium conditions were used, the sum of the bond forces over the splice length must equal the bar force at the loaded splice end, and the sum of the bond forces between the start of the loaded end of the splice length and the strain gauge at 50 mm must equal the change in bar force over the 50 mm interval. These two conditions allow the calculation of $\tau_{o,max}$ and c based on the bar force to initiate cracking. Once $\tau_{o,max}$ is known, the value of c at any crack length and bar force level can be calculated by satisfying the condition that the bond forces over the splice length equal the bar force at the end of the splice. In order to implement this calculation the residual bond stress must be estimated (see Section 8.3). It is then assumed that this residual bond stress constant along the crack length and the value of residual bond decreased as the crack progressed. The detailed to calculate $\tau_{o,max}$ are presented in Appendix C and are described further below.

The first condition was that the total bond force on a bar over the length of the splice should be enough to transfer the force in the bar to the concrete over the length of the splice, illustrated as follows:

Full splice length (From 0 to 300 mm)

Before splitting crack occurs (L_c)

$$\Delta F = \sigma_{no}\,(A_b) \qquad \text{Equation (8.18)}$$

$$= \int_0^{150} \pi d_b \tau_{o,max} exp^{-cx} dx + \int_{150}^{300} \pi d_b \tau_{o,max} exp^{-c(L_s-x)} dx$$

After splitting crack occurs (L_c)

$$\Delta F = \sigma_{no}\,(A_b) \qquad \text{Equation (8.19)}$$

$$= \tau_r L_c \pi d_b + \int_0^{150-L_c} \pi d_b \tau_{o,max} exp^{-cx} dx + \int_{150}^{300-L_c} \pi d_b \tau_{o,max} exp^{-c(L_s-x)} dx$$

Where

ΔF: Change of normal force in the bar along the splice length (N)

σ_{no}: Normal stress on the bar at the beginning of the splice length (MPa)

A_b: Area of the bar (mm^2)

d_b: Bar diameter (mm)

$\tau_{o,max}$: The peak bond stress at the crack tip (MPa)

c: A constant that depends on crack length and beam confinement

x: The distance from the crack tip within the uncracked length (mm)

τ_r: Residual bond stress within the crack length (MPa) (Equation 8.1)

L_c: Splitting crack length (mm)

The second condition, which was that the total bond forces between two strain gauge locations at the loaded end of the splice should equal the difference in bar force, determined from the strain gauge readings. In the current study, the two strain gauges placed at the beginning of the splice length and at 50 mm away from the beginning of the splice region were used to calculate the value of $\tau_{o,max}$ as illustrated bellow

From 0 to 50 mm bonded length

Before splitting crack (L_c) occurs

$$\Delta F_{(0-50)} = \sigma_{no}\,(A_b) - \sigma_{n50}\,(A_b) \qquad \text{Equation (8.20)}$$

$$= \int_0^{50} \pi d_b \tau_{o,max} exp^{-cx} dx$$

After splitting crack (L_c) occurs

$$\Delta F_{(0-50)} = \sigma_{no}\,(A_b) - \sigma_{n50}\,(A_b) \qquad \text{Equation (8.21)}$$

$$= \tau_r L_c \pi d_b + \int_0^{50-L_c} \pi d_b \tau_{o,max} exp^{-cx} dx$$

Where

$\Delta F_{(0-50)}$: Change of normal force in the at distance from 0 to 50 mm where the strain gauges were applied (N)

σ_{n50}: Normal stress on the bar at distance of 50 mm from the beginning of the spliced region (MPa)

Typical normal and bond stress distributions of an unconfined lap splice beam at load levels before and after the initiation of a splitting crack are shown in Figures 8.16 (a) and 8.16 (b), respectively. At a load of 80 kN (just before a splitting crack appears) the unrestrained beam was in a fully bonded state and the bond stress decreased exponentially from a maximum at the beginning of the spliced region. Once the splitting crack occurred and exceeded 50 mm length where the second strain gauge was applied, the reading of that strain gauge increased suddenly. Subsequently, as the load and the crack length increased the slope of the line from 0 to 50 mm decreased (Figure 8.16 (a) indicating a continually reducing residual bond stress. As the load increased, the c value which describes the shape of the exponential curve decreased and the total bond stress represented by the area under the curve in Figure 8.16 (b) increased until the tensile stresses in the horizontal plane at the height of the bars reached the concrete tensile strength and the beam failed suddenly by separation of the concrete below the bars from the beam allowing the bars to slip out of the concrete keys between the lugs. Examination of the failed beams revealed still intact concrete keys above the bars.

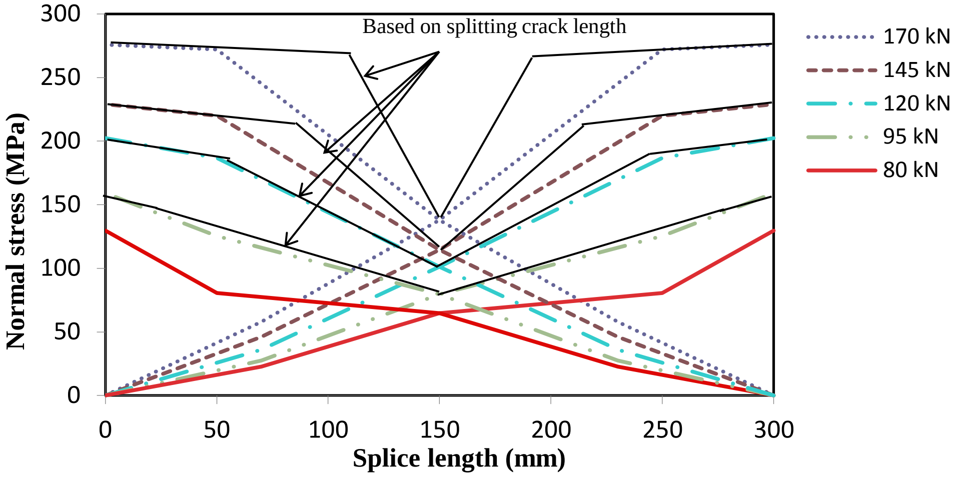

(a) Normal stress

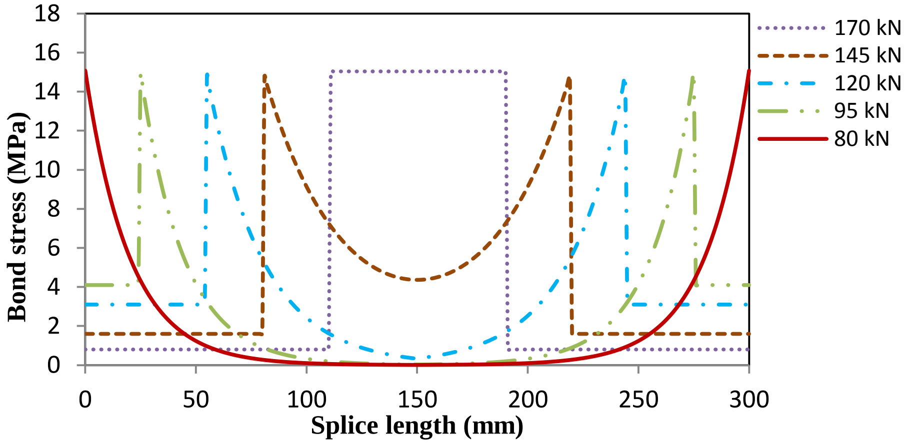

(b) Bond stress

Figure 8.16 Normal and bond stress distributions along the splice length of an unconfined beam specimen (LS-M2-T-C)

In the confined beams the splitting crack initiated at a load 105 of kN. Also, the rate of propagation of the splitting crack with load in the confined beam was lower than for the unconfined beam. Figure 8.17 (a) and Figure 8.17 (b) show the typical normal and bond stress distributions of a confined lap splice beam at different load levels as the splitting crack propagated. The bond stress distribution of the confined beams was similar to those of the unconfined beams until the crack length reached about 120 mm. However, the residual bond stress values in the confined beams were higher than in the unconfined beams where the confinement constrained the splitting crack from widening which enhanced the friction between the reinforcing bar and the surrounding concrete.

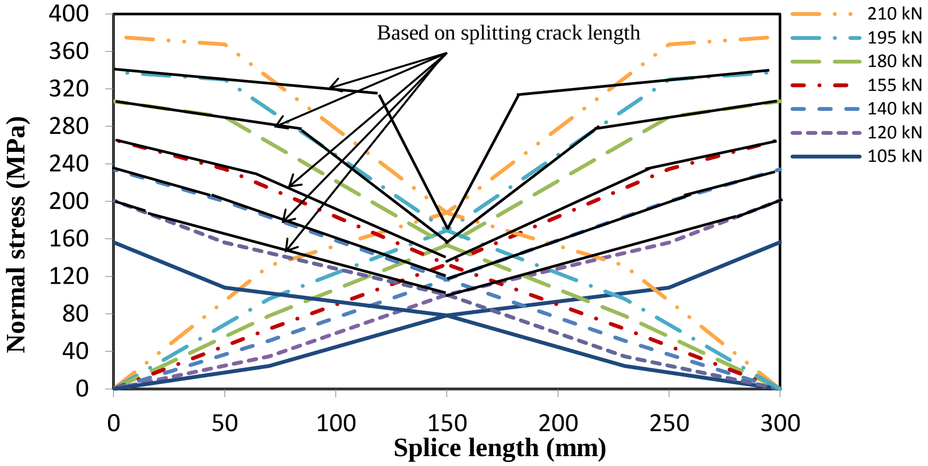

(a) Normal stress

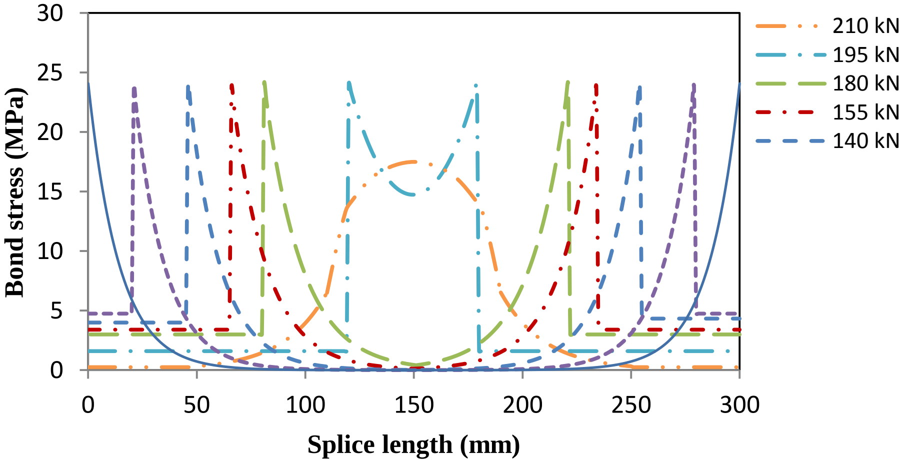

(b) Bond stress

Figure 8.17 Typical normal stress and bond stress distributions along the splice length of a confined beam specimen (LS-M2-T-C)

The c values, which described the bond stress distribution along the splice length as the crack propagated, of the unconfined beam were different than the beam confined with transverse reinforcement (Figure 8.18). The c value for a given beam decreased as the splitting crack length increased. To find out the c values along the splice length after finding the $\tau_{o,max}$ and c value immediately before splitting crack occurred, as the crack propagated, the $\tau_{o,max}$ was assumed to be constant and the c values was changed by trial and error based on the crack length to fulfill the equilibrium conditions (the first and the second conditions). The crack length (initiation and propagation) was determined by monitoring and recording the propagation of the splitting crack as the load increased. In the unconfined beams, the splitting crack initiated and the bar slip started earlier than the confined beams, thus they had lower c values than the confined beams. The transverse confinement delayed crack initiation and slowed the rate of the crack propagation. Since the crack growth cannot be monitored in the beams confined by FRP sheet, the c versus crack length distribution was assumed to follow the behavior of crack propagation in the beams confined with transverse reinforcement.

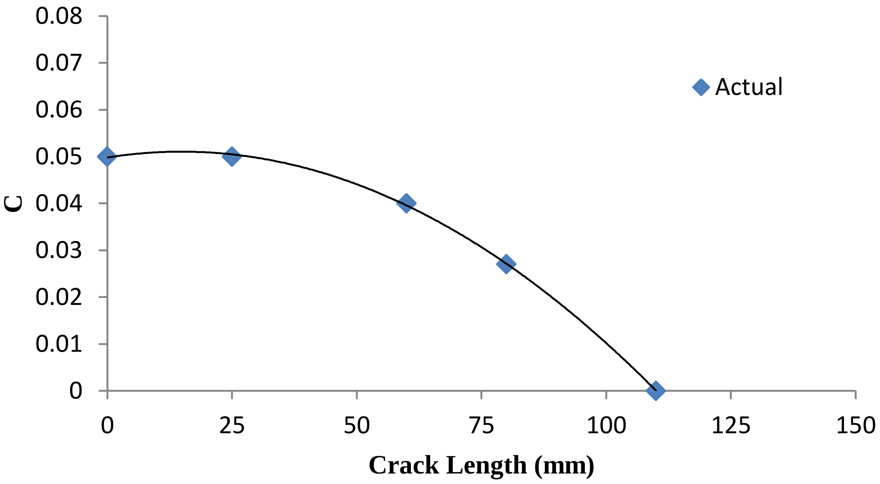

(a) Unconfined beams

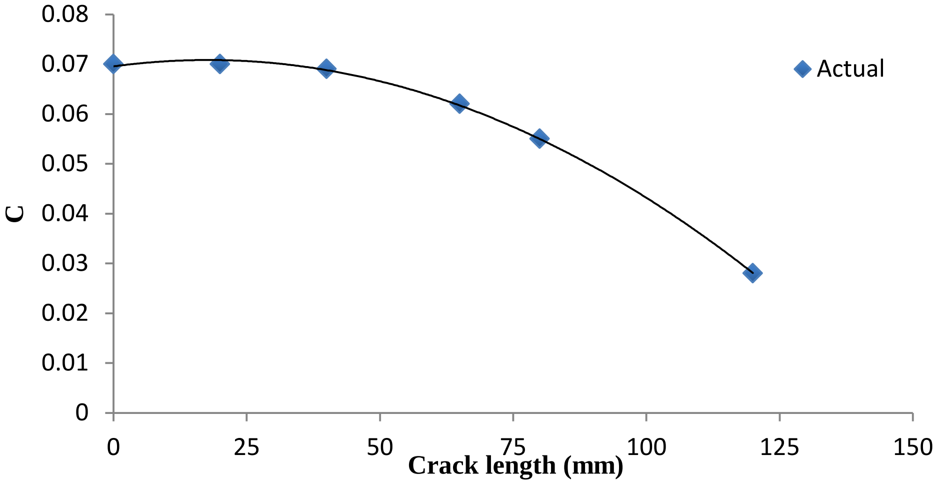

(b) Beams confined with transverse reinforcement

Figure 8.18 The variation of the value of C with crack length

Chapter 9: Conclusions and Recommendations for Future Work

9.1 Introduction

This chapter discusses the conclusions, contributions of this research and recommendations for future work. A total of 36 beams-end specimens and 24 lap splice beams were constructed and tested up to failure. The beam-end specimens were subjected static tensile loading to determine the effect of different level of corroded rebar (5% 7.5%, 10% and 15% mass loss) on the bond strength of four development lengths (200 mm, 250 mm, 300 mm and 350 mm). The corroded bars were cleaned and repaired with four different types of concrete. Also, twenty-four lap splice beams were tested statically to study the effect of confinement (transverse reinforcement and FRP sheets) on the bond behavior of cleaned corroded bars with 7.5% and 15% mass loss levels. The typical partial depth repair concrete that was also used for the beam-end specimens was used to repair the lap splice beams. Based on the observations and the analysis of the results of this research, the following conclusions can be drawn.

9.2 Conclusions from the Beam-End Specimens

1. As corrosion level increased, the cleaned rebar surface roughness of the bar increased. Thus, the friction resistance was enhanced leading to decrease the bar slip. As well, the mechanical bond appears to have increased due to the roughen surface and corrosion pits.

2. For the beam-end specimens with 200 mm, 250 mm and 300 mm bonded length, all of the specimens failed by splitting of the concrete. However, the beam-end specimens with 350 mm bonded length, the failure mode was combined between pullout and splitting failure, or bar yield and splitting failure.

3. Generally, for all 200 mm, 250 mm, 300 mm and 350 mm bonded length, the average bond strength of repaired corroded rebar was enhanced by up to 17% at rebar mass loss

level of 15% compared to the uncorroded control specimens.

4. As the bonded length increased, the average bond strength decreased and the corresponding bar slip increased. However, the changes in bond strength and the corresponding slip was not proportional to the change in bonded length as was expected. That could be explained by the mode of failure of the bond whereas the loaded end is more effective than the free end in transferring bond forces (ACI 408, 2003).

5. For the same bonded length, the average bond strength increased with increasing corrosion level due to the decrease in the cross-sectional area of the rebar. Therefore, as the bar diameter decreases, the bond force at failure decreases at rate more slowly than the decrease the bar area. (ACI 408, 2003). Also, the corresponding bar slip decreased due to the increase the roughness of the bar surface.

6. For all corrosion levels and for different bonded lengths, the average bond strength for monolithic beam-end specimens was higher than the average bond strength of all types of the partial depth repair especially for the shorter bonded length. This was because the partial depth repairs places on the substrate concrete to be behaving as two layers. So, with applying the tensile force on the bar, the whole pocket of partial depth repair region tended to move and be resisted by the transverse reinforcement. That caused internal shear cracks at the interface between the partial depth repair and the substrate concrete.

7. The monolithic concrete (M1) had compressive strength lower than the self-compacting concrete with 8 mm coarse aggregate (SCC1), however, it had better bond. That because the quantity and the size of the coarse aggregate in M1 mix was greater than it in SCC1, which leaded to increase the splitting strength and the fracture energy of M1 compared to SCC1. Also, is could be because the SCC1 was placed as a repair on the substrate concrete, however the M1 was cast as the same time with the main cast. Thus, the shear cracks between the two layers was avoided in M1.

8. Self-consolidating concrete showed higher average bond strength than normal concrete,

due better bond between the repair concrete and substrate. This was supported by reduced internal shear cracks in the beam-end specimens repaired with self-consolidation concrete. It assumed that the use of silica fume and reduced water to cement ration in the self-consolidating concrete enhanced bond with the substrate concrete.

9. The partial depth repair SCC2 had higher average bond strength than SCC3 mainly because of having silica fume and bonding agent, which increased the shear bond strength at the interface between the substrate concrete and the partial depth repair concrete.

10. The average bond strength was significantly affected by changing the bonded length as the mass loss increased.

9.3 Conclusions from the Lap Splice Beams

1. All of the lap splice unconfined beams and the beams confined with transverse reinforcement or FRP sheets failed by a splitting bond failure.
2. For all unconfined and confined lap splice beams, the average bond strength increased with increasing bar mass loss level due to the decrease in the cross sectional area of the rebar. Therefore, as the bar diameter decrease, the bond force at failure decreases at rate more slowly that decreasing the bar area. (ACI 408, 2003). Also, as corrosion level increased, the cleaned rebar surface roughness increased, which possibly increased the mechanical bond contribution.

3. The unconfined beams had a sudden brittle failure associated with loud sound. In contrast, the confined beams had a more ductile mode of failure compared to the unconfined beams.

4. At failure, the lap splice beams confined with transverse reinforcement or FRP sheets produced smaller pieces of concrete than those of the unconfined beams. Also, the beams

confined with FRP sheets produced smaller pieces of concrete compared to beams confined with transverse reinforcement.

5. The presence of repair materials did not reduce the bond strength of the lap splice beams when SCC with 50% of coarse aggregate was used. The partial depth repair SCC50 had similar tensile strength and fracture energy to the beam concrete (M1 and M2). The partial depth repair SCC50 had a similar or slightly higher average bond strength than the monolithic concrete presumably due to the inclusion of silica fume and a lower water-to-cement ratio in the SCC50 material, which led to increase the bond properties. Unlike the beam-end specimens, the lap splice beams repaired with the partial depth repair SCC50 concrete enhanced the average bond strength compared to the monolithic beams. That was explained because the absence of the shear cracking along the boundary between the substrate concrete and the repair material where there is no shear in the splice region.

6. Although the partial depth repair concrete SCC0 had the highest compressive strength of the mixes, it had the lowest average bond strength. That was because the absence of the coarse aggregate in SCC0 led to a decrease in concrete splitting strength and fracture energy, and thus led to decrease the average bond strength.

7. The beams wrapped with FRP sheets had a higher maximum load and corresponding deflection than the unwrapped beams by 49 % and 191 %, respectively.

8. The ultimate load at failure and the corresponding deflection of the beams confined with transverse reinforcement increased by 36% and 64% compared to the unconfined beams, respectively.

9. The beams confined with FRP sheets had a higher ultimate load and corresponding deflection than the beams confined with transverse reinforcement.

10. The bond strength of beams repaired with FRP sheets was higher than that of the beams confined with transverse reinforcement. The transverse reinforcement increased the average bond strength and the corresponding slip by (15% - 29%) and (32% - 62%)

compared to the unconfined beams, respectively. However, the beams confined with FRP sheets showed an increase in the bond strength and the corresponding slip by (34 - 49%) and (56 - 260%) compared to the unconfined beams, respectively.

11. The beams confined with transverse reinforcement experienced a later start and slower growth of the splitting cracks than the unconfined beams.

12. As the mass loss increased, the bond strength increased more significantly when confinement was present.
13. Predicted bond strength by ACI 408 equation was consistent with experimental results for control lap splice beams. As mass loss increased, ACI 408 equation became more conservative except for SCC0.

14. As mass loss increased, the difference between predicted and experimental bond strength became more pronounced in confined beams.

9.4 Research Contributions

There are many RC structures around the world that are exposed to severe environments (e.g, structures subjected to marine environment or to de-icing salts) that may cause corrosion in concrete structures. As reinforcement corrosion become more severe, the structure could be in a dangerous situation and may collapse. This research has made two main contributions in regards to the bond of reinforcement in structures where corroded reinforcement has be subjected to partial depth repair concrete.

- ➢ This research is the first published study to provide an understanding of the bond behaviour of cleaned corroded RC member repaired with partial depth repair concrete specifically:
  - The cleaned corroded bar in a partial depth repair increases the bond strength relative to the non-corroded bars.

- The presence of the repair concrete had a significant effect in decreasing the bond strength in anchorage bond situations. It did not have an effect in splice bond situations.

- Internal shear cracks at the interface between the repair and substrate concrete and within the repair concrete can develop under anchorage bond conditions as the bar force is transferred to the substrate. The presence of these cracks will reduce bond in anchorage situations and should be addressed as part of the repair design.

- A model was proposed to describe the bond stress distribution as the bond splitting crack progresses in lap splice beams under static loading.

- The research provides an indication of the effect of different variables such as mass loss level, bonded length and the presence of repair concrete on the bond strength.

➢ The research findings will help engineers choose the most suitable repair technique to rehabilitate corroded RC member where reinforcement bond is a concern. Specifically:

- Partial depth repair concrete cannot fully restore reinforcement bond in anchorage bond situations

- Providing external confinement, for example using FRP sheets, along with the repair concrete in can restore and enhance the bond in anchorage bond situations.

- Partial depth repair concrete can restore bond in lap splice beams when suitable repair concrete is used, and external confinement may not be needed.

- Repair concrete materials should have specific properties to ensure good reinforcement bond conditions:

    - Good consolidation around the reinforcement and against the substrate concrete (SCC is better than NC)

    - Low bleeding

- Using repair procedures to enhance bond with the substrate concrete (i.e., roughening and preparing the substrate concrete, using a bonding agent or using silica fume in the repair concrete)

- High concrete toughness (G_f) and splitting tensile strength (f_t) are more important than compressive strength (f'_c) in repairing critical bond regions. In order to avoid situations where tensile strength and toughness are low relative to compressive strength, repair concrete with limited coarse aggregate content should be avoided.

9.5 Recommendations for Future Work

The current research has contributed knowledge on the performance of a cleaned corroded reinforcing bars repaired with partial depth repair, transverse reinforcement and FRP sheets. Based on the work done, additional work to increase the knowledge of the bond behaviour of cleaned corroded bars should include:

- Study the effect of corrosion mass loss up to 20%. Failure mode may to change where the bar ribs could be eliminated from the severe corrosion, which might lead to pull-out failure resulting from decreasing the mechanical interlock from the bar ribs. As well, failure due to bar yield or rupture may occur due to the reduction section.
- Study the effect of different steel bar diameters to investigate the effect of bar diameter with a different level of corrosion on the bond strength accompanied with the other variables.
- Examine the effect of using high strength partial depth repair concrete on the bond behavior of cleaned corroded reinforcing bar. It is expected that the high strength of repair concrete might give a significant cooperation of friction of cleaned corroded rebar. Also, high strength of repair concrete might give a better bond to the substrate concrete.
- Increase the number of strain gauges on the reinforcing bars to monitor the crack propagation and the corresponding normal stress distribution, which will help to calculate the local bond stress. For the anchorage bond, it is suggested that the strain

gauges be located near the loaded end where the splitting crack started and propagated. This should give a good indication of the bond stress distribution and the residual bond that can be calculated from the normal stress distribution.

- Test cleaned corroded reinforcing bars in lap splice beams under fatigue loading to study the effect of cycling loading on the bond behavior of cleaned corroded bars.
- Investigate the effect of bidirectional FRP sheets for the wrapping reinforcement on the bond behavior of beam repaired with partial depth repair especially in the anchorage bond which might decrease the effect of the internal shear cracks by inhibiting the repair concrete pocket from movement.
- Investigate the effect of Textile Reinforced Mortars (TRM) with cement based on the bond behavior rather than an epoxy.

References

ACI Committee 222. (2001). “Protection of Metals in Concrete Against Corrosion” (ACI 222-01). Farmington Hills: American Concrete Institute, 41 pages.

ACI Committee 364.10T. (2014) “Rehabilitation of Structure with Reinforcement Section Loss” (ACI 364.10T-14). Farmington Hills: American Concrete Institute, 4 pages.

ACI Committee 408. (2003). “Bond and Development of Straight Reinforcing Bars in Tension” (ACI 408R-03). Farmington Hills, MI: American Concrete Institute, 49 pages.

ACI Committee 408. (2012). “Report on Bond of Steel Reinforcing Bars Under Cyclic Loads.” (*ACI408.2R-12)*, Farmington Hills, MI, 37 pages.

ACI Committee 440. (1996). “State-of-the-Art Report on Fiber Reinforced Plastic Reinforcement for Concrete Structures, Manual of Concrete Practice.” (ACI440R-96), Farmington Hills, M, 35 pages

ACI Committee 440. (2007). “Report on Fibre-Reinforced Polymer (FRP) Reinforcement for Concrete Structures” (ACI 440R-07). Farmington Hills, MI: American Concrete Institute, 100 Pages.

Akçaoğlu, T., Tokyay, M., & Çelik, T. (2002). “Effect of Coarse Aggregate Size on Interfacial Cracking Under Uniaxial Compression”. *Materials letters*, Vol. *57, No.*4, pp. 828-833.

Alavi-Fard, M., and Marzouk, H. (2002). “Bond Behavior of High Strength Concrete under Reversed Pull-out Cyclic Loading,” *Canadian Journal of Civil Engineering*, pp.191-200.

ASTM A 944-05, “Standard Test Method for Comparing Bond Strength of Steel Reinforcing Bars to Concrete Using Beam-End Specimens”, *Annual Book of ASTM Standards*, American Society for Testing and Materials, West Conshohocken, Pennsylvania, USA, 4 pages.

Badawi, M. A. (2007). “Monotonic and Fatigue Flexural Behaviour of RC Beams Strengthened with Prestressed NSM CFRP rods.” PhD. thesis, Department of Civil and Environmental Engineering, University of Waterloo, Waterloo, Ontario, 433 pages.

Bamonte, P., & Gambarova, P. (2007). “High-Bond Nars in NSC and HPC: Study on Size Effect and on the Local Bond Stress-Slip Law”. *Journal of Structural Engineering*, *133*, pp. 225-234.

Benmokrane, B., & Tighiouart, B. (1996). “Bond Strength and Load Distribution of Composite GFRP Reinforcing Bars in Concrete”. *ACI Materials Journal*, 93(3), Vol. 3, 6 pages

Beygi, M. H., Kazemi, M. T., Vaseghi Amiri, J., Nikbin, I. M., Rabbanifar, S., & Rahmani, E. (2014). “Evaluation of the Effect of Maximum Aggregate Size on Fracture Behavior of Self Compacting Concrete”. *Construction and Building Materials*, 55, pp.202-211.

Bissonnette, B., Vaysburd, A. M., & von Fay, K. F. (2012). “Best Practices for Preparing Concrete Surfaces Prior to Repairs and Overlays” (No. MERL 12-17).

Boel, V. (2006), “Microstructure of Self-Compacting Concrete in Relation with Gas Permeability and Durability Aspects”, PhD Thesis, Ghent University, 176 pages.

Bournas, D. and Triantafillou, T. (2011). ”Bond Strength of Lap-Spliced Bars in Concrete Confined with Composite Jackets.” *J. Compos. Constr.* 15, Special Issue in Honor of Professor Urs Meier, pp. 156–167.

Bousias, S., Spathis, A., and Fardis, M. (2007). “Seismic Retrofitting of Columns with Lap Spliced Smooth Bars through FRP or Concrete Jackets.” *J. Earthquake Eng.*, Vol. 11, No. 5, pp. 653–674.

Broomfield, J. P. (2006). “Corrosion of Steel in Concrete: Understanding, Investigation and Repair”. CRC Press, 276 pages.

Butler, L. (2012). “Evaluation of Recycled Concrete Aggregate Performance in Structural Concrete” (Doctoral dissertation, University of Waterloo). 433 pages

Carino, N. J., and Lew, H. S., (1982). “Re-Examination of the Relation between Splitting Tensile and Compres- sive Strength of Normal Weight Concrete,” ACI Journal, *Proceedings* V. 79, No. 3, May-June, pp. 214-219.

Craig, B., & Soudki, K. (2005). “Post-repair Performace of Corroded Bond Critical RC Beams Repaired with CFRP”. *Proceedings: FRP Reinforcement for Concrete Structures (FRPRCS-7), 7th International Symposium* (pp. 563 - 578). Shield, C. et al. Eds., ACI SP-230.

Chan, Y. W., & Chu, S. H. (2004). “Effect of Silica Fume on Steel Fiber Bond Characteristics in Reactive Powder Concrete”. *Cement and Concrete Research*, Vol. *34, No.*7, pp. 1167-1172.

Canadian Standards Association, (2004). “Design of Concrete Structures”, (CSA A23.3-04), Toronto, Ontario, Canada.

Darwin, D., Barham, S., Kozul, R., and Luan, S. (2001). “Fracture Energy of High-Strength Concrete”, ACI Materials Journal, Vol. 98, No. 5, pp. 410 – 417.

Darwin, D.; Tholen, M. L.; Idun, E. K.; and Zuo, J. (1996a). “Splice Strength of High Relative Rib Area Reinforcing Bars,” *ACI Structural Journal*, V. 93, No. 1, Jan.-Feb., pp. 95-107.

Desnerck, P., De Schutter, G., & Taerwe, L. (2010). “A Local Bond Stress-Slip Model for Reinforcing Bars in Self-Compacting Concrete”. In 7th International Conference on Fracture Mechanics of Concrete and Concrete Structures (FraMCoS-7) (Vol. 2). Hanrimwon Co Ltd, pp. 771-778.

Detwiler, R. J., Fapohunda, C. A., & Natale, J. (1994). “Use of Supplementary Cementing Materials to Increase the Resistance to Chloride Ion Penetration of Concretes Cured at Elevated Temperatures”. *Materials Journal*, Vol. *91, No.* 1, pp. 63-66.

El-Hacha, R., El-Agroudy, H., & Rizkalla, S. H. (2006). “Bond Characteristics of High-Strength Steel Reinforcement”. *ACI Structural Journal*, Vol. *103, No.* 6, 12 pages.

EL-Maaddawy, T. A., and Soudki, K. A. (2003). “Effectiveness of impressed current technique to simulate corrosion of steel reinforcement in concrete” *Journal of Materials in Civil Engineering, ASCE*, Vol. 15, No. 3, pp. 41-47.

Emberson, N. K., & Mays, G. C. (1996). “Significance of Property Mismatch in the Patch Repair of Structural Concrete”. Part 3: Reinforced concrete members in flexure. *Magazine of concrete research*, Vol. *48, No.* 174, 13 pages.

Fagundo, F., Gergely, P., and Whute, R. (1979). “The Behavior of Lapped Spliced in Reinforced Concrete Beams Subject to Repeated Loads.” *Report No.79-1*, Department of Structural Engineering, Cornell University, Ithaca, NY.

FIB. (2000).“Bond of Reinforcement in Concrete, State-of-Art Report”. Switzerland: International Federation for Structural Concrete.

Garcia, R., Helal, Y., Pilakoutas, K., and Guadagnini, M. (2013). “Bond Strength of Short Lap Splices in RC Beams Confined with Steel Stirrups or External CFRP.” *Mater. Struct.*, Vol. 48, No.1-2, pp. 277–293.

Gibson, R. F. (1994) “Principles of Composite Material Mechanics”, New York: McGraw-Hall Inc.

Giuriani, E., Plizzari, G., & Schumm, C. (1991). “Role of Stirrups and Residual Tensile Strength of Cracked Concrete on Bond”. *Journal of Structural Engineering, 117*, pp. 1 - 18.

Guizani, L., & Chaallal, O. (2011). An Experimental Study on Bond-Slip in Moderately Confined Concrete Subjected to Monotonic and Cyclic Loading Using an Experimental Plan. *Canadian Journal in Civil Engineering*, 38, pp. 272 - 282.

Hamad, B.S., Rteil, A.A. and Soudki, K.A. (2004a). “Bond Strength of Tension Lap Splices in High Strength Concrete Beams Strengthened with Glass Fiber Reinforced Polymer Wraps,” *Journal of Composites for Construction*, Vol. 8, No. 1, pp. 14-21.

Hamad, B.S.; Rteil, A.A.; Selwan, B. and Soudki, K.A. (2004b). “Behavior of Bond-Critical Regions Wrapped with Fiber-Reinforced Polymer Sheets in Normal and High-Strength Concrete,” *Journal of Composites for Construction*, Vol. 8, No. 3, pp. 248-257.

Harajli, M., Hamad, B., & Rteil, A. (2004). “Effect of Confinement on Bond Strength Between Steel Bars and Concrete”. *ACI Structural Journal, Vol. 101, No.* 5, pp. 595 - 603.

Hillerborg, A. (1986). “The Theoretical Basis of a Method to Determine the Fracture Energy Gf of Concrete”, *Materials and Structures*, Vol. 18, No. 106. pp. 291 – 296.

Hong, S., & Park, S. K. (2012). “Uniaxial Bond Stress-Slip Relationship of Reinforcing Bars in Concrete”. *Advances in Materials Science and Engineering*, Vol. 1155. 12 pages.

Igarashi, S. I., Bentur, A., & Kovler, K. (2000). “Autogenous Shrinkage and Induced Restraining Stresses in High-Strength Concretes”. *Cement and Concrete Research*, Vol. *30, No.* 11, pp. 1701-1707.

ISIS Canada (2001). “Reinforcing Concrete Structures with Fibre Reinforced Polymers.” *Intelligent Sensing for Innovative Structures (ISIS) Manual*, No. 2. Winnipeg, Manitoba, Canada.

Jones, R, (1998). “Mechanics of Composite Materials” Taylor & Francis, 2nd Edition, PA, USA, 507 pages.

Keer, J. G., Chadwick, J. R., & Thompson, D. M. (1990). “Protection of Reinforcement by Concrete Repair Materials Against Chloride-Induced Corrosion”. *Corrosion of Reinforcement in Concrete*, pp. 420-432.

Khayat, K. H., & Feys, D. (Eds.). (2010). “Design, Production and Placement of Self-Consolidating Concrete”, Proceedings of SCC2010, Montreal, Canada, September 26-29, 2010 (Vol. 1). Springer Science & Business Media, 458 pages.

Khoe, C., Sen, R., & Bhethanabotla, V. (2012). “Oxygen Permeability of FRP-Concrete Repair Systems”. *Journal of Composites for Construction, Vol. 16, No.* 3, pp. 277-285.

Kluge, R. W., & Tuma, E. C. (1945). “Lapped Bar Splices in Concrete Beams”. *Journal of Research of the National Bureau of Standards*, Vol. 35, pp. 13-33.

Kozul, R., & Darwin, D. (1997). “Effects of Aggregate Type, Size, and Content on Concrete Strength and Fracture Energy”. University of Kansas Center for Research, Inc. Structural Engineering and Engineering Materials, No. 43, 85 pages.

Lukose, K., Gergely, P., and White, R. N. (1982). “Behavior of Reinforced Concrete Lapped Splices for Inelastic Cyclic Loading.” *Journal Proceedings*, Vol. 79, No. 5, pp. 355-365.

MacGregor, J.G. and Bartlett, F.M. (2000). “Reinforced Concrete Mechanics and Design”, First Edition, Prentice Hall Canada Inc., Toronto, Ontario, Canada, 2000, 1042 pages.

Malumbela, G., Alexander, M., & Moyo, P. (2011). “Serviceability of Corrosion-Affected RC Beams After Patch Repairs and FRPs Under Load”. *Materials and Structures*, Vol. 44, No. 1, pp. 331-349.

Mangant, P., & Elgarf, M. (1999). “Bond Characteristics of Corroded Reinforcement in Concrete Beams”. *Materials and Structures*, 32, pp. 89-97.

Mangat, P. S., & Elgarf, M. S. (1999). “Strength and Serviceability of Repaired Reinforced Concrete Beams Undergoing Reinforcement Corrosion”. *Magazine of concrete research*, Vol. *51*, *No.* 2, pp. 97-112.

Martin, J., Stanton, J., Mitra, N., and Lowes, L.N.(2007). “Experimental Testing to Determine Concrete Fracture Energy Using Simple Laboratory Test Setup”, ACI Materials Journal, Vol. 104, No.5, pp. 575 – 584.

Masoud, S., Soudki, K., & Topper, T. (2005). “Postrepair Fatigue Performance of FRP-Repaired Corroded RC Beams: Experimental and Analytical Investigation”. *ASCE Journal of Composites for Construction, Vol. 9, No.* 5, pp. 441 - 449.

Momayez, A., Ehsani, M. R., Ramezanianpour, A. A., & Rajaie, H. (2005). “Comparison of Methods for Evaluating Bond Strength Between Concrete Substrate and Repair Materials”. *Cement and concrete research*, Vol. *35, No.* 4, pp. 748-757.

Neville, A.M. (1997). “Aggregate Bond and Modulus of Elasticity of Concrete”, *ACI Materials Journal*, Vol. 94, No. 1, Jan. – Feb. 1997, pp. 71 – 74.

Nikbin, I. M., Beygi, M. H. A., Kazemi, M. T., Amiri, J. V., Rahmani, E., Rabbanifar, S., & Eslami, M. (2014). “Effect of Coarse Aggregate Volume on Fracture Behavior of Self Compacting Concrete”. *Construction and Building Materials*, *52*, pp. 137-145.

Orangun, C., J. Jirsa, and J. Breen. (1977). “A Reevaluation of test Data on Development Length and Splices.” *ACI Journal*, Vol. 74, No. 3, pp. 114-122.

Pacholka, K., Rezansoff, T., and Sparling, B. F. (1999). “Stirrup Distribution Across the Beam width in Tension Lap Splices.” *Canadian Journal of Civil Engineering*, Vol. *26, No.* 1, pp. 83-95.

Richard E. Prince (2012). “Using FRP Reinforcement for Structures” Retrieved from http://www.build-on-prince.com

RILEM. (1985). “Determination of the Fracture Energy of Mortar and Concrete by Means of Three-Point Bend Tests on Notched Beams”, RILEM Recommendation, *Materials and Structures*, Vol. 18, No. 106, 1985, pp. 287 – 290.

Rio, O., Andrade, C., Izquierdo, D., & Alonso, C. (2005). “Behavior of Patch-Repaired Concrete Structural Elements Under Increasing Static Loads to Flexural Failure”. *Journal of materials in civil engineering*, Vol. *17, No.* 2, pp. 168-177.

Rteil, Ahmad. (2002). “Analytical and Experimental Evaluation of Bond Strength of Tension Lap Splice in High Strength Concrete Wrapped With Fiber Reinforced Polymer.” MSc. Thesis, Department of Civil and Environmental Engineering, American University of Beirut.

Safiuddin, M., West, J. S., & Soudki, K. A. (2010). “Hardened Properties of Self Consolidating High Performance Concrete Including Rice Husk Ash”. *Cement and Concrete Composites*, Vol. 32, No. 9, pp. 708-717.

Sagoe-Crentsil, K.K., Brown, T., and Taylor, A.H. (2001). “Performance of Concrete Made with Commercially Produced Coarse Recycled Concrete Aggregate”, *Cement and Concrete Research*, Vol. 31. pp. 707 – 712.

Sakurada, T., Morohashi, N., and Tanaka, R. (1993). “Effect of Transverse Reinforcement on Bond Splitting Strength of Lap Splices.” *Transactions of the Japan Concrete Institute, 15,* pp. 573-580.

Seliem, H., Hosny, A., Rizkalla, S., Zia, P., Briggs, M., Miller, S., Darwin, D., Browning, J., Glass, G., Hoyt, K., Donnelly, K., and Jirsa, J. (2009). “Bond Characteristics of ASTM A1035 Steel Reinforcing Bars.” *ACI Structural Journal*, Vol. 106, No. 4, pp. 530-539.

Sharif, A., Rahman, M. K., Al-Gahtani, A. S., & Hameeduddin, M. (2006). “Behaviour of Patch Repair of Axially Loaded Reinforced Concrete Beams”. *Cement and Concrete Composites*, Vol. 28, No. 8, pp. 734-741.

Shin, H. C., & Wan, Z. (2010). “Interfacial Shear Bond Strength Between Old and New Concrete”. Fracture Mechanics of Concrete and Concrete Structures–Assessment, Durability, Monitoring and Retrofitting of Concrete Structures, *KCI*, Seoul, 6 pages

Soudki, K., & Sherwood, T. (2000). “Behaviour of Reinforced Concrete Beams Strengthened with Carbon Fiber Reinforced Polymer Laminates Subjected to Corrosion Damage”. *Canadian Journal of Civil Engineering, Vol. 27, No.* 5, pp. 1005 - 1010.

Sparling, B., and Rezansoff, T. (1986). “The Effect of Confinement on Lap Splices in Reversed Cyclic Loading.” *Canadian Journal of Civil Engineering*, Vol. 13, No. 6, pp. 681-692.

Tastani, S. P., and Pantazopoulou, S. J. (2012). “Reinforcement and Concrete Bond: State Determination along the Development Length.” *Journal of Structural Engineering*, Vol. *139, No.* 9, pp. 1567-1581.

Tepfers, R. (1973). “A Theory of Bond Applied to Overlapped Tensile Reinforcement Splices for Deformed Bars.” *Chalmers University of Technology*, Sweden. 328 pages.

Tepfers, R. (1988). “Overlap Splices for Ribbed Bars for Free Use in a Concrete Structure.” *Nordic Concrete Research*, Vol. 7, pp. 273-283.

Tocci, AD. (1981). “The Behavior and Strength of Lapped Splices in Reinforced Concrete Beams Subjected to Cyclic Loading.” PhD thesis, Cornell University, 512 pages.

TÜRK, K., Benli, A., & Calayir, Y. (2009). “Bond Strength of Tension Lap-Splices in Full Scale Self-Compacting Concrete Beams”. *Turkish Journal of Engineering and Environmental Sciences*, Vol. *32, No.* 6, pp. 377-386.

Uomoto, T., Tsuji, K., & Kakizawa, T. (1984). “Deterioration Mechanism of Concrete Structures Caused by Corrosion of Reinforcing Bars”. *Transactions of japan Concrete Institute*, *6*, pp. 163 - 170.

Valcuende, M., & Parra, C. (2009). “Bond Behaviour of Reinforcement in Self-Compacting Concretes”. *Construction and Building Materials*, Vol. *23, No.* 1, pp. 162-170.

Wahab, N., Topper, T., and Soudki, K. A. (2015). “Modelling experimental bond fatigue failures of concrete beams strengthened with NSM CFRP rods.” *Composites Part B: Engineering*, *70*, pp. 113-121.

West, J. S., Larosche, C. J., Koester, B. D., Breen, J. E., & Kreger, M. E. (1999). “State-of-the-Art Report about Durability of Post-Tensioned Bridge Substructures*”, Centre for Transportation Research Bureau of Engineering Research, University of Texas at Austin*. Research Report 1405-1, 172 pages.

Yamao, L. Chou, J. Niwa, C. (1984). “Experimental Study on Bond Stress Slip Relationship,” Proceedings of Japan Society of Civil Engineers, Vol. 343, pp. 219–228, 1984.

Zuo, J., & Darwin, D. (2000). “Splice Strength of Conventional and High Relative Rib Area Bars in Normal and High-strength Concrete”. *ACI Structural Journal*, Vol. *97, No.* 4, pp. 630-641.

Zhu, W., Sonebi, M., & Bartos, P. J. M. (2004). “Bond and Interfacial Properties of Reinforcement in Self-compacting Concrete”. *Materials and Structures*, Vol. *37, No.* 7, pp. 442-448.

Appendix A - Induced Corrosion

The time required to achieve a certain level of corrosion, using accelerated corrosion technique, was calculated based on Faraday's Law as follow:

$$m_l = \frac{MIT}{z\,F}$$

Where:

m_l: Mass loss (g)

M: The atomic weight of the metal = 56g for Fe

I: Corrosion current (A) = i x s_a

i: Corrosion current density (μA/cm^2)

s_a: The surface area of the corroded steel (cm^2)

T: Time (s)

z: The valence of the corroding metal (2 for iron)

F: Faraday's constant = 96,500 A.s

Example :

To calculate the time required to achieve 5% mass loss in 20M bar of 400 length and whereas the current density is 150μA/cm^2:

$s_a = \pi dl = \pi \times 2 \times 40 = 251.2\ cm^2$

$I = i \times s_a = 150 \times 251.2 = 38\ mA$

Area of the bar = 314 mm^2 = 3.14 cm^2

$$Mass\ loss\ (\%) = \frac{Mass\ loss\ (g)}{Original\ mass} \rightarrow Mass\ loss\ (g) = Mass\ loss\ (\%) \times Original\ mass$$

$Mass\ loss\ (\%) = 5\%$

$Original\ mass = Density \times Volumn = Density \times A \times L = 7.85 \frac{g}{cm^3} \times 3.14 cm^3 \times 40 cm = 986$ g

$Mass\ loss\ (g) = 0.05 \times 986 = 49\ g$

$$T = \frac{m_l ZF}{MI} = \frac{49 \times 2 \times 96500}{56 \times 38 \times 10^{-3}} = 4444078.95\ second = 52\ days$$

Accordingly, the time (days) required to achieve the following desired mass losses was as follows:

Mass loss (%)	**Time (days)**
5	52
10	105

Appendix B Statistical Analysis by ANOVA

Total sum of squares = sum of squares between groups + sum of squares within groups

	Group 1		Group 2		Group 3		Group 4	
	200 mm		250 mm		300 mm		350 mm	
Mix	β	(β – Avg)^2	β	(β – Avg)^2	β	(β – Avg)^2	Slope	(β – Avg)^2
M	0.0098	2.4336E-06	0.0099	1.3225E-06	0.0052	4.4944E-06	0.0095	2.25E-08
SCC1	-	-	0.0122	1.3225E-06	-	-	0.0098	2.25E-08
SCC2	0.0109	2.116E-07	-	-	0.006	1.7424E-06	-	-
SCC3	0.0119	2.916E-07	-	-	0.0081	6.084E-07	-	-
NC	0.012	4.096E-07	-	-	0.0075	3.24E-08	-	-
	Avg.	Total	Avg.	Total	Avg.	Total	Avg.	Total
	0.01136	0.000004052	0.01105	0.000002645	0.00732	0.000013028	0.00965	0.000000045

Sum of squares within Groups (SSW) = Total (group 1) + Total (group 2) + Total (group 3) + Total (group 4)

SSW = 0.0000112

Sample number	β	(β – Avg)2
1	0.0098	1.6E-07
2	0.0122	0.00000784
3	0.0109	0.00000225
4	0.0119	0.00000625
5	0.012	0.00000676
6	0.0099	0.00000025
7	0.0052	0.00001764
8	0.0098	1.6E-07
9	0.006	0.00001156
10	0.0081	0.00000169
11	0.0075	0.00000361
12	0.0095	1E-08
	Avg.	Total
	0.0094	0.00005818

Total sum of squares (TSS) = total of all groups = 0.00005818

Sum of squares between groups = Total sum of squares - sum of squares within groups

Sum of squares between groups = 0.00005818 - 0.0000112 = 0.00004698

Degrees of freedom (Numerator) = number of groups - 1 =4 – 1 = 3

$$\frac{Sum\ of\ squares\ between\ groups}{\text{Degrees of freedom (Numerator)}} = 0.000001566$$

Degree of freedom (Denominator) = number of samples - number of groups =12 – 4 = 8

$$\frac{Sum\ of\ squares\ within\ groups}{\text{Degrees of freedom (Denominator)}} = 0.0000014$$

$$F_{(3,8)} = \frac{0.0000156}{0.0000014} = 11.18$$

At degree of freedoms of 3 and 8, and at significance level of 5% ($\alpha = 0.05$),

The critical value (F_{crit}) = 4.07

Appendix C Bond Stress Distribution

Steps to calculate $\tau_{0,max}$ and c of the bond stress distribution of lap splice beam with 300 mm bonded length. The force distribution is shown in the Figure below.

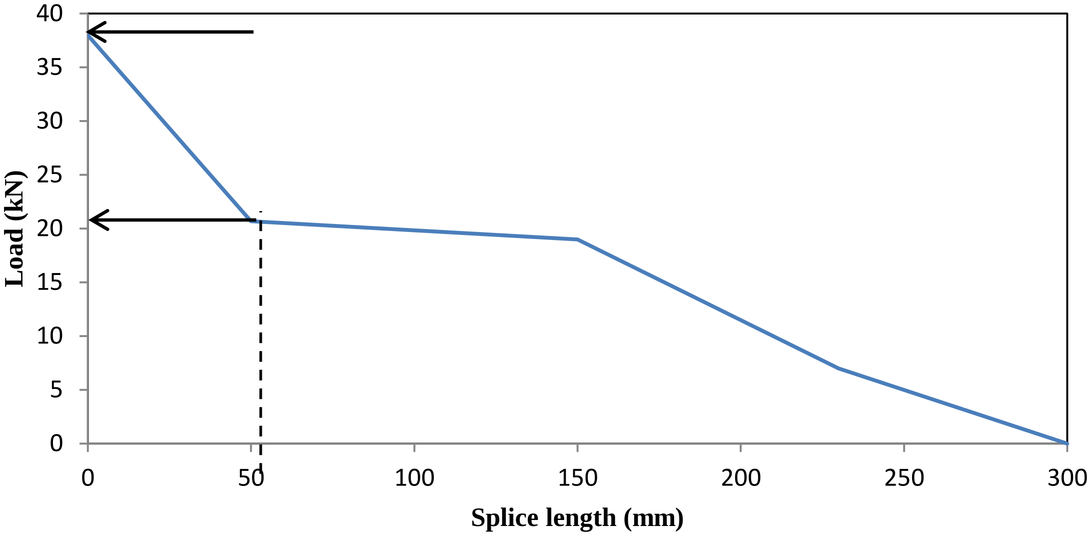

- Use the load immediately before cracking
- Use the two equilibrium conditions

$\sum F_{0-300} = F_{b0-300}$ (First condition, total force in the bar = total bond force)

$\sum F_{0-50} = F_{b0-50}$ (Second condition, change the force in the bar from 0 – 50 mm = change in bond force from 0-50 mm)

ΔF_{0-300}= 38-0 = 38,000 N -------- (A)

ΔF_{0-50} = 38-21 = 17,000 N -------- (B)

- Assume any values for $\tau_{0,max}$ and c
- Calculate

From 0 to 150 mm

$\tau_{(x)} = \tau_{o,max} e^{-C*x}$

From 150 to 300

$\tau_{(x)} = \tau_{o,max} e^{-C*(Ls - x)}$

- Calculate total bond force

  Total bond force $= \sum_{0}^{300} \tau_x \, \pi d l$ ----------- (1)

- Calculate bond force from 0 - 50 mm

  Bond force from 0 to 50 mm $= \sum_{0}^{50} \tau_x \, \pi d l$ ----------- (2)

Then, by Solver using Excel

Set (1) = (A) and (2) = (B) by changing $\tau_{0,max}$ and c

Appendix D: Normal Stress Distribution and Bond Stress Distribution of Lap Splice Beams

LS-M1-UN-7.5

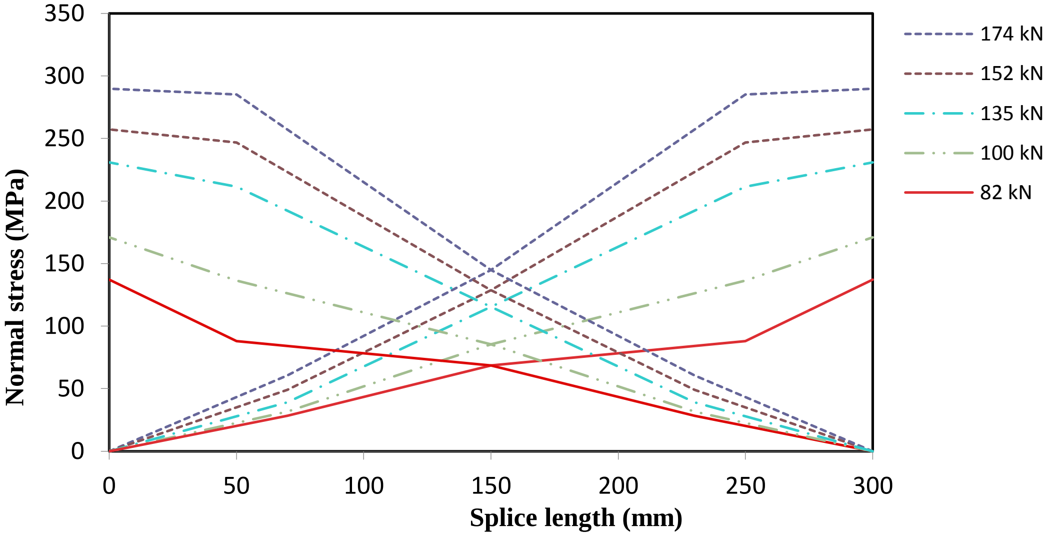

Normal stress distribution

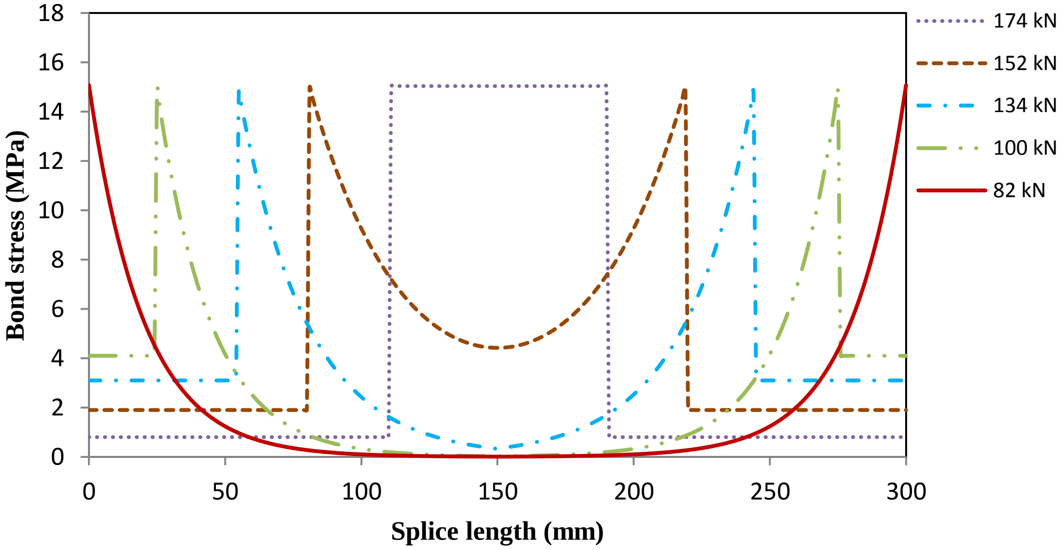

Bond stress distribution

LS-M1-UN-15

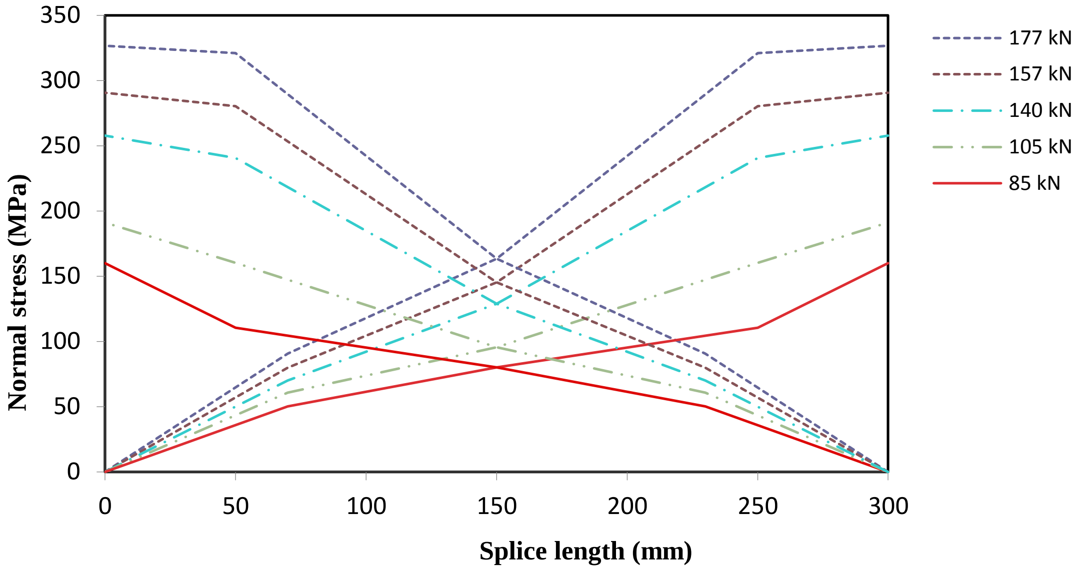

Normal stress distribution

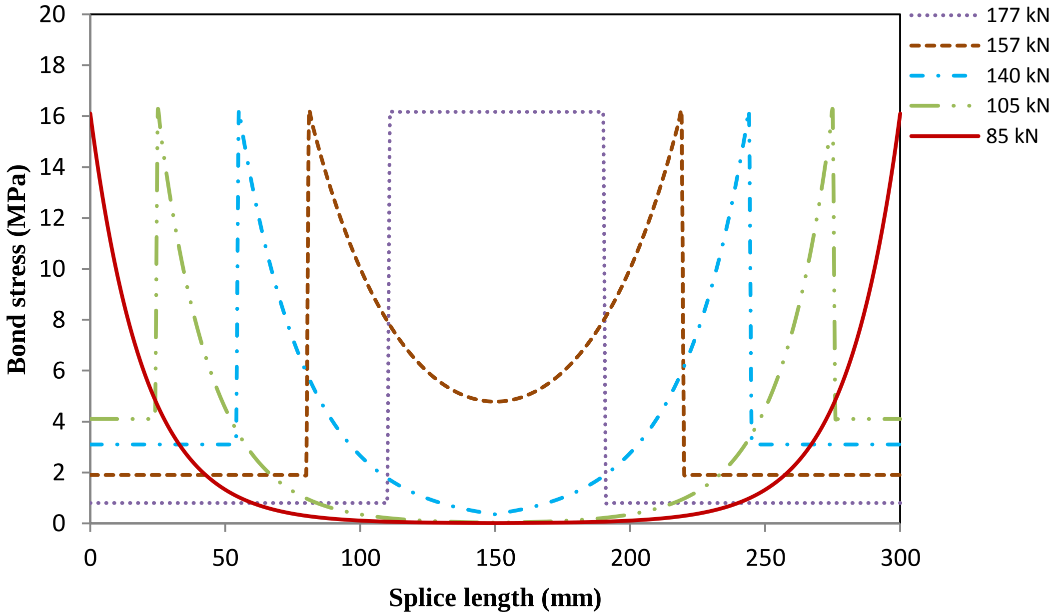

Bond stress distribution

LS-SCC50-UN-C

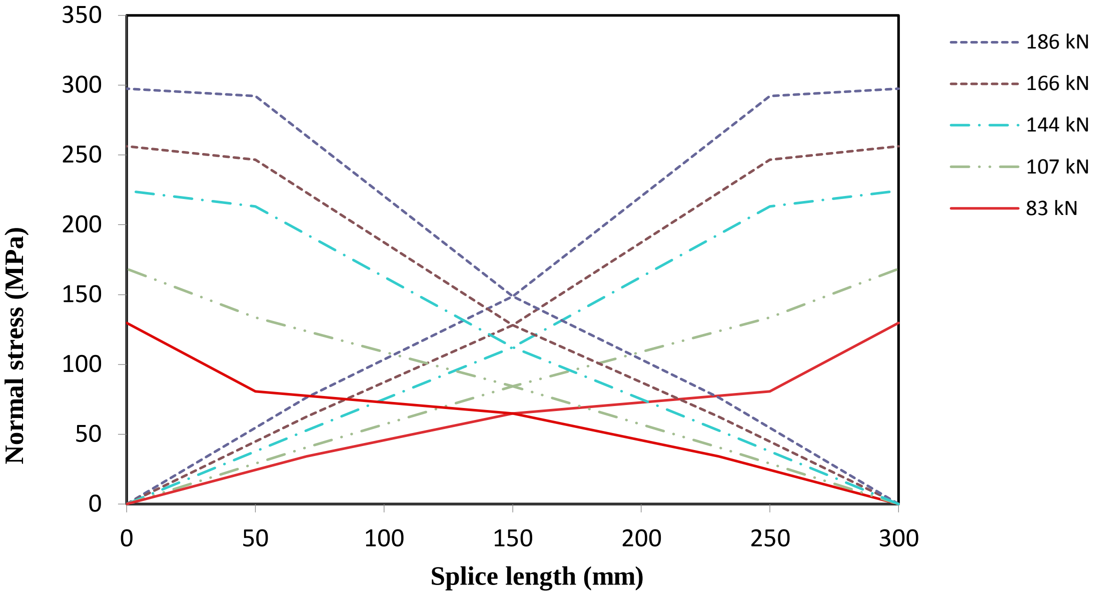

Normal stress distribution

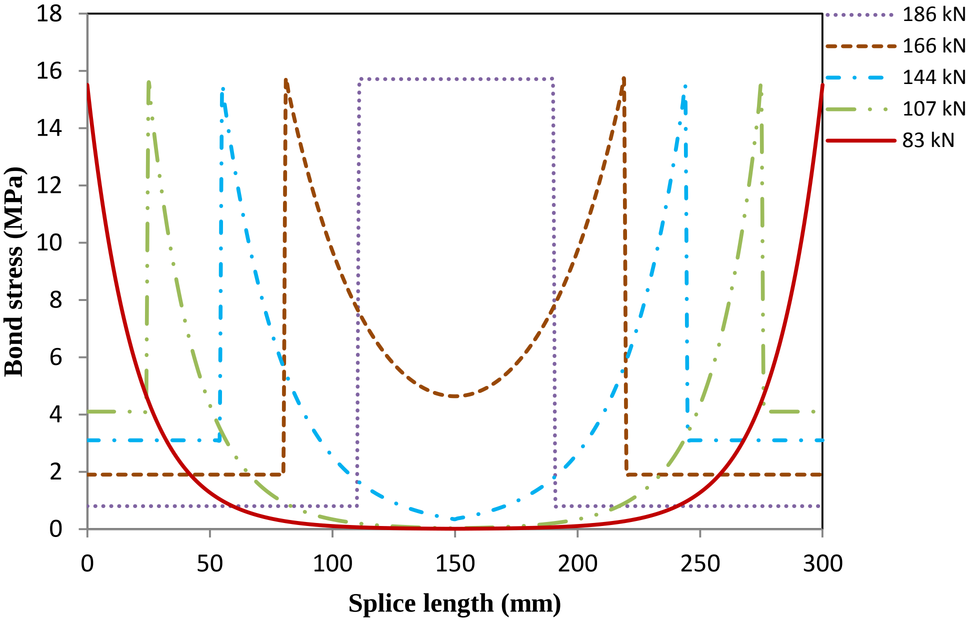

Bond stress distribution

LS-SCC50-UN-7.5%

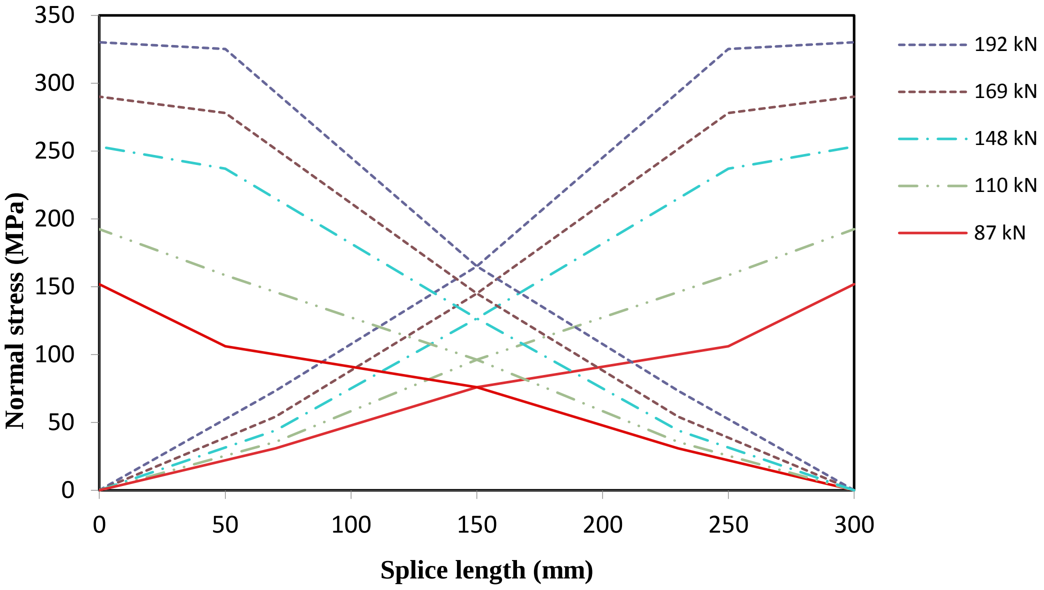

Normal stress distribution

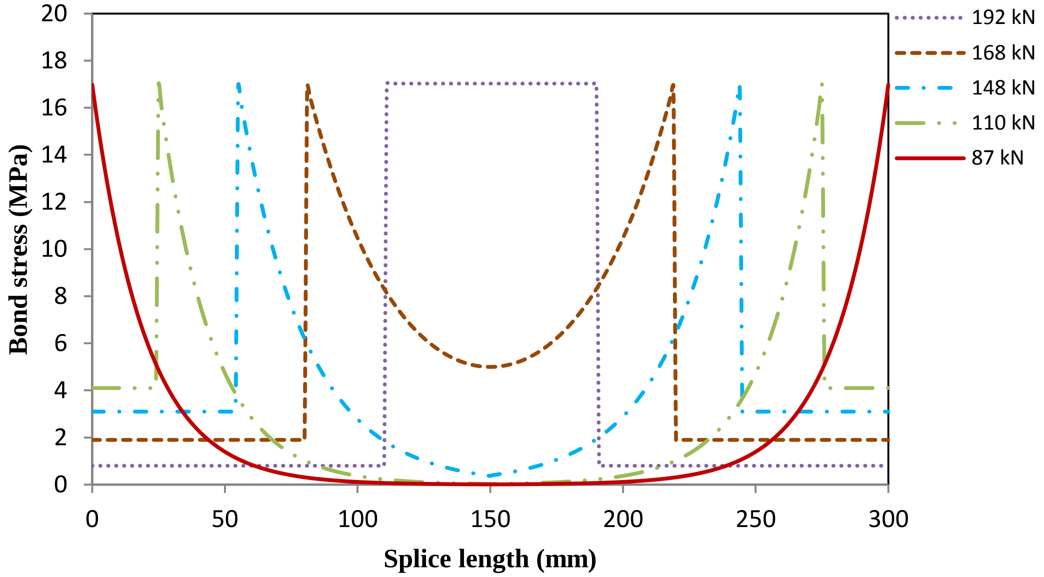

Bond stress distribution

LS-SCC50-UN-15%

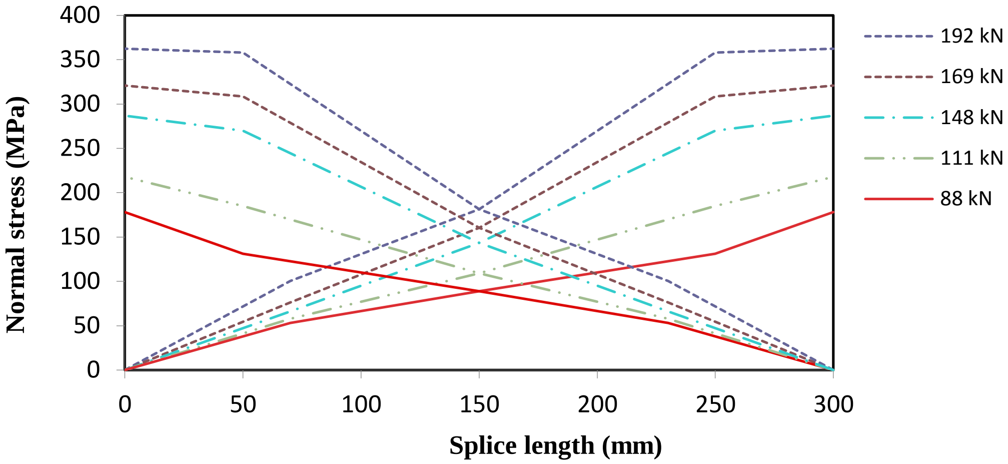

Normal stress distribution

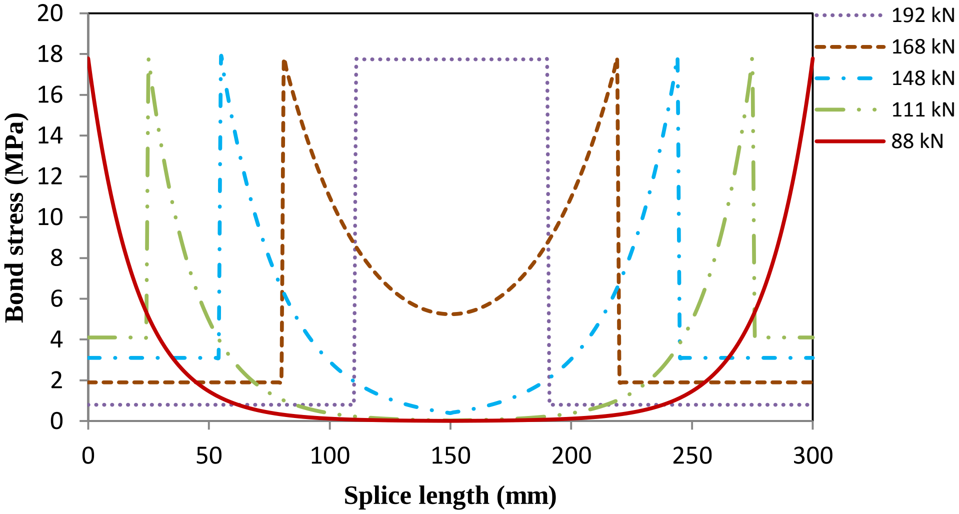

Bond stress distribution

LS-SCC0-UN-C

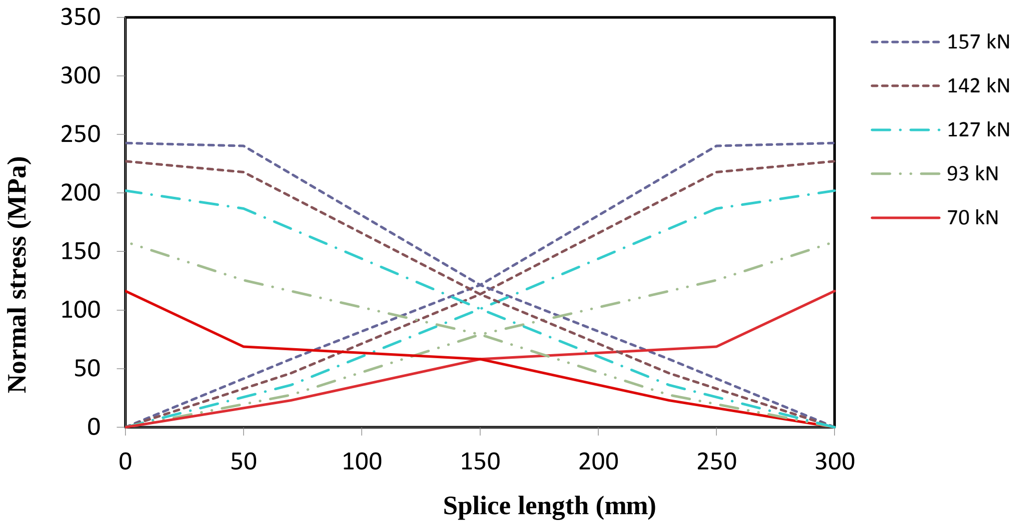

Normal stress distribution

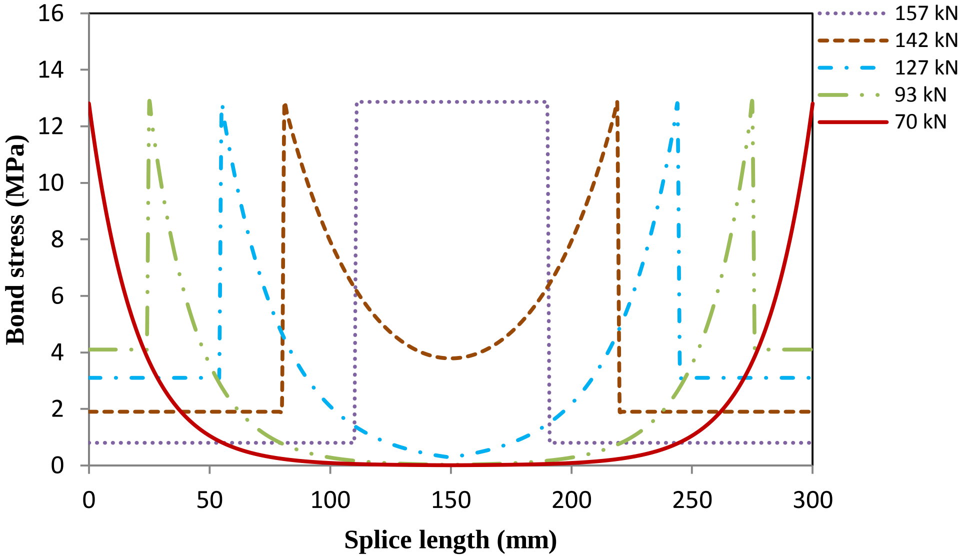

Bond stress distribution

LS-SCC0-UN-7.5%

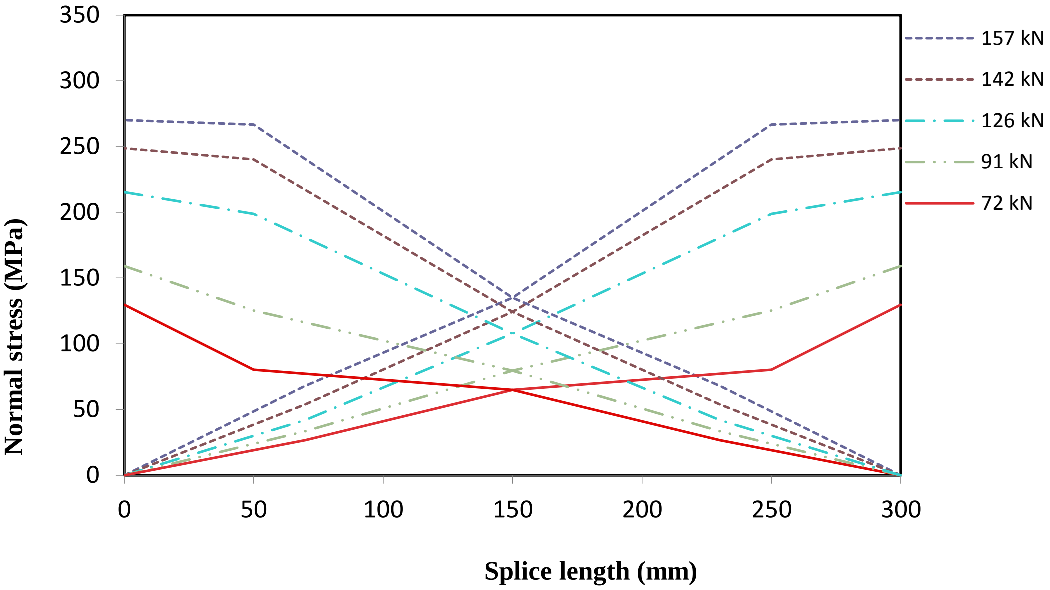

Normal stress distribution

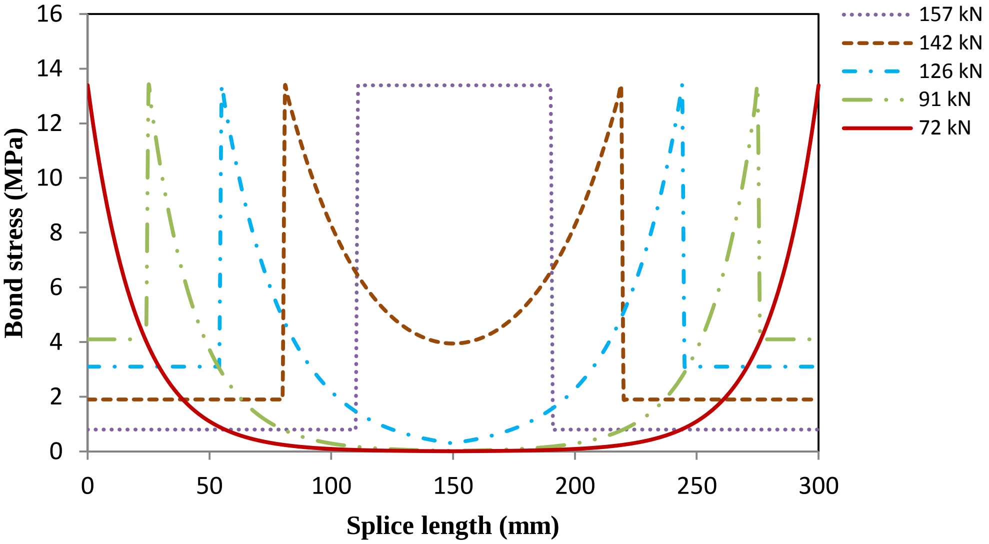

Bond stress distribution

LS-SCC0-UN-15%

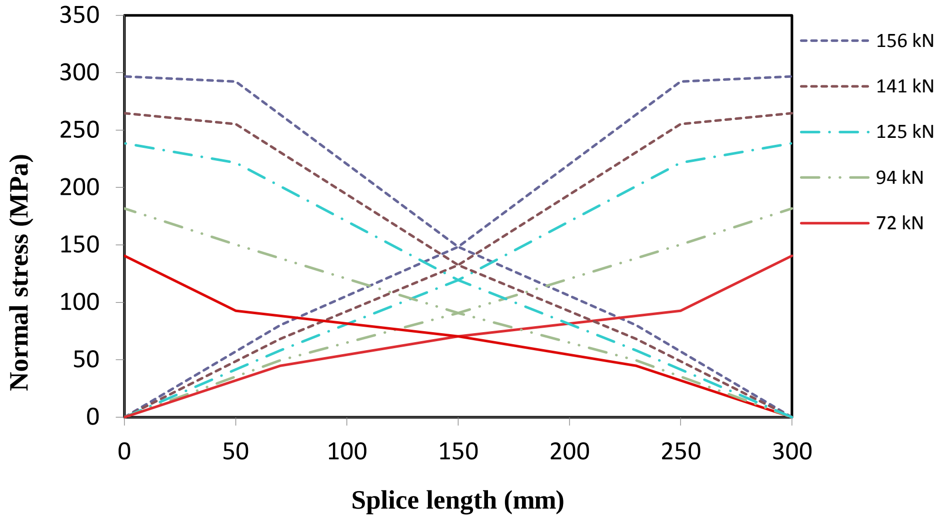

Normal stress distribution

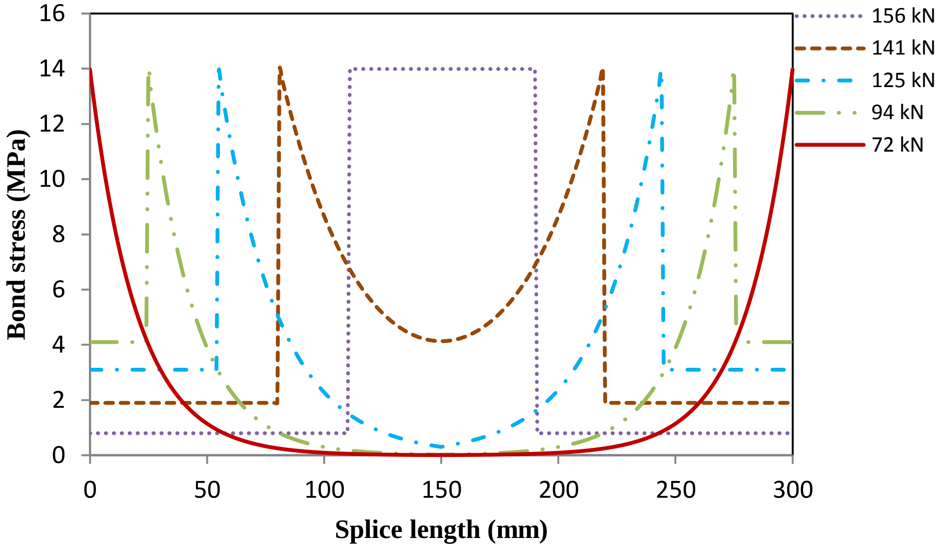

Bond stress distribution

LS.M2-T-7.5

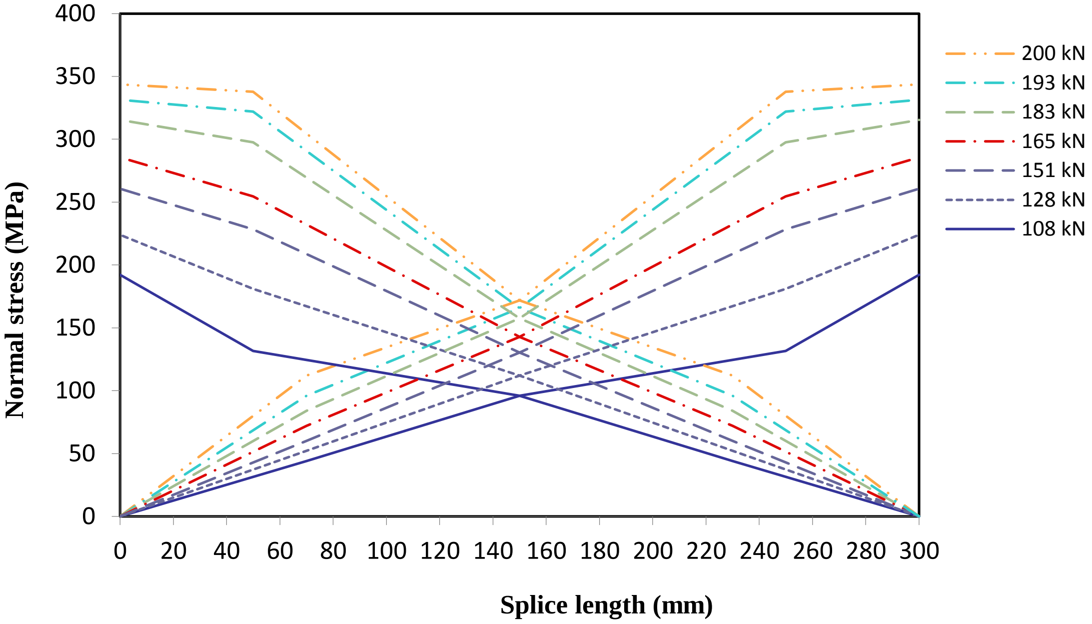

Normal stress distribution

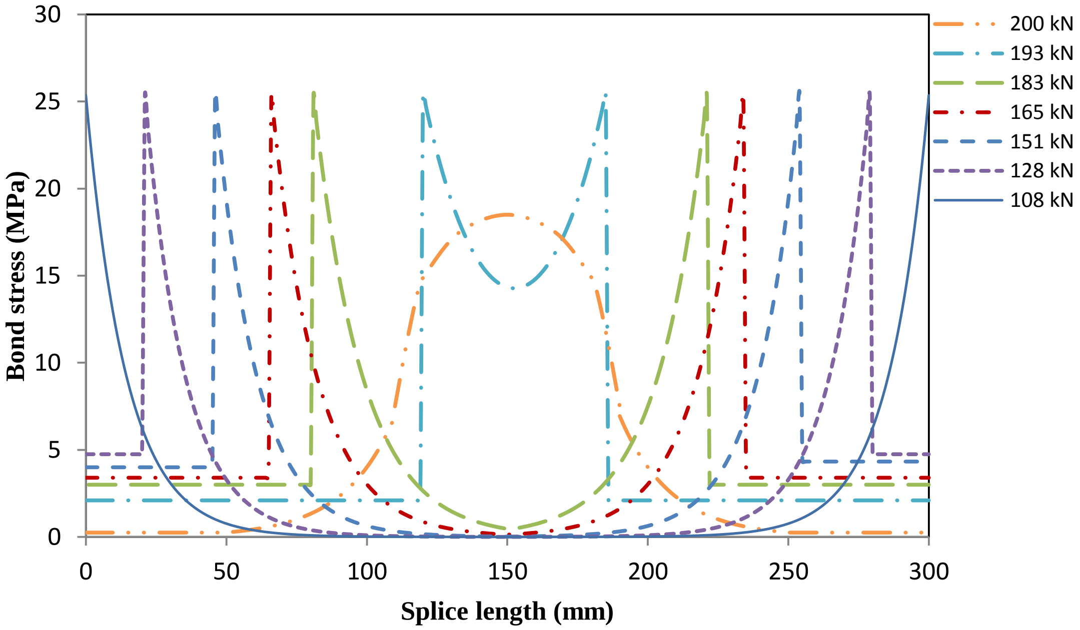

Bond stress distribution

LS.M2-T-15

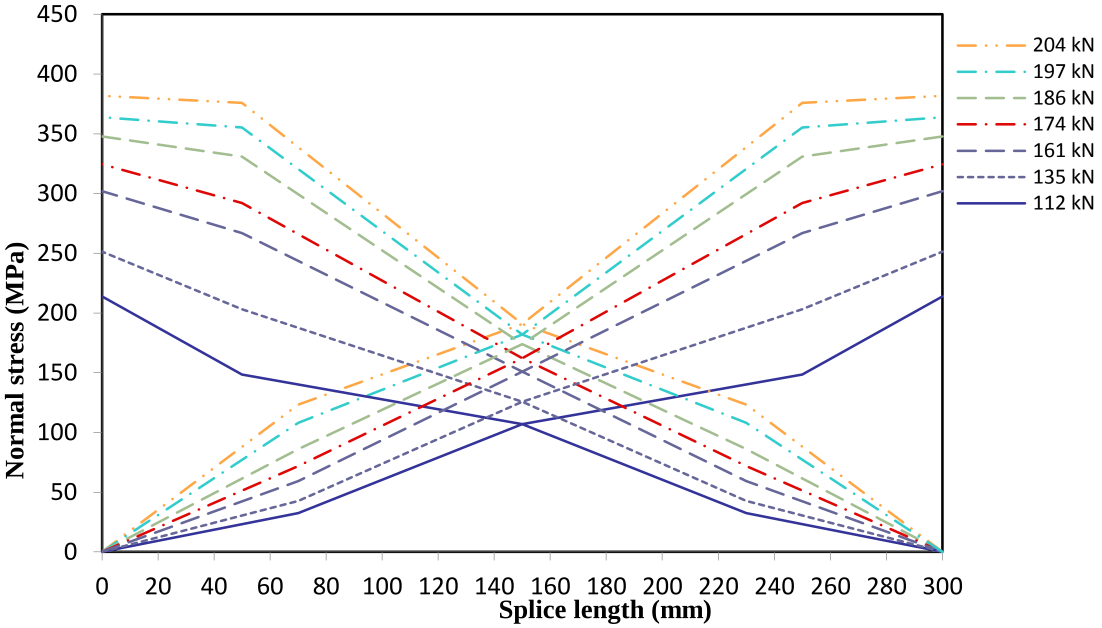

Normal stress distribution

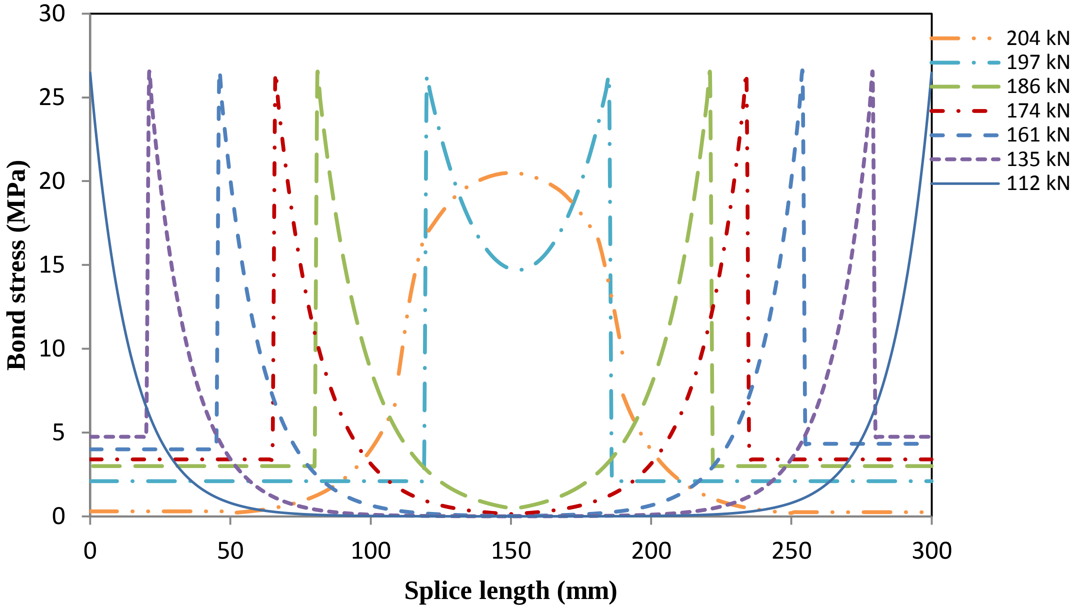

Bond stress distribution

LS.SCC50-T-C

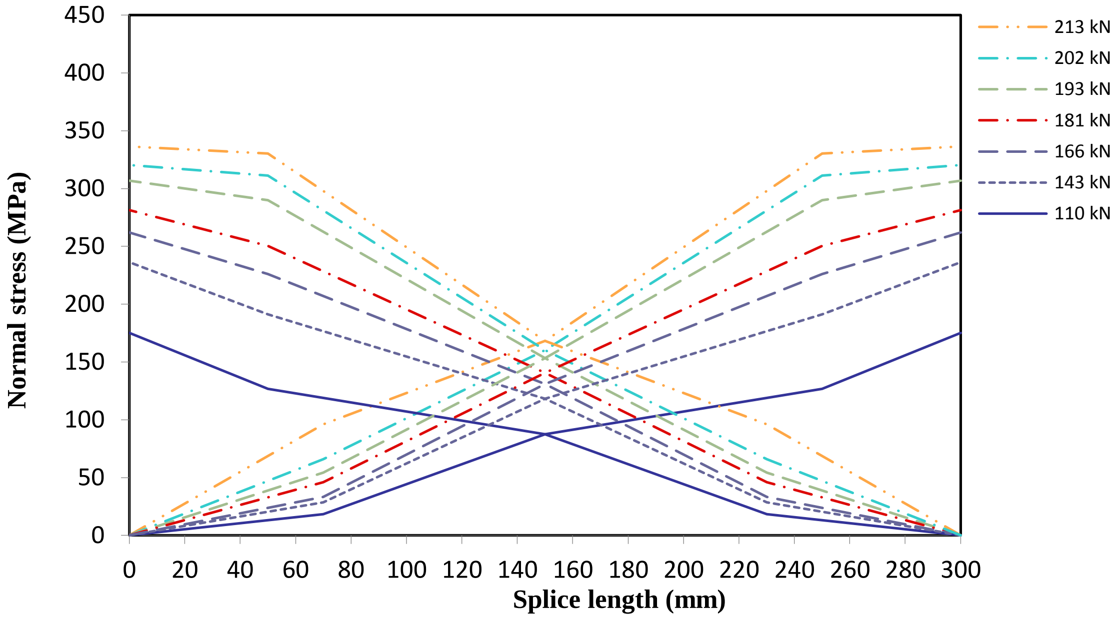

Normal stress distribution

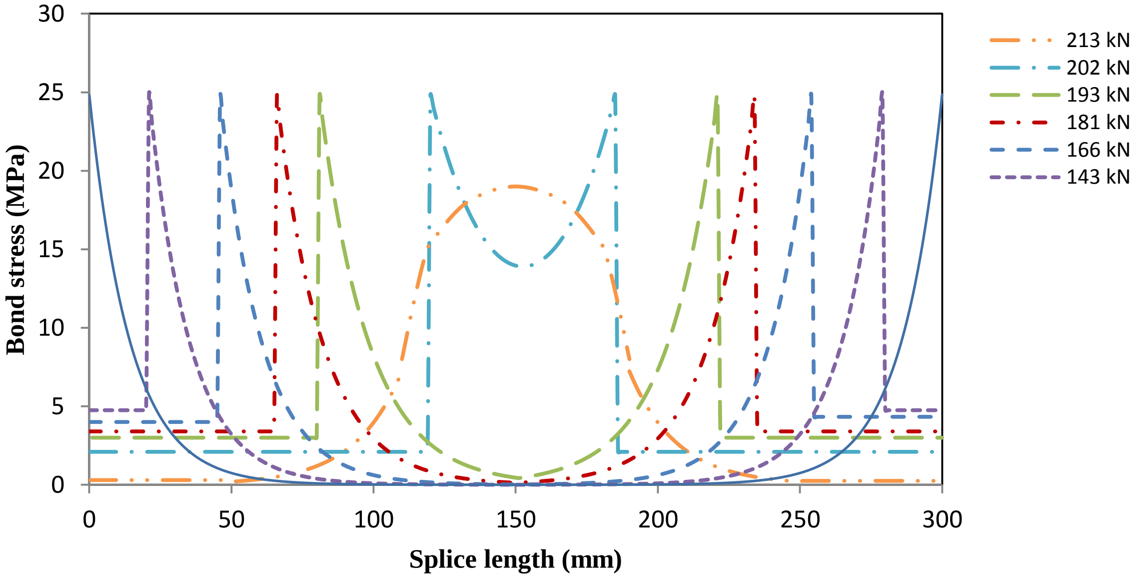

Bond stress distribution

LS.SCC50-T-7.5

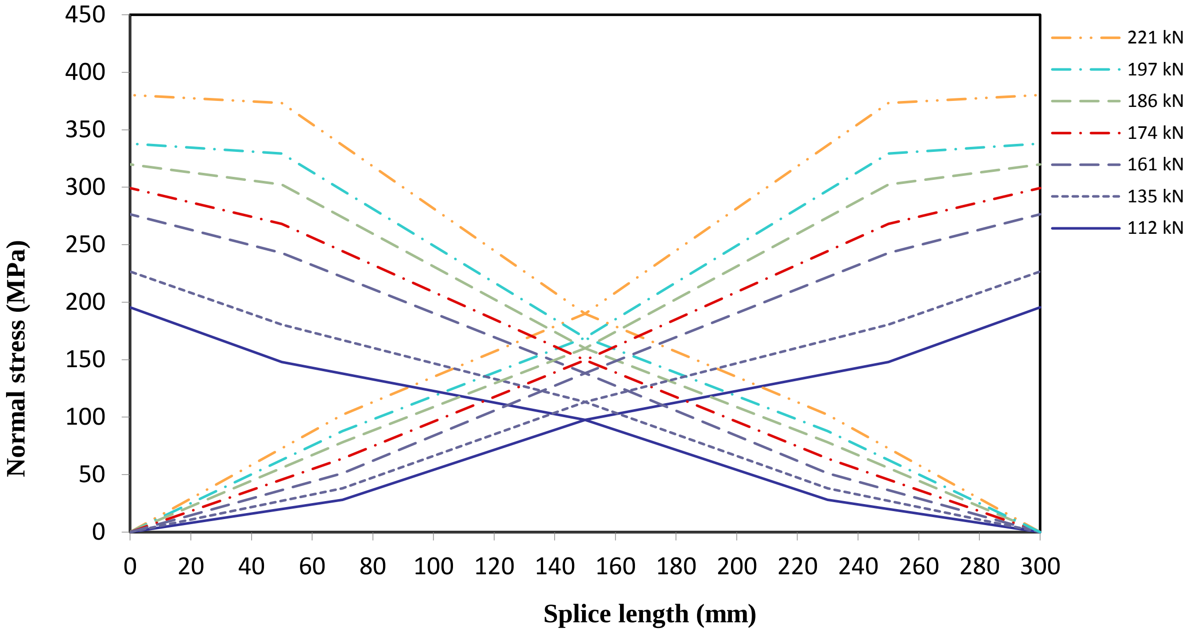

Normal stress distribution

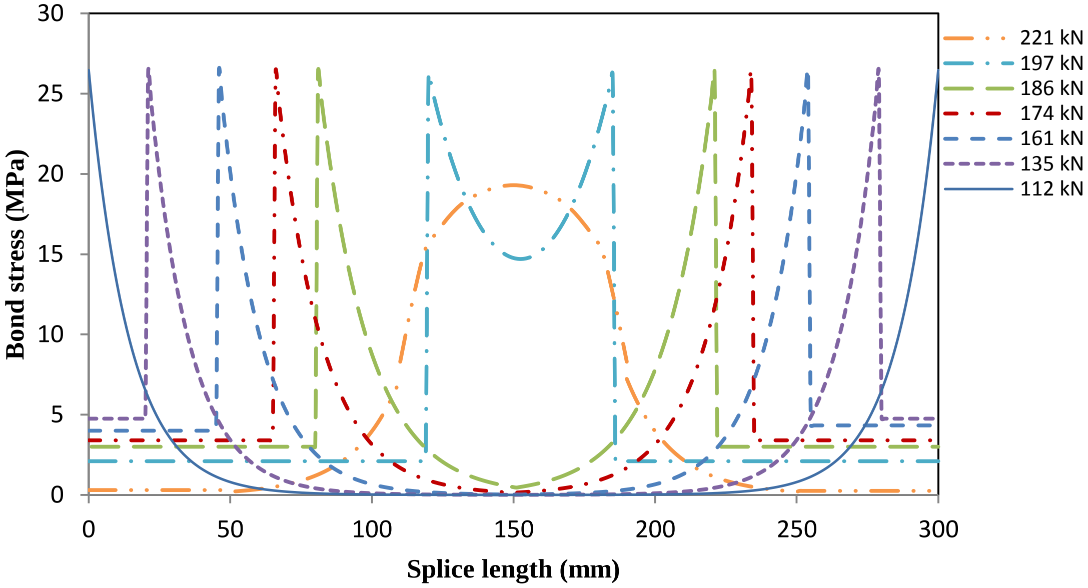

Bond stress distribution

LS.SCC50-T-15

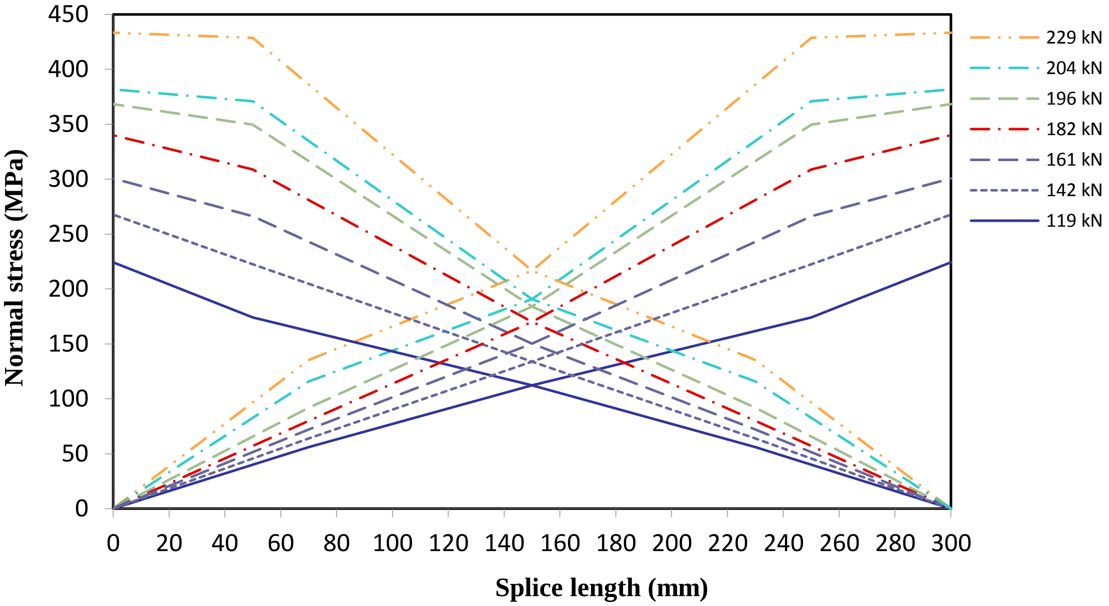

Normal stress distribution

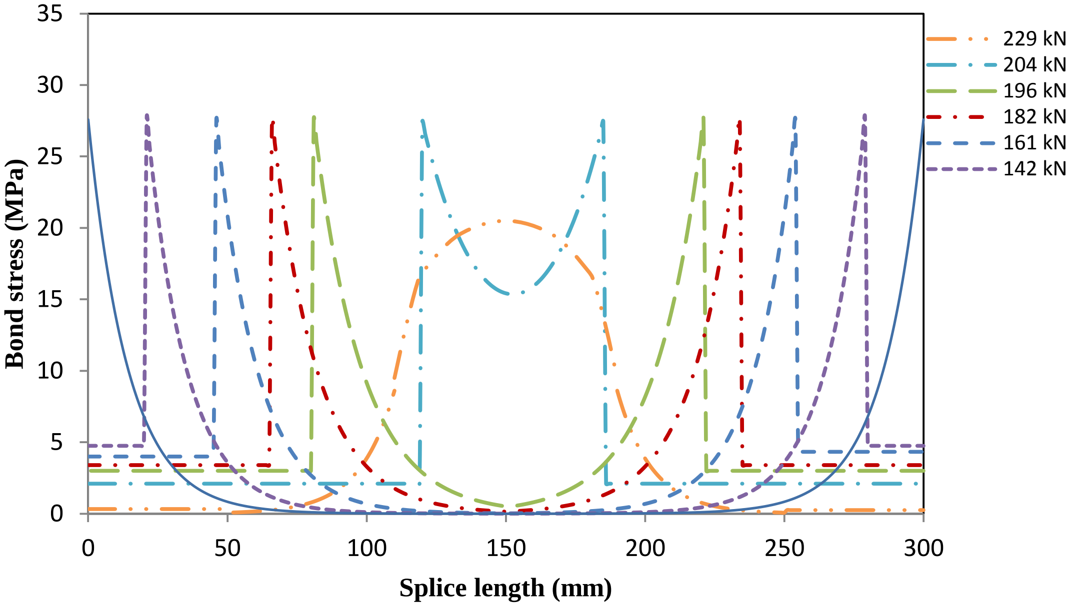

Bond stress distribution